

UNIVERSITY OF BIRMINGHAM

DECIPHEPHERING INHERITABLE DRIVERS OF ATRIAL ARRHYTHMIA - FROM CELLULAR MICRODOMAINS IN MODELS TO PHENOTYPES IN PATIENTS

by

LAURA CHARLOTTE SOMMERFELD

A thesis submitted to the University of Birmingham for the degree of

DOCTOR OF PHILOSOPHY

Institute of Cardiovascular Sciences

College of Medical and Dental Sciences

University of Birmingham, United Kingdom

September 2022

UNIVERSITY OF
BIRMINGHAM

University of Birmingham Research Archive

e-theses repository

This unpublished thesis/dissertation is copyright of the author and/or third parties. The intellectual property rights of the author or third parties in respect of this work are as defined by The Copyright Designs and Patents Act 1988 or as modified by any successor legislation.

Any use made of information contained in this thesis/dissertation must be in accordance with that legislation and must be properly acknowledged. Further distribution or reproduction in any format is prohibited without the permission of the copyright holder.

Table of Content

Table of Content i
List of Figures (excluding those in publications and preprints) iii
Declaration iv
Acknowledgements v
Abstract 1
Project Outcomes 2
1 Chapter I - Introduction 6
1.1 Cardiac action potentials and arrhythmia syndromes 7
1.2 Arrhythmogenic Right Ventricular Cardiomyopathy (ARVC) 8
1.2.1 Desmosomes, area composita and intercalated disc 9
1.2.2 Plakoglobin 14
1.2.3 Plakoglobin and ARVC 14
1.2.4 Heterozygous plakoglobin-deficient mice as a model for ARVC 15
1.2.5 Atrial arrhythmia in ARVC 16
1.3 Atrial fibrillation and arrhythmia mechanisms 17
1.3.1 Ectopic activity: abnormal action potential triggering 18
1.3.2 Re-entry: abnormal action potential propagation 19
1.3.3 Genetic factors and hereditability of AF 20
1.3.4 Cardiac voltage-gated sodium channel and links to AF 21
1.3.5 Point mutation in the cardiac sodium channel associated with familial atrial fibrillation 23
1.4 Modifiers of disease penetrance and clinical outcome 24
1.5 Thesis motivation and structure 26
1.6 References Chapter I 29
2 Chapter II - Continuation of the introduction: Medical therapy in Arrhythmogenic Right Ventricular Cardiomyopathy (ARVC) 35
3 Chapter III - Methods: Effects of genetic background, sex and age on murine atrial electrophysiology 46
4 Chapter IV - Methods: High resolution optical mapping of cardiac electrophysiology in pre-clinical models 76
5 Chapter V - Methods: JavaCyte, a novel open-source tool for automated quantification of key hallmarks of cardiac structural remodeling 104
6 Chapter VI - Results: Male sex hormone and reduced plakoglobin jointly impair atrial conduction and cardiac sodium currents 132
7 Chapter VII - Results: Familial atrial fibrillation mutation M1875T-SCN5A increases early sodium current and dampens the effect of flecainide 201

8 Chapter VIII - Conclusions 244
8.1 Thesis outcomes 244
8.2 General conclusions and limitations 245
8.2.1 Limitations of electrophysiological studies in murine models 245
8.2.2 Eligibility of murine models to decipher ARVC 246
8.2.3 Eligibility of murine models to decipher AF 247
8.3 Outlook 248
8.4 References Chapter VIII 252

List of Figures (excluding those in publications and preprints)

Figure 1: Cross-sectional view of the human heart and atrial and ventricular action potentials with underlying currents 7
Figure 2: Traditional model of the intercalated disc connecting adjacent cardiomyocytes 10
Figure 3: Molecular components of the cardiac desmosome 11
Figure 4: Molecules in the intercalated disc region of cardiomyocytes 12
Figure 5: Crystal structure of the plakoglobin arm domain and identified ARVC-causing mutations .. 15
Figure 6: Normal ventricular action potential (black) with possible EAD and DAD (green) 18
Figure 7: Cardiac wavelength and the influence of the effective refractory period (ERP) and conduction velocity (CV) 19
Figure 8: Alpha subunit of the voltage-gated sodium channel 21
Figure 9: Interacting Nav1.5 C-termini leading to proposed formation of homo-dimers 22
Figure 10: Close-up of the proposed Nav1.5 C-terminal interaction site for homo-dimer formation . 23

Declaration

I hereby declare that the work presented here in this thesis titled,

"DECIPHEPHERING INHERITABLE DRIVERS OF ATRIAL ARRHYTHMIA -
FROM CELLULAR MICRODOMAINS IN MODELS TO PHENOTYPES IN PATIENTS"

is the work of my own, unless otherwise stated. The work here was written and submitted by me to the School of Medical and Dental Sciences, University of Birmingham, United Kingdom, as fulfilment of the degree of Doctor of Philosophy. I further declare that this work has not been submitted to any other university for the award of any other degree, diploma or equivalent course



Laura Charlotte Sommerfeld

Acknowledgements

First and foremost, I would like to express my sincere thanks to Prof Larissa Fabritz. Thank you for not only providing the strongest support on so many levels during the past years, but also for putting me in a supportive network. I appreciate the generous support to participate in numerous meetings and being introduced to internationally renowned experts in the field. You taught me the value of collaboration and international networks and made me feel like a valued member of the group right from the start. Thank you for all the trust and flexibility when it came to adapting to circumstances.

A special note of thanks goes to Dr Katja Gehmlich, Dr James Winter and Dr Martyn Chidgey for additional superb supervision as well as Dr Katharine Dibb and Prof Niels Voigt for taking on the role as examiners for this thesis.

A heartfelt 'Thank you' to the whole Translational Research on Heart Failure and Arrhythmias Cluster for a warm welcome in Birmingham, scientific discussions, rehearsals, friendly advice, helpful criticism, transfer of lab skills and introduction to British culture and vocabulary: Prof Paulus Kirchhof, Dr Davor Pavlovic, Dr Andrew Holmes, Dr Christopher O'Shea, Dr Winnie Chua, Nashitha Kabir, Dr Molly O'Reilly, Dr Daniel Johnson, Dr Jasmeet Reyat, Dr Sophie Broadway-Stringer, Amar Azad, Dr Jonathan Law, Areej Aljehani, Tania Kew and Dr Claire Hepburn.

Thanks to the COMPARE members Dr Jeremy Pike and Dr Deirdre Kavanagh for all your expert help and for fueling my fascination for microscopy.

I am also grateful to the BMSU and ICVS infrastructure and administrative team, including Donna Wiles, Christine Lloyd and Helen Matthews.

Thank you, Dr Lisa Fortmüller for all your help as well as teaching - remotely - even before it became the new normal for the rest of the world.

I would like to extend my grateful thanks to Hartwig Wieboldt for all the support and high spirits during the past year.

I feel incredibly fortunate to have received invaluable years of training in Göttingen which has been instrumental in putting me in a position to feel prepared to take on a PhD abroad. Prof Susanne Lutz, I will always be grateful for your care and encouragement.

I also want to acknowledge the scientific community I met along the way; people from all over the world united in open-mindedness, ambition and dedication to tackle complex tasks. You truly impress me.

To my peers I met along the way in Göttingen, Birmingham and Hamburg and can proudly call my friends now: Thank you. I feel so lucky to have crossed your path. You certainly always have my back and bring so much joy to my life. This thesis would not have been completed without you.

- Danke, dass ich von Euch allen lernen durfte und darf. -

Abstract

Background and Aim

Atrial fibrillation (AF), the most common sustained cardiac arrhythmia, is a frequent symptom of inheritable cardiac arrhythmia syndromes. The clinical picture of AF develops due to a multitude of mechanisms which are aggravated by external factors and comorbidities, complicating explanatory research. Hence, studying inheritable drivers of atrial arrhythmia represents a valuable approach to pinpoint molecular pathomechanisms of AF.

Aim of this thesis therefore was to gain knowledge on atrial arrhythmia mechanisms driven by genetic predisposition. Additionally, we set out to investigate the impact of elevated androgenic steroid concentrations as an extrinsic factor.

Methods

Clinical observations were used as a basis for murine experimental study designs. Employing two murine models, one for arrhythmogenic right ventricular cardiomyopathy (ARVC) and one for familial AF, enabled us to study atrial arrhythmia mechanisms at different scale, from in vivo to ex vivo, from the living animal to ion channels in atrial cardiomyocytes. Effects of the mutations and interventions on atrial structure, function and electrophysiology were revealed by a variety of methods, including echocardiography, electrocardiograms (ECGs), optical mapping, monophasic action potential recordings, histology, RNA sequencing and super-resolution microscopy. Moreover, atrial involvement in human ARVC was studied in digital patient ECGs.

Results and Conclusions

Atrial arrhythmias are a common clinical feature of ARVC and are accompanied by impaired conduction, observed in both, patients and the murine model. Vulnerable desmosomes and increased concentrations of androgenic steroids jointly impair atrial conduction and cardiac sodium current.

The studied point mutation of the cardiac sodium channel alpha-subunit $Na_v1.5$, associated with familial AF, leads to a gain-of-function and atria show a blunted response to the clinically used sodium channel blocker flecainide.

Our findings underline that murine models represent a valuable tool to decipher drivers of atrial arrhythmia seen in patients.

Project Outcomes

The following publications / preprints constitute this thesis:

Book chapter (Chapter II)
Medical therapy in ARVC.
Laura Sommerfeld, Areej Aljehani, Manish Kalla, Larissa Fabritz. Published in Current Concepts in Arrhythmogenic Cardiomyopathy, Second Edition. Cardiotext Publishing. 2020

Publication 1 (Chapter III)
Effects of genetic background, sex, and age on murine atrial electrophysiology.
Obergassel J, O'Reilly M, **Sommerfeld LC**, Kabir SN, O'Shea C, Syeda F, Eckardt L, Kirchhof P, Fabritz L. Europace. 2021 Jan 19. pii: 6104222. doi: 10.1093/europace/euaa369.

Publication 2 (Chapter IV)
High resolution optical mapping of cardiac electrophysiology in pre-clinical models.
O'Shea C, Winter J, Kabir SN, O'Reilly M, Wells SP, Baines O, **Sommerfeld LC**, Correia J, Lei M, Kirchhof P, Holmes AP, Fabritz L, Rajpoot K, Pavlovic D. Sci Data. 2022 Mar 31;9(1):135. doi: 10.1038/s41597-022-01253-1.

Publication 3 (Chapter V)
JavaCyte, a novel open-source tool for automated quantification of key hallmarks of cardiac structural remodelling.
Winters J, von Braunmuhl ME, Zeemering S, Gilbers M, Brink TT, Scaf B, Guasch E, Mont L, Batlle M, Sinner M, Hatem S, Mansour MK, Fabritz L, **Sommerfeld LC**, Kirchhof P, Isaacs A, Stoll M, Schotten U, Verheule S. Sci Rep. 2020 Nov 18;10(1):20074. doi: 10.1038/s41598-020-76932-3.

Preprint 1 (Chapter VI)
Male sex hormone and reduced plakoglobin jointly impair atrial conduction and cardiac sodium currents.
Sommerfeld LC, Holmes AP, Yu TY, O'Shea C, Kavanagh DM, Pike JA, Wright T, Syeda F, Aljehani A, Kew T, Cardoso VR, Kabir SN, Hepburn C, Menon PM, Broadway-Stringer S, O'Reilly M, Witten A, Fortmueller L, Lutz S, Kulle A, Gkoutos GV, Pavlovic D, Arlt W, Lavery GG, Steeds R, Gehmlich K, Stoll M, Kirchhof P, Fabritz L. biorXiv. 2022, doi: 10.1101/2022.06.03.494748

Preprint 2, in revision (Chapter VII)
Familial atrial fibrillation mutation M1875T-SCN5A increases early sodium current and dampens the effect of flecainide.
O'Reilly M*, **Sommerfeld LC***, O'Shea C, Broadway-Stringer S, Andaleeb S, Reyat JS, Kabir SN, Stastny D, Malinova A, Delbue D, Fortmueller L, Gehmlich K, Pavlovic D, Skryabin BV, Holmes AP, Kirchhof P, Fabritz L. biorXiv. 2022, doi: 10.1101/2022.01.18.476646

*These authors share first authorship

Through work undertaken for this thesis, the following additional outputs have been produced:

Publication

Diminished PLK2 Induces Cardiac Fibrosis and Promotes Atrial Fibrillation.
Kunzel SR, Hoffmann M, Weber S, Kunzel K, Kammerer S, Gunscht M, Klapproth E, Rausch JSE, Sadek MS, Kolanowski T, Meyer-Roxlau S, Piorkowski C, Tugtekin SM, Rose-John S, Yin X, Mayr M, Kuhlmann JD, Wimberger P, Grutzmann K, Herzog N, Kupper JH, O'Reilly M, Kabir SN, **Sommerfeld LC**, Guan K, Wielockx B, Fabritz L, Nattel S, Ravens U, Dobrev D, Wagner M, El-Armouche A. Circ Res. 2021 Oct;129(8):804-820. doi: 10.1161/CIRCRESAHA.121.319425.

Preprint

Characterisation of Patients Referred to a Tertiary-Level Inherited Cardiac Condition Clinic with Suspected Arrhythmogenic Right Ventricular Cardiomyopathy (ARVC).
Aljehani A, Kew T, Baig S, Cox H, **Sommerfeld LC**, Ensam B, Kalla M, Steed R, Fabritz L. 25 July 2022, PREPRINT (Version 1) available at Research Square [https://doi.org/10.21203/rs.3.rs-1804660/v1]

Published Abstracts

The SCN5A point mutation M1875T, associated with familial atrial fibrillation, causes a gain-of-function effect of the cardiac Nav1.5 channel in atrial cardiomyocytes.
O'Reilly M, **Sommerfeld LC**, O'Shea C, Broadway-Stringer S, Andaleeb S, Malinova A, Reyat JS, Fortmueller L, Pavlovic D, Skryabin BV, Holmes AP, Kirchhof P, Fabritz L. May 2021. Europace 23 (Supplement 3), doi: 10.1093/europace/euab116.547

Desmosomal vulnerability renders left atria more susceptible to detrimental effects of androgenic anabolic steroids.
Sommerfeld LC, Holmes AP, Kavanagh DM, Pike JA, O'Shea C, Cardoso VR, Kabir, Kabir SN, Pavlovic D, Gehmlich K, Stoll M, Gkoutos GV, Kirchhof P, Fabritz L. May 2021. Europace 23 (Supplement 3), doi: 10.1093/europace/euab116.551

Effect of age, genetic background and experimental conditions on left atrial monophasic action potential duration, effective refractory period and activation time in Langendorff-perfused murine hearts.
Obergassel J, Kabir SN, O'Reilly M, **Sommerfeld LC**, O'Shea C, Eckardt L, Kirchhof P, Fabritz L. June 2020. Europace 22 (Supplement 1), doi: 10.1093/europace/euaa162.172

Conference and scientific meeting presentations

- Posters

10/2019 Annual Meeting of the German Cardiac Society (DGK), Basic Science Meeting
Berlin, Germany
"Androgenic anabolic steroids induce atrial sodium channel remodelling in plakoglobin-deficient mice"

03/2019 Dutch-German Joint Meeting of the Molecular Cardiology Working Groups
Göttingen, Germany
"Plakoglobin deficiency predisposes to cardiac sodium channel remodelling in response to androgenic anabolic steroids"

03/2020 Dutch-German Joint Meeting of the Molecular Cardiology Working Groups
Utrecht, Netherlands - accepted for poster presentation, cancelled due to pandemic
"Androgenic anabolic steroids impair sodium channel localization at the membrane of plakoglobin-deficient atrial cardiomyocytes"

06/2022 Annual Meeting of the European Working Group on Cardiac Cellular Electrophysiology (EWGCCE)
Toledo, Spain
"Atrial fibrillation in arrhythmogenic right ventricular cardiomyopathy (ARVC) patients"

- Oral talks

09/2019 Foundation Leducq Transatlantic Network of Excellence, Deciphering the Genomic Topology of Atrial Fibrillation
Athens, Greece
"Atrial cardiomyocyte STORM"

03/2020 Pre-Meeting of the Dutch-German Joint Meeting of the Molecular Cardiology Working Groups
Utrecht, Netherlands - accepted for oral presentation, cancelled due to pandemic
"Androgenic anabolic steroids impair sodium channel localization at the membrane of plakoglobin-deficient atrial cardiomyocytes"

04/2021 Annual Meeting of the European Working Group on Cardiac Cellular Electrophysiology (EWGCCE)
held online in conjunction with the Annual Meeting of the European Heart Rhythm Association (EHRA)
"Desmosomal vulnerability renders left atria more susceptible to detrimental effects of androgenic anabolic steroids"

04/2022 Annual Meeting of the German Cardiac Society (DGK)
Mannheim, Germany
"Increased early sodium current provokes familial atrial fibrillation and reduces effectiveness of sodium channel block"

07/2022 German Center for Cardiovascular Research (DZHK) Science on Friday Seminar Series held online
DZHK Rhythm - *"Desmosomes, sex hormones and arrhythmias"*

Awards

10/2019	Hans-Jürgen-Bretschneider-Poster Award Annual Meeting of the German Cardiac Society (DGK), Basic Science Meeting
06/2020	Cardiovascular Webinar Engagement Award International Society for Heart Research (ISHR), Cardiovascular Webinar Series
04/2021	Best Abstract Award Annual Meeting of the European Working Group on Cardiac Cellular Electrophysiology (EWGCCE)
06/2022	Poster Award Annual Meeting of the European Working Group on Cardiac Cellular Electrophysiology (EWGCCE)

Travel/Conference Fee Awards

10/2019	German Cardiac Society (DGK) for attendance of the Basic Science Meeting, Berlin, Germany	200 €
08/2021	YoungDGK European Society of Cardiology (ESC) ESC Congress Fee	[equivalent to 295 €]
04/2022	European Heart Rhythm Association (EHRA) EHRA Congress Educational Grant	500 €

1 Chapter I - Introduction

This chapter provides an overview on inheritable cardiac arrhythmia syndromes, with a special focus on arrhythmogenic right ventricular cardiomyopathy (ARVC). It is outlined that atrial involvement is a common feature of arrhythmia syndromes. This warrants to interconnect gained knowledge on underlying mechanisms of atrial arrhythmogenesis in these conditions with a subset of pathways leading to atrial fibrillation (AF), the most common cardiac arrhythmia, in the general population. Current concepts of arrhythmia development and the genetic impact on AF are described. Particular attention is paid to the cardiac sodium channel and its dysregulation as a driver for arrhythmia. Finally, modifiers of disease penetrance and clinical outcome shared by ARVC and AF are reported.

1.1 Cardiac action potentials and arrhythmia syndromes

The human heart contains four chambers, two atria and two ventricles and their regular contraction ensures blood flow to the whole body. Excitation of cardiac muscle cells, cardiomyocytes, is facilitated by a multitude of electrical currents resulting from ion exchange between the intra- and extracellular space. The net change in voltage across the cardiomyocyte membrane can be recorded as action potentials. Different excitable cells throughout the heart possess different action potential shapes, depending on their location and therefore function within the organ. Figure 1 summarizes the two main types of myocardial action potentials in human atria and ventricles and provides a simplified summary of involved ion currents across the different phases of action potentials.

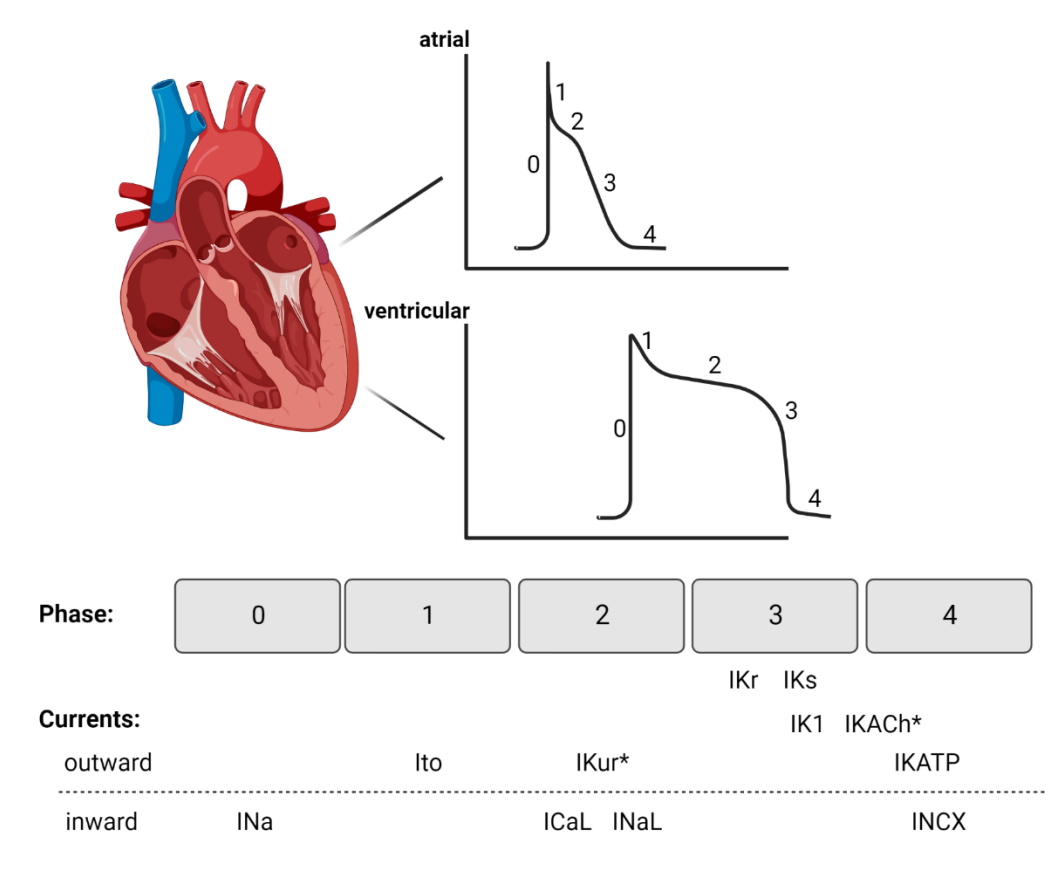


Figure 1: Cross-sectional view of the human heart and atrial and ventricular action potentials with underlying currents

Graphs on the right illustrate the relative change in voltage across the atrial/ventricular cardiomyocyte membrane over time. Different phases are indicated and main underlying currents (I) are summarized below.
* indicates currents exclusive to or more important in atrial cardiomyocytes.
Created with BioRender.com; adapted from Tamargo et al. [1]

The tightly regulated opening and closing of ion channels in cardiac cell membranes generating action potentials and the propagation of the latter through coupled cells in tissue, provides the basis for an orderly excitation-induced contraction of the heart muscle. Disturbances in electrical properties of cardiac cells or tissue will therefore lead to maladjusted contraction of the heart, causing insufficient pumping of blood and hence insufficient oxygen and nutrient supply of other organs, making it a life-threatening condition. Uncontrolled, irregular electrical activity and beating can occur in both atria and ventricles.

Since changes in the cardiac pacemaker and conduction system are often observed during ageing, cardiac arrhythmias are a common disease of the elderly population [2, 3]. However, electrical disturbances giving rise to arrhythmia can also occur due to inherited mutations, constituting the group of hereditary cardiac (arrhythmia) syndromes. The disease phenotype will manifest much earlier in these patients depending on the underlying genetic cause and can involve severe cardiac complications including sudden cardiac death. In fact, an estimated number of 3 in 100,000 people under 40 years of age in Germany and North America will suffer from sudden cardiac death [4]. The predominantly autosomal-dominant syndromes encompass channelopathies including long QT syndrome (LQTS) and Brugada syndrome (BrS), and also hypertrophic cardiomyopathy (HCM), dilated cardiomyopathy (DCM) as well as arrhythmogenic right ventricular cardiomyopathy (ARVC).

1.2 Arrhythmogenic Right Ventricular Cardiomyopathy (ARVC)

Sudden cardiac death in young people and athletes is often caused by arrhythmogenic right ventricular cardiomyopathy (ARVC) [5]. About one tenth of sudden cardiac death cases in the young are caused by ARVC [6] and a northern Italy study found that ARVC was the most common underlying reason for sudden cardiac death in athletes (22% of cases) [7]. The syndrome has a prevalence of up to 1:1,000 in regions of Europe and 1:5,000 in the US [8] and was first identified in clinical reports of individuals on the Greek island of Naxos as well as in India and Ecuador [9-11] presenting with clustering of cardiocutaneous phenotypes. Those included abnormal, wooly hair, keratosis and ventricular tachycardias as well as enlarged ventricles [12].

Due to the high risk of arrhythmias occurring before the development of heart failure, and because of structural changes predominantly observed in the myocardium of the right ventricle, the disease was initially recognized by the WHO as a distinct class of cardiomyopathy termed „Arrhythmogenic Right Ventricular Cardiomyopathy/Dysplasia (ARVC/D)“ in 1995 [13]. However, the involvement of the left ventricle was appreciated in at least half of the affected patients [14, 15]. Due to the high and early incidence of arrhythmias compared to other cardiomyopathies primarily resulting in heart failure, the syndrome is now also referred to as „Arrhythmogenic Cardiomyopathy (AC or ACM“ [16]). Histological features include degenerative replacement of the myocardium by fibrous tissue initiated in the epicardium then progressing towards the endocardium, with the interventricular septum being spared [14].

The current therapeutic regimen in ARVC is summarized in Chapter II. Due to the lack of detailed knowledge on underlying mechanisms, only symptomatic treatment is available. Known key concepts of the cardiomyopathy are outlined below.

1.2.1 Desmosomes, area composita and intercalated disc

Now referred to as Naxos and Carbajal syndrome, these two ARVC founder mutations depict autosomal recessive forms of the disease and were later on associated with proteins of the desmosome.

Desmosomes, as a type of intercellular junctions, are vital structures ensuring integrity of e.g., epithelial and cardiac tissue by linking intermediate filaments of adjacent cells [17]. Mechanical stability is of special importance in the contracting heart muscle, which is constantly exposed to high mechanical stress. Molecular structures ensuring cardiomyocyte integrity, including desmosomes, are located in the intercalated discs, as depicted in Figure 2.

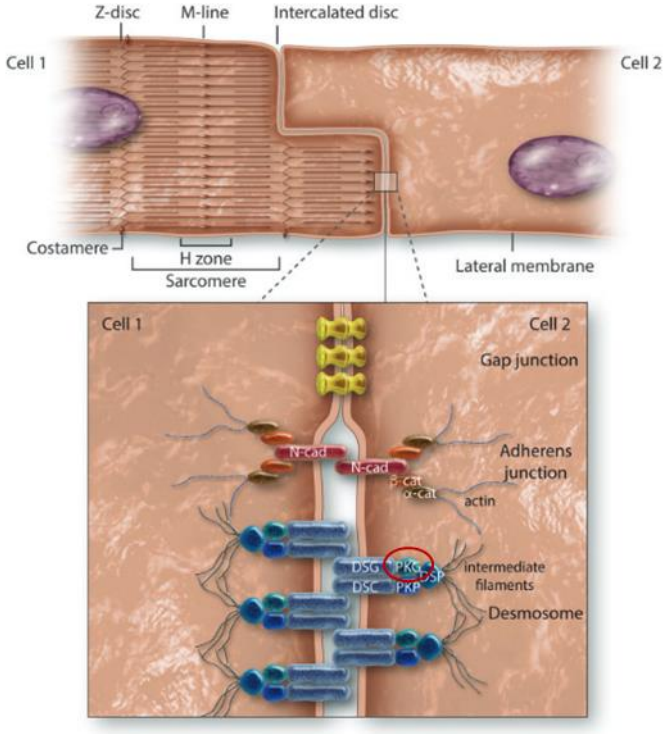


Figure 2: Traditional model of the intercalated disc connecting adjacent cardiomyocytes

Highlighted in red is PKG - Plakoglobin, a desmosomal gene heterozygously depleted in the mouse model used to study ARVC (Chapter VI). Adapted from Vermij et al. [18]

Five proteins (genes) are identified to participate in cardiac desmosome formation: desmoglein 2 (DSG2) and desmocollin 2 (DSC2), plakoglobin (PKG/JUP) and plakophilin-2 (PKP-2) as well as desmoplakin (DSP). The cardiac desmosome is depicted in Figure 3. In heart muscle, these desmosomal proteins anchor the intermediate filament desmin to the plasma membrane and cadherins [19].

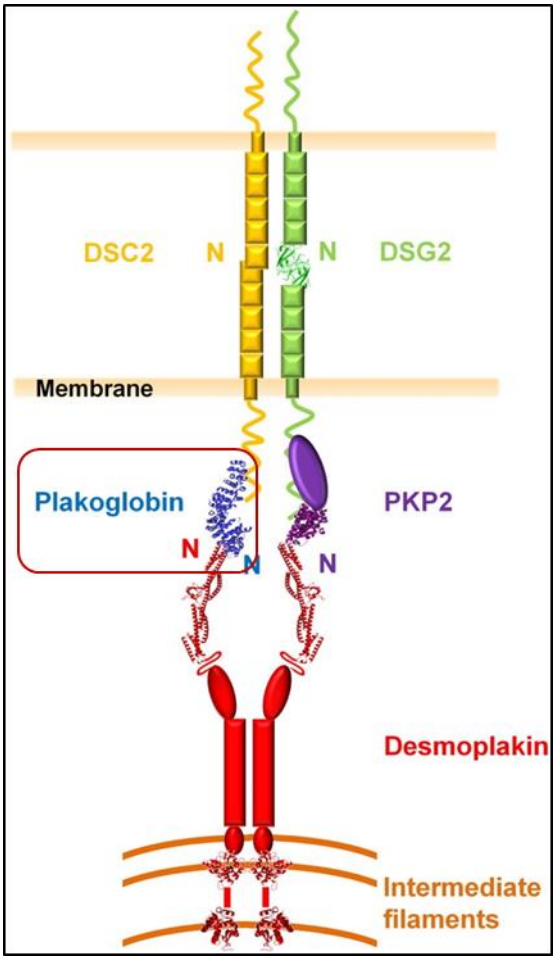


Figure 3: Molecular components of the cardiac desmosome

DSC2: Desmocollin 2, DSG2: Desmocollin 2, PKP2: Plakophilin-2, DSC2 and DSG2 can interact in both a homophilic and heterophilic fashion. Desmosomes link to the intermediate filament desmin in the heart. Plakoglobin is marked with a red box as a mouse model with heterozygous depletion of this desmosomal protein was employed in Chapter VI. Adapted from Al-Jassar et al. [20]

Along with desmosomes, adherens junctions (also known as „fascia adherens“ in cardiac tissue) as a second type of mechanical adhesion and gap junctions, establishing chemical and electrical communication between cells [21, 22], were identified to localize to the intercalated disc region (also see Figure 2).

Traditionally, participating structural proteins were thought to localize exclusively to one of these connection units. However, the concept of macromolecular complexes, interacting mechanically and electrically, is evolving [18, 23]. In higher organisms the components of desmosomes and adherens junctions were found to form hybrid complexes, the so-called „area composita“ [24]. Area composita

formation progressively increases postnatally in mammalian vertebrates, whereas this is not observed in non-mammals [25]. A more recent intercalated disc model including the area composita is depicted in Figure 4.

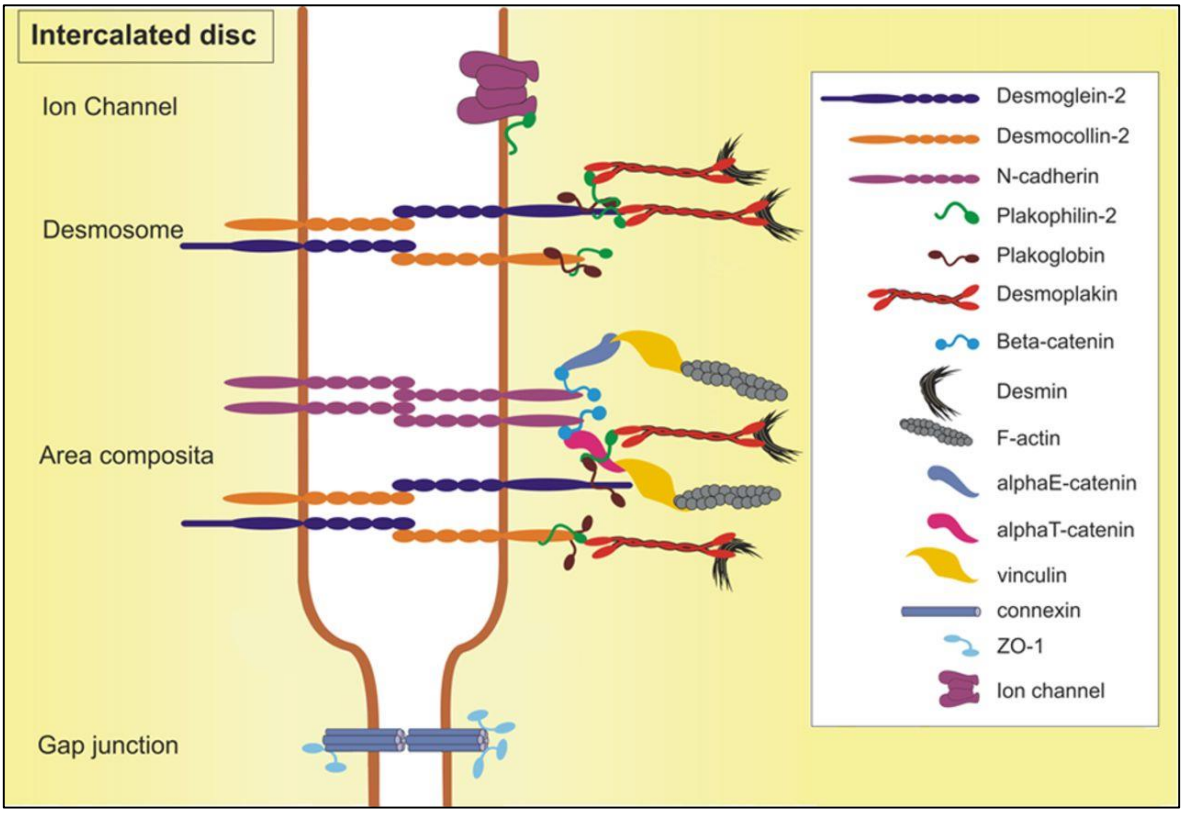


Figure 4: Molecules in the intercalated disc region of cardiomyocytes

Adapted from Rampazzo et al. [23]
Of note, both desmosomes and ion channels are found at the intercalated disc and in close proximity. The desmosomal proteins Plakophilin-2[26], Desmoglein 2[27] and Desmoplakin[28] have been reported to interact with the cardiac sodium channel $Na_v1.5$.

As mentioned, intercalated disc regions connecting adjacent cardiac myocytes also harbour gap junctions. The latter are hexameric hemichannels consisting of connexins (Cx). 21/20 Cx isoforms have been identified in the human/mouse genome, respectively. Cardiac mouse isoforms are Cx30, 30.2, 37, 40, 43, 45 and 46 with different spatial expression in the individual chambers and throughout development [29]. Remodeling of connexins, including alterations in their expression, phosphorylation and spatial distribution is indicated to be an underlying cause of cardiac arrhythmia manifestation [30-32].

Desmosomal proteins were shown to associate with Cx and might have an essential role for their formation. For example, a truncating frame-shift mutation of desmocollin 2a (DSC2a) has been found to be associated with reduced Cx43 levels in a myocardial biopsy of the affected patient [33]. An *in vitro* pulldown assay confirmed interaction of the cytoplasmic portion of wild type DSC2a and Cx43. Furthermore, a knockdown of plakophilin-2 led to abolished Cx43 expression levels and less Cx43 localization to the intercellular junction, resulting in reduced cell coupling as assessed by dye loading [34]. Connexin remodeling, including alteration in its expression and spatial distribution is recognized as a pro-arrhythmic mechanism [35]. A C-terminal truncation of Cx43 was found to induce severe arrhythmias in mice, which was accompanied by a sodium current loss [36]. This finding furthermore underlines the concept of crosstalk between different proteins in intercellular connections and indicates that also ion channels can take part in it. In fact, a functional interaction of desmosomes and the cardiac voltage-gated sodium channel α-subunit ($Na_v1.5$) was found in mice heterozygously deficient for plakophilin 2. Isolated ventricular cardiomyocytes showed decreased sodium current amplitudes and alterations in I_{Na} kinetics, although overall $Na_v1.5$ expression levels were not changed compared to wild type cells [37]. This finding is further supported by plakophilin 2-deficient HL1 cells and induced pluripotent stem cell-derived cardiomyocytes (iPSC-CMs) from a patient with plakophilin 2 deficiency, both exhibiting reduced I_{Na} amplitudes [37, 38].

Immunoreactive signal for Cx43, plakoglobin and/or $Na_v1.5$ was found to be reduced and/or disturbed at the intercalated disc in left and right ventricular septal biopsies of 15 ARVC patients compared to to 5 healthy control tissues [39]. The majority of these ARVC patients carried a mutation in plakophilin-2, but also desmoglein mutations were identified. Plakophilin-2 signal was only reduced in subjects carrying a deletion mutation for the gene, whereas it was not subject to alteration in other types of plakophilin-2 ARVC mutations. However, plakoglobin signal was reduced and/or disturbed in its distribution in the majority of the cases, although no underlying mutation in the gene was identified.

1.2.2 Plakoglobin

The first identified genetic cause of ARVC, specifically of Naxos disease, is a 2 base pair deletion in the *JUP* gene, encoding for the desmosomal protein plakoglobin, leading to C-terminal truncation [40]. In humans, the *JUP* gene is located on Chr17q21 [41]. Plakoglobin, also known as "γ-catenin", is one of the armadillo proteins known to localize in cardiac intercellular junctions and is a component of both adherens junctions and desmosomes [42]. The protein is composed of a central armadillo domain containing 12 non-identical arms, each consisting of 42 amino acids, flanked by a C-terminal tail, and an N-terminal head region. The superhelix tertiary structure created by the arm domain creates a positively-charged groove allowing for the binding of interaction partners [20].

1.2.3 Plakoglobin and ARVC

Interestingly, the cardiac phenotype in the first identified Naxos patients harbouring the mutation was 100% penetrant and sudden cardiac death was observed in a subset of individuals. By now, other ARVC-causing plakoglobin mutations have been identified: „S39_K40insS", for example is characterized by the addition of a serine residue in position 39, while „T19I", presents a missense mutation of a threonine in the phosphorylation-sensitive head domain, giving rise to an exclusively cardiac disease phenotype [43]. A number of ARVC-associated plakoglobin mutations were also located in the arm domain and are depicted in Figure 5.

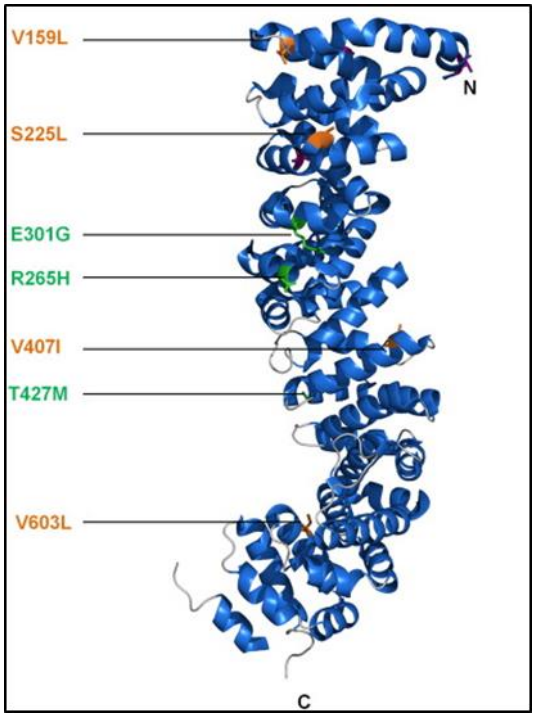


Figure 5: Crystal structure of the plakoglobin arm domain and identified ARVC-causing mutations

Buried residues are marked in orange, surface-exposed residues are highlighted in green. Adapted from Al-Jassar et al. [20], PDB code: 3IFQ

1.2.4 Heterozygous plakoglobin-deficient mice as a model for ARVC

Even before the recognition of plakogobin as the mutation-harbouring gene in Naxos disease, Ruiz and colleagues generated a mouse model carrying a *null* mutation of the gene and causing depletion of the protein [42]. Only heterozygous animals are born, suggesting an essential role of plakoglobin for the development of the embryo. Homozygous mice were found to die *in utero* between day E12 and E16 due to heart defects including pericardial blood infiltrates and ruptured ventricles. Formation of cardiac desmosomes was impaired, and these junctions were already absent at around day E8, even before high mechanical stress due to contraction is initiated. Interestingly, only cardiac but not epithelial desmosomes seemed to be affected on a microscopic level. This could be explained by compensation of other isoforms of desmosomal proteins being expressed in epithelial, but not in cardiac desmosomes. Although β-catenin, an armadillo protein homologous to plakoglobin is expressed in the heart, plakoglobin appears indispensable for cardiac desmosome formation.

Since mice heterozygous for plakoglobin deletion are viable and do not show any noticeable phenotype during the first weeks of life, they can be used as a model to study cardiac desmosomal integrity. Plakoglobin localization to the intercalated disc seems not to be disturbed by partial deficiency of the protein, as assessed in right ventricular tissue sections [44]. Importantly, the heterozygous mice (Plakoglobin$^{+/-}$) were found to exhibit an ARVC-like phenotype after ageing and/or endurance exercise, with right ventricles showing enlargement and increased incidence of ventricular arrhythmias [45]. A nitrate and loop diuretics-based pre-load reducing therapy abolishes the training-induced ventricular disease phenotype [44]. Therapy also partially restored connexin 43 protein levels, which were shown to be reduced in the myocardium of Plakoglobin$^{+/-}$ mice, providing further indication for a crosstalk between desmosomal and gap junctional proteins.

1.2.5 Atrial arrhythmia in ARVC

Clinical observational studies report that more than 40% of ARVC patients also suffer from sustained atrial arrhythmia [46], making it a common symptom of the disease, which is also associated with adverse clinical outcome. For example, in a patient cohort of the multicentre Zurich ARVD Registry 28% of ARVC patients experienced inappropriate ICD shocks, mostly from single chamber devices, due to atrial fibrillation or flutter with rapid ventricular conduction [47]. Furthermore, the subgroup of ARVC patients in end-stage heart failure, hence having received heart transplants or having suffered from sudden cardiac arrest, had a higher prevalence of atrial fibrillation and atrial flutter. The authors of the study evaluated the ability of transthoracic echocardiography to identify patients at increased risk of those atrial arrhythmia events and found that in addition to a reduced RV function (defined as RV fractional area change <27%) increased left atrial dimensions (≥24.4mm/m^2) were indicative parameters. Left atrial enlargement in ARVC patients with atrial arrhythmias was also observed by another study involving 248 patients [48]. The group of patients affected by atrial arrhythmic events during a 5.78 years follow-up period comprised 14% of the cohort and symptoms developed at a mean age of 43 ± 14 years. Again, this subgroup of patients was at a higher risk of heart failure and

death. Interestingly, not only older age, but also male gender was associated with the development of atrial arrhythmias.

Work undertaken to investigate atrial involvement in ARVC constitutes Chapter VI of this thesis. The chapter also contains a summary of atrial arrhythmia prevalence in published ARVC cohorts.

1.3 Atrial fibrillation and arrhythmia mechanisms

Atrial fibrillation (AF) is the most common cardiac arrhythmia and both its incidence and prevalence in developed countries are still predicted to rise due to advancements in screening modalities and increased life expectancy [49]. AF is not only associated with an increase in all-cause mortality [50, 51] but also a risk for other cardiovascular complications such as heart failure and stroke and hence increased morbidity [52-55].

Moreover, AF is a common symptom of inherited cardiac arrhythmia syndromes and can even be the first clinical manifestation of them, as reported for inherited ion channel dysfunction [56, 57].

Outlining all paradigms of atrial (and ventricular) arrhythmia onset and maintenance would be beyond the scope of this chapter. Instead, arrhythmia mechanisms relevant for the interpretation of findings in Chapter VI and VII are covered below.

1.3.1 Ectopic activity: abnormal action potential triggering

Electrical stimuli arising outside of the sinoatrial node (SAN) tissue can perturb sinus rhythm by creation of new activation sites and are referred to as "foci of ectopic activity" [58]. When cardiomyocyte groups commence their own pacemaker activity, they can uncouple from the SAN-initiated cardiac activation pattern and cause arrhythmia. Escape of the SAN-dictated rhythm can be caused by higher intrinsic rate of the ectopic foci (compared to SAN rate) or malfunction of the SAN. Accordingly, slow intrinsic heart rates can increase susceptibility to ectopic activity.

Cardiomyocytes can also exhibit aberrant, intrinsically-caused depolarization events during or after the repolarization phase of a normal action potential, called "afterdepolarizations". These aberrant depolarizations can be divided into "early" [59] and "delayed" [60] afterdepolarizations, occurring in phase 2/3 or 4 (or just after) of the action potential, respectively, as depicted in Figure 6. These depolarization events can in turn elicit new action potentials and thereby sustain the ectopic activity [61]. Prolongation of the action potential at slow intrinsic heart rates can increase the likelihood of afterdepolarizations [62].

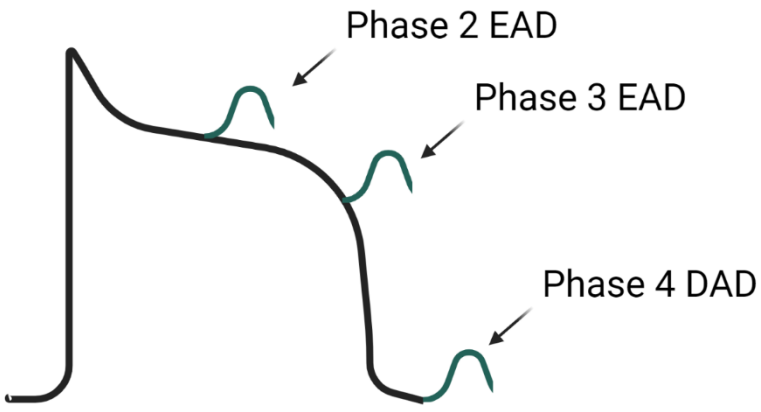


Figure 6: Normal ventricular action potential (black) with possible EAD and DAD (green)

These afterdepolarizations can induce action potentials or triggered activity in both ventricular and atrial cardiomyocytes. EAD: early afterdepolarization; DAD: delayed afterdepolarization
Created with BioRender.com; Adapted from Tse [63]

1.3.2 Re-entry: abnormal action potential propagation

Arrhythmia, whether atrial or ventricular, can also be caused by abnormal propagation of action potentials across the myocardium. A unidirectional block within the cardiac tissue can lead to formation of circuits, where the activation wave travels around the blocked area. The circuit can sustain itself, leading to re-entrant arrhythmia [64]. The likelihood of re-entry circuit formation can be estimated by calculating the cardiac wavelength, which describes the shortest circuit size sufficient to sustain re-entry [65]. The cardiac wavelength (WL) is equal to ERP multiplied by CV, where ERP is the effective refractory period and CV the conduction velocity. As illustrated in Figure 7, taking an atrium as an example, with decreased ERP or CV, the number of possible re-entrant waves per tissue area rises, thereby increasing the probability of arrhythmia, i.e., AF, becoming sustained.

Conduction slowing and inter- as well as intra-atrial conduction defects seem to be more common in patients experiencing AF episodes [66]. Interestingly, atrial CV slowing immediately before the onset of AF has been observed in patients [45]. Changes in atrial conduction can be captured by sophisticated ECG analyses. Biphasic P wave in lead V1 [67] and altered P wave duration have been described to be associated with increased risk of AF [68].

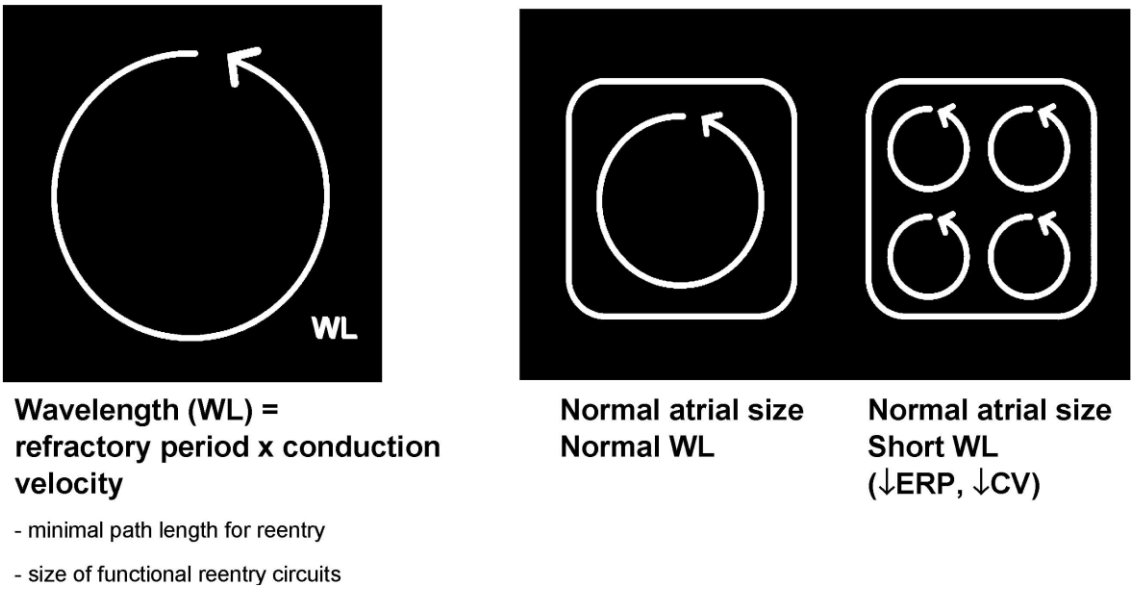


Figure 7: Cardiac wavelength and the influence of the effective refractory period (ERP) and conduction velocity (CV)

Adapted from Shiroshita-Takeshita et al. [65]

Beyond that, AF is a progressive disease and can exacerbate itself, which has been evaluated in animal studies resulting in the concept of "AF begetting AF" [69]. However, especially onset and progression of the disease are not targeted by currently available pharmacotherapy, highlighting the lack of sufficient knowledge on the underlying mechanisms. Research is hindered by the fact that primary molecular mechanisms of AF are often hard to distinguish from those initiated by the multitude of comorbidities and risk factors [70].

As described above, initial remodeling of the atria could be of electrical or structural nature. By providing a substrate for the arrhythmia, fibrosis of the atria is a major contributor to the formation, maintenance and recurrence of AF.

Mechanistic dissection of underlying changes in models and patients is aided by techniques outlined in Chapter III and IV (electrical) and Chapter V (structural).

1.3.3 Genetic factors and hereditability of AF

AF is a common disease in elderly patients who are often suffering from a variety of comorbidities, posing the question if AF can be classified a primary disease entity. During the past decades, genome-wide association studies (GWAS) revealed common genetic risk factors for AF [71], which were significantly associated with the disease even when corrected for genetically-caused comorbidities like diabetes and heart failure. On top of this, a family history of AF is significantly associated with risk of AF [72], indicating an existence of molecular pathways specific to AF. Indeed, familial cases of AF have been reported. Comprehensive research to understand the role of these genes and related proteins has been initiated by using genetically-modified animal models. Experimental models, e.g., murine models harboring depletion of or mutations in single genes, provide a unique tool to study individual disease aspects in a very controlled manner and have successfully been employed to unravel pro-arrhythmic mechanisms underlying AF [73].

Identified mutations associated with AF lie in genes or intronic regions next to genes encoding transcription factors [74-76], desmosome components [77], regulators of calcium homeostasis [78] or ion channels. The latter include mutations in potassium [79-83] and sodium [84, 85] channel subunits.

1.3.4 Cardiac voltage-gated sodium channel and links to AF

Voltage-gated sodium channels carry the rapid influx of sodium ions into the myocyte thereby causing depolarization, initiating the cardiac action potential. The main cardiac isoform of the sodium channel, carrying the sodium current (I_{Na}) is $Na_v1.5$ [86, 87], encoded by the *SCN5A* gene.

The unit of sodium channels is composed of one large alpha-subunit forming the ion-conducting pore which is functional on its own but can be accessorized with one or two beta-subunits. As depicted in Figure 8, the alpha-subunit consists of four membrane-spanning voltage-sensitive domains, interlinking loops, as well as an N- and C-terminus.

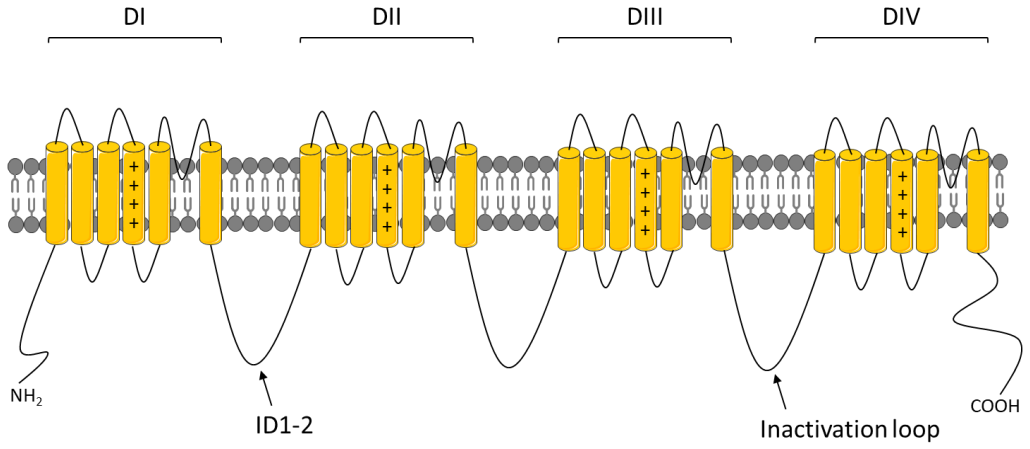


Figure 8: Alpha subunit of the voltage-gated sodium channel

The subunit consists of four membrane-spanning, voltage-sensitive (indicated by "+") domains (DI-IV). Intracellular parts play an important role for regulation (inactivation) and interaction with other proteins (many of them at the C-terminus).

$Na_v1.5$ is described to reside in macromolecular complexes, e.g., at the intercalated disc as shown and described in Figure 4. Many of the identified $Na_v1.5$-interacting proteins target a binding site within the C-terminus of the channel. Examples of such proteins are calmodulin [88] and fibroblast growth factor homologous factor 1B [89]. $Na_v1.5$ is proposed to function as dimers [90] and structural models predict an intermolecular interaction of C-termini [91], as depicted in Figure 9.

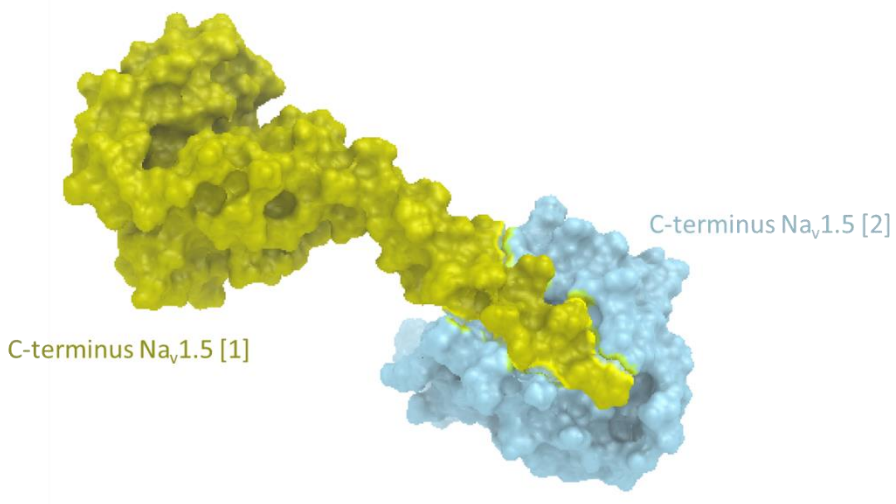


Figure 9: Interacting Nav1.5 C-termini leading to proposed formation of homo-dimers

Structural display of two interacting C-termini in yellow [1] and blue [2] in a modelled Na$_v$1.5 homo-dimer. Visualized in Molsoft ICM-Browser Pro; PDB accession number: 4OVN

Due to its key role in cardiac action potential initiation and propagation, it is not far to seek that abnormalities in sodium current can contribute to arrhythmogenesis. Mutations in the *SCN5A* gene have indeed been linked to a number of arrhythmia syndromes, including LQTS type 3, BrS as well as AF [92-95]. On top of that, alterations in cardiac sodium channel function have been described for overlap syndromes of the before-mentioned phenotypes [96, 97], as a cause for structural cardiac diseases, i.e., dilated cardiomyopathy [95, 98] and also for ARVC [37, 99, 100].

Reduced peak I_{Na} has been shown to be accompanied by reduced atrial myocardial expression of Na$_v$1.5 in patients suffering from AF [101]. Reduced I_{Na} can cause CV slowing [102] which is arrhythmogenic, as discussed above. On the other hand, pharmacological inhibition of sodium channels can exert anti-arrhythmic effects in certain conditions. The sodium channel blocker flecainide, a class Ic antiarrhythmic agent, can be used for termination or chronic suppression of AF [103], which highlights that the link between sodium currents and AF is not restricted to **dys**function of cardiac sodium channels.

1.3.5 Point mutation in the cardiac sodium channel associated with familial atrial fibrillation

As mentioned above, described sodium channel mutations associated with AF have typically been loss-of-function variants. Makiyama and colleagues reported a point mutation resulting in a Met to Thr exchange at position 1875 of the $Na_v1.5$ protein to cause familial AF with an autosomal-dominant heredity [104]. Affected individuals experienced premature atrial contractions causing palpitations, progressing to paroxysmal and eventually persistent AF already in their 30s. Not only were the arrhythmia inert to ablation in many cases, but also did pharmacological intervention with sodium channel blockers lack efficacy. Patients presented with this atrial electrical phenotype without underlying structural heart disease [104]. Based on *in vitro* data gained from HEK cell expression systems, the variant was hypothesized to cause a gain-of-function of the cardiac sodium channel. To date, this is the first gain-of-function mutation in the *SCN5A* gene described to cause AF. Furthermore, despite carrying a gain-of-function $Na_v1.5$ mutation, affected individuals possess normal QT-intervals, implicating a hitherto undescribed mechanism of atrial arrhythmogenesis.

According to structural models of the $Na_v1.5$ homo-dimer formed by interaction of two C-termini, the surface of the affected methionine residue is taking place in the molecular interaction, as highlighted in Figure 10.

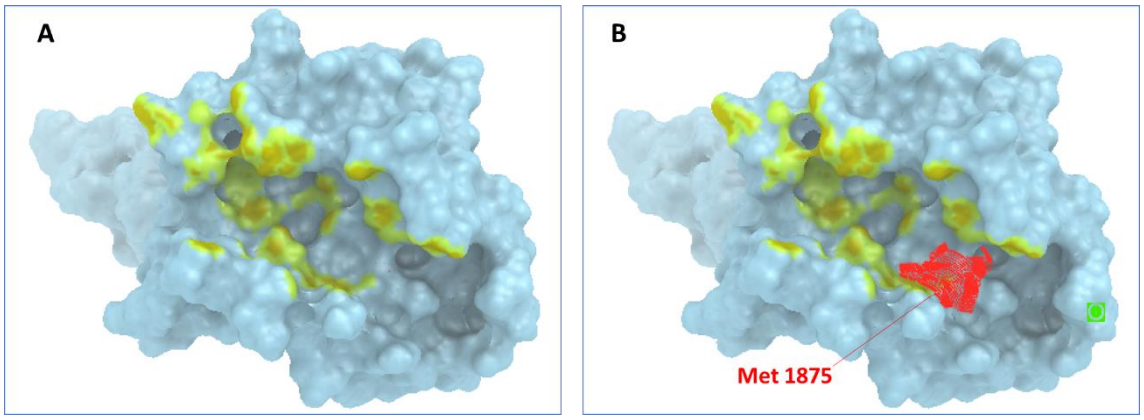


Figure 10: Close-up of the proposed Nav1.5 C-terminal interaction site for homo-dimer formation

A) One $Na_v1.5$ C-terminus as depicted in Figure 9, with the homo-dimer interaction surface coloured in yellow. B) Same depiction as in A, with the affected methionine residue at position 1875 highlighted in red. Visualized in Molsoft ICM-Browser Pro; PDB accession number: 4OVN

The methionine residue at position 1875 is highly conserved across different sodium channel isoforms and across different species [104]. We created a mouse model carrying the corresponding point mutation of the cardiac sodium channel. Phenotypic characterization of these mice at young adult age comprises Chapter VII.

1.4 Modifiers of disease penetrance and clinical outcome

Although underlying genetic mutations seem to have been identified, arising mechanisms leading to development of ARVC and its progression remain poorly understood. Identical mutations can lead to varying disease phenotypes even among family members pointing towards an influence of environmental factors on penetrance of the disease. As mentioned before, athletes can comprise a group of ARVC patients with severe complications including sudden cardiac death. This observation is mainly based on extensive physical exercise being a trigger of silent cardiovascular conditions [105]. Patients often only present with clinical phenotypes after such a trigger, leading to increased diagnosis rates in this patient group.

Endurance exercise appears to be a strong trigger for cardiac arrhythmic events in ARVC patients [106], a disease phenotype which is also reflected in the plakoglobin$^{+/-}$ murine model [44]. Suggested underlying mechanisms include excessive (right) ventricular wall stress during extensive exercise and subsequent insufficient recovery leading to microscopic, pro-arrhythmic remodeling of the cardiac muscle [107]. Clinical recommendations for high-risk ARVC patients therefore include restriction of exercise [108]. However, this can only be realized after diagnosis and might not prevent severe cardiac events happening prior to that. Comprehensive understanding of disease progression mechanisms is still elusive.

Another recognized modifier of severity outcome of ARVC are serum concentrations of sex hormones. Sex differences in cardiac electrophysiology, modifying arrhythmia risk and development, are well recognized [109] and male gender itself was suggested to worsen outcome in ARVC. Akdis and colleagues were able to demonstrate a direct relationship between plasma sex hormone levels and

occurrence of major arrhythmic cardiovascular events in patients with diagnosed ARVC [110]. Males with elevated serum total testosterone concentrations (>13.5 nmol/L) were at significantly higher risk to experience those events compared to males with serum levels below this identified cut-off (sensitivity 84%, specificity 75%). Vice versa, female ARVC patients with higher estradiol levels had a lower risk for severe events, compared to those with lower estradiol levels. The disease-modifying role of sex hormones was furthermore investigated *in vitro* in iPSC-derived cardiomyocytes from an ARVC patient carrying a plakophilin-2 mutation and revealed that after 2 weeks of testosterone treatment, cardiomyocyte apoptosis and lipid accumulation was significantly increased. Estradiol treatment resulted in decreased apoptosis rates and lipid droplet accumulation. In contrast, apoptosis rate and lipid accumulation was not significantly changed by sex hormone treatment of control iPSC-derived cardiomyocytes. The association of blood testosterone concentrations and an increased incidence of adverse arrhythmic events in ARVC has since been confirmed in an additional study [111]. The authors even implicated testosterone concentrations as possible biomarker for arrhythmia risk prediction in ARVC.

An association between the male sex hormone testosterone and AF has also been established. Increased blood concentrations of testosterone were shown to associate with an elevated risk for AF in men [112]. Males generally exhibited a higher age-standardized incidence for AF than females in this multi-ethnic study of 4883 individuals and the same has been observed in a worldwide epidemiological study in 2010 [113]. Increased testosterone levels as a shared disease modifier of ARVC and AF warrant the study design of the project constituting Chapter VI of this thesis.

Similar to testosterone concentrations, endurance exercise impacts disease onset and severity of both ARVC and AF. An increase in risk for experiencing AF has been shown for extensive participation in different kinds of endurance exercise, including jogging [114], marathon running [115], cycling [116] and cross-country skiing [117, 118].

1.5 Thesis motivation and structure

The general INTRODUCTION is continued by Chapter II (Book chapter) delineating current medical treatment options for ARVC. Only symptomatic treatment is available. Neither onset, nor early progression of the disease can yet be targeted. The same holds true for AF. A more comprehensive understanding of the individual drivers of remodeling and arrhythmogenesis in both conditions could improve prevention and detection of these complex cardiac diseases. Murine models allow for the dissection of isolated pathways in a very controlled fashion, adjustable for factors like sex, age and stage of the disease. (Atrial) electrophysiology and consequences of disturbances can be studied in murine models at different scales applying a variety of state-of-the-art techniques.

METHODS performed in projects comprising this thesis are listed below.

Insights gained on	**Studied scale**	**Technique**
Cardiac structure	In vivo, macroscopically	Echocardiography
	Ex vivo, microscopically	Histological analysis
Spread of depolarization, action potentials and underlying ion currents	In vivo	ECG
	Ex vivo, e.g., intact hearts intact atria, or isolated cardiomyocytes	Optical mapping
		Monophasic action potential recordings
		Microelectrode recordings*
		Patch-clamp*
Subcellular localization of ion channels	Ex vivo, microdomains in isolated cardiomyocytes	Super-resolution microscopy: Direct Stochastic Optical Reconstruction Microscopy (dSTORM)

*Methods not conducted by myself

Considerations for the experimental design when studying atrial electrophysiology in mouse models can be concluded from analyses comprising **Chapter III**. With the aim to systematically test which factors influence murine atrial electrophysiology, we compared atrial monophasic action potentials

(MAP) and effective refractory periods (ERP) collected from wildtype mice of different genetic background, sex and age.

Chapter IV and Chapter V outline methods used to optically study spatio-temporal spread of cardiac depolarization in intact hearts and atria ex vivo as well as atrial structure on histological level, respectively. As discussed above, both features are major drivers for arrhythmogenesis when remodeled.

The study comprising Chapter IV aimed at providing a rich set of high resolution optical mapping data collected at the Institute of Cardiovascular Sciences, University of Birmingham, to the scientific community. It can be employed to develop, test and validate analysis algorithms for mapping data.

Development and validation of an open-source tool for semi-automatic and therefore robust analysis of atrial tissue composition and microscopic level, including extracellular matrix content, cardiomyocyte size and fibroblast count, built the aim for Chapter V. Whilst the original tool was developed using human and goat specimen, we applied it for the analysis of murine atrial tissue sections from models studied in Chapter VI and VII.

Chapter VI and Chapter VII provide **RESULTS** from experimental studies.

Chapter VI comprises one of the major experimental studies for this thesis investigating atrial involvement in ARVC in a murine model. It expands to clinical data from ARVC patients linking observed phenotypes. Male sex and elevated androgen concentrations appear to be a disease modifier for both ARVC and AF. We therefore hypothesized that desmosomal vulnerability caused by heterozygous knock-out of plakoglobin and chronically elevated testosterone levels induced by implantation of osmotic mini pumps releasing 5α-dihydrotestosterone (DHT) synergistically impair atrial electrophysiology and studied this in mice.

Chapter VII encompasses another study employing a murine model to study mechanisms of clinical observations. We employed a newly created mouse model carrying the homologue of a point mutation in the cardiac sodium channel, discovered in a family with lone atrial fibrillation at young

age. The induced amino acid change lies in the C-terminus of the sodium channel and we aimed to study its functional consequences in young adult mice.

This thesis is an alternative format thesis which consists of published work or work currently under review for publication and/or uploaded to a publically-available preprint server as indicated above and under 'Project Outcomes'. All subsequent chapters are preceded by a statement setting out the thesis author's contribution to the work. Due to the inclusion of published work, references are listed for each chapter individually.

1.6 References Chapter I

[1] Tamargo J, Caballero R, Gomez R, Delpon E. I(Kur)/Kv1.5 channel blockers for the treatment of atrial fibrillation. *Expert Opin Investig Drugs* 2009; **18**: 399-416.
[2] Fleg JL, Kennedy HL. Cardiac arrhythmias in a healthy elderly population: detection by 24-hour ambulatory electrocardiography. *Chest* 1982; **81**: 302-307.
[3] Diez-Villanueva P, Alfonso F. Atrial fibrillation in the elderly. *Journal of geriatric cardiology : JGC* 2019; **16**: 49-53.
[4] Beckmann BM, Pfeufer A, Kaab S. Inherited cardiac arrhythmias: diagnosis, treatment, and prevention. *Deutsches Arzteblatt international* 2011; **108**: 623-633; quiz 634.
[5] Pilichou K, Thiene G, Bauce B, Rigato I, Lazzarini E, Migliore F, et al. Arrhythmogenic cardiomyopathy. *Orphanet journal of rare diseases* 2016; **11**: 33.
[6] Corrado D, Fontaine G, Marcus FI, McKenna WJ, Nava A, Thiene G, et al. Arrhythmogenic right ventricular dysplasia/cardiomyopathy: need for an international registry. Study Group on Arrhythmogenic Right Ventricular Dysplasia/Cardiomyopathy of the Working Groups on Myocardial and Pericardial Disease and Arrhythmias of the European Society of Cardiology and of the Scientific Council on Cardiomyopathies of the World Heart Federation. *Circulation* 2000; **101**: E101-106.
[7] Corrado D, Basso C, Schiavon M, Thiene G. Screening for hypertrophic cardiomyopathy in young athletes. *N Engl J Med* 1998; **339**: 364-369.
[8] Patel DM, Green KJ. Desmosomes in the heart: a review of clinical and mechanistic analyses. *Cell communication & adhesion* 2014; **21**: 109-128.
[9] Protonotarios N, Tsatsopoulou A, Patsourakos P, Alexopoulos D, Gezerlis P, Simitsis S, et al. Cardiac abnormalities in familial palmoplantar keratosis. *British heart journal* 1986; **56**: 321-326.
[10] Rao BH, Reddy IS, Chandra KS. Familial occurrence of a rare combination of dilated cardiomyopathy with palmoplantar keratoderma and curly hair. *Indian heart journal* 1996; **48**: 161-162.
[11] Carvajal-Huerta L. Epidermolytic palmoplantar keratoderma with woolly hair and dilated cardiomyopathy. *Journal of the American Academy of Dermatology* 1998; **39**: 418-421.
[12] Protonotarios NI, Tsatsopoulou AA, Gatzoulis KA. Arrhythmogenic right ventricular cardiomyopathy caused by a deletion in plakoglobin (Naxos disease). *Cardiac electrophysiology review* 2002; **6**: 72-80.
[13] Richardson P, McKenna W, Bristow M, Maisch B, Mautner B, O'Connell J, et al. Report of the 1995 World Health Organization/International Society and Federation of Cardiology Task Force on the Definition and Classification of cardiomyopathies. *Circulation* 1996; **93**: 841-842.
[14] Corrado D, Basso C, Thiene G, McKenna WJ, Davies MJ, Fontaliran F, et al. Spectrum of clinicopathologic manifestations of arrhythmogenic right ventricular cardiomyopathy/dysplasia: a multicenter study. *J Am Coll Cardiol* 1997; **30**: 1512-1520.
[15] Basso C, Corrado D, Marcus FI, Nava A, Thiene G. Arrhythmogenic right ventricular cardiomyopathy. *Lancet (London, England)* 2009; **373**: 1289-1300.
[16] Basso C, Bauce B, Corrado D, Thiene G. Pathophysiology of arrhythmogenic cardiomyopathy. *Nature reviews Cardiology* 2011; **9**: 223-233.
[17] Garrod D, Chidgey M. Desmosome structure, composition and function. *Biochimica et biophysica acta* 2008; **1778**: 572-587.
[18] Vermij SH, Abriel H, van Veen TA. Refining the molecular organization of the cardiac intercalated disc. *Cardiovascular research* 2017; **113**: 259-275.
[19] Bolling MC, Jonkman MF. Skin and heart: une liaison dangereuse. *Experimental dermatology* 2009; **18**: 658-668.
[20] Al-Jassar C, Bikker H, Overduin M, Chidgey M. Mechanistic basis of desmosome-targeted diseases. *Journal of molecular biology* 2013; **425**: 4006-4022.

[21] Kanno Y, Loewenstein WR. LOW-RESISTANCE COUPLING BETWEEN GLAND CELLS. SOME OBSERVATIONS ON INTERCELLULAR CONTACT MEMBRANES AND INTERCELLULAR SPACE. *Nature* 1964; **201**: 194-195.
[22] Lawrence TS, Beers WH, Gilula NB. Transmission of hormonal stimulation by cell-to-cell communication. *Nature* 1978; **272**: 501-506.
[23] Rampazzo A, Calore M, van Hengel J, van Roy F. Intercalated discs and arrhythmogenic cardiomyopathy. *Circ Cardiovasc Genet* 2014; **7**: 930-940.
[24] Franke WW, Borrmann CM, Grund C, Pieperhoff S. The area composita of adhering junctions connecting heart muscle cells of vertebrates. I. Molecular definition in intercalated disks of cardiomyocytes by immunoelectron microscopy of desmosomal proteins. *European journal of cell biology* 2006; **85**: 69-82.
[25] Pieperhoff S, Borrmann C, Grund C, Barth M, Rizzo S, Franke WW. The area composita of adhering junctions connecting heart muscle cells of vertebrates. VII. The different types of lateral junctions between the special cardiomyocytes of the conduction system of ovine and bovine hearts. *European journal of cell biology* 2010; **89**: 365-378.
[26] Sato PY, Musa H, Coombs W, Guerrero-Serna G, Patino GA, Taffet SM, et al. Loss of plakophilin-2 expression leads to decreased sodium current and slower conduction velocity in cultured cardiac myocytes. *Circ Res* 2009; **105**: 523-526.
[27] Rizzo S, Lodder EM, Verkerk AO, Wolswinkel R, Beekman L, Pilichou K, et al. Intercalated disc abnormalities, reduced Na(+) current density, and conduction slowing in desmoglein-2 mutant mice prior to cardiomyopathic changes. *Cardiovascular research* 2012; **95**: 409-418.
[28] Zhang Q, Deng C, Rao F, Modi RM, Zhu J, Liu X, et al. Silencing of desmoplakin decreases connexin43/Nav1.5 expression and sodium current in HL1 cardiomyocytes. *Mol Med Rep* 2013; **8**: 780-786.
[29] Verheule S, Kaese S. Connexin diversity in the heart: insights from transgenic mouse models. *Frontiers in pharmacology* 2013; **4**: 81.
[30] Vaidya D, Tamaddon HS, Lo CW, Taffet SM, Delmar M, Morley GE, et al. Null mutation of connexin43 causes slow propagation of ventricular activation in the late stages of mouse embryonic development. *Circ Res* 2001; **88**: 1196-1202.
[31] Severs NJ, Coppen SR, Dupont E, Yeh HI, Ko YS, Matsushita T. Gap junction alterations in human cardiac disease. *Cardiovascular research* 2004; **62**: 368-377.
[32] Lubkemeier I, Andrie R, Lickfett L, Bosen F, Stockigt F, Dobrowolski R, et al. The Connexin40A96S mutation from a patient with atrial fibrillation causes decreased atrial conduction velocities and sustained episodes of induced atrial fibrillation in mice. *J Mol Cell Cardiol* 2013; **65**: 19-32.
[33] Gehmlich K, Lambiase PD, Asimaki A, Ciaccio EJ, Ehler E, Syrris P, et al. A novel desmocollin-2 mutation reveals insights into the molecular link between desmosomes and gap junctions. *Heart rhythm* 2011; **8**: 711-718.
[34] Oxford EM, Musa H, Maass K, Coombs W, Taffet SM, Delmar M. Connexin43 remodeling caused by inhibition of plakophilin-2 expression in cardiac cells. *Circ Res* 2007; **101**: 703-711.
[35] Desplantez T. Cardiac Cx43, Cx40 and Cx45 co-assembling: involvement of connexins epitopes in formation of hemichannels and Gap junction channels. *BMC cell biology* 2017; **18**: 3.
[36] Agullo-Pascual E, Lin X, Leo-Macias A, Zhang M, Liang FX, Li Z, et al. Super-resolution imaging reveals that loss of the C-terminus of connexin43 limits microtubule plus-end capture and NaV1.5 localization at the intercalated disc. *Cardiovascular research* 2014; **104**: 371-381.
[37] Cerrone M, Lin X, Zhang M, Agullo-Pascual E, Pfenniger A, Chkourko Gusky H, et al. Missense mutations in plakophilin-2 cause sodium current deficit and associate with a Brugada syndrome phenotype. *Circulation* 2014; **129**: 1092-1103.
[38] Kim C, Wong J, Wen J, Wang S, Wang C, Spiering S, et al. Studying arrhythmogenic right ventricular dysplasia with patient-specific iPSCs. *Nature* 2013; **494**: 105-110.
[39] Noorman M, Hakim S, Kessler E, Groeneweg JA, Cox MG, Asimaki A, et al. Remodeling of the cardiac sodium channel, connexin43, and plakoglobin at the intercalated disk in patients with arrhythmogenic cardiomyopathy. *Heart rhythm* 2013; **10**: 412-419.

[40] McKoy G, Protonotarios N, Crosby A, Tsatsopoulou A, Anastasakis A, Coonar A, et al. Identification of a deletion in plakoglobin in arrhythmogenic right ventricular cardiomyopathy with palmoplantar keratoderma and woolly hair (Naxos disease). *Lancet (London, England)* 2000; **355**: 2119-2124.
[41] Aberle H, Bierkamp C, Torchard D, Serova O, Wagner T, Natt E, et al. The human plakoglobin gene localizes on chromosome 17q21 and is subjected to loss of heterozygosity in breast and ovarian cancers. *Proc Natl Acad Sci U S A* 1995; **92**: 6384-6388.
[42] Ruiz P, Brinkmann V, Ledermann B, Behrend M, Grund C, Thalhammer C, et al. Targeted mutation of plakoglobin in mice reveals essential functions of desmosomes in the embryonic heart. *J Cell Biol* 1996; **135**: 215-225.
[43] Asimaki A, Syrris P, Wichter T, Matthias P, Saffitz JE, McKenna WJ. A novel dominant mutation in plakoglobin causes arrhythmogenic right ventricular cardiomyopathy. *American journal of human genetics* 2007; **81**: 964-973.
[44] Kirchhof P, Fabritz L, Zwiener M, Witt H, Schafers M, Zellerhoff S, et al. Age- and training-dependent development of arrhythmogenic right ventricular cardiomyopathy in heterozygous plakoglobin-deficient mice. *Circulation* 2006; **114**: 1799-1806.
[45] Lalani GG, Schricker A, Gibson M, Rostamian A, Krummen DE, Narayan SM. Atrial conduction slows immediately before the onset of human atrial fibrillation: a bi-atrial contact mapping study of transitions to atrial fibrillation. *J Am Coll Cardiol* 2012; **59**: 595-606.
[46] Chu AF, Zado E, Marchlinski FE. Atrial arrhythmias in patients with arrhythmogenic right ventricular cardiomyopathy/dysplasia and ventricular tachycardia. *The American journal of cardiology* 2010; **106**: 720-722.
[47] Saguner AM, Ganahl S, Kraus A, Baldinger SH, Medeiros-Domingo A, Saguner AR, et al. Clinical role of atrial arrhythmias in patients with arrhythmogenic right ventricular dysplasia. *Circulation journal : official journal of the Japanese Circulation Society* 2014; **78**: 2854-2861.
[48] Camm CF, James CA, Tichnell C, Murray B, Bhonsale A, te Riele AS, et al. Prevalence of atrial arrhythmias in arrhythmogenic right ventricular dysplasia/cardiomyopathy. *Heart rhythm* 2013; **10**: 1661-1668.
[49] Colilla S, Crow A, Petkun W, Singer DE, Simon T, Liu X. Estimates of current and future incidence and prevalence of atrial fibrillation in the U.S. adult population. *The American journal of cardiology* 2013; **112**: 1142-1147.
[50] Benjamin EJ, Wolf PA, D'Agostino RB, Silbershatz H, Kannel WB, Levy D. Impact of atrial fibrillation on the risk of death: the Framingham Heart Study. *Circulation* 1998; **98**: 946-952.
[51] Andersson T, Magnuson A, Bryngelsson IL, Frobert O, Henriksson KM, Edvardsson N, et al. All-cause mortality in 272,186 patients hospitalized with incident atrial fibrillation 1995-2008: a Swedish nationwide long-term case-control study. *European heart journal* 2013; **34**: 1061-1067.
[52] Stewart S, Hart CL, Hole DJ, McMurray JJ. A population-based study of the long-term risks associated with atrial fibrillation: 20-year follow-up of the Renfrew/Paisley study. *Am J Med* 2002; **113**: 359-364.
[53] Wolf PA, Abbott RD, Kannel WB. Atrial fibrillation as an independent risk factor for stroke: the Framingham Study. *Stroke; a journal of cerebral circulation* 1991; **22**: 983-988.
[54] Krahn AD, Manfreda J, Tate RB, Mathewson FA, Cuddy TE. The natural history of atrial fibrillation: incidence, risk factors, and prognosis in the Manitoba Follow-Up Study. *Am J Med* 1995; **98**: 476-484.
[55] Kirchhof P, Benussi S, Kotecha D, Ahlsson A, Atar D, Casadei B, et al. 2016 ESC Guidelines for the management of atrial fibrillation developed in collaboration with EACTS. *European heart journal* 2016; **37**: 2893-2962.
[56] Antzelevitch C, Brugada P, Borggrefe M, Brugada J, Brugada R, Corrado D, et al. Brugada syndrome: report of the second consensus conference: endorsed by the Heart Rhythm Society and the European Heart Rhythm Association. *Circulation* 2005; **111**: 659-670.
[57] Pappone C, Radinovic A, Manguso F, Vicedomini G, Sala S, Sacco FM, et al. New-onset atrial fibrillation as first clinical manifestation of latent Brugada syndrome: prevalence and clinical significance. *European heart journal* 2009; **30**: 2985-2992.

[58] Holmes AP, Yu TY, Tull S, Syeda F, Kuhlmann SM, O'Brien SM, et al. A Regional Reduction in Ito and IKACh in the Murine Posterior Left Atrial Myocardium Is Associated with Action Potential Prolongation and Increased Ectopic Activity. *PLoS One* 2016; **11**: e0154077.
[59] Cranefield PF. Action potentials, afterpotentials, and arrhythmias. *Circ Res* 1977; **41**: 415-423.
[60] January CT, Fozzard HA. Delayed afterdepolarizations in heart muscle: mechanisms and relevance. *Pharmacol Rev* 1988; **40**: 219-227.
[61] Schotten U, Verheule S, Kirchhof P, Goette A. Pathophysiological mechanisms of atrial fibrillation: a translational appraisal. *Physiological reviews* 2011; **91**: 265-325.
[62] Fabritz L, Kirchhof P, Franz MR, Eckardt L, Monnig G, Milberg P, et al. Prolonged action potential durations, increased dispersion of repolarization, and polymorphic ventricular tachycardia in a mouse model of proarrhythmia. *Basic Res Cardiol* 2003; **98**: 25-32.
[63] Tse G. Mechanisms of cardiac arrhythmias. *J Arrhythm* 2016; **32**: 75-81.
[64] Mines GR. On circulating excitations in heart muscles and their possible relation to tachycardia and fibrillation1914.
[65] Shiroshita-Takeshita A, Brundel BJ, Nattel S. Atrial fibrillation: basic mechanisms, remodeling and triggers. *J Interv Card Electrophysiol* 2005; **13**: 181-193.
[66] Heida A, van der Does WFB, van Staveren LN, Taverne Y, Roos-Serote MC, Bogers A, et al. Conduction Heterogeneity: Impact of Underlying Heart Disease and Atrial Fibrillation. *JACC Clin Electrophysiol* 2020; **6**: 1844-1854.
[67] Ishida K, Hayashi H, Miyamoto A, Sugimoto Y, Ito M, Murakami Y, et al. P wave and the development of atrial fibrillation. *Heart rhythm* 2010; **7**: 289-294.
[68] Nielsen JB, Kuhl JT, Pietersen A, Graff C, Lind B, Struijk JJ, et al. P-wave duration and the risk of atrial fibrillation: Results from the Copenhagen ECG Study. *Heart rhythm* 2015; **12**: 1887-1895.
[69] Wijffels MC, Kirchhof CJ, Dorland R, Allessie MA. Atrial fibrillation begets atrial fibrillation. A study in awake chronically instrumented goats. *Circulation* 1995; **92**: 1954-1968.
[70] Fabritz L, Guasch E, Antoniades C, Bardinet I, Benninger G, Betts TR, et al. Expert consensus document: Defining the major health modifiers causing atrial fibrillation: a roadmap to underpin personalized prevention and treatment. *Nature reviews Cardiology* 2016; **13**: 230-237.
[71] Roselli C, Chaffin MD, Weng LC, Aeschbacher S, Ahlberg G, Albert CM, et al. Multi-ethnic genome-wide association study for atrial fibrillation. *Nat Genet* 2018; **50**: 1225-1233.
[72] Lubitz SA, Yin X, Fontes JD, Magnani JW, Rienstra M, Pai M, et al. Association between familial atrial fibrillation and risk of new-onset atrial fibrillation. *JAMA* 2010; **304**: 2263-2269.
[73] Riley G, Syeda F, Kirchhof P, Fabritz L. An introduction to murine models of atrial fibrillation. *Frontiers in physiology* 2012; **3**: 296.
[74] Syeda F, Holmes AP, Yu TY, Tull S, Kuhlmann SM, Pavlovic D, et al. PITX2 Modulates Atrial Membrane Potential and the Antiarrhythmic Effects of Sodium-Channel Blockers. *J Am Coll Cardiol* 2016; **68**: 1881-1894.
[75] Jiang JQ, Shen FF, Fang WY, Liu X, Yang YQ. Novel GATA4 mutations in lone atrial fibrillation. *Int J Mol Med* 2011; **28**: 1025-1032.
[76] Wang XH, Huang CX, Wang Q, Li RG, Xu YJ, Liu X, et al. A novel GATA5 loss-of-function mutation underlies lone atrial fibrillation. *Int J Mol Med* 2013; **31**: 43-50.
[77] Alhassani S, Deif B, Conacher S, Cunningham KS, Roberts JD. A large familial pathogenic Plakophilin-2 gene (PKP2) deletion manifesting with sudden cardiac death and lone atrial fibrillation: Evidence for alternating atrial and ventricular phenotypes. *HeartRhythm Case Rep* 2018; **4**: 486-489.
[78] Di Pino A, Caruso E, Costanzo L, Guccione P. A novel RyR2 mutation in a 2-year-old baby presenting with atrial fibrillation, atrial flutter, and atrial ectopic tachycardia. *Heart rhythm* 2014; **11**: 1480-1483.
[79] Yang Y, Xia M, Jin Q, Bendahhou S, Shi J, Chen Y, et al. Identification of a KCNE2 gain-of-function mutation in patients with familial atrial fibrillation. *American journal of human genetics* 2004; **75**: 899-905.
[80] Chen YH, Xu SJ, Bendahhou S, Wang XL, Wang Y, Xu WY, et al. KCNQ1 gain-of-function mutation in familial atrial fibrillation. *Science (New York, NY)* 2003; **299**: 251-254.

[81] Ravn LS, Aizawa Y, Pollevick GD, Hofman-Bang J, Cordeiro JM, Dixen U, et al. Gain of function in IKs secondary to a mutation in KCNE5 associated with atrial fibrillation. *Heart rhythm* 2008; **5**: 427-435.
[82] Lundby A, Ravn LS, Svendsen JH, Hauns S, Olesen SP, Schmitt N. KCNE3 mutation V17M identified in a patient with lone atrial fibrillation. *Cell Physiol Biochem* 2008; **21**: 47-54.
[83] Xia M, Jin Q, Bendahhou S, He Y, Larroque MM, Chen Y, et al. A Kir2.1 gain-of-function mutation underlies familial atrial fibrillation. *Biochem Biophys Res Commun* 2005; **332**: 1012-1019.
[84] Darbar D, Kannankeril PJ, Donahue BS, Kucera G, Stubblefield T, Haines JL, et al. Cardiac sodium channel (SCN5A) variants associated with atrial fibrillation. *Circulation* 2008; **117**: 1927-1935.
[85] Ellinor PT, Nam EG, Shea MA, Milan DJ, Ruskin JN, MacRae CA. Cardiac sodium channel mutation in atrial fibrillation. *Heart rhythm* 2008; **5**: 99-105.
[86] Fozzard HA, Hanck DA. Structure and function of voltage-dependent sodium channels: comparison of brain II and cardiac isoforms. *Physiological reviews* 1996; **76**: 887-926.
[87] Rogart RB, Cribbs LL, Muglia LK, Kephart DD, Kaiser MW. Molecular cloning of a putative tetrodotoxin-resistant rat heart Na+ channel isoform. *Proc Natl Acad Sci U S A* 1989; **86**: 8170-8174.
[88] Nathan S, Gabelli SB, Yoder JB, Srinivasan L, Aldrich RW, Tomaselli GF, et al. Structural basis of cytoplasmic NaV1.5 and NaV1.4 regulation. *J Gen Physiol* 2021; **153**.
[89] Liu CJ, Dib-Hajj SD, Renganathan M, Cummins TR, Waxman SG. Modulation of the cardiac sodium channel Nav1.5 by fibroblast growth factor homologous factor 1B. *J Biol Chem* 2003; **278**: 1029-1036.
[90] Clatot J, Hoshi M, Wan X, Liu H, Jain A, Shinlapawittayatorn K, et al. Voltage-gated sodium channels assemble and gate as dimers. *Nature communications* 2017; **8**: 2077.
[91] Gabelli SB, Boto A, Kuhns VH, Bianchet MA, Farinelli F, Aripirala S, et al. Regulation of the NaV1.5 cytoplasmic domain by calmodulin. *Nature communications* 2014; **5**: 5126.
[92] Rivaud MR, Delmar M, Remme CA. Heritable arrhythmia syndromes associated with abnormal cardiac sodium channel function: ionic and non-ionic mechanisms. *Cardiovascular research* 2020; **116**: 1557-1570.
[93] Remme CA, Bezzina CR. Sodium channel (dys)function and cardiac arrhythmias. *Cardiovasc Ther* 2010; **28**: 287-294.
[94] Ruan Y, Liu N, Priori SG. Sodium channel mutations and arrhythmias. *Nature reviews Cardiology* 2009; **6**: 337-348.
[95] Olson TM, Michels VV, Ballew JD, Reyna SP, Karst ML, Herron KJ, et al. Sodium channel mutations and susceptibility to heart failure and atrial fibrillation. *JAMA* 2005; **293**: 447-454.
[96] Bezzina C, Veldkamp MW, van Den Berg MP, Postma AV, Rook MB, Viersma JW, et al. A single Na(+) channel mutation causing both long-QT and Brugada syndromes. *Circ Res* 1999; **85**: 1206-1213.
[97] Remme CA, Verkerk AO, Nuyens D, van Ginneken AC, van Brunschot S, Belterman CN, et al. Overlap syndrome of cardiac sodium channel disease in mice carrying the equivalent mutation of human SCN5A-1795insD. *Circulation* 2006; **114**: 2584-2594.
[98] Olson TM, Keating MT. Mapping a cardiomyopathy locus to chromosome 3p22-p25. *J Clin Invest* 1996; **97**: 528-532.
[99] Te Riele AS, Agullo-Pascual E, James CA, Leo-Macias A, Cerrone M, Zhang M, et al. Multilevel analyses of SCN5A mutations in arrhythmogenic right ventricular dysplasia/cardiomyopathy suggest non-canonical mechanisms for disease pathogenesis. *Cardiovascular research* 2017; **113**: 102-111.
[100] Cerrone M, Noorman M, Lin X, Chkourko H, Liang FX, van der Nagel R, et al. Sodium current deficit and arrhythmogenesis in a murine model of plakophilin-2 haploinsufficiency. *Cardiovascular research* 2012; **95**: 460-468.
[101] Sossalla S, Kallmeyer B, Wagner S, Mazur M, Maurer U, Toischer K, et al. Altered Na(+) currents in atrial fibrillation effects of ranolazine on arrhythmias and contractility in human atrial myocardium. *J Am Coll Cardiol* 2010; **55**: 2330-2342.
[102] Papadatos GA, Wallerstein PM, Head CE, Ratcliff R, Brady PA, Benndorf K, et al. Slowed conduction and ventricular tachycardia after targeted disruption of the cardiac sodium channel gene Scn5a. *Proc Natl Acad Sci U S A* 2002; **99**: 6210-6215.

[103] Echt DS, Ruskin JN. Use of Flecainide for the Treatment of Atrial Fibrillation. *The American journal of cardiology* 2020; **125**: 1123-1133.
[104] Makiyama T, Akao M, Shizuta S, Doi T, Nishiyama K, Oka Y, et al. A novel SCN5A gain-of-function mutation M1875T associated with familial atrial fibrillation. *J Am Coll Cardiol* 2008; **52**: 1326-1334.
[105] Corrado D, Migliore F, Basso C, Thiene G. Exercise and the risk of sudden cardiac death. *Herz* 2006; **31**: 553-558.
[106] James CA, Bhonsale A, Tichnell C, Murray B, Russell SD, Tandri H, et al. Exercise increases age-related penetrance and arrhythmic risk in arrhythmogenic right ventricular dysplasia/cardiomyopathy-associated desmosomal mutation carriers. *J Am Coll Cardiol* 2013; **62**: 1290-1297.
[107] Heidbuchel H, Prior DL, La Gerche A. Ventricular arrhythmias associated with long-term endurance sports: what is the evidence? *British journal of sports medicine* 2012; **46 Suppl 1**: i44-50.
[108] Wang W, Orgeron G, Tichnell C, Murray B, Crosson J, Monfredi O, et al. Impact of Exercise Restriction on Arrhythmic Risk Among Patients With Arrhythmogenic Right Ventricular Cardiomyopathy. *Journal of the American Heart Association* 2018; **7**.
[109] Gillis AM. Atrial Fibrillation and Ventricular Arrhythmias: Sex Differences in Electrophysiology, Epidemiology, Clinical Presentation, and Clinical Outcomes. *Circulation* 2017; **135**: 593-608.
[110] Akdis D, Saguner AM, Shah K, Wei C, Medeiros-Domingo A, von Eckardstein A, et al. Sex hormones affect outcome in arrhythmogenic right ventricular cardiomyopathy/dysplasia: from a stem cell derived cardiomyocyte-based model to clinical biomarkers of disease outcome. *European heart journal* 2017; **38**: 1498-1508.
[111] Ren J, Chen L, Zhang N, Chen X, Zhao Q, Chen K, et al. Plasma testosterone and arrhythmic events in male patients with arrhythmogenic right ventricular cardiomyopathy. *ESC Heart Fail* 2020; **7**: 1547-1559.
[112] O'Neal WT, Nazarian S, Alonso A, Heckbert SR, Vaccarino V, Soliman EZ. Sex hormones and the risk of atrial fibrillation: The Multi-Ethnic Study of Atherosclerosis (MESA). *Endocrine* 2017; **58**: 91-96.
[113] Chugh SS, Havmoeller R, Narayanan K, Singh D, Rienstra M, Benjamin EJ, et al. Worldwide epidemiology of atrial fibrillation: a Global Burden of Disease 2010 Study. *Circulation* 2014; **129**: 837-847.
[114] Aizer A, Gaziano JM, Cook NR, Manson JE, Buring JE, Albert CM. Relation of vigorous exercise to risk of atrial fibrillation. *The American journal of cardiology* 2009; **103**: 1572-1577.
[115] Molina L, Mont L, Marrugat J, Berruezo A, Brugada J, Bruguera J, et al. Long-term endurance sport practice increases the incidence of lone atrial fibrillation in men: a follow-up study. *Europace : European pacing, arrhythmias, and cardiac electrophysiology : journal of the working groups on cardiac pacing, arrhythmias, and cardiac cellular electrophysiology of the European Society of Cardiology* 2008; **10**: 618-623.
[116] Baldesberger S, Bauersfeld U, Candinas R, Seifert B, Zuber M, Ritter M, et al. Sinus node disease and arrhythmias in the long-term follow-up of former professional cyclists. *European heart journal* 2008; **29**: 71-78.
[117] Myrstad M, Lochen ML, Graff-Iversen S, Gulsvik AK, Thelle DS, Stigum H, et al. Increased risk of atrial fibrillation among elderly Norwegian men with a history of long-term endurance sport practice. *Scand J Med Sci Sports* 2014; **24**: e238-244.
[118] Andersen K, Farahmand B, Ahlbom A, Held C, Ljunghall S, Michaelsson K, et al. Risk of arrhythmias in 52 755 long-distance cross-country skiers: a cohort study. *European heart journal* 2013; **34**: 3624-3631.

2 Chapter II - Continuation of the introduction: Medical therapy in Arrhythmogenic Right Ventricular Cardiomyopathy (ARVC)

Book chapter. This chapter was published in "Current Concepts in Arrhythmogenic Cardiomyopathy, Second Edition".

Medical therapy in Arrhythmogenic Right Ventricular Cardiomyopathy (ARVC).

Laura Sommerfeld, Areej Aljehani, Manish Kalla, Larissa Fabritz. Published in Current Concepts in Arrhythmogenic Cardiomyopathy, Second Edition. *Cardiotext Publishing. 2020*

Author contributions in this book chapter

I wrote the manuscript and produced the figure. The primary manuscript was then reviewed and edited by all authors.

Medical therapy in ARVC

Laura Sommerfeld MSc, Areej Aljehani MSc, Manish Kalla MD, Larissa Fabritz MD

Institute of Cardiovascular Sciences and Department of Cardiology, University Hospital Birmingham, UK

One of the most widely accepted advice for patients with arrhythmogenic right ventricular cardiomyopathy (ARVC) is adaptation of life style, mainly restriction of sports at high, competitive level (Class Ic recommendation), probably already for asymptomatic mutation carriers [1]. This is based on preclinical and clinical data convincingly illustrating that high-level endurance training accelerates the development of ARVC, manifesting both as arrhythmic events and as right heart dilatation [1-6].

Due to the limited number of diagnosed patients, systematic data on therapeutic management and long-term outcome, especially mortality, are still scarce. However, registries and joint efforts from multiple specialised centres across the world have facilitated planned and ongoing randomized studies. This chapter aims to provide an overview of current medical strategies in AVRC as well as ongoing research to identify molecular targets for medical therapy (Figure 1).

Traditionally, medical therapy in patients with ARVC was mainly used to prevent ventricular arrhythmias and sudden death. ***Antiarrhythmic therapy*** is currently often used as an adjunct to defibrillation and ablation therapy [7]. A multicentre, retrospective study including 110 patients did not show any significant advancement of ventricular tachycardia burden in those patients who underwent ablation therapy alone, over those receiving pharmacological therapy [8]. Whilst heart failure medication, including diuretics, are in clinical use to limit heart failure symptoms in patients with ARVC and heart failure, there is very little evidence on the prognostic effects of these drugs in patients with ARVC. Currently, there is no medical therapy with proven effects on disease progression or prognosis. The need for new medical therapeutic concepts and clinical studies of novel and traditional concepts therefore remains high.

Beta-blockers

As an effective and generally safe anti-arrhythmic agent, beta-blockers are integrated into the management of ARVC [1]. Their use limits autonomic (adrenergic) dysfunction which is known to contribute to the disease phenotype, as increased adrenergic stimulation in ARVC facilitates norepinephrine release in the heart. In addition, inhibition of the norepinephrine uptake and subsequent reduction of postsynaptic β-adrenoceptor density have been described [9-11]. Prophylactic

use in pre-symptomatic gene-carriers is currently not recommended [7]c. Apart from preventing exercise-related catecholaminergic ventricular arrhythmias, beta-blockers also affect after- and preload.

Load-reducing therapy

High preload acutely increases right ventricular size. Global longitudinal and circumferential strain rates appear to be lower in right ventricles of ARVC patients compared to healthy controls [12]. Decreased wall motion subjects areas in the triangle of dysplasia (apex, RVOT, tricuspid valve) to high mechanical stress. Reduction of mechanical stress via load reduction has therefore been suggested and was successfully tested in a genetic murine model of ARVC. The combination of nitrates and a diuretic not only prevented exercise-induced right-ventricular enlargement, but also reduced occurrence of sustained ventricular tachycardia in hearts of young adult mice [13]. This successful experimental study, employing the decrease of venous return delivered by nitrates and a decrease in systemic blood volume by diuretics, has been translated into a clinical trial plan (PreVent-ARVC). The suggested medical strategy of preload reduction can be achieved by several drug combinations of choice, including e.g. long-acting nitrates (Pentaerithrityl tetranitrate, PETN) or the combination of a thiazide and a potassium-saving diuretic [14].

ACE-inhibitors, sartans, and mineralocorticoid receptor antagonists

Angiotensin-converting enzyme (ACE)-inhibitors have been considered as part of the therapeutic armamentarium in ARVC, following their effectiveness in left ventricular failure and considering their effect on preload and afterload. Additionally, Angiotensin II is known as an important mediator of cardiac remodelling and can influence matrix metalloproteinase (MMP) transcription [15]. Preliminary results from a small French cohort of ARVC patients suggest that ACE-inhibitors can have an effect on extracellular matrix proteins, detected by ratios of MMP9 and its inhibitors tissue inhibitor of metalloproteinase (TIMP)1 and TIMP2 in blood samples. Patients who received beta-blockers only, showed an increase in MMP9/TIMP1 and MMP9/TIMP2 ratios after one year, indicating disruption of the extracellular matrix homeostasis. The latter seemed to be stabilized in patients treated with ACE-inhibitors on top of beta-blockers [16]. This observation led to the design of a controlled clinical trial 'Counteracting myocardial fibrotic remodelling by Blockade of the Renin-Angiotensin-Aldosterone System in Patients With Arrhythmogenic Right Ventricular Dysplasia (BRAVE, ClinicalTrials.gov Identifier: NCT03593317)' [16]. Commencing in 2021 and conducted in 26 centres in France, this double-blinded, parallel, prospective, randomized study will compare disruption of the renin-angiotensin-

aldosterone signalling (RAAS) pathway to placebo in a total of 120 participants. It is currently validated whether the trial will utilize spironolactone, an aldosterone inhibitor, instead of the ACE-inhibitor ramipril, as originally proposed. The diuretic action of spironolactone is very likely additionally beneficial, as discussed above. Treatment duration for each patient will be 3 years. Primary outcome of the trial is to show reduction in right ventricular deterioration as well as in ventricular arrhythmia.

The approach of RAAS-modulation is also followed up by a Dutch study conducted in a founder mutation cohort of phospholamban R14del carriers (Intervention in PHOspholamban RElated CArdiomyopathy Study, i-PHORECAST, ClinicalTrials.gov Identifier: NCT01857856). Patients with this mutation may develop dilated cardiomyopathy and/or ARVC with early manifestation of cardiac fibrosis (remodelling). The trial will compare the mineralocorticoid receptor antagonist eplerenone to no therapy in mutation carriers with no or only minimal disease signs. The investigators aim to show reduced disease progression and postponed onset of overt disease. With 84 enrolled patients the study is estimated to be completed in 2021.

Antiarrhythmic drugs

Beta-blockers and non-dihydropyridine calcium channel blockers (verapamil or diltiazem) have been shown to suppress inducible ventricular arrhythmias in patients with ARVC [17]. The non-selective beta-blocker and potassium channel blocker sotalol has long been used to improve symptoms in patients with frequent ventricular ectopy or non-sustained ventricular arrhythmia and a high efficacy has been reported in a retrospective study [17, 18]. Yet, neither sotalol nor other beta-blockers have been shown to reduce re-entry ventricular arrhythmia burden in patients with ARVC. When beta-blockers, verapamil, or sotalol are ineffective, the antiarrhythmic drug amiodarone is often used, based on expert opinion and some observational data [1, 17, 19]. Despite relatively high recurrence of ventricular tachycardia due to disease progression, ablation therapy is increasingly used (see elsewhere in this book). The combination of mexiletine and sotalol has been empirically used in some UK centres, often suppressing ectopic activity and arrhythmia sufficiently to avoid such invasive procedures like epicardial ablation in patients with ARVC.

A randomized clinical trial conducted by Kannankeril and colleagues showed that the class Ic antiarrhythmic flecainide on top of beta-blocker therapy reduced exercise-induced arrhythmia in Catecholaminergic Polymorphic Ventricular Tachycardia (CPVT) patients [20]. Ermakov and colleagues reported positive outcomes from 3 case reports when using a combination of sotalol and flecainide, after insufficient arrhythmia control under monotherapy. Of note, patients presented with an isolated right-ventricular disease phenotype and were already implanted with a cardioverter-defibrillator [21].

Adapting this strategy to treat other patient subgroups is not without risk, not least because the sodium channel blocker flecainide should usually be avoided in structural heart disease. Studies in murine models of ARVC implicated an impairment of functional sodium channel availability based on decreased sodium current density [22, 23], and this observation would not favour medical sodium channel block in ARVC. The ongoing 'Pilot Randomized Trial With Flecainide in ARVC Patients' investigates the drug's potential to reduce the number of ventricular ectopic beats in ARVC patients who are protected by an implantable cardioverter-defibrillator (ClinicalTrials.gov Identifier: NCT03685149, 2019-2021).

Anticoagulants

Thromboembolism due to ventricular dilatation, aneurysms and wall motion abnormalities or even due to atrial fibrillation might be an accompanying complication of the disease [24]. The annual incidence of thromboembolic events in ARVC in a retrospective study of 126 patients (mean follow-up period of 99+/-64 months) was reported to be 0.5% [24].

Oral anticoagulation treatment is recommended for secondary prevention in ARVC patients diagnosed with intracavitary thrombosis or venous/systemic thromboembolism. Prophylactic anticoagulation for primary prevention however is not [7].

Developing medical therapy to slow or prevent disease progression

Therapeutic management of ARVC is currently limited to symptomatic treatment that can often not impede the progressive nature of the disease. Targeting molecular processes taking place during the early, concealed phase prior to clinical manifestation could be a very elegant approach towards active treatment and long-term outcome benefit. Pre-clinical research suggests that electrophysiological changes can precede the morphological disease phenotype. This was for instance established in a conditional Plakophilin-2 knockout mouse model by Kim and colleagues. The group showed increased calcium spark frequency in cardiomyocytes and phosphorylation of ryanodine receptors (RyR) at a threonine residue indicated in gating of the channel, specifically in the right ventricle. Normalization of calcium spark frequency back to control levels was achieved via protein kinase C (PKC) inhibition [25]. Widening of the intercellular space due to mechanical junction instability in ARVC might cause dislodgment of signalling molecules like PKC, releasing them from their regulation in their subcellular compartment, causing adverse disease-specific off-target phosphorylation events. The induced abnormal calcium handling during the concealed phase might later on trigger structural abnormalities as observed in the overt phase of ARVC. Suppression of calcium release from the sarcoplasmic

reticulum therefore appears to be an attractive therapeutic approach. Some of the beneficial effects of beta-blockers might be attributed to restoration of normal RyR2 channel function [26].

Other pathways indicated in ARVC include Wnt/β-catenin signalling. Plakoglobin (γ-catenin) dislocation from the cardiac intercalated disc has been postulated in ARVC [27, 28]. Translocation into the cytoplasm might cause interference with canonical Wnt signalling components, most likely with its structural homologue β-catenin, disturbing homeostasis of the pathway. Downregulated Wnt/β-catenin signalling was for instance observed in a transgenic mouse model harbouring a human desmoglein-2 non-sense mutation [29]. Alterations in the activity of GSK3β, a core component of the catenin destruction complex, are implicated to contribute to ARVC pathogenesis. Inhibition of GSK3β (and thereby presumably upregulation of Wnt signalling) was beneficial in terms of preventing cardiomyocyte injury and cardiac dysfunction in two genetic mouse and *in vitro* models of the disease [30]. Triggering Wnt signalling, however, is not without risk since increased Wnt activity is found in carcinogenesis of different tissues and knowledge on Wnt activity in other organs of ARVC patients is limited. Tissue-specific drug delivery or identification of cardiac/ cardiomyocyte-specific players of the signalling cascade might lead the way towards safer therapy approaches targeting this pathway.

Canonical Wnt activity alteration in ARVC was also proposed to be caused by abnormal activation of peroxisome proliferator-activated receptors (PPAR), transcriptional regulation factors of fatty acid metabolism [31, 32]. Abnormal activation of PPARγ, leading to a decrease in Wnt signalling, might contribute to exaggerated lipogenesis and cardiomyocyte death. Based on this observation, PPARγ agonists like rosiglitazone should be avoided in ARVC patients. Further studies in different models are ongoing.

Necrosis of cardiomyocytes has been described in ARVC and demonstrated to initiate myocardial injury followed by an inflammatory response of the myocardium [33]. Activation of the immune response has been observed in several ARVC models, based on the presence of antibodies against desmoglein-2 [34]. This cardiac immune response includes increased production and release of inflammatory cytokines and exaggerated activation of NF-κB. Inhibition of this transcription factor using a small molecule reduced cytokine production and release *in vitro*, studying human induced pluripotent stem cell-derived cardiomyocytes, as well as *in vivo,* using a genetic mouse model [35]. This implies immune modulation as a further possible approach.

Treatment strategies and suggested approaches based on pre-clinical data discussed in this chapter are summarized in Figure 1. Clearly, these therapeutic concepts that appear promising in preclinical models require validation and testing in patients with ARVC. Fortunately, such studies have started or are in the planning phase.

Medical therapy for ARVC – does one size fit all?

This overview is generalized, since observations are derived from pre-clinical models harbouring different ARVC-causing mutations, which translate into diverse disease phenotypes. These are also recognized in patients, as Chen and colleagues very recently established subtype-specific human ARVC pathology based on distinct genetics [36]. Hence, different mutations might require different personalized treatment strategies. Moreover, sex hormone levels seem to influence clinical outcome of the disease [37]. Understanding the molecular basis of these observations will improve medical therapy. The same is true for deciphering disease phase-specific disturbances at molecular level, in particular during the concealed phase, to enable early detection and prevent progression of ARVC to reduce mortality.

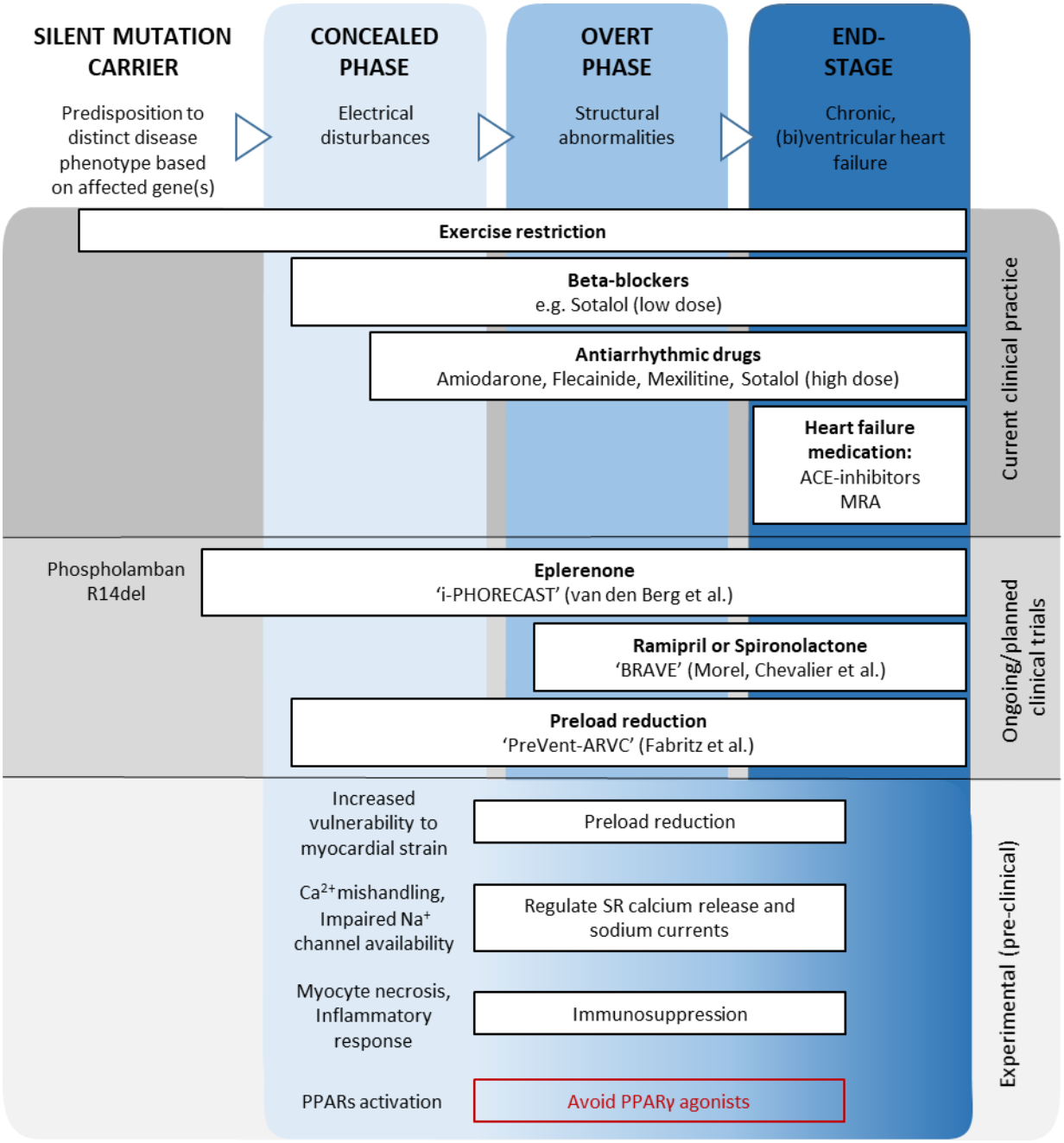


Figure 1: Summary of current treatment strategies, planned and ongoing clinical trials and possible new

MRA: Mineralocorticoid receptor antagonist, SR: Sarcoplasmic reticulum

References

[1] Priori SG, Blomstrom-Lundqvist C, Mazzanti A, Blom N, Borggrefe M, Camm J, et al. 2015 ESC Guidelines for the management of patients with ventricular arrhythmias and the prevention of sudden cardiac death: The Task Force for the Management of Patients with Ventricular Arrhythmias and the Prevention of Sudden Cardiac Death of the European Society of Cardiology (ESC). Endorsed by: Association for European Paediatric and Congenital Cardiology (AEPC). *European heart journal* 2015; **36**: 2793-2867.
[2] Ruwald AC, Marcus F, Estes NA, 3rd, Link M, McNitt S, Polonsky B, et al. Association of competitive and recreational sport participation with cardiac events in patients with arrhythmogenic right ventricular cardiomyopathy: results from the North American multidisciplinary study of arrhythmogenic right ventricular cardiomyopathy. *European heart journal* 2015; **36**: 1735-1743.
[3] James CA, Bhonsale A, Tichnell C, Murray B, Russell SD, Tandri H, et al. Exercise increases age-related penetrance and arrhythmic risk in arrhythmogenic right ventricular dysplasia/cardiomyopathy-associated desmosomal mutation carriers. *J Am Coll Cardiol* 2013; **62**: 1290-1297.
[4] Kirchhof P, Fabritz L, Zwiener M, Witt H, Schafers M, Zellerhoff S, et al. Age- and training-dependent development of arrhythmogenic right ventricular cardiomyopathy in heterozygous plakoglobin-deficient mice. *Circulation* 2006; **114**: 1799-1806.
[5] Corrado D, Migliore F, Basso C, Thiene G. Exercise and the risk of sudden cardiac death. *Herz* 2006; **31**: 553-558.
[6] Heidbuchel H, Hoogsteen J, Fagard R, Vanhees L, Ector H, Willems R, et al. High prevalence of right ventricular involvement in endurance athletes with ventricular arrhythmias. Role of an electrophysiologic study in risk stratification. *European heart journal* 2003; **24**: 1473-1480.
[7] Corrado D, Wichter T, Link MS, Hauer RN, Marchlinski FE, Anastasakis A, et al. Treatment of Arrhythmogenic Right Ventricular Cardiomyopathy/Dysplasia: An International Task Force Consensus Statement. *Circulation* 2015; **132**: 441-453.
[8] Mahida S, Venlet J, Saguner AM, Kumar S, Baldinger SH, AbdelWahab A, et al. Ablation compared with drug therapy for recurrent ventricular tachycardia in arrhythmogenic right ventricular cardiomyopathy: Results from a multicenter study. *Heart rhythm* 2019; **16**: 536-543.
[9] Wichter T, Hindricks G, Lerch H, Bartenstein P, Borggrefe M, Schober O, et al. Regional myocardial sympathetic dysinnervation in arrhythmogenic right ventricular cardiomyopathy. An analysis using 123I-meta-iodobenzylguanidine scintigraphy. *Circulation* 1994; **89**: 667-683.
[10] Paul M, Meyborg M, Boknik P, Gergs U, Gerss J, Schmitz W, et al. Autonomic dysfunction in patients with arrhythmogenic right ventricular cardiomyopathy: biochemical evidence of altered signaling pathways. *Pacing Clin Electrophysiol* 2014; **37**: 173-178.
[11] Wichter T, Schafers M, Rhodes CG, Borggrefe M, Lerch H, Lammertsma AA, et al. Abnormalities of cardiac sympathetic innervation in arrhythmogenic right ventricular cardiomyopathy : quantitative assessment of presynaptic norepinephrine reuptake and postsynaptic beta-adrenergic receptor density with positron emission tomography. *Circulation* 2000; **101**: 1552-1558.
[12] Heermann P, Hedderich DM, Paul M, Schulke C, Kroeger JR, Baessler B, et al. Biventricular myocardial strain analysis in patients with arrhythmogenic right ventricular cardiomyopathy (ARVC) using cardiovascular magnetic resonance feature tracking. *J Cardiovasc Magn Reson* 2014; **16**: 75.
[13] Fabritz L, Hoogendijk MG, Scicluna BP, van Amersfoorth SC, Fortmueller L, Wolf S, et al. Load-reducing therapy prevents development of arrhythmogenic right ventricular cardiomyopathy in plakoglobin-deficient mice. *J Am Coll Cardiol* 2011; **57**: 740-750.
[14] Fabritz L, Fortmuller L, Yu TY, Paul M, Kirchhof P. Can preload-reducing therapy prevent disease progression in arrhythmogenic right ventricular cardiomyopathy? Experimental evidence and concept for a clinical trial. *Prog Biophys Mol Biol* 2012; **110**: 340-346.
[15] Rouet-Benzineb P, Gontero B, Dreyfus P, Lafuma C. Angiotensin II induces nuclear factor-kappa B activation in cultured neonatal rat cardiomyocytes through protein kinase C signaling pathway. *J Mol Cell Cardiol* 2000; **32**: 1767-1778.

[16] Morel E, Manati AW, Nony P, Maucort-Boulch D, Bessiere F, Cai X, et al. Blockade of the renin-angiotensin-aldosterone system in patients with arrhythmogenic right ventricular dysplasia: A double-blind, multicenter, prospective, randomized, genotype-driven study (BRAVE study). *Clin Cardiol* 2018; **41**: 300-306.
[17] Wichter T, Borggrefe M, Haverkamp W, Chen X, Breithardt G. Efficacy of antiarrhythmic drugs in patients with arrhythmogenic right ventricular disease. Results in patients with inducible and noninducible ventricular tachycardia. *Circulation* 1992; **86**: 29-37.
[18] Wichter T, Paul TM, Eckardt L, Gerdes P, Kirchhof P, Bocker D, et al. Arrhythmogenic right ventricular cardiomyopathy. Antiarrhythmic drugs, catheter ablation, or ICD? *Herz* 2005; **30**: 91-101.
[19] Marcus GM, Glidden DV, Polonsky B, Zareba W, Smith LM, Cannom DS, et al. Efficacy of antiarrhythmic drugs in arrhythmogenic right ventricular cardiomyopathy: a report from the North American ARVC Registry. *J Am Coll Cardiol* 2009; **54**: 609-615.
[20] Kannankeril PJ, Moore JP, Cerrone M, Priori SG, Kertesz NJ, Ro PS, et al. Efficacy of Flecainide in the Treatment of Catecholaminergic Polymorphic Ventricular Tachycardia: A Randomized Clinical Trial. *JAMA Cardiol* 2017; **2**: 759-766.
[21] Ermakov S, Hoffmayer KS, Gerstenfeld EP, Scheinman MM. Combination drug therapy for patients with intractable ventricular tachycardia associated with right ventricular cardiomyopathy. *Pacing and clinical electrophysiology : PACE* 2014; **37**: 90-94.
[22] Rizzo S, Lodder EM, Verkerk AO, Wolswinkel R, Beekman L, Pilichou K, et al. Intercalated disc abnormalities, reduced Na(+) current density, and conduction slowing in desmoglein-2 mutant mice prior to cardiomyopathic changes. *Cardiovascular research* 2012; **95**: 409-418.
[23] Cerrone M, Noorman M, Lin X, Chkourko H, Liang FX, van der Nagel R, et al. Sodium current deficit and arrhythmogenesis in a murine model of plakophilin-2 haploinsufficiency. *Cardiovascular research* 2012; **95**: 460-468.
[24] Wlodarska EK, Wozniak O, Konka M, Rydlewska-Sadowska W, Biederman A, Hoffman P. Thromboembolic complications in patients with arrhythmogenic right ventricular dysplasia/cardiomyopathy. *Europace : European pacing, arrhythmias, and cardiac electrophysiology : journal of the working groups on cardiac pacing, arrhythmias, and cardiac cellular electrophysiology of the European Society of Cardiology* 2006; **8**: 596-600.
[25] Kim JC, Perez-Hernandez M, Alvarado FJ, Maurya SR, Montnach J, Yin Y, et al. Disruption of Ca(2+)i Homeostasis and Connexin 43 Hemichannel Function in the Right Ventricle Precedes Overt Arrhythmogenic Cardiomyopathy in Plakophilin-2-Deficient Mice. *Circulation* 2019; **140**: 1015-1030.
[26] Reiken S, Wehrens XH, Vest JA, Barbone A, Klotz S, Mancini D, et al. Beta-blockers restore calcium release channel function and improve cardiac muscle performance in human heart failure. *Circulation* 2003; **107**: 2459-2466.
[27] Noorman M, Hakim S, Kessler E, Groeneweg JA, Cox MG, Asimaki A, et al. Remodeling of the cardiac sodium channel, connexin43, and plakoglobin at the intercalated disk in patients with arrhythmogenic cardiomyopathy. *Heart rhythm* 2013; **10**: 412-419.
[28] Asimaki A, Tandri H, Huang H, Halushka MK, Gautam S, Basso C, et al. A new diagnostic test for arrhythmogenic right ventricular cardiomyopathy. *N Engl J Med* 2009; **360**: 1075-1084.
[29] Calore M, Lorenzon A, Vitiello L, Poloni G, Khan MAF, Beffagna G, et al. A novel murine model for arrhythmogenic cardiomyopathy points to a pathogenic role of Wnt signalling and miRNA dysregulation. *Cardiovascular research* 2019; **115**: 739-751.
[30] Chelko SP, Asimaki A, Andersen P, Bedja D, Amat-Alarcon N, DeMazumder D, et al. Central role for GSK3beta in the pathogenesis of arrhythmogenic cardiomyopathy. *JCI Insight* 2016; **1**.
[31] Kim C, Wong J, Wen J, Wang S, Wang C, Spiering S, et al. Studying arrhythmogenic right ventricular dysplasia with patient-specific iPSCs. *Nature* 2013; **494**: 105-110.
[32] Djouadi F, Lecarpentier Y, Hebert JL, Charron P, Bastin J, Coirault C. A potential link between peroxisome proliferator-activated receptor signalling and the pathogenesis of arrhythmogenic right ventricular cardiomyopathy. *Cardiovascular research* 2009; **84**: 83-90.
[33] Pilichou K, Remme CA, Basso C, Campian ME, Rizzo S, Barnett P, et al. Myocyte necrosis underlies progressive myocardial dystrophy in mouse dsg2-related arrhythmogenic right ventricular cardiomyopathy. *J Exp Med* 2009; **206**: 1787-1802.

[34] Chatterjee D, Fatah M, Akdis D, Spears DA, Koopmann TT, Mittal K, et al. An autoantibody identifies arrhythmogenic right ventricular cardiomyopathy and participates in its pathogenesis. *European heart journal* 2018; **39**: 3932-3944.
[35] Chelko SP, Asimaki A, Lowenthal J, Bueno-Beti C, Bedja D, Scalco A, et al. Therapeutic Modulation of the Immune Response in Arrhythmogenic Cardiomyopathy. *Circulation* 2019.
[36] Chen L, Song J, Chen X, Chen K, Ren J, Zhang N, et al. A novel genotype-based clinicopathology classification of arrhythmogenic cardiomyopathy provides novel insights into disease progression. *European heart journal* 2019; **40**: 1690-1703.
[37] Akdis D, Saguner AM, Shah K, Wei C, Medeiros-Domingo A, von Eckardstein A, et al. Sex hormones affect outcome in arrhythmogenic right ventricular cardiomyopathy/dysplasia: from a stem cell derived cardiomyocyte-based model to clinical biomarkers of disease outcome. *European heart journal* 2017; **38**: 1498-1508.

3 Chapter III - Methods: Effects of genetic background, sex and age on murine atrial electrophysiology

Publication 1. This research was originally published in EP Europace.

Effects of genetic background, sex, and age on murine atrial electrophysiology.

Obergassel J, O'Reilly M, **Sommerfeld LC**, Kabir SN, O'Shea C, Syeda F, Eckardt L, Kirchhof P, Fabritz L.

Europace. 2021 Jan 19. pii: 6104222. doi: 10.1093/europace/euaa369.

Author contributions in publication 1

Results reported are based on experiments performed by our research groups at the University of Muenster (2005-2011) and at the University of Birmingham (2011–2019). I set up the summary analysis database with Julius Obergassel, performed re-analysis of original recordings and produced figures.

Effects of genetic background, sex and age on murine atrial electrophysiology

Julius Obergassel[1,2], Molly O'Reilly[1], Laura C. Sommerfeld[1], S Nashitha Kabir[1], Christopher O'Shea[1], Fahima Syeda[1], Lars Eckardt[3], Paulus Kirchhof[1,2,4,5,6], Larissa Fabritz[1,4]

[1] Institute of Cardiovascular Sciences, University of Birmingham, Birmingham, UK

[2] University Heart and Vascular Center, University Hospital Hamburg-Eppendorf, Hamburg, Germany

[3] Department of Cardiology II - Electrophysiology, University Hospital Münster, Münster, Germany

[4] Department of Cardiology UHB NHS Trust, Birmingham, UK

[5] Department of Cardiology, SWBH NHS Trust, Birmingham City Hospital, Birmingham, UK

[6] German Center for Cardiovascular Research, partner site Hamburg/Kiel/Lübeck, Germany

Corresponding author:

Professor Dr Larissa Fabritz
Institute of Cardiovascular Sciences
University of Birmingham
Edgbaston Birmingham
B15 2TT, UK
United Kingdom
Tel:
E-Mail:

Abstract

Aims

Genetically altered mice are powerful models to investigate mechanisms of atrial arrhythmias, but normal ranges for murine atrial electrophysiology have not been robustly characterized.

Methods and results

We analyzed results from 221 electrophysiological (EP) studies in isolated, Langendorff-perfused hearts of wildtype mice (114 female, 107 male) from 2.5 to 17.7 months (mean 7 months) with different genetic backgrounds (C57BL/6, FVB/N, MF1, 129/Sv, Swiss agouti). Left atrial monophasic action potential duration (LA-APD), interatrial activation time (IA-AT), and atrial effective refractory period (ERP) were summarized at different pacing cycle lengths (PCLs). Factors influencing atrial electrophysiology including genetic background, sex, and age were determined.

LA-APD70 was 18 ± 0.5 ms, atrial ERP was 27 ± 0.8 ms, and IA-AT was 17 ± 0.5 ms at 100 ms PCL. LA-APD was longer with longer PCL (+17% from 80 to 120 ms PCL for APD70), while IA-AT decreased (−7% from 80 to 120 ms PCL). Female sex was associated with longer ERP (+14% vs. males). Genetic background influenced atrial electrophysiology: LA-APD70 (−20% vs. average) and atrial ERP (−25% vs. average) were shorter in Swiss agouti background compared to others. LA-APD70 (+25% vs. average) and IA-AT (+44% vs. average) were longer in 129/Sv mice. Atrial ERP was longer in FVB/N (+34% vs. average) and in younger experimental groups below 6 months of age.

Conclusion

This work defines normal ranges for murine atrial EP parameters. Genetic background has a profound effect on these parameters, at least of the magnitude as those of sex and age. These results can inform the experimental design and interpretation of murine atrial electrophysiology.

Introduction

The burden of disease associated with atrial fibrillation (AF) and its recently identified genomic basis make research into the genetic, genomic and molecular mechanisms a priority for cardiac electrophysiologists [1]. Sex and age shape the presentation and outcome of cardiovascular diseases including AF [2-4].

Isolated, Langendorff-perfused hearts from wildtype (WT) and genetically altered murine models are widely studied to understand the electrophysiological effects of specific genetic mutations [5]. Functional findings can be correlated with signalling studies and the effects of pharmacological interventions within the same model.

Systematic comparisons have found that genetic background, sex and age affect murine *ventricular* action potential duration (APD), activation time (AT), and effective refractory period (ERP) in WT murine hearts [6]. Whether similar differences exist in *atrial* electrophysiological parameters is unknown. Here we report the range of normal atrial electrophysiological parameters in isolated murine WT hearts and present the effects of genetic background, sex and age on these measurements.

Methods

Experiment selection for analysis

This is a retrospective analysis of experimental data from a range of atrial electrophysiological studies in the isolated beating Langendorff heart (see **Figure 1** for workflow). Isolated, Langendorff-perfused murine WT atrial electrophysiology experiments were carried out by our research groups at the University of Münster (2005–2011) and at the University of Birmingham (2011–2019) and collated for analysis. Animals were fed standard chow diet and kept under controlled conditions (12 hours light cycle, 22°C room temperature, 55% humidity).

All experiments in Birmingham were conducted according to the Animals (Scientific Procedures) Act 1986 and approved by the Home Office (Home Office References 30/2967 and PFDAAF77F) and the institutional review board at the University of Birmingham. All experiments in Münster were approved by the regional authority (licence numbers G61/99, G83/2004).

Heart isolation, preparation, and electrophysiological recordings

Experimental details have been described previously [7-9]. Deep terminal anaesthesia was achieved by intraperitoneal injection of either urethane (2 g/kg body weight (BW)) or sodium pentobarbital (Euthatal; 100 µL at 200 µg/µL) or by inhalation of 5% isoflurane with an O_2 flow rate of 3 L/min. Murine hearts were extracted under heparinisation, cannulated via the ascending aorta and mounted on a vertical Langendorff-apparatus (Hugo Sachs/Harvard Apparatus, Germany) for retrograde perfusion of the aorta with Krebs-Henseleit (KH) buffer [9-12]. Protocols aimed for constant aortic pressure (100 ± 5 mmHg), coronary flow rate (4 ± 1 ml/min) and temperature (36 ± 1°C). Preparation time, defined as time from extraction to start of perfusion, was logged and aimed to be ≤5 mins in 4°C KH solution or ≤2 mins at room temperature. Deviation from these norms led to experimental exclusion. Before starting the electrophysiological study, stimulation and measurements, extracted hearts were given time to adjust to KH-buffer perfusion and temperature.

Stimulation was conducted via an octapolar electrophysiological (EP) catheter inserted through the vena cava or a small hole into the right atrium (RA, see **Figure 2** and **Graphical Abstract**). Atrial monophasic action potentials (MAPs) were recorded using a left atrial epicardial spring-loaded MAP-catheter. Pre-amplified (Model 2000, EP Technologies Inc, California) MAP signals were analysed semi-automatically under manual quality control using either a custom-made (based on LabVIEW, National Instruments, Texas) or commercially available software (ecgAUTO, EMKA Technologies, France).

Stimulation protocols and analysis of electrophysiological parameters

Isolated hearts were paced from the RA using two electrodes of the EP-catheter at different pacing cycle lengths (PCLs) of 80, 100 and 120 ms. Left atrial APD (LA-APD), atrial ERP and interatrial activation time (IA-AT) were analysed.

LA-APD was measured at different constant steady state S1-PCLs as the time from the fastest upstroke to 30, 50, 70 and 90% (APD30, APD50, APD70 and APD90, respectively) repolarisation, with 0% defined as the peak of the MAP upstroke. Full (100%) repolarisation was defined as return to the mean baseline diastolic electrical activity on the LA-MAP-electrode. During review, MAPs were quality coded according to standard criteria and experiments were excluded if less than three criteria were fulfilled. Standard criteria were: stable baseline, stable MAP morphology, fast upstroke without inflections, upstroke duration <2 ms, MAP amplitude >1 mV and rapid repolarization without early plateau.

For atrial ERP measurements, the RA was stimulated with a train of eight S1-stimuli at a constant PCL (80, 100 and 120 ms) followed by a single extra stimulus (S2) with an initial S2-coupling-interval of 50 ms. The interval was decreased by 1 ms after each series. Atrial ERP was defined as the shortest S2-interval which still resulted in depolarisation of the LA.

IA-AT was defined as the time from the RA stimulus artefact to the steepest upstroke of the MAP signal. The time of the stimulus artefact was captured either together with the MAP itself as a farfield artefact, or on the intracardial ECG recorded by the electrodes of the EP-catheter located in the RA.

Data storing, archiving, querying, outlier handling and statistical analysis

Data analysis workflow is illustrated in **Figure 1**. A relational database scheme was developed to structure and harmonise all murine model parameters and to ensure correct linkage of these parameters to the same isolated heart experiment. Harmonisation of unstructured raw data was performed semi-automatically depending on raw data format. With knowledge of existing experiments, the data collection was optimised, exemplarily by manual search for obviously missing data. During this optimisation process acquired data was again injected into the semi-automatic harmonisation process and stored in the database. SQL-based queries were developed to obtain data in different arrangements for analysis and for consistency checks. A statistic-based outlier analysis identified outlier data points. Related experiments were re-analysed by a second observer (**Supplement 1**).

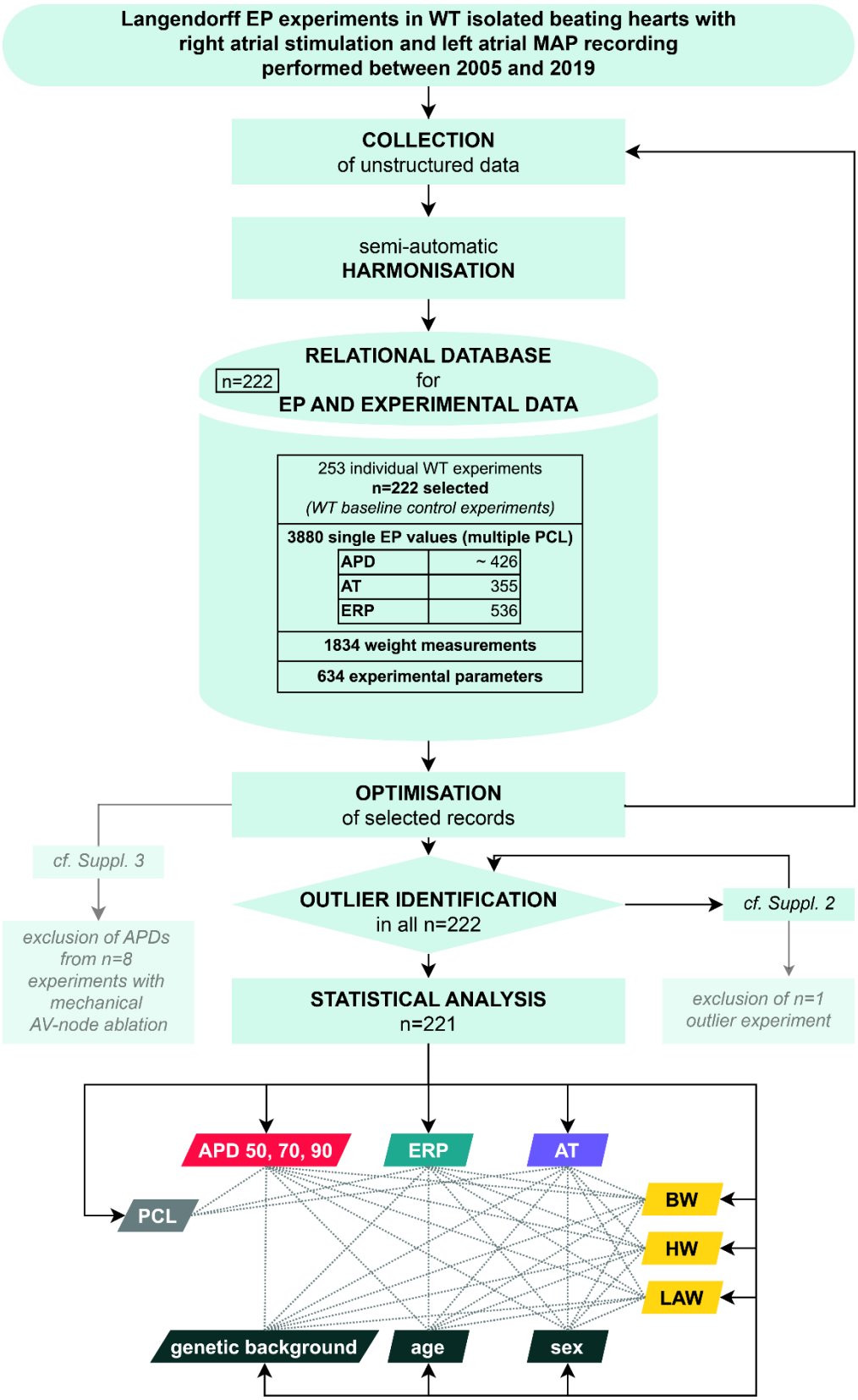


Figure 1: Analysis workflow. Electrophysiological (EP); Wildtype (WT); Monophasic action potential (MAP); Pacing cycle length (PCL); Action potential duration at 50, 70 and 90% repolarisation (APD50, APD70, APD90); Activation time (AT); Body weight (BW); Heart weight (HW); Left atrium weight (LAW).

Descriptive, explorative, and inductive statistical analysis was performed semi-automatically in SPSS 26 (IBM, California) and using common data science packages in Python 3.8 (Pandas, NumPy, SciPy, ResearchPy). Data was visualised using Seaborn in Python 3.8, as well as GraphPad Prism 8 and Adobe Illustrator 24.

Normal distribution was evaluated via Q-Q-plots and Shapiro-Wilk testing. If grouped data were not normally distributed, square root or logarithmic transformation was applied to normalise data. If data were normally distributed or could be normalised, paired t-tests and repeated-measures analysis of variance (ANOVA) were employed to compare experiments in which multiple electrophysiological parameters were obtained at different conditions, e.g. APD at different PCL. Unpaired t-tests and one-way ANOVA were employed when comparing different age groups, sex categories or genetic backgrounds. Bonferroni-correction was used for post-hoc testing after one-way ANOVA. Welch's correction was used if variances were heterogeneous. Kruskal-Wallis tests with Dunn's tests for post-hoc analysis was used if data could not be transformed into Gaussian distributions. In this case, medians and IQR are reported in text and tables. If not stated otherwise, values in graphs, text and tables report means ± standard error of the mean (SEM).

Results

Animals and experimental conditions

This report encompasses intact isolated beating heart "*ex vivo"* atrial electrophysiological studies from 221 WT murine hearts, 114 females and 107 males, from five different genetic backgrounds (C57BL/6J [n=76], FVB/N [n=23], MF1 [n=33], 129/Sv [n=69], Swiss agouti [n=20]) between 2 and 18 months (11 and 76 weeks) of age. Murine age distribution was not different between sex categories. The sex distribution was similar in most genetic backgrounds. **Table 1** summarises the murine characteristics.

		Total		**C57BL/6**		**FVB/N**		**MF1**		**129/Sv**		**Swiss agouti**	
N		221		76		23		33		69		20	
Sex	Female	114	(52%)	32	(42%)	16	(70%)	19	(58%)	40	(58%)	7	(35%)
	Male	107	(48%)	44	(58%)	7	(30%)	14	(42%)	29	(42%)	13	(65%)
Age (weeks)	Total	28.1	± 1.1	25.6	± 1.3	16.9	± 1	24.3	± 4.2	34.4	± 2.1	32.9	± 1.8
	Female	27.9	± 1.5	24.3	± 1.6	17.2	± 1.5	21	± 4.6	37	± 2.7	32.9	± 2.8
	Male	28.3	± 1.5	26.7	± 2.0	16.2	± 0.6	29.7	± 8.2	30.8	± 3.2	32.9	± 2.4
Body weight (g) ***median/IQR**	Total	29.4	± 10.4	29.3	± 11.4	26.9	± 3.0	36.6	± 7.5	27.2	± 7.1	36	± 6.5
	Female	26.5	± 8.1	24.3	± 4.0	26	± 2.7	34.2	± 3.4	24.8	± 4	33.7	± 4.6
	Male	33.2	± 9.6	31.4	± 6.6	30.6	± 2.6	39.6	± 4.6	29.2	± 7.6	39.4	± 5.7
Heart weight (mg)	Total	197.9	± 3.8	184.8	± 6.0	163.4	± 5.9	246.2	± 9.9	192	± 6.4	224.6	± 8.4
	Female	171.4	± 3.8	159.4	± 5.9	155.2	± 6.5	211	± 8.2	161.5	± 4.8	203.5	± 10.4
	Male	221.6	± 5.2	203.8	± 8.1	176.4	± 9.8	281.4	± 9.9	224	± 6.3	235.9	± 10.6
HWBW ratio (mg/g)	Total	6.5	± 0.1	6.3	± 0.2	6.1	± 0.2	6.6	± 0.3	6.9	± 0.1	6.2	± 0.2
	Female	6.3	± 0.1	6.3	± 0.2	6.2	± 0.3	6.1	± 0.5	6.5	± 0.1	5.9	± 0.3
	Male	6.6	± 0.1	6.3	± 0.2	5.9	± 0.4	7.1	± 0.3	7.3	± 0.2	6.3	± 0.2
LA weight (mg) ***median/IQR**	Total	3.7	± 2.4	2.9	± 1.2	4	± 1.3	6	± 2.2	3.5	± 1.4	4.8	± 2.5
	Female	3.2	± 1.8	2.6	± 0.9	3.9	± 1.3	5.4	± 1.7	2.8	± 1.3	4.5	± 2.3
	Male	4.1	± 2.4	3.3	± 1.7	4.1	± 1.8	6.8	± 2.3	3.7	± 1.6	5.1	± 2.3

Table 1: Characteristics of included mice and background distribution. *Stated are means with percentages for sex distributions, means ± SEM for age, heart weight and heart-weight-to-body-weight-ratio (HWBW ratio), and median and interquartile range (IQR) for body weight and LA weight, respectively.*

Due to strict quality standards and variability in protocols, not all measurements (LA-APD, atrial ERP and IA-AT) were consistently available from all experiments. The number of conducted experiments in different genetic backgrounds and sex categories can be retrieved from Table 1. Table 2

summarises all electrophysiological parameters and states numbers of available measurements for each parameter.

Experimental conditions were constant over the timespan of data collection. Mean coronary flow rate was 4.0 ± 0.1 ml/min and temperature was 36.4 ± 0.1 °C without changes over time. Despite the decade long time span for these experiments performed by different staff in two institutions, electrophysiological parameters did not vary over time. Slight variations in preparation time, flow rate or temperature did not significantly affect atrial electrophysiology in this analysis.

PCL-adaption of murine LA-APD and characteristics of atrial ERP and IA-AT

Murine LA-MAPs showed a typical triangular shape with a steep upstroke during depolarization and a fast, early depolarization lacking a plateau (**Figure 2A)** [13]. Mean APD at 70% repolarization in the LA (LA-APD70) was 16 ± 0.4 ms at 80 ms PCL, 18 ± 0.5 ms at 100 ms PCL and 19 ± 0.6 ms at 120 ms PCL (**Table 2)**. APD (LA-APD50, LA-APD70 and LA-APD90) was prolonged at longer PCL (**Figure 2B)**. Atrial APD70 prolonged by 11% ($p<0.0001$) from 80 ms to 100 ms PCL while prolongation from 100 ms to 120 ms PCL was only 5% ($p<0.0001$) suggesting a non-linear PCL-adaption of APD (**Figure 2B, Supplement 2)**.

While LA-APD adapted to longer steady state PCL by LA-APD prolongation, atrial ERP was not PCL-dependent in the range of PCL tested and therefore ERP/APD90-ratio varied between 1.2 ± 0.1 at 80 ms and 1.0 ± 0.05 at 120 ms PCL ($p<0.0001$, **Figure 2B and 2D)**. Mean atrial ERP was 26 ± 1.0 ms at 80 ms PCL, 25 ± 0.9 ms at 100 ms PCL and 26 ± 1.0 ms at 120 PCL.

IA-AT at 80 ms PCL was 17 ± 0.7 ms, 17 ± 0.5 ms at 100 ms PCL and 16 ± 0.5 ms at 120 ms PCL (**Table 2**). IA-AT decreased by 5% from 80 ms to 100 ms PCL and by another 3% to 120 ms PCL, suggesting a linear correlation between PCL and IA-AT. IA-AT total decrease between 80 ms and 120 ms PCL was 7% ($p<0.0001$, **Figure 2C)**. Neither heart weight (HW, 6.5 ± 0.1 mg, **Table 1**) nor LA weight (LAW, 3.7 ± 2.4 mg, **Table 1**) showed significant effects on IA-AT in this study.

		Left Atrial Action Potential Duration (LA-APD) (ms)									Atrial Effective Refractory Period (Atrial ERP) (ms)			Interatrial Activation Time (IA-AT) (ms)		
		APD50			APD70			APD90								
PCL [ms]		**120**	**100**	**80**	**120**	**100**	**80**	**120**	**100**	**80**	**120**	**100**	**80**	**120**	**100**	**80**
Genetic background	**C57BL/6**	13 ± 0.4	12 ± 0.3	11 ± 0.3	19 ± 0.6	18 ± 0.5	16 ± 0.5	29 ± 0.9	29 ± 0.7	25 ± 0.7	26 ± 1	25 ± 0.9	26 ± 1	15 ± 0.4	15 ± 0.5	15 ± 0.6
	n=76															
	FVB/N	12 ± 1.2	11 ± 0.9	10 ± 0.8	22 ± 1.9	20 ± 1.9	16 ± 1.5	33 ± 2.5	29 ± 2.2	29 ± 1.6	36 ± 3.2	36 ± 2.9	36 ± 3.1	16 ± 2.3	17 ± 2	17 ± 2
	n=23															
	MF1	11 ± 0.8	10 ± 0.5	10 ± 0.5	17 ± 1.3	16 ± 0.9	16 ± 0.8	29 ± 2	27 ± 1.5	26 ± 1.3	30 ± 2.2	30 ± 2.3	30 ± 2.6	16 ± 0.8	17 ± 1.3	18 ± 1.3
	n=33															
	129/Sv	17 ± 1.6	16 ± 1.7	13 ± 1.4	23 ± 2.5	22 ± 2.3	19 ± 1.9	36 ± 3.3	36 ± 3.7	28 ± 2.7	27 ± 1.4	26 ± 1.4	26 ± 1.5	23 ± 1.8	24 ± 2.1	28 ± 3.6
	n=69															
	Swiss agouti	9 ± 0.7	10 ± 0.8		14 ± 1.0	14 ± 1.0		24 ± 2.1	25 ± 2.1		19 ± 1.8	20 ± 2.2	17 ± 3.8	15 ± 1.4	16 ± 1.3	14 ± 2.5
	n=20															
Total	**Mean**	**12**	**12**	**11**	**19**	**18**	**16**	**30**	**29**	**26**	**27**	**27**	**27**	**16**	**17**	**17**
	SEM	0.4	0.3	0.3	0.6	0.5	0.4	0.8	0.7	0.6	0.8	0.8	0.9	0.5	0.5	0.7
	SD	4.1	3.6	2.9	6.3	5.7	4.5	8.7	7.7	6.2	10.5	10.6	11.3	5.1	6.1	7.2
	N	122	132	116	124	135	115	119	123	109	166	186	168	110	122	100

Table 2: Reference values for left atrial action potential duration (LA-APD), atrial effective refractory period (ERP) and interatrial activation time (IA-AT) for five different genetic backgrounds. *Mean values ± SEM for LA-APD50, LA-APD70 and LA-APD90, as well as atrial ERP and IA-AT are displayed in milliseconds for pacing cycle lengths (PCL) 80 ms, 100 ms and 120 ms and five different genetic backgrounds and in summary, respectively.*

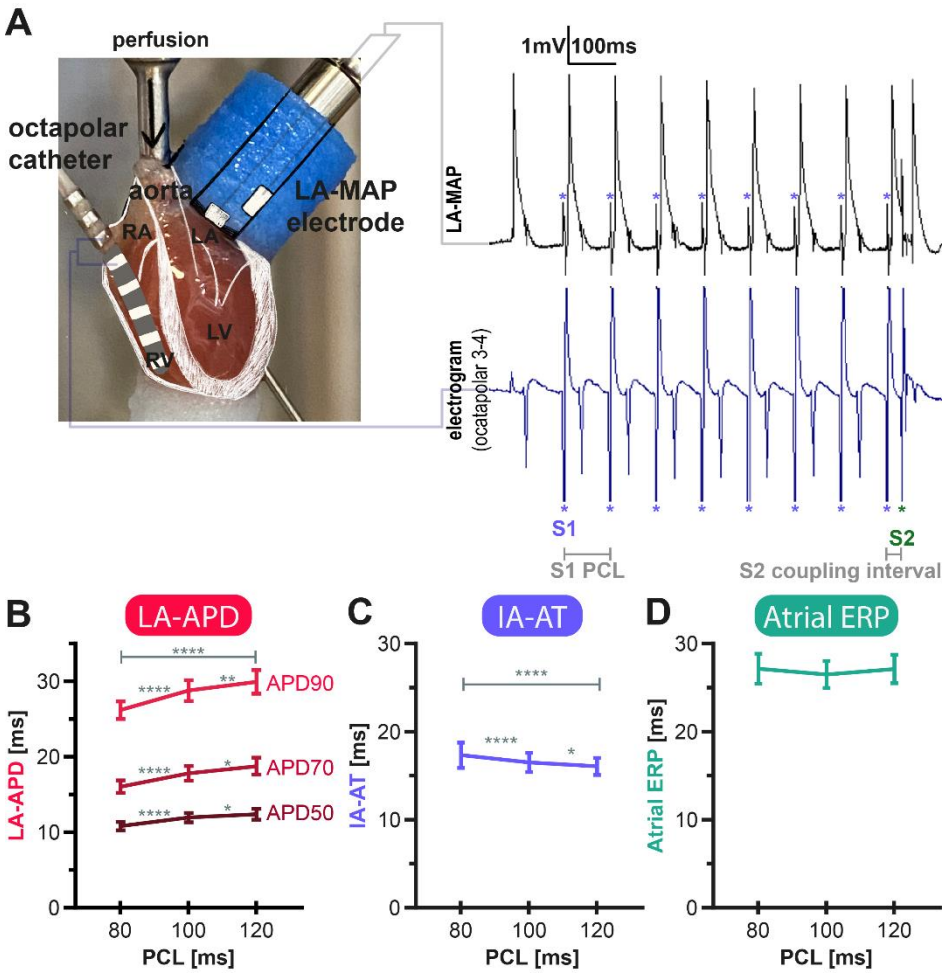


Figure 2: Isolated Langendorff murine heart electrophysiological study and left atrial monophasic action potential cycle-length dependency. A: *Setup of the Langendorff experiment and original murine left atral monophasic action potentials at a train-of-eight S1-paced beats (purple asterix) with an S1 pacing cycle length (PCL) of 100 ms and one coupled extra stimulus (S2; green asterix) with a coupling interval of 35 ms. Below the MAP signals, the bipolar trace between atrial and ventricular electrodes of the octapolar EP catheter are shown. Astertix indicate stimulation artefacts examplarily (*).* ***B:*** *Left-atrial action potential duration (LA-APD) at 50, 70 and 90% repolarization plotted over steady state PCL. LA-APD at all stages of repolarization is PCL-dependent leading to longer APDs at longer PCLs.* ***C:*** *PCL-function of atrial effective refractory period (Atrial ERP). Atrial ERP did not adapt to S1-PCL within the investigated range.* ***D:*** *Interatrial activation time (IA-AT) was steady state PCL-dependent and decreased with higher PCL. Data derived from the pooled cohort of all genetic backgrounds, sexes and ages from experiments in which data points at each PCL were available. Plotted are means with 95% confidence intervals of the mean. * p<0.05, ** p<0.01, **** p<0.001.*

Murine genetic background affects atrial electrophysiology

Genetic background influenced atrial APD70 ($p<0.01$). In Swiss agouti, atrial APD70 at 100 ms PCL was between 11% (vs. MF1, ns) and 36% (vs. 129/Sv, $p<0.05$) shorter compared to other genetic backgrounds (20% shorter vs. C57BL/6, ns, 27% shorter vs. FVB/N, ns, **Figure 3A)**. Atrial ERP at 100

ms PCL was significantly different between genetic backgrounds (p<0.0001) and shorter in Swiss agouti compared to FVB/N (-44%, p<0.0001) and MF1 (-33%, p<0.05). Atrial ERP was 37% longer in FVB/N compared to 129/Sv (p<0.01) and 42% longer compared to C57BL/6 mice (p<0.05, **Figure 3B)**. IA-AT was longer in 129/Sv compared to other genetic backgrounds, +60% vs. C57BL/6 (p<0.001), +53% vs. Swiss agouti (p<0.01) and +41% vs. MF1 (p<0.05, **Figure 3C**).

Genetic background also influenced BW, HW and LAW (all p<0.0001, **Table 1**): MF1 and Swiss agouti mice were between 17% and 51% heavier than C57BL/6, FVB/N and 129/Sv mice and hearts, respectively (**Figure 3D**). LAW was higher in MF1 mice compared to C57BL/6 (107%, p<0.0001), FVB/N (52%, p<0.01), 129/Sv (71%, p<0.0001) and higher in Swiss agouti compared to C57BL/6 (66%, p<0.01). In contrast, heart weight/body weight (HWBW) ratios were much more stable between different genetic backgrounds: only 129/Sv mice had slightly higher HWBW ratios compared to C57BL/6 (+9%, p<0.05), FVB/N (+14%, p<0.05) and Swiss agouti (+12%, p<0.01) genetic backgrounds (**Figure 3E**).

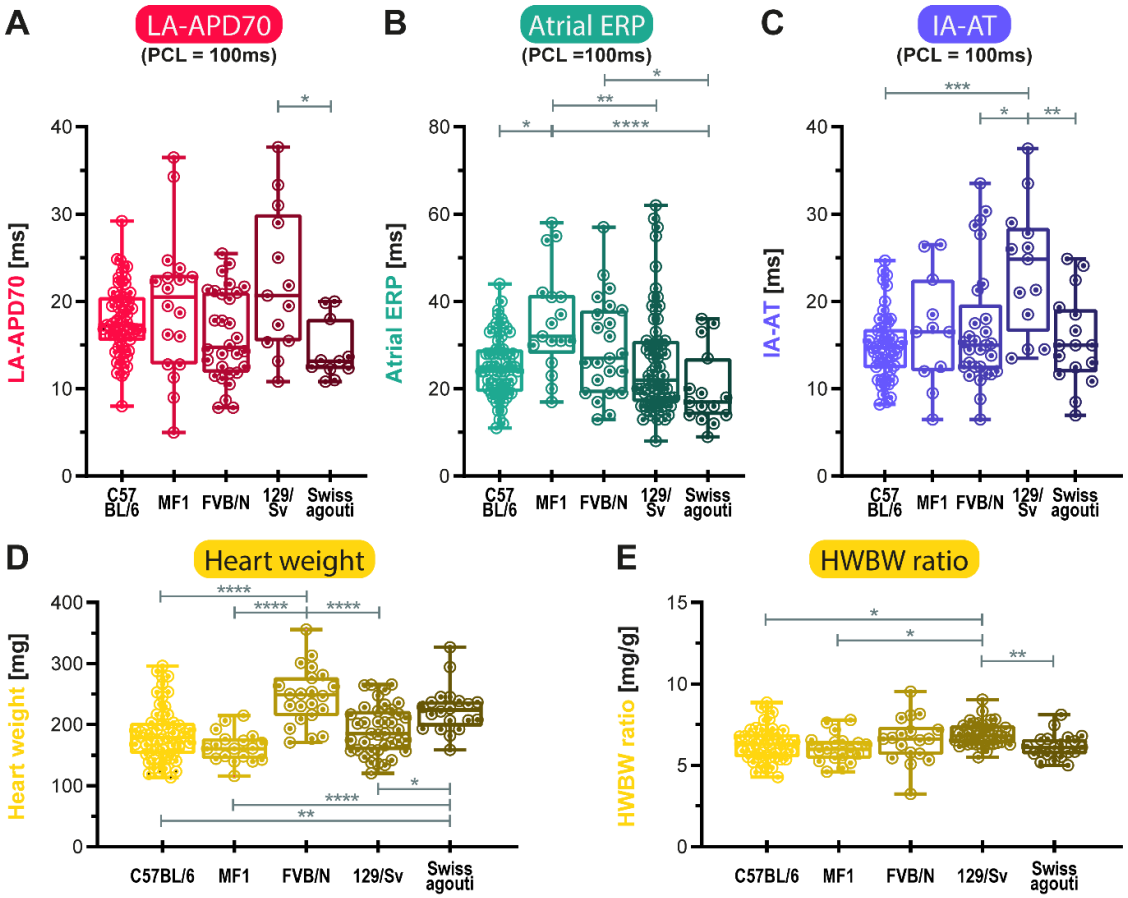


Figure 3: Effects of genetic background on electrophysiological parameters and weights. *Left atrial action potential duration at 70% repolarization (LA-APD70), (**A**), atrial effective refractory period (ERP), (**B**), interatrial activation time (IA-AT), (**C**), each at 100 ms pacing cycle length (PCL), as well as heart weight (**D**) and heart-weight-to-body-weight-ratio (HWBW ratio), (**E**), are shown for each background and statistically tested dependent whether they were in or could be transformed to Gaussian distribution by one-way ANOVA or alternatively Kruskal-Wallis-test. All tested electrophysiological parameters, as well as mouse and heart weights were background dependent. * p<0.05, ** p<0.01, *** p<0.001, **** p<0.0001.*

Sex affects atrial ERP

Considering the whole dataset using a univariate approach, mean atrial ERP at 100 ms PCL was 25 ± 1 ms in male mice compared to 28 ± 1 ms in females, and therefore 14% longer in females ($p<0.05$, **Figure 4A)**. This effect was tested independent of genetic background and age. LA-APD and IA-AT were not affected by sex in the range of PCL tested in this study (**Figure 4B and 4C**).

Male HW and LAW was 29% and 28% ($p<0.0001$ and $p<0.05$) heavier than in females respectively, whilst BW of males was 25% larger ($p<0.0001$, **Figure 4D**). Sex differences in HW were most pronounced in the 129/Sv background (39% higher in males) whilst HW differences were small in FVB/N mice (14% higher). HWBW ratio was different between male and female mice (5%, $p<0.05$, **Figure 4E**), while LAW/BW ratio was not.

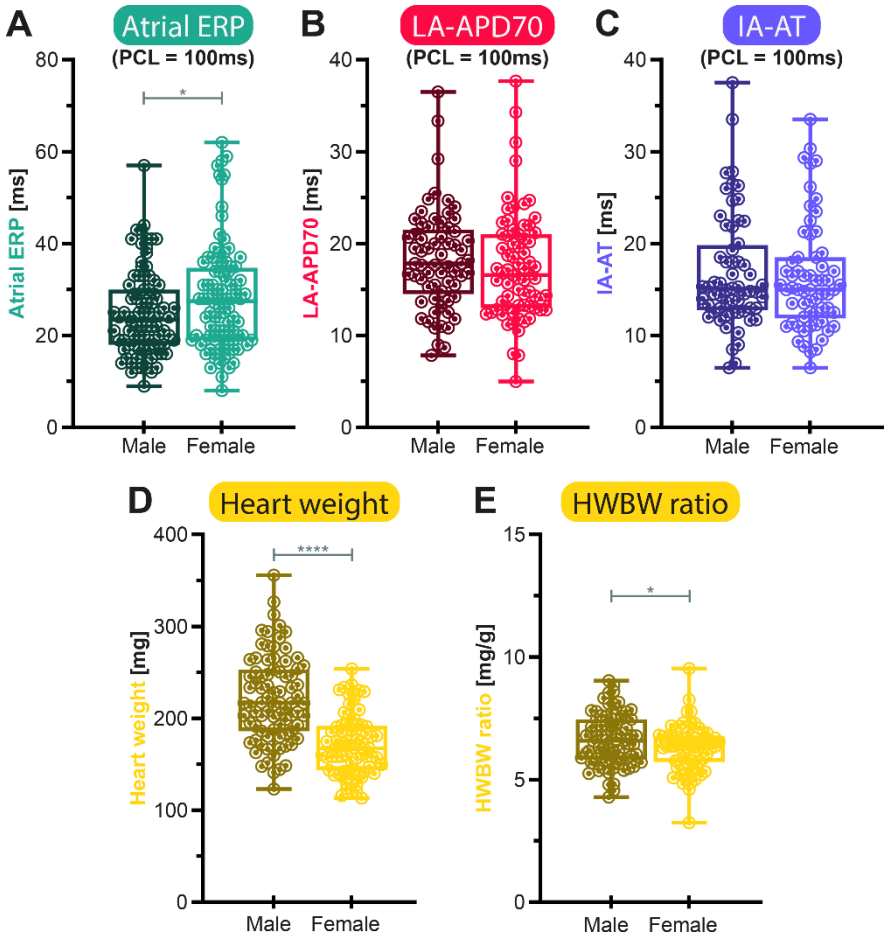


Figure 4: Sex-specific differences in left atrial electrophysiology, heart weight and heart-weight-to-body-weight-ratio (HWBW ratio). *Left atrial action potential duration (LA-APD70), (A), atrial effective refractory period (ERP), (B) and interatrial activation time (IA-AT), (C) as electrophysiological parameters, as well as heart weight (HW), (D) and HWBW ratio (E) were compared between both sex-categories by unpaired Student's t-test. Atrial ERP varied between female and male animals with a 14.5% prolongation in females. The other tested electrophysiological values did not vary significantly between sex categories in this study. HW was higher in males. * p<0.05, **** p<0.0001.*

Age affects atrial ERP

With age as a continuous variable, neither IA-AT, LA-APD, nor atrial ERP showed a clear linear correlation in this cohort. However, there was a trend towards shorter atrial ERP in older mice (**Figure 5A1)**. For further analysis, experiments were clustered in four age groups: hearts from young adult (2-3 months), mature adult (3-6 months), middle-aged (6-12 months) and old mice (12-24 months). Stratified, the dataset revealed age-dependent shortening of atrial ERP at 100 ms PCL comparing young mice between 2 and 3 months of age to older groups ($p<0.0001$ vs. 6-12 months and $p<0.05$ vs. 12-24 months, **Figure 5A2**). Also, mature adults had higher atrial ERPs compared to middle-aged mice ($p<0.001$, **Figure 5A2**). LA-APD and IA-AT were neither affected by age in a linear correlation nor categorical age groups in this study (ANOVA $p>0.05$, **Figure 5B and 5C**).

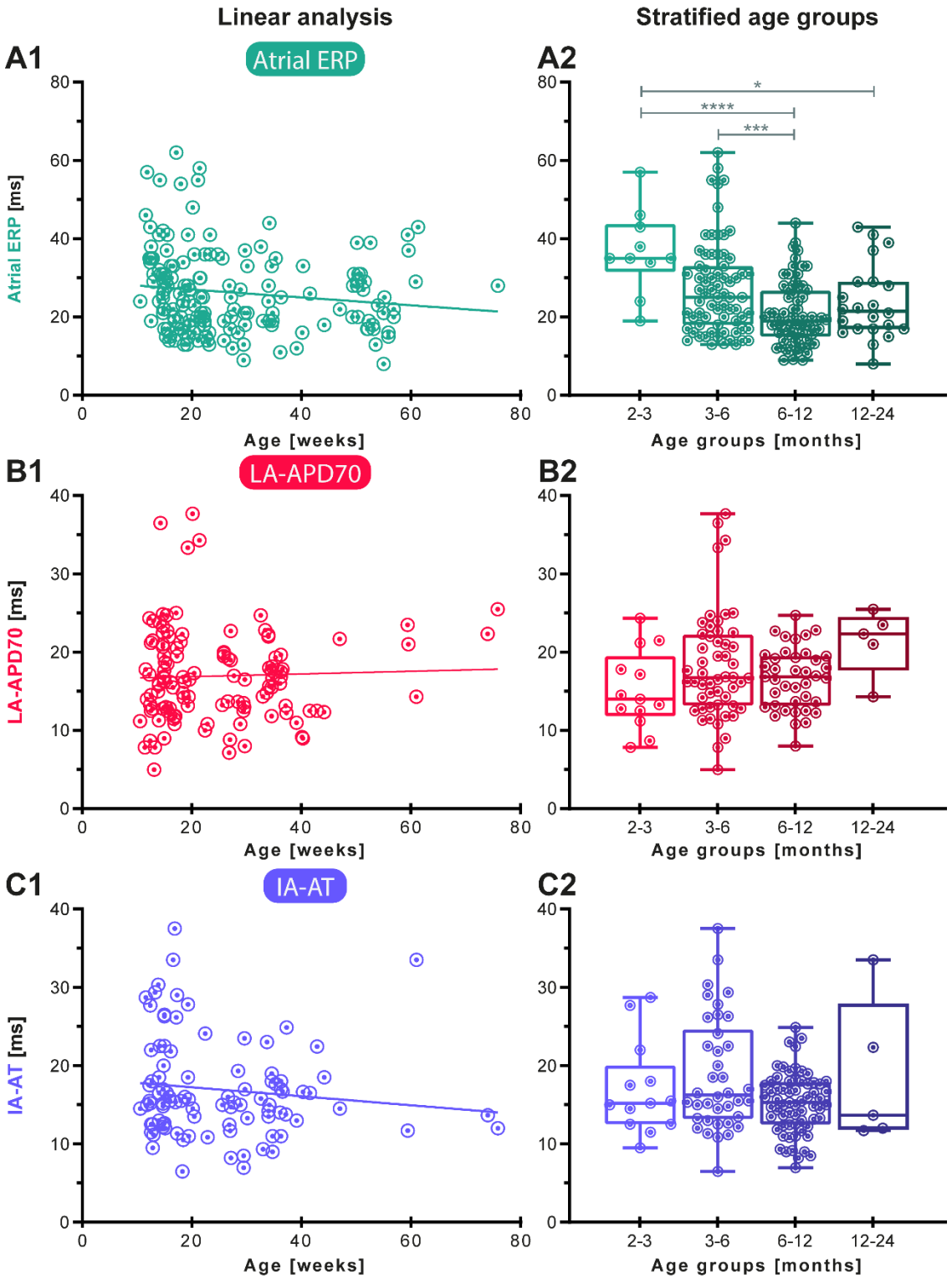


Figure 5: Continuous and stratified effects of age on left atrial action potential duration (LA-APD), atrial effective refractory period (ERP) and interatrial activation time (IA-AT). *Graphs in the left column show atrial ERP (**A1**), LA-APD70 (**B1**) and IA-AT (**C1**), each at 100 ms pacing cycle length (PCL), plotted over mouse age in weeks at the time of experiment and results of linear regression. Linear regression was not statistically significant for all three parameters. Mice were then stratified in age groups (**A2, B2, C2**) and atrial ERP was found to be affected by age (A2; ANOVA p<0.0001). In Bonferroni-corrected post-hoc testing, atrial ERP at 100 ms PCL was increased in younger groups (<3 months and 3-6 months) compared to older groups (6-12 and 12-24 months). * p<0.05, *** p<0.001, **** p<0.0001.*

Discussion

The analysis provides a robust reference for normal murine atrial electrophysiological parameters based on a dataset of over 200 isolated *ex vivo* Langendorff-perfused beating WT hearts from five different genetic strains (**Table 2**). Experiments were performed over a decade without systematic changes in parameters, confirming the robustness of the experimental setup. Detailed interrogation of the dataset identified the following findings:

- Different genetic backgrounds have a distinct electrophysiological footprint: C57BL/6 and Swiss agouti show a smaller APD/ERP ratio. 129/Sv show markedly longer IA-AT and longer LA-APDs.
- Pacing at shorter PCL shortened LA-APD.
- IA-AT increases with shorter atrial PCL, suggesting reduced conduction velocity at shorter PCL.
- Female hearts show longer atrial ERPs than male hearts.
- Atrial ERP is shorter in old hearts.
- Body weight, heart weight, or left atrial weight do not affect atrial electrophysiological parameters in WT murine hearts when mice were kept on normal chow diet.

Genetic background strain modifies murine LA-APD, atrial ERP and IA-AT

We observed a distinct atrial electrophysiological profile for each different murine genetic background concordant to findings in ventricular myocardium. Similar to our report of left atrial parameters, *ventricular* APD was longer in FVB/N mice compared to C57BL/6 in an earlier study [6]. Comparisons of cardiac electrophysiology between different genetic backgrounds are still limited. However, several studies found inter-strain differences in cardiac electrophysiology [6, 14, 15].

Expression differences in ultra-rapid delayed rectifier K^+ currents between male CD-1 and male C57BL/6 mice were suggested to cause differences in repolarisation between these two strains and are thought to be caused by different testosterone levels [16]. The occurrence of ventricular arrhythmias varied in a comparison between four inbred strains and were postulated to be caused by different beta-adrenergic responses as observed by others [17], intracellular calcium handling, ion channel expression and phosphorylation [14]. Of note, our study was conducted in isolated beating hearts *ex vivo*. Therefore, differences in tone of the autonomic nervous system are unlikely to account for genetic background related differences.

In a study comparing strain-specific differences in sodium currents in cardiomyocytes, sodium currents in neonatal cardiomyocytes varied between C57BL/6, FVB/N and 129/Sv genetic background [18]. Remme et al. found an mRNA and protein reduction of the cardiac sodium channel beta subunit in ventricles from the 129 genetic background compared to FVB/N associated with changes in

activation kinetics [19]. A trend to differential atrial expression of *Kcnc4* between MF1, Swiss agouti and CD-1 strains was observed [20].

Our study provides systematic data on genetic background-dependent differences in *atrial* electrophysiological parameters measured is isolated hearts *ex vivo*, providing a reference for their interpretation and highlighting the importance of genetic background for the design and interpretation of research in murine models. Further research into the molecular mechanisms is warranted.

Age- and sex-dependency of atrial murine electrophysiological parameters

This study found shorter atrial ERP at older age (**Figure 5**). While the distribution of sex categories was balanced within each age group, the different genetic backgrounds were not. As genetic background also influenced atrial ERP in isolated testing (**Figure 3B**), it cannot be excluded as a confounder of the observed effect. Multifactorial testing was not possible due to the limited number of experiments available. It was recently postulated that atrial APs would be prolonged by age based on differences in ion channel expression in human atrial tissue [21]. Our study did not find relevant age-dependent changes in LA-APD in the range of PCLs studied. Longer *ventricular* APDs and ERPs in female mice [6] have been attributed to different concentrations of repolarising ion channels related to sex hormone concentrations [16]. In line with this, progesterone was shown to elicit an AP-prolonging effect on hearts of ovariectomised mice [22]. In our study, female mice had a longer atrial ERP. It is not unlikely that a small effect of sex on LA-APD was masked by the greater variability of LA-APD compared to atrial ERP (**Figure 4**).

We analysed combined effects of genetic background and sex on LA-APD70, atrial ERP and IA-AT at 100 ms PCL in a two-way ANOVA with the knowledge that subgroups within this large dataset are still limited in size to perform robust multifactorial analysis. Two-way ANOVA was significant for all variables when combining genetic background and sex within the model as described in detail in Supplement 3. It is likely that combinations of the factors genetic background, sex and age have effects beyond those found in univariate analysis. Proof of this hypothesis would require verification in an even larger dataset.

Cycle-length-dependency of murine LA-APD and IA-AT

Murine left atrial APs have not been characterized in a dataset as large as this before. However, different sites of the heart, even within the same chamber, have distinct electrophysiological profiles and functions and therefore require separate characterization in health and disease [5, 11]. The durations seen in this analysis (e. g. LA-APD50 (12 ± 0.4 ms), LA-APD70 (18 ± 0.6 ms) and LA-APD90

(29 ± 0.8 ms) at 120 ms PCL) are in the same range as found in a previous study on 21 isolated, murine Langendorff-perfused hearts of unknown genetic background in a perpendicular setup using miniature contact MAP electrodes at a PCL of 130ms [13] and are comparable to APDs recorded using optical mapping [10-12]. The mean values for IA-AT and atrial ERP presented here are also comparable to those reported from *in vivo* transvenous stimulation recordings [23].

BW, HW and LAW, or weight ratios, did not affect atrial electrophysiological parameters in this WT cohort with only minor variations in normal weight on a standard chow diet. Thus, normal ranges of HW and BW do not induce electrical signs of atrial AP-prolonging effects of hypertrophy [6]. In contrast, obesity has been associated with changes in atrial electrophysiology and found to cause atrial remodelling [24].

Rate-dependent shortening of APD and slowing of conduction velocity is a well-known feature of the myocardium and is vital to retain a sufficient diastole at faster heart rates. However, alterations in rate adaption are hypothesised to be implicated in genesis of cardiac arrhythmias [25]. Shortening of APDs at shorter PCL as observed in this study in the murine LA was also seen in other studies [11, 12]. A constant atrial ERP/APD ratio over a range from 300 ms to 700 ms PCL was reported in human RA [26], while this study observed adaptation of LA-APD, but not atrial ERP, to PCL in the range of PCL tested, leading to slight variation in ERP/APD-ratios. The lack of murine left atrial ERP shortening with shorter PCL in this study may be caused by the observed increase in IA-AT from RA pacing site to LA MAP recording site with shorter PCL or by the short range of tested PCLs in the current atrial experimental setting. Of note, a similar flat PCL-ERP relationship was observed in murine ventricles over a range of PCLs from 100 to 300 ms [6].

Limitations

This study reports a resource for murine left atrial electrophysiological parameters based on a large dataset and is therefore relatively robust. Influences of age, sex and genetic background on electrophysiological parameters were found in univariate analysis and influences of animal weights were reported earlier [6]. Although containing over 200 experiments, the dataset was too small to detect minute differences and to perform a robust multifactorial multivariate analysis and regression models.

Effects of BW and HW on *atrial* electrophysiology were smaller than those found on *ventricular* electrophysiology using a similar approach [6]. Although this dataset is limited by only few animals being studied after senescence, shortening effects of age on atrial ERP were observed. To make robust statements of influences of aging on left atrial electrophysiology, a study including animals from a large and continuous age range would be ideal.

While the electrophysiological isolated heart investigation offers a wide range of opportunities partially described in this paper and has been lauded for animal welfare aspects, the electrophysiological study can also be performed *in vivo* [27] and it may be particularly intriguing to perform an EP study *in vivo* and subsequently in the isolated heart.

This study did not require further sacrifice of animals, as the dataset is based on our group's previously collected data comparing effects of disease modelling genetic mutations to WT littermate controls.

Conclusion

This study provides unparalleled, robust reference values for murine LA-APD, atrial ERP and IA-AT based on 221 WT Langendorff-perfused murine hearts. The dataset identifies effects of genetic background, sex and age on atrial electrophysiological parameters. The effects of genetic background are at least of the magnitude as those of age and in this model, illustrating the impact of genetic background on atrial electrophysiology. Reported findings can guide the planning of experimental design and interpretation of murine electrophysiological research.

Funding

This work was partially supported by the European Commission [grant number 633196 "CATCH ME"] to L.F. and P.K., Deutsche Forschungsgemeinschaft (DFG) [grant number FA413] to L.F., British Heart Foundation (BHF) [grant numbers FS/13/43/30324, AA/18/2/34218] to L.F. and P.K. and Leducq Foundation to PK. J.O. has received financial support for abroad studies within his scholarship of the Studienstiftung des deutschen Volkes (German Academic Scholarship Foundation).

Acknowledgements

The authors would like to thank Lisa Fortmüller, Nina Kreienkamp and Daniela Volkery for expert help. The authors also thank Winnie Chua for statistical discussion of data.

Conflicts of interest

L.F. has received institutional research grants from governmental and charity funding agencies (EU, DFG, MRC, and BHF). L.F. has received institutional research grants from industry in the past (Gilead). P.K. and L.E. have received research support from several drug and device companies active in atrial fibrillation and have received honoraria from several such companies in the past. L.F. and P.K. are listed as inventors on two patents held by University of Birmingham (Atrial Fibrillation Therapy WO 015140571, Markers for Atrial Fibrillation WO 2016012783).

Ethics approval

All experiments in Birmingham were conducted according to the Animals (Scientific Procedures) Act 1986 and approved by the home office (Home Office References 30/2967 and PFDAAF77F) and the institutional review board at the University of Birmingham. All experiments in Münster were approved by the regional authority (Licence numbers G61/99, G83/2004). All experimental protocols conform with the Guide for the Care and Use of Laboratory Animals published by the US National Institutes of Health (NIH Publication No. 85-23, revised 1996). The manuscript does not contain clinical studies or patient data.

Data Availability Statement

The data underlying this article will be shared on reasonable request to the corresponding author.

References

[1] Kotecha D, Breithardt G, Camm AJ, Lip GYH, Schotten U, Ahlsson A, et al. Integrating new approaches to atrial fibrillation management: the 6th AFNET/EHRA Consensus Conference. *Europace* 2018; **20**: 395-407.

[2] Yarnoz MJ, Curtis AB. More reasons why men and women are not the same (gender differences in electrophysiology and arrhythmias). *Am J Cardiol* 2008; **101**: 1291-1296.

[3] Kloosterman M, Chua W, Fabritz L, Al-Khalidi HR, Schotten U, Nielsen JC, et al. Sex differences in catheter ablation of atrial fibrillation: results from AXAFA-AFNET 5. *Europace* 2020.

[4] Fabritz L, Crijns H, Guasch E, Goette A, Haeusler KG, Kotecha D, et al. Dynamic risk assessment to improve quality of care in patients with atrial fibrillation: The 7th AFNET/EHRA Consensus Conference. *Europace* 2020; **in press**.

[5] Riley G, Syeda F, Kirchhof P, Fabritz L. An introduction to murine models of atrial fibrillation. *Front Physiol* 2012; **3**: 296.

[6] Waldeyer C, Fabritz L, Fortmueller L, Gerss J, Damke D, Blana A, et al. Regional, age-dependent, and genotype-dependent differences in ventricular action potential duration and activation time in 410 Langendorff-perfused mouse hearts. *Basic Res Cardiol* 2009; **104**: 523-533.

[7] Kirchhof P, Kahr PC, Kaese S, Piccini I, Vokshi I, Scheld HH, et al. PITX2c is expressed in the adult left atrium, and reducing Pitx2c expression promotes atrial fibrillation inducibility and complex changes in gene expression. *Circ Cardiovasc Genet* 2011; **4**: 123-133.

[8] Blana A, Kaese S, Fortmuller L, Laakmann S, Damke D, van Bragt K, et al. Knock-in gain-of-function sodium channel mutation prolongs atrial action potentials and alters atrial vulnerability. *Heart Rhythm* 2010; **7**: 1862-1869.

[9] Kirchhof P, Fabritz L, Fortmuller L, Matherne GP, Lankford A, Baba HA, et al. Altered sinus nodal and atrioventricular nodal function in freely moving mice overexpressing the A1 adenosine receptor. *Am J Physiol Heart Circ Physiol* 2003; **285**: H145-153.

[10] Yu TY, Syeda F, Holmes AP, Osborne B, Dehghani H, Brain KL, et al. An automated system using spatial oversampling for optical mapping in murine atria. Development and validation with monophasic and transmembrane action potentials. *Prog Biophys Mol Biol* 2014; **115**: 340-348.

[11] Holmes AP, Yu TY, Tull S, Syeda F, Kuhlmann SM, O'Brien SM, et al. A Regional Reduction in Ito and IKACh in the Murine Posterior Left Atrial Myocardium Is Associated with Action Potential Prolongation and Increased Ectopic Activity. *PLoS One* 2016; **11**: e0154077.

[12] Syeda F, Holmes AP, Yu TY, Tull S, Kuhlmann SM, Pavlovic D, et al. PITX2 Modulates Atrial Membrane Potential and the Antiarrhythmic Effects of Sodium-Channel Blockers. *J Am Coll Cardiol* 2016; **68**: 1881-1894.

[13] Knollmann BC, Schober T, Petersen AO, Sirenko SG, Franz MR. Action potential characterization in intact mouse heart: steady-state cycle length dependence and electrical restitution. *Am J Physiol Heart Circ Physiol* 2007; **292**: H614-621.

[14] Jelinek M, Wallach C, Ehmke H, Schwoerer AP. Genetic background dominates the susceptibility to ventricular arrhythmias in a murine model of beta-adrenergic stimulation. *Sci Rep* 2018; **8**: 2312.

[15] Maguire CT, Wakimoto H, Patel VV, Hammer PE, Gauvreau K, Berul CI. Implications of ventricular arrhythmia vulnerability during murine electrophysiology studies. *Physiol Genomics* 2003; **15**: 84-91.

[16] Brouillette J, Rivard K, Lizotte E, Fiset C. Sex and strain differences in adult mouse cardiac repolarization: importance of androgens. *Cardiovasc Res* 2005; **65**: 148-157.

[17] Berthonneche C, Peter B, Schupfer F, Hayoz P, Kutalik Z, Abriel H, et al. Cardiovascular response to beta-adrenergic blockade or activation in 23 inbred mouse strains. *PLoS One* 2009; **4**: e6610.

[18] Mille M, Koenig X, Zebedin E, Uhrin P, Cervenka R, Todt H, et al. Sodium current properties of primary skeletal myocytes and cardiomyocytes derived from different mouse strains. *Pflugers Arch* 2009; **457**: 1023-1033.

[19] Remme CA, Scicluna BP, Verkerk AO, Amin AS, van Brunschot S, Beekman L, et al. Genetically determined differences in sodium current characteristics modulate conduction disease severity in mice with cardiac sodium channelopathy. *Circ Res* 2009; **104**: 1283-1292.

[20] Kahr PC, Piccini I, Fabritz L, Greber B, Scholer H, Scheld HH, et al. Systematic analysis of gene expression differences between left and right atria in different mouse strains and in human atrial tissue. *PLoS One* 2011; **6**: e26389.

[21] Biliczki P, Boon RA, Girmatsion Z, Bukowska A, Ordog B, Kaess BM, et al. Age-related regulation and region-specific distribution of ion channel subunits promoting atrial fibrillation in human left and right atria. *Europace* 2019; **21**: 1261-1269.

[22] Saba S, Zhu W, Aronovitz MJ, Estes NA, 3rd, Wang PJ, Mendelsohn ME, et al. Effects of estrogen on cardiac electrophysiology in female mice. *J Cardiovasc Electrophysiol* 2002; **13**: 276-280.

[23] Kaese S, Verheule S. Cardiac electrophysiology in mice: a matter of size. *Frontiers in Physiology* 2012; **3**.

[24] Mahajan R, Lau DH, Brooks AG, Shipp NJ, Manavis J, Wood JP, et al. Electrophysiological, Electroanatomical, and Structural Remodeling of the Atria as Consequences of Sustained Obesity. *J Am Coll Cardiol* 2015; **66**: 1-11.

[25] Garfinkel A, Kim YH, Voroshilovsky O, Qu Z, Kil JR, Lee MH, et al. Preventing ventricular fibrillation by flattening cardiac restitution. *Proc Natl Acad Sci U S A* 2000; **97**: 6061-6066.

[26] Bode F, Kilborn M, Karasik P, Franz MR. The repolarization-excitability relationship in the human right atrium is unaffected by cycle length, recording site and prior arrhythmias. *Journal of the American College of Cardiology* 2001; **37**: 920-925.

[27] Gehrmann J, Berul CI. Cardiac electrophysiology in genetically engineered mice. *J Cardiovasc Electrophysiol* 2000; **11**: 354-368.

Supplementary Materials of

Effects of genetic background, sex and age on murine atrial electrophysiology

Julius Obergassel[1,2], Molly O'Reilly[1], Laura C. Sommerfeld[1], S Nashitha Kabir[1], Christopher O'Shea[1], Fahima Syeda[1], Lars Eckardt[3], Paulus Kirchhof[1,2,4,5,6], Larissa Fabritz[1,4]

[7] Institute of Cardiovascular Sciences, University of Birmingham, Birmingham, UK

[8] University Heart and Vascular Center, University Hospital Hamburg-Eppendorf, Hamburg, Germany

[9] Department of Cardiology II - Electrophysiology, University Hospital Münster, Münster, Germany

[10] Department of Cardiology UHB NHS Trust, Birmingham, UK

[11] Department of Cardiology, SWBH NHS Trust, Birmingham City Hospital, Birmingham, UK

[12] German Center for Cardiovascular Research, partner site Hamburg/Kiel/Lübeck, Germany

Corresponding author:

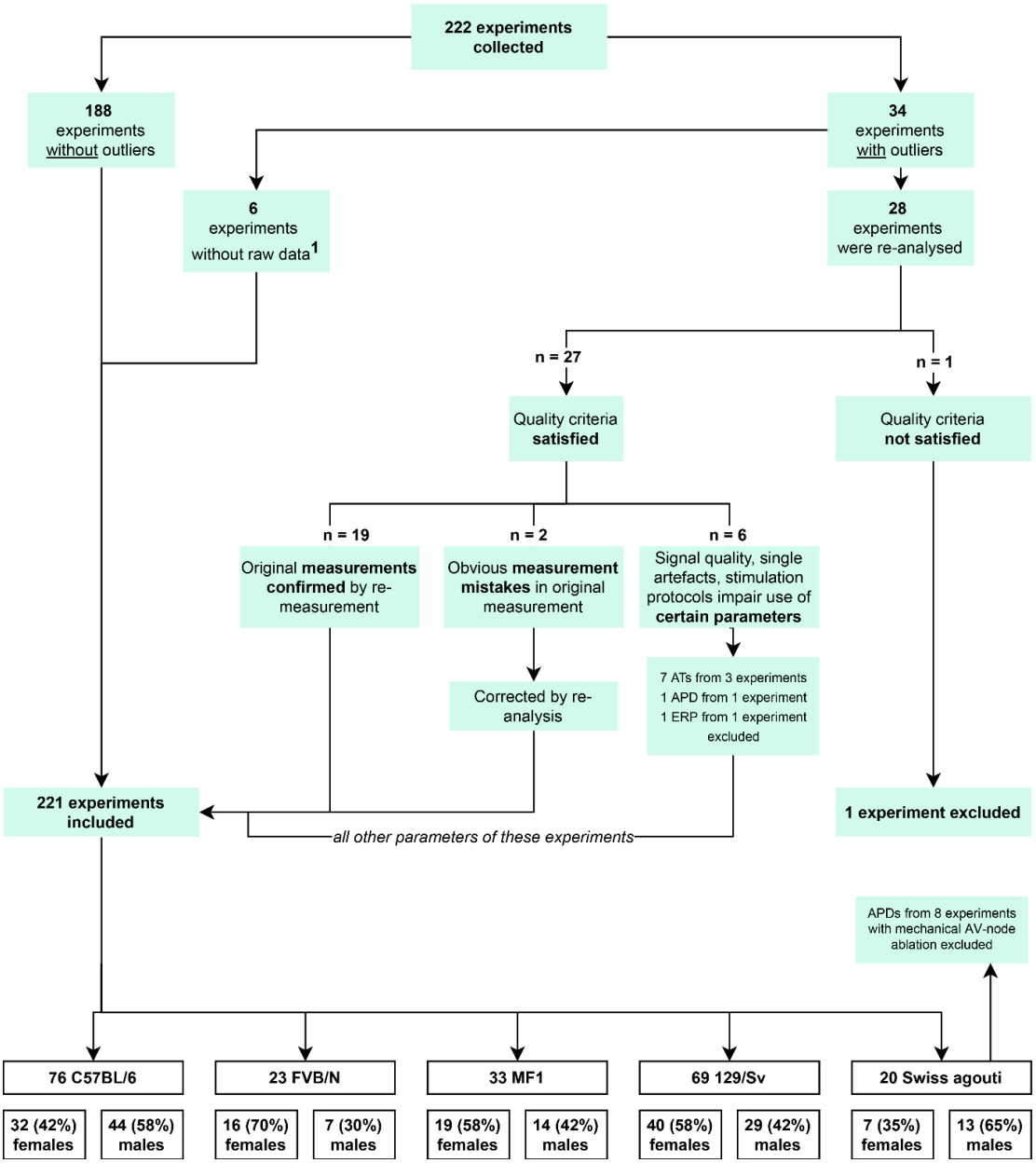
Professor Dr Larissa Fabritz
Institute of Cardiovascular Sciences
University of Birmingham
Edgbaston Birmingham
B15 2TT, UK
United Kingdom
Tel:
E-Mail:

Supplement 1: Supplementary Methods and Results: Outlier handling

The dataset was clustered by genetic background and sex before being screened for moderate and extreme outliers within each group. Moderate outliers were defined as falling above the third quartile (Q3) plus 1.5-fold interquartile range (IQR) [$> \ Q3 \ + \ 1.5 \ x \ IQR$] or below the first quartile (Q1) minus 1.5-fold IQR [$< \ Q1 \ - \ 1.5 \ x \ IQR$]. Extreme outliers fell above $Q3 \ + \ 3 \ x \ IQR$ or below $Q1 - \ 3 \ x \ IQR$. Identified moderate and extreme outliers were inspected and re-analysed by a second observer. Outliers in weight variables were compared to original lab log recordings. Electrophysiological outliers were re-analysed if original data recordings were accessible. Raw data of 6 experiments from 2005 which are already published after quality control could not be accessed due to software incompatibility. All other experiments were re-analysed: 27 experiments met the previously described quality criteria while one experiment was excluded. During re-analysis, 19 measurements were confirmed, 2 measurements were corrected, and 6 measurements were excluded for the following reasons: artefacts in MAPs affected accurate measurements (exclusion of n=1 LA-APD), stimulation artefacts could not clearly be identified (exclusion of n=7 IA-AT at different PCLs from 3 experiments) or stimulation protocol was not correctly followed (exclusion of n=1 atrial ERP).

In a subset of 8 hearts with a Swiss agouti background, the atrioventricular node (AV-node) was ablated mechanically by applying gentle pressure against the septal part of the anulus fibrosus just proximal to the His-bundle to slow ventricular rate and thereby slowing ventricular rate and disconnecting the farfield ventricular signal from the late atrial repolarisation phase, resulting in permanent AV block as published earlier [1–4].

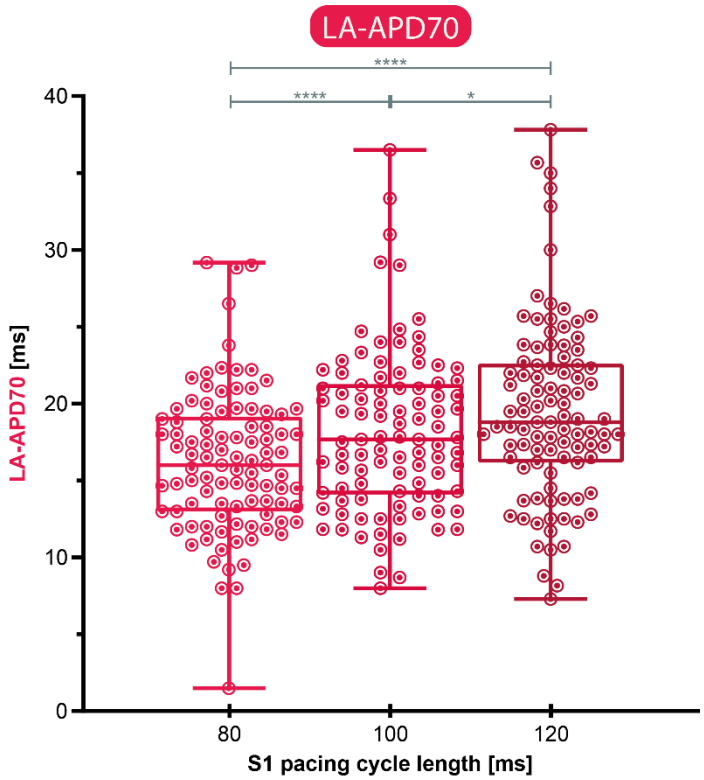
To examine potential effects of mechanical AV-node ablation on the measured data, a subcohort of 20 similar experiments, sharing the same genetic background (Swiss agouti), conducted during similar conditions was selected. This cohort contains all 8 mechanical AV node ablation experiments and 12 controls. Effects of mechanical AV node ablation were assessed by unpaired Student's t-test or Mann-Whitney-U-test depending on whether data was or could be transformed into a Gaussian distribution. LA-APD at 70% and 90% repolarisation varied significantly between both groups. Sex could not be perfectly balanced in this sub-analysis. Because it cannot be excluded that mechanical AV-node ablation affected LA-APD, APD measurements from experiments with mechanical AV-node ablation were excluded from the total dataset.



Supplementary Figure 1: Included experiments and outlier handling. *From 222 initially collected experiments, 221 experiments could be included in final analysis while one experiment was excluded due to unmet quality criteria. In total, 7 single activation times from 3 experiments, 1 action potential duration (APD) and 1 effective refractory period (ERP) were excluded due to unmet stimulation protocols or signal artefacts which affected accurate measurements. Two experiments were corrected, and 19 experiments were confirmed by re-analysis. APDs from 8 experiments with mechanical AV-node ablation were excluded during revision.*

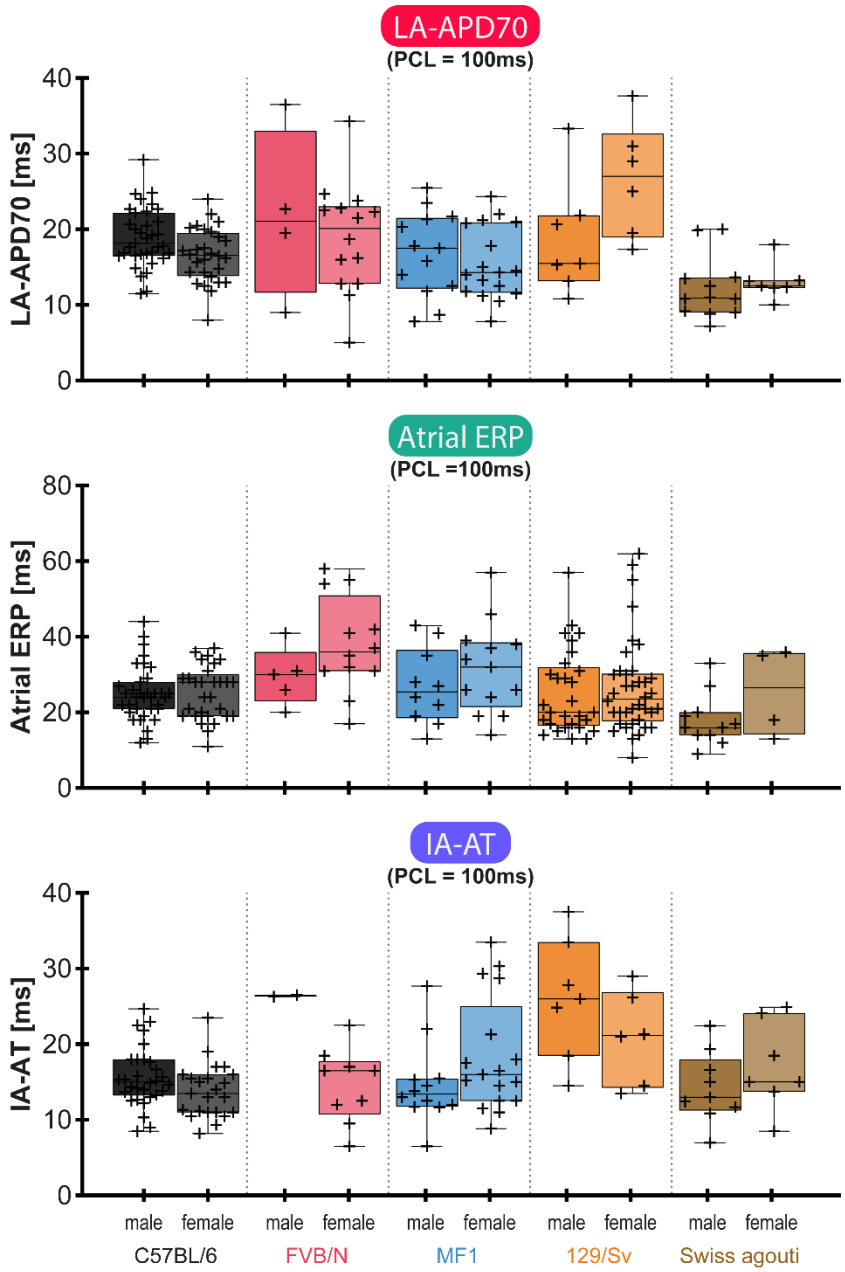
[1]Although raw data were not accessible due to software incompatibility, all data from these six experiments were reviewed carefully during initial publication.

Supplement 2: Single data for APD70 at 80, 100 and 120 ms S1 pacing cycle length



Supplementary Figure 2: *APD70 from n=104 left atria plotted over S1 pacing cycle length. The graph shows a probably not-linear pacing cycle length adaption of left atrial action potential duration (LA-APD). * p<0.05, **** p<0.0001.*

Supplement 3: Combined effects of genetic background and sex on atrial electrophysiological parameters.



Supplementary Figure 3: Combined effects of genetic background and sex on atrial electrophysiological parameters. *Left atrial action potential duration at 70% repolarization (LA-APD70), (**A**), atrial effective refractory period (ERP), (**B**), interatrial activation time (IA-AT), (**C**), each at 100 ms pacing cycle length (PCL) are shown clustered by genetic background and sex. Two-way ANOVA of logarithmic-transformed data was performed. **A:** Two-way ANOVA ($p<0.001$) and the effect of genetic background ($p<0.001$) were significant. Effects of genetic background in male animals only and in female animals only on LA-APD70 were not significant. **B:** Two-way ANOVA ($p<0.01$), effects of genetic background ($p< 0.01$) and sex ($p<0.05$) were significant. Effects of genetic background in male animals only and in female animals only on atrial ERP were significant. **C:** Two-way ANOVA ($p<0.001$), effects of genetic background ($p<0.001$) and the interaction of genetic background*sex ($p<0.01$) were significant. Effects of genetic background in male animals only and in female animals only on IA-AT were significant.*

Supplement References

[1] Fabritz L, Kirchhof P, Franz MR, Eckardt L, Monnig G, Milberg P, et al. Prolonged action potential durations, increased dispersion of repolarization, and polymorphic ventricular tachycardia in a mouse model of proarrhythmia. *Basic Res Cardiol* 2003; **98**: 25-32.

[2] Fabritz L, Kirchhof P, Franz MR, Nuyens D, Rossenbacker T, Ottenhof A, et al. Effect of pacing and mexiletine on dispersion of repolarisation and arrhythmias in DeltaKPQ SCN5A (long QT3) mice. *Cardiovasc Res* 2003; **57**: 1085-1093.

[3] Blana A, Kaese S, Fortmuller L, Laakmann S, Damke D, van Bragt K, et al. Knock-in gain-of-function sodium channel mutation prolongs atrial action potentials and alters atrial vulnerability. *Heart Rhythm* 2010; **7**: 1862-1869.

[4] Kirchhof PF, Fabritz CL, Franz MR. Postrepolarization refractoriness versus conduction slowing caused by class I antiarrhythmic drugs: antiarrhythmic and proarrhythmic effects. *Circulation* 1998; **97**: 2567-2574.

4 Chapter IV - Methods: High resolution optical mapping of cardiac electrophysiology in pre-clinical models

Publication 2. This research was originally published in Scientific Data.

High resolution optical mapping of cardiac electrophysiology in pre-clinical models.

O'Shea C, Winter J, Kabir SN, O'Reilly M, Wells SP, Baines O, **Sommerfeld LC**, Correia J, Lei M, Kirchhof P, Holmes AP, Fabritz L, Rajpoot K, Pavlovic D. *Sci Data. 2022 Mar 31;9(1):135. doi: 10.1038/s41597-022-01253-1.*

Author contributions in publication 2

I contributed to experiments investigating the effect of flecainide on atria (Figure 7) and revised the manuscript. I furthermore initially worked with James Winter on optical mapping of murine whole heart preparations, transferred knowledge of the methodology to other co-authors and trained colleagues and students. Optical mapping of murine atria was applied in preprint 1 and 2, Chapter VI and VII.

Title

High resolution optical mapping of cardiac electrophysiology in pre-clinical models

Authors

Christopher O'Shea[1*], James Winter[1], S. Nashitha Kabir[1], Molly O'Reilly[1,2], Simon P Wells[1,3], Olivia Baines[1], Laura C Sommerfeld[1,7], Joao Correia[1], Ming Lei[4], Paulus Kirchhof[1,4,5], Andrew P Holmes[1,6], Larissa Fabritz[1,4,7], Kashif Rajpoot[8], Davor Pavlovic[1]

*Corresponding Author

Affiliations

1. Institute of Cardiovascular Sciences, University of Birmingham, Birmingham, UK

2. Heart Center, Department of Clinical and Experimental Cardiology, Amsterdam UMC, location AMC, Amsterdam, The Netherlands

3. William Harvey Research Institute, Queen Mary University of London, London, UK

4. Department of Pharmacology, University of Oxford, Oxford, UK

5. Department of Cardiology, University Heart and Vascular Centre, University Medical Center Hamburg-Eppendorf, Germany and German Center for Cardiovascular Research (DZHK) partner site Hamburg/Kiel/Lubeck, Germany

6. Institute of Clinical Sciences, University of Birmingham, Birmingham, UK

7. Center of Cardiovascular Science, UKE, Hamburg, Germany

8. School of Computer Science, University of Birmingham, Birmingham, UK

corresponding author: Christopher O'Shea

Abstract

Optical mapping of animal models is a widely used technique in pre-clinical cardiac research. It has several advantages over other methods, including higher spatial resolution, contactless recording and direct visualisation of action potentials and calcium transients. Optical mapping enables simultaneous study of action potential and calcium transient morphology, conduction dynamics, regional heterogeneity, restitution and arrhythmogenesis. In this dataset, we have optically mapped Langendorff perfused isolated whole hearts (mouse and guinea pig) and superfused isolated atria (mouse). Raw datasets (consisting of over 400 files) can be combined with open-source software for processing and analysis. We have generated a comprehensive post-processed dataset characterising the baseline cardiac electrophysiology in these widely used pre-clinical models. This dataset also provides reference information detailing the effect of heart rate, clinically used anti-arrhythmic drugs, ischaemia-reperfusion and sympathetic nervous stimulation on cardiac electrophysiology. The effects of these interventions can be studied in a global or regional manner, enabling new insights into the prevention and initiation of arrhythmia.

Background & Summary

Organised depolarisation, propagation, and repolarisation of the cardiac action potential is key to coordinated contraction and relaxation of the heart. Local, regional, or global abnormalities in action potential generation, propagation and repolarisation can disturb the normal rhythm or beating rate of the heart, known as cardiac arrhythmia. Arrhythmias are common and contribute to several cardiovascular complications including sudden cardiac death, heart failure and stroke[1]. The mechanisms underpinning complex arrhythmias, and how to best treat these conditions, remain incompletely understood[2]. This has fuelled a substantial and ongoing global research effort.

Cardiac optical mapping is a fluorescence-based technique which offers unparalleled spatial resolution to study the dynamics of cardiac electrophysiology[3,4]. Using potentiometric dyes, action potential propagation and morphology in multi-cellular cardiac preparations, including *ex-vivo* animal hearts, are visualised. Optical mapping has several advantages over traditional electrode measurements[5]. High spatial resolution enables local and/or regional alterations in cardiac electrophysiology to be observed (e.g. different chambers of the heart, apico-basal gradients)[6,7]. Furthermore, optical mapping enables direct contactless recording of optical action potentials, whereas multi electrode array techniques make indirect recordings of extracellular field potentials which require direct or close electrode-tissue contact[8,9]. By using calcium indicators, optical mapping can also be used to directly image calcium transience, the rise and fall of intracellular calcium concentration that initiates the contraction and relaxation of cardiac muscle cells[10,11]. These features make optical mapping an extremely powerful pre-clinical technique for studying arrhythmogenesis and the electrophysiological effects of physiological, pathophysiological, and pharmacological stimuli.

Here, we provide a large database of cardiac optical mapping data from intact mouse and guinea pig whole hearts, and isolated mouse left atria. In total, 45 optical mapping datasets and over 400 individual files are provided. The dataset contains high resolution data obtained at multiple physiologically relevant pacing frequencies, both at baseline and in response to pharmacological agents (flecainide, carbenoxolone, ibutilide, cyclopiazonic acid, HMR 1556, and noradrenaline) or physiological interventions (ischaemia-reperfusion and sympathetic nervous stimulation). The data provided map cardiac electrophysiology both in

sinus (intrinsic) rhythm and epicardial pacing, and during arrhythmic phenomena such as alternans and ventricular fibrillation.

Due to their high spatio-temporal nature, the datasets produced by optical mapping are large and complex. The data can also be limited by poor signal quality or corruption by motion artefacts[5,12]. Therefore, the database described here, as well as providing ideal for high-resolution regional integration of the interventions applied, will act as a resource to understanding of optical mapping data, detailed mapping analysis and potential limitations of the technique. Our group has previously designed, validated and released an open-source software ElectroMap for analysis of optical mapping[13]. Several other open-source tools are also available[14–17], including specialised software to analyse fibrillation dynamics[18] and alternans behaviour[19]. These tools allow effective exploration of the optical mapping data provided, without significant prior expertise. Furthermore, the database we provide represents a freely available resource for development, testing and validation of novel mapping algorithms to further improve analysis capabilities.

Methods

(Animal Welfare) Ethics declarations

All experiments were undertaken in accordance with ethical guidelines set out by the United Kingdom Animals (Scientific Procedures) Act 1986 and Directive 2010/63/EU of the European Parliament on the protection of animals used for scientific purposes. Studies conformed to the Guide for the Care and Use of Laboratory Animals published by the U.S. National Institutes of Health under assurance number A5634-01. Studies were approved by the UK Home Office and relevant ethical committees at King's College London (guinea pig, PPL: PF75E5F7F) and University of Birmingham (mouse, PPL: PPL 30/2967 and PFDAAF77F) respectively.

Guinea pig whole heart optical mapping

Optical mapping of the innervated guinea pig whole heart was conducted as previously described (n=23), where the entire rib cage is resected rather than just the heart[11,20,21]. This approach leaves intact the cardiac autonomic innervation, enabling stimulation of the sympathetic nervous system via the spinal cord as described below.

Adult male guinea pigs were anesthetised using sodium pentobarbitone (160mg/kg, intraperitoneal injection). Following confirmation of deep anaesthesia, an incision was made below the diaphragm. The rib cage was then removed, allowing isolation and cannulation of the descending aorta, and ligation of subclavian and carotid vessels. The preparation was then transferred to the optical mapping setup (Fig 1a) where the heart was Langendorff perfused via the descending aorta. Hearts were perfused with warmed and oxygenation (37^{o}C, 95% O_2/5% CO_2) buffer solution at a pressure of 65-75mmHg. Buffer solution contained in mM: NaCl 114, KCl 4.0, $CaCl_2$ 1.6, $NaHCO_3$ 24.0, $MgSO_4$ 1.0, NaH_2PO_4 1.1, glucose 11, sodium pyruvate 1 and decamethonium bromide 0.01. Hearts were mechanically uncoupled with blebbistatin (15 µM) to prevent motion artefacts. Where appropriate, pharmacological agents (see data records), were added directly into the perfusate following baseline recordings. Sympathetic nervous stimulation (SNS) was achieved by bi-lateral stimulation of efferent sympathetic nerves by a decapolar 5- French catheter in the spinal column. The catheter was inserted up to the 5–7th cervical vertebrae. The distal poles of the catheter were excited by pulse stimulation (40 V, duration 2ms). Electrical stimulation

frequency was varied between 3-8 Hz following testing at the beginning of each experiment to achieve a steady state heart rate of 320-340 bpm during SNS.

Langendorff perfused hearts were loaded with potentiometric (transmembrane voltage) dye di-8-anepps (1 mg/ml in DMSO; 200–300 µL) or rh-237 (2.5 mg/ml in DMSO; 25–50 µL) for action potential recording, Fig, 1a-c. For dual recording of action potentials and calcium transience, rh-237 was combined with intracellular calcium indicator rhod-2AM (200 µg dissolved in 200 µL DMSO + 20 µL 20% pluronic F-127). Hearts were excited by LED illumination at 530/50 nm, and emission light collected at >610 nm for di-8-anepps, >710 nm for rh-237 and 585/40 nm for rhod-2. Emission photons were imaged by Evolve Delta 512×512pixel EMCCD cameras (500 Hz sampling rate, 64×64pixels, 320 µm/pixel). During recordings, hearts were paced from left ventricular epicardial apex through silver bipolar pacing wires. Hearts were paced with a ramp protocol, starting at 160 ms pacing cycle length (PCL). PCL was then reduced by 10 ms every 10 beats until induction of ventricular fibrillation (VF).

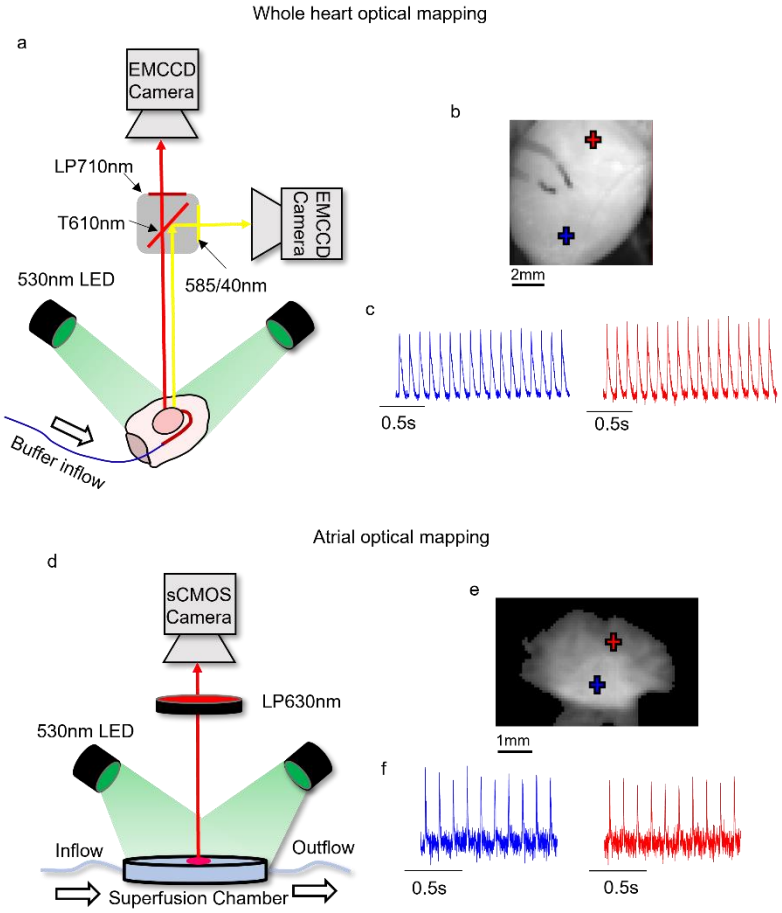


Figure 1 Optical mapping experimental setups. a) Schematic diagram of optical mapping setup used for guinea pig and mouse whole heart optical mapping data in this dataset. **b)** Fluorescent image of mouse whole heart loaded with di-4-anepps. **c)** Example signals from marked locations collected from di-4-anepps loaded heart. **d)** Schematic diagram of optical mapping setup used for mouse atrial optical mapping data in this dataset. **e)** Fluorescent image of mouse atria loaded with di-4-anepps. **f)** Example signals from marked locations collected from di-4-anepps loaded atria. LP=Long pass, T=Transmission, EMCCD= Electron multiplied charged coupled device, sCMOS= Scientific complementary metal oxide semiconductor.

Murine whole heart optical mapping

Optical mapping of the mouse whole heart was conducted using a modified version of the above protocol as previously described (n=12)[22]. Adult male mice were terminally anesthetized with isoflurane (4-5% in 100% O_2, 1.5 L/min). Hearts were Langendorff perfused with warmed and oxygenated carbonated (37°C, 95% O_2/5% CO_2) buffer solution at a pressure of 70-80 mmHg. Buffer solution contained in mM: NaCl 114, KCl 4, $CaCl_2$ 1.4, $NaHCO_3$ 24, NaH_2PO_4 1.1, glucose 11 and sodium pyruvate 1. Hearts were mechanically

uncoupled with blebbistatin (15 µM) to prevent motion artefacts. Where appropriate, pharmacological agents (see data records), were added directly into the perfusate following baseline recordings. For ischaemia-reperfusion experiments, global low-flow ischaemia was induced by reduction of flow rate by 75% for 3 minutes, with flow rate returned to original levels for reperfusion.

Hearts were loaded by injection of rh-237 (1.25 mg/mL in DMSO) into the perfusion line over a 5-minute period. Hearts were illuminated at 530/50 nm and emitted light collected at >710 nm. Emission photons were imaged by Evolve Delta 512 × 512pixel EMCCD cameras (1000 Hz sampling rate, 51 × 51pixels, 156 µm/pixel). During recordings, hearts were paced from the left ventricular epicardial surface through silver bipolar pacing wires at a PCL of 110ms. Recording time was 5 seconds.

Murine left atrial optical mapping

Murine left atrial optical mapping experiments were conducted as previously reported (n = 10, 6 Male, 4 Female)[23–26]. Adult mouse hearts were excised under deep terminal isoflurane-induced anesthesia (4--5% in O_2, 1.5 L min^{-1}). Whole hearts were isolated and Langendorff perfused via the ascending aorta at a flow rate of 2-4 mL/minute with standard bicarbonate buffered Krebs–Henseleit solution containing in mM: NaCl 118; $NaHCO_3$ 24.88; KH_2PO_4 1.18; Glucose 11.0; $MgSO_4$ 0.83; $CaCl_2$ 1.80; KCl 3.52 (37°C, 95% O_2/5% CO_2). Potentiometric dye, di-4-anepps (0.125 mg/mL), was loaded over 5-10 minutes via bolus injection into the perfusion line. The left atrium was then removed, pinned in the superfusion chamber, and transferred to the optical mapping setup (Fig. 1d). In the optical mapping setup, atria were superfused with oxygenated Krebs–Henseleit solution (37°C, 95% O_2/5% CO_2), and blebbistatin (42.75 µM) was added to the superfusate for mechanical uncoupling. Where appropriate, pharmacological agents (see data records), were added directly into the superfusate following baseline recordings. Atria were paced using platinum bipolar electrodes, initially at 1000 ms or 330 ms PCL for 10 minutes in dark conditions to allow equilibration.

For recordings, four LEDs at 530/50 nm illuminated the atria and filtered fluorescence (>630 nm) was collected using ORCA flash 4.0 sCMOS camera. Images were collected at 1000 Hz

sampling rate with a maximal resolution of 200x2048 pixels (71µm/pixel). Atria were paced at with one of two 'ramp' protocols. Atria were paced at either 150 ms or 120 ms, and PCL was reduced by 10 ms every 20 stimuli down respectively. Recording time was between 30 seconds and 1 minute.

Data analysis

All data analysis performed herein used the ElectroMap software. ElectroMap configuration files are provided with all datasets to recreate analysis outlined, and detailed analysis instructions are available within our previous publications[13,27]. Raw data were pre-processed by application of a 3x3 Gaussian spatial filter (standard deviation σ = 1.5). When required, baseline correction was performed using a top-hat kernel (200 ms length for guinea pig data, 100 ms for mouse)[28]. Automated PCL identification was applied, and the last 10 beats at respective PCLs were ensemble averaged to improve signal quality (other than for alternans and optical wave similarity (OWS) analysis, where single beat analysis is required).

Action potential duration to 80% (APD80) was calculated as the time from maximum upstroke velocity to 80% repolarisation. Activation time was defined as the midpoint of depolarisation. Conduction velocity (CV) was derived from activation maps using an implementation of the multi-vector method of Bayly et al. with a 5x5 window size[29]. Heterogeneity in APD and CV was calculated as the difference between the 95th and 5th percentiles, divided by the median. APD80 alternans magnitude (ΔAPD80) was calculated as the absolute difference between APD80 of one action potential compared to the previous. OWS, as a measure of temporal regularity, was calculated as described previously in detail[21]. Briefly, OWS was calculated by measuring the cosine similarity between individual amplitude normalised optical action potentials at a given pacing cycle length. OWS was then defined as the weighted sum of the similarity between all optical action potentials in the sequence. The result is OWS approaches 1 for temporally stable signals, and 0 for temporally irregular signals[21].

For dominant frequency mapping, the frequency spectrum of the signal was computed using fast Fourier transform, with a Hann window applied. Zero padding was applied to achieve a frequency resolution of 0.05 Hz, and the frequency range studied was from 0.5 to 50 Hz[30].

Statistical methods

All data are presented as mean ± standard error of the mean. Group differences or effects of interventions such as changes in pacing cycle length were studied using one-way or two-way ANOVA as appropriate, with Tukey or Sidak's correction respectively. Significance was defined as an adjusted P value < 0.05. Specific statistical tests used for each analysis presented are given in the figure legend. All statistics were performed using Prism 9 (GraphPad Software, San Diego, California).

Data Records

The data associated with this database are summarised in Table 1 and available from figshare (https://figshare.com/s/9b7ddd01cb76dc56d341)[31]. All data are provided in .mat format, and organised so that each folder contains an individual experiment (i.e. whole heart or isolated atrium). All PCLs are within single experimental files. .txt are also provided that contain suggested settings for use in ElectroMap.

Technical Validation

To validate the optical mapping data presented in this dataset, we performed baseline recordings, pharmacological and physiological interventions with known effects on cardiac electrophysiology and time control experiments to ensure signal stability over time in absence of intervention.

Guinea pig whole heart validation: cardiac restitution

To validate the data collected in the innervated guinea pig heart, we first quantified APD and CV as a function of PCL. As heart rate increases, (e.g. PCL decreases), the action potential duration in larger mammals such as the guinea pig shortens by modulation of several ionic mechanisms to enable a sufficient diastolic interval[32]. A further response to a decreased PCL is a reduced conduction velocity, primarily caused by a reduced availability of sodium channels which remain inactive following the previous excitation[33,34]. Collectively, the response of the cardiac tissue to heart rate/PCL is termed cardiac restitution.

Fig. 2 demonstrates these expected restitution dynamics in the guinea pig data presented here. As PCL is decreased during the ramp protocol, APD80 decreases, Fig. 2a-b. For example, at a PCL of 160 ms, mean APD80 is 108.2±0.63 ms, which decreases to 89.1±0.57 ms when PCL is 110 ms ($P<0.0001$). Equally, CV decreases as a function of decreased PCL, both when measured from the whole heart surface (Fig. 2c-d) and from a defined area near the apical pacing site (Fig. 2e-f). At a PCL of 160 ms, mean CV across the ventricular is 89.3±2.4 cm/s, which decreases to 84.9±2.1 cm/s when PCL is 110 ms ($P<0.0001$). Similarly, when analysis is restricted to an area near the pacing site, CV slows from 68.0±2.1 cm/s at 160 ms PCL to 65.6±1.8 cm/s at 110 ms PCL ($P=0.0002$). The changes in measured CV values

depending on analysis area are discussed below (see *Usage notes*). Collectively, these data validate the pacing frequency response of the guinea pig data in this dataset.

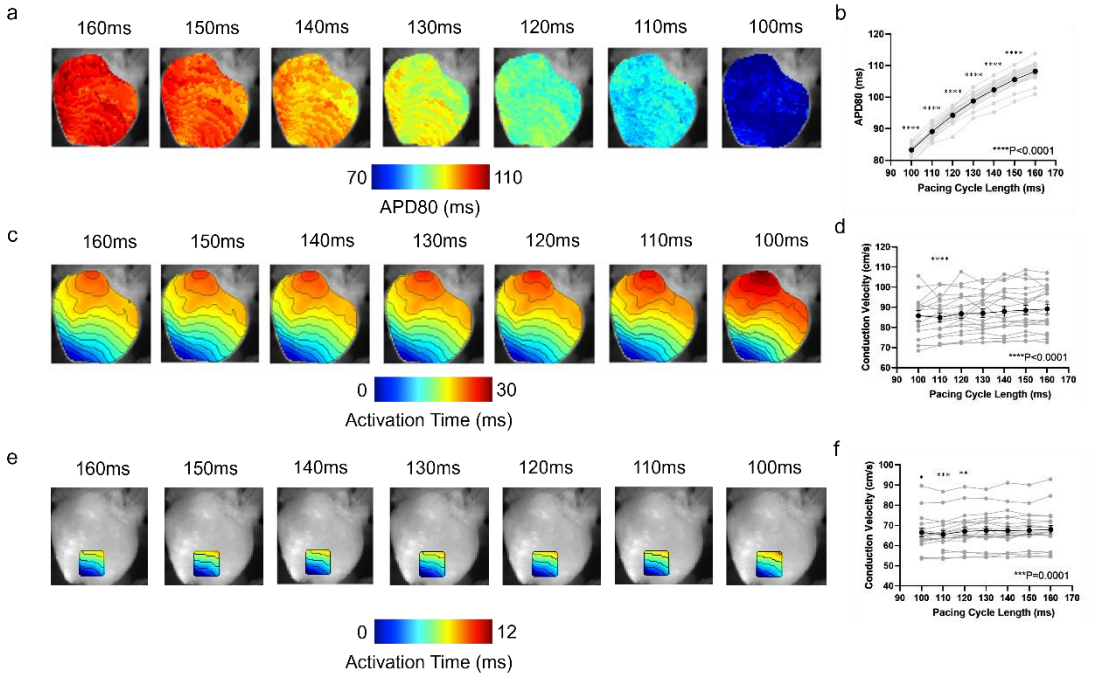


Figure 2 Restitution dynamics of guinea pig heart. a) Example action potential duration 80 (APD80) images from guinea pig whole heart at decreasing pacing cycle lengths (PCL). **b)** Grouped data of APD80 as a function of PCL. **c)** Example activation images from guinea pig whole heart at decreasing PCLs. **d)** Grouped data of conduction velocity as a function of decreasing PCLs. **e)** Example activation images from guinea pig whole heart at decreasing PCLs with analysis area restricted to an area at the apex of the heart. **f)** Grouped data of conduction velocity as a function of decreasing PCLs with restricted analysis area. n=20. One-way ANOVA. ***P<0.001, ****P<0.0001 for overall interaction of APD80/CV with PCL, shown above x-axis. Multiple comparisons are for each PCL against the slowest PCL (160ms). Significance (*P<0.05, **P<0.01, ***P<0.001, ****P<0.0001) are shown above respective PCL where a significant difference versus 160ms pacing was identified.

Guinea pig whole heart validation: ibutilide-induced action potential prolongation and sympathetic nervous stimulation -induced shortening

Ibutilide is a class III anti-arrhythmic drug that's primary mechanism of action is blockade of the rapid component of the delayed rectifier potassium current, I_{Kr}[35]. As such, it is expected to prolong action potential duration. To validate pharmacological modulation of action potential morphology in these data, we mapped APD80 in the guinea pig whole heart before and after administration of ibutilide (100 nM), Fig. 3a. As further validation, we also repeated

these measurements with application of sympathetic nervous stimulation (SNS), which is known to shorten rather than prolong APD[11,36].

Fig. 3a-b demonstrates that, as expected, ibutilide prolonged APD in both control conditions and during application of SNS. In control conditions, ibutilide prolonged APD80 from 110.1±1.1 ms to 121.1±1.8 ms (P=0.0008). Similarly, with application of SNS, ibutilide prolonged APD80 from 100.2±2.2 ms to 109.7±3.6 ms (P=0.0055). Furthermore, SNS significantly shortened APD80 from 110.1±1.1 ms to 100.2±2.2 ms (P=0.026). Ibutilide-induced effects were homogeneous across the ventricular surface (Fig. 3bii), however SNS did significantly increase APD heterogeneity from 0.0722±0.006 to 0.145±0.016 (P=0.0007). Again, these results are expected owing to the heterogenous distribution of cardiac neurons[36]. Fig. 3c reveals neither ibutilide nor SNS significantly altered conduction dynamics. These results validate pharmacological and physiological induced perturbations of action potential morphology within these data.

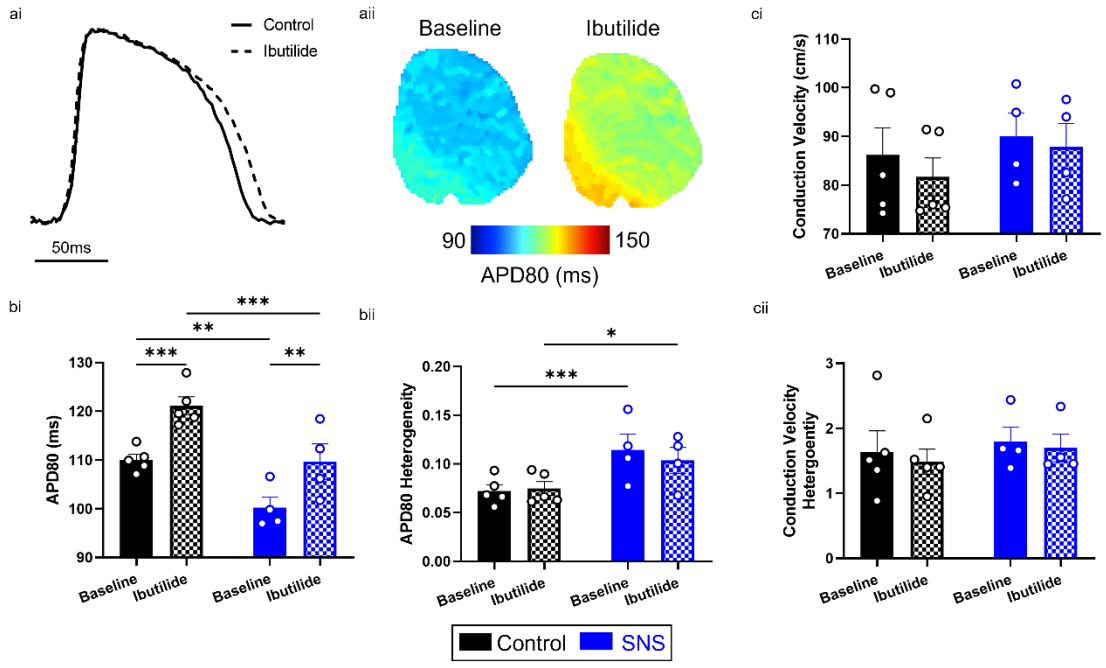


Figure 3 Effects of ibutilide and sympathetic nervous stimulation (SNS) in guinea pig heart. **a)** Example optical action potential recordings **(i)** and action potential duration 80 (APD80) maps **(ii)** in control conditions and following ibutilide treatment. **b)** Grouped data of APD80 (i) and APD80 heterogeneity (ii) before and after ibutilide treatment, both without (black) and with (blue) SNS. **c)** Grouped data of conduction velocity (i) and conduction velocity heterogeneity (ii) before and after ibutilide treatment, both without (black) and with (blue) SNS. n=5 for control, 4 for SNS. Two-way ANOVA. *P<0.05, **P<0.01. Multiple comparisons are made between all Baseline and ibutilide treated groups, and between control and SNS. Pacing cycle length = 160ms.

Guinea pig whole heart validation: Pacing induced arrhythmia

Rapid pacing of *ex-vivo* cardiac perpetrations is a common approach for induction of pro-arrhythmic phenomena such as cardiac alternans, and indeed arrhythmias such as atrial and ventricular fibrillation (AF/VF). To validate the use of these data for studying arrhythmogenesis, we applied dominant frequency, alternans (ΔAPD80) and optical wave similarity (OWS) analysis before and during onset of VF induced by the 'ramp' pacing protocol (Fig. 4a). Fig. 4b demonstrates that during physiological pacing, the dominant frequency of the action potential signal is homogenous across the tissue and dictated by the pacing frequency. In contrast, during VF, the dominant frequency is greater and extremely heterogenous, as has been demonstrated in several previous studies[12,18].

Fig. 4c-e demonstrates the onset of temporal irregularity in the action potential signal at faster PCLs preceding (and during) VF onset. OWS (a measure of the morphological similarity of one action potential with all others at the same pacing frequency based on the whole waveform[21]) decreases at shorter PCLs, Fig. 4ci & d ($P<0.0001$). For example, at a PCL of 160 ms, OWS = 0.98±0.007 which decreases to 0.78±0.021 when PCL decreases to 90 ms ($P=0.0066$). During VF, OWS further reduces to 0.37±0.02. Concurrently, APD alternans magnitude (a comparison of APD of successive action potentials) increases with decreased PCL, Fig. 4cii & e ($P<0.0001$). At a PCL of 160 ms, ΔAPD80 = 0.53±0.043 ms, which increases to 10.2±1.50 ms at a PCL of 90 ms ($P=0.0108$). ΔAPD80 could not be measured during VF due to the impracticality of defining APD during fibrillation. Taken together, these results validate the induction of temporal irregularity, alternans, and VF in the data provided in this dataset.

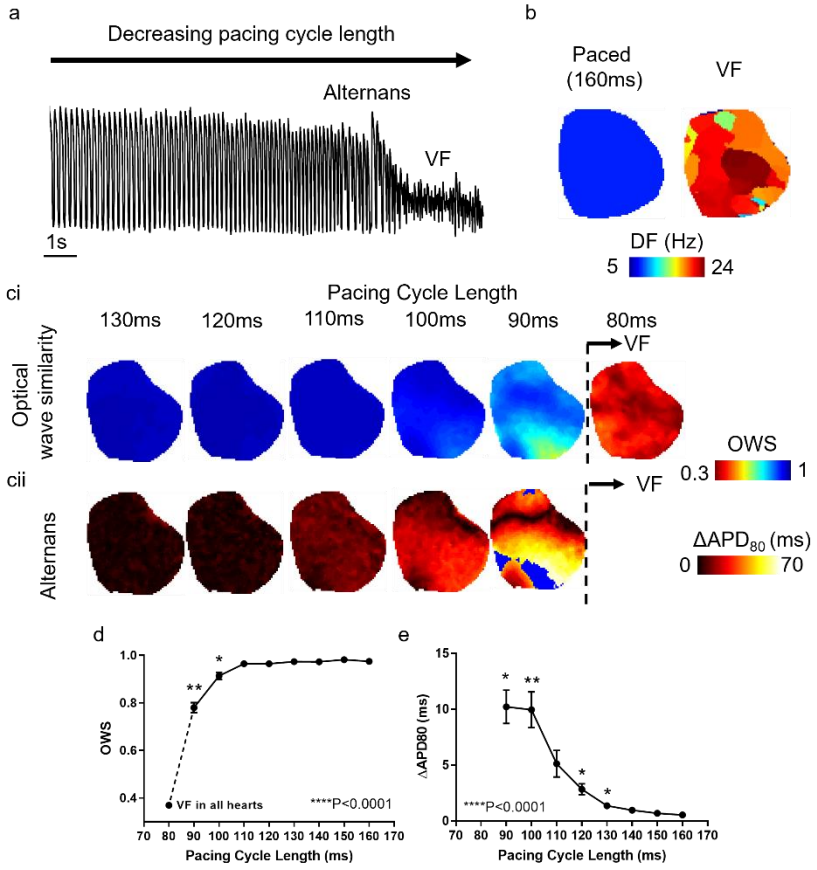


Figure 4. Ramp protocol induced arrhythmia in guinea pig whole hearts. a) Example trace from guinea pig heart during ramp pacing protocol (initial pacing cycle length of 170ms, which is decreased by 10m every 20 stimuli until onset of fibrillation) inducing alternans and ventricular fibrillation (VF). **b)** Example dominant frequency (DF) maps during physiological pacing and VF. **c)** Example optical wave similarity (OWS, i) and action potential duration 80 alternans (ΔAPD80, ii) maps at decreasing PCLs. Note: blue areas in alternans maps denote areas where ΔAPD80 could not be calculated. **d)** Grouped data showing OWS as a function of PCL and during VF. **e)** Grouped data showing ΔAPD80 as a function of PCL. n=6. One-way ANOVA. ****P<0.0001 for overall interaction of OWS/ΔAPD80 with PCL, shown above x-axis. Multiple comparisons are for each PCL against the slowest PCL (160ms). Significance (*P<0.05, **P<0.01) are shown above respective PCL were a significant difference versus 160ms pacing was identified.

Mouse whole heart validation: Flecainide and carbenoxolone induced conduction slowing

Flecainide and carbenoxolone are two pharmacological agents known to slow cardiac CV by different mechanisms. Flecainide is an antiarrhythmic drug that primarily blocks sodium channels, which whilst prolonging the refractory period also leads to slowing conduction[37,38]. Carbenoxolone reduces gap junction coupling, and hence reduces the conductance between neighbouring cells, resulting in slowed action potential propagation[39]. To validate the

provided data in the mouse whole heart, we therefore measured CV at increasing concentrations of flecainide and carbenoxolone.

Fig. 5 demonstrates, as expected, both agents slowed cardiac CV in a dose-dependent manner. In the case of flecainide, CV slowed from 53.86±1.4 cm/s to 40.36±1.3 cm/s (1 µM, P=0.0016), 32.01±1.8 cm/s (2 µM, P=0.005) and 30.86±2.4 cm/s (3 µM, P=0012) respectively, Fig. 5a-b. 10 µM carbenoxolone did not significantly reduce CV. However, higher doses of carbenoxolone slowed CV from 55.75±2.0 cm/s to 43.07±1.1 cm/s (30 µM, P<0.0001) and 40.07±0.75 cm/s (50 µM, P<0.0001) respectively, Fig. 5c-d. These results validate the pharmacological response of the mouse whole heart data presented herein.

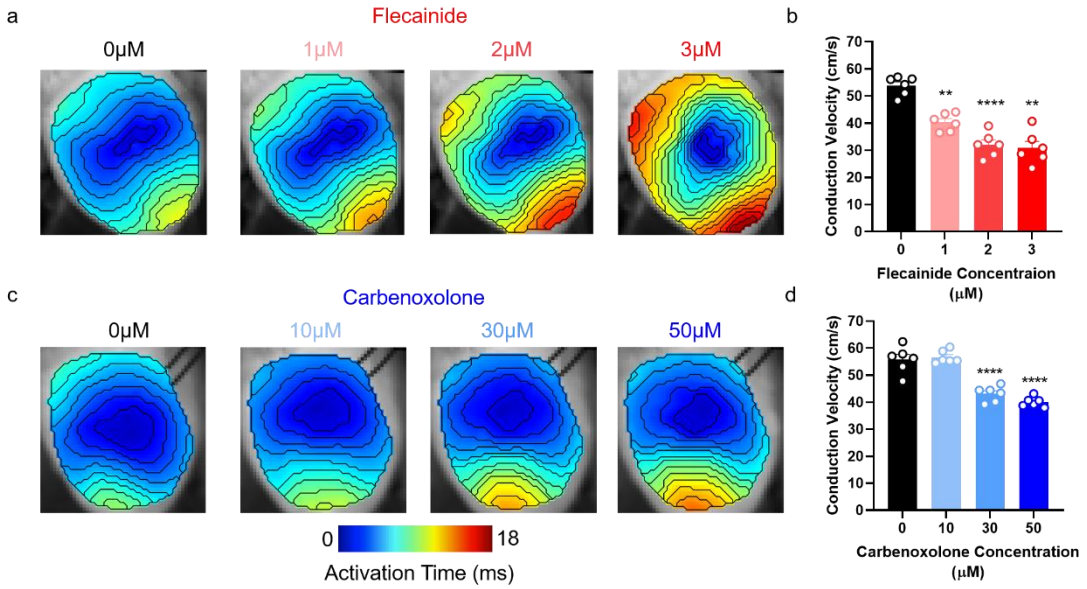


Figure 5 Flecainide and carbenoxolone induced conduction slowing in mouse whole hearts. **a)** Example activation maps from mouse whole heart at increasing concentrations of flecainide. **b)** Grouped conduction velocity data from mouse whole heart at increasing concentrations of flecainide. **c)** Example activation maps from mouse whole heart at increasing concentrations of carbenoxolone. **d)** Grouped conduction velocity data from mouse whole heart at increasing concentrations of carbenoxolone. n=6 for both experiments. One-way ANOVA, **P<0.01, ***P<0.001, ****P<0.0001 against 0µM flecainide/carbenoxolone respectively. Pacing cycle length = 110ms.

Mouse whole heart validation: Acute ischaemia-reperfusion-induced conduction slowing and action potential shortening

Ischaemia-reperfusion injury exerts several effects on cardiac electrophysiology. Ischaemia (restriction of blood flow) results in metabolic stress, cell acidification and increased concentration of potassium in the extracellular space[40]. This can increase the resting membrane potential which reduces sodium channel availability, thereby leading to slowing of CV. Strong activation of K_{ATP} channels also causes severe APD shortening. Therefore, we measured CV and APD following acute (3 minutes) ischaemia in our mouse whole heart data, and following 3 minutes reperfusion, to validate the physiological response of the cardiac tissue in the data presented here.

Fig. 6a-b demonstrates that, as expected, ischaemia reduced cardiac CV. CV reduced from 56.72±1.7 cm/s in control conditions to 38.59±1.24 cm/s following ischaemia (P<0.0001). 3 minutes reperfusion restored CV to 55.04±1.5 cm/s (P=0.14 vs control, P<0.0001 vs ischaemia). Furthermore, Fig. 6c-d demonstrates that ischaemia reduced APD80 from 42.68±1.07 ms to 38.83±1.15 ms (P=0.0294). Unlike CV, reperfusion did not restore APD80 which further reduced to 34.28±0.8 ms (P<0.0001 vs control, P=0.009 vs ischaemia). These results validate the physiological response to ischaemia-reperfusion of the mouse whole heart data presented here.

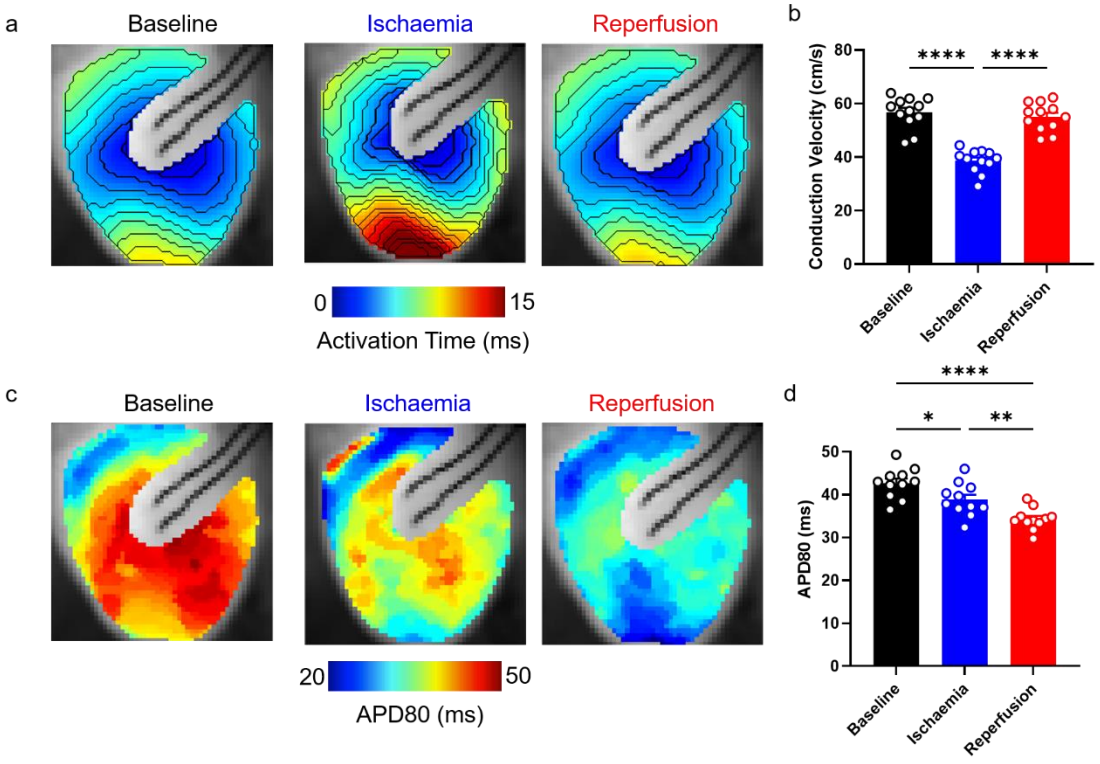


Figure 6 Ischaemia induced conduction slowing and action potential shortening in mouse whole hearts. a) Example activation maps from mouse whole heart in before (black), during (blue, ischaemia) and after (red, reperfusion) low-flow ischaemia. **b)** Grouped conduction velocity data from mouse whole heart in control, ischaemia and reperfusion conditions. **c)** Example action potential duration 80 (APD80) maps from mouse whole heart at baseline (black), during (blue, ischaemia) and after (red, reperfusion) low-flow ischaemia. **d)** Grouped APD80 data from mouse whole heart in control, ischaemia, and reperfusion conditions. n=12. One-way ANOVA, *P<0.05, **P<0.01. ****P<0.0001. Multiple comparisons are made between all groups (Baseline, Ischaemia, Reperfusion). Pacing cycle length = 110ms.

Mouse isolated left atria validation: Flecainide induced conduction slowing and time control data

As stated above, flecainide is an antiarrhythmic drug that blocks sodium channels, slowing the onset of the action potential and thus slowing conduction[37]. Therefore, to validate our data generated in isolated mouse left atria, we measured CV at baseline and following 1 µM flecainide treatment. Fig. 7a-b. As expected, flecainide significantly slowed CV at all PCLs tested (P=0.0009). For example, at 100 ms PCL, flecainide slowed CV from 43.70±2.3 cm/s to 33.73±3.1 cm/s (P<0.0001). Furthermore, as observed in the guinea pig data, decreased PCL slowed CV (P=0.0195).

To validate the temporal stability of these preparations and drug-induced effects, we concurrently performed time control experiments. These were identical to the flecainide experiments in terms of experimental setup, recording time, pacing frequency, dye concentration and blebbistatin concentration, but did not include addition of 1 µM flecainide to the superfusate. Fig. 7c demonstrates that over the experimental time (20 minutes) there is a small but non-significant reduction in CV (P=0.3105). For example, at 100 ms PCL, 20 minutes on the experimental setup slowed CV from 43.39±1.5 cm/s to 42.82±1.4 cm/s (P=0.927). These results validate the pharmacological response to flecainide of the mouse atrial data presented here.

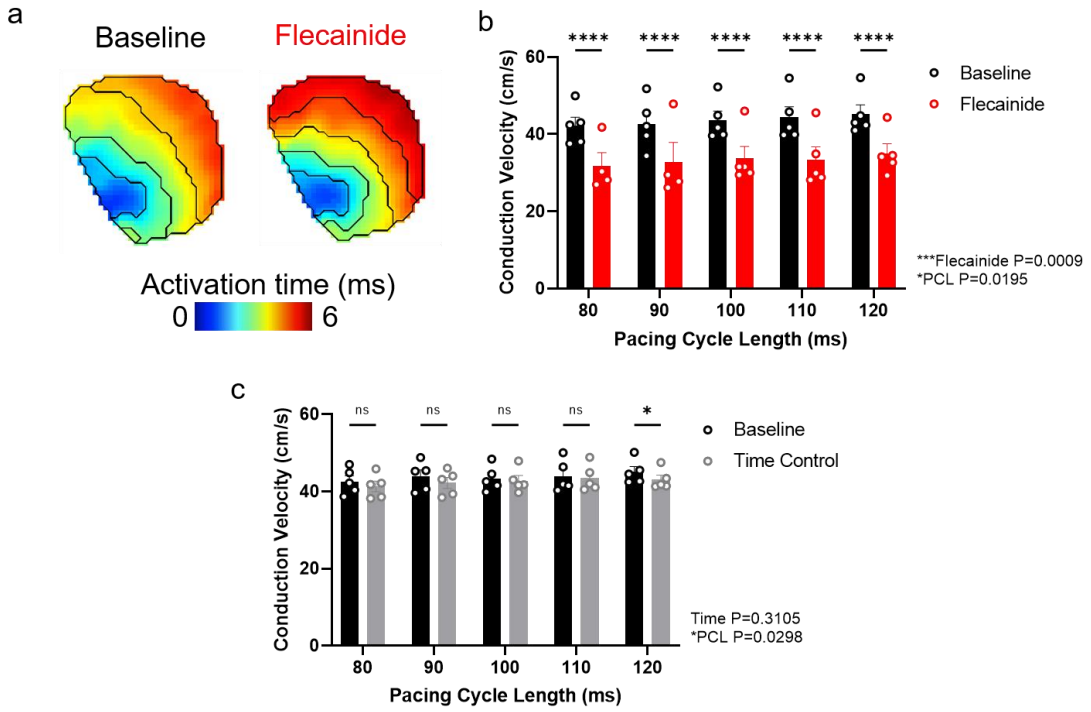


Figure 7 Flecainide-induced conduction slowing in mouse left atria. a) Example activation maps at baseline and following 1 µM flecainide treatment of mouse left atria. **b)** Group data of conduction velocity before and following 1 µM flecainide treatment of mouse left atria at a range of pacing cycle lengths (PCLs). **c)** Grouped data of conduction velocity at baseline and 20 minutes later from mouse left atria at a range of PCLs. n=5. Two-way ANOVA, *P<0.05, ***P<0.001, ****P<0.00001 between baseline and flecainide/time control respectively. Overall interaction of CV with PCL and flecainide/time is shown to the bottom right of the figures *P<0.05, ***P<0.001.

Usage Notes

As stated in the Methods, all data analysis provided here has been undertaken using ElectroMap software (https://github.com/CXO531/ElectroMap). For help with use of this data within ElectroMap, example setting configuration files are provided will all datasets than can easily be loaded into ElectroMap. For further instruction on use of this software, the reader is directed towards our previous publications[13,27].

Furthermore, several other open software packages are also available which can be used with the provided data[14,15,17–19,41,42].

Limitations and considerations in optical mapping

There are several aspects of optical mapping experiments, and the data produced, that should be considered when using and interpreting these data and others. Firstly, effective recording of the action potential (or calcium transient) morphology requires uncoupling of the mechanical contraction of the heart (although progress is being made to realise optical mapping in the freely beating heart[12,43,44]). Commonly, this is achieved using excitation-contraction uncouplers, such as Blebbistatin in the data presented herein. The uncoupled heart lacks bidirectional interaction between mechanical and electrical activity (e.g. stretch activated ion channels[45]), and has reduced oxygen and energy demand[43]. There are also reports that Blebbistatin exerts direct effects on cardiac electrical activity[46], although there are several reports to the contrary[12,47]. Nevertheless, the potential effects of mechanical uncoupling should be considered when interpreting optical mapping data. Further, there is evidence other compounds required for optical mapping, such as the voltage dye di-4-anepps, may exert effects on cardiac electrophysiology such as conduction slowing[48].

Optically recording signals in intact tissue can alter signal morphology due to the interaction of tissue and light[22,49–51]. Although minimal, excitation light will propagate into the tissue, and excite fluorophores away from the imaged surface, typically the epicardium. Therefore, the recorded signals will be a sum of optically recorded action potentials/calcium transients from surface cells, but also to some extent from cells below in the myocardium (or opposite atrial wall in the isolated mouse atria preparations).

Another important aspect is the effect data analysis methods can have on data interpretation. For example, in these data we have applied the 'depolarisation midpoint' method to define activation time. The reason for this is that other methods, such as commonly used 'maximum upstroke velocity', are limited by sampling rate[52]. This reduces

the tissue proportion in which effective CV analysis can take place, as large areas of the tissue will be measured to have simultaneous activation times (making effective CV infinity)[13]. This is particularly problematic in the murine atrial data presented herein, where the entire tissue activates in ca. 5ms. However, previous work suggests the 'time of maximum upstroke velocity' of the optical action potential is the best measure of local activation time[53], despite the issue of sampling rate. Furthermore, several studies demonstrate the recorded optical amplitude and upstroke morphology, from which the 'depolarisation midpoint' and 'time of maximum upstroke velocity' are derived, is altered by asynchronous activation times, transmural propagation direction, optical scattering and pixel integration from several cells[22,50,51]. Within the ElectroMap software, we therefore include both these methods for activation time calculation (and more) for use with these data and others.

Finally, it is also important to consider underlying conduction dynamics of intact tissue when quantifying parameters such as CV in optical mapping datasets. For example, when conduction analysis is applied across the entire imaged surface, the baseline (defined as slowest PCL measured without intervention) ventricular CV of the mouse heart (e.g., 55.04±1.5 cm/s, Fig 6) is measured to be markedly slower than that of the guinea pig (89.3±2.4 cm/s, Fig 2c-d). However, a potential explanation for the increased CV observed in the guinea pig heart here is the increased size of the guinea tissue and pacing from the apex of the heart. The further from the pacing site, the more likely that propagation is no longer parallel to the epicardial surface due to fibre orientation in the heart and potential activation of conduction pathways such as the Purkinje network. This phenomenon, often termed 'epicardial breakthrough', can distort activation patterns as observed at the epicardial surface, artificially increasing measured CV values[22,49]. Indeed, in Fig 2c the isochronal lines spread as the activation wave moves away from the pacing site suggesting epicardial breakthrough. In contrast, in the smaller mouse tissue paced from the centre, this phenomenon is not observed (Fig 5a and c). In support of the vastly increased CV of the guinea pig heart compared to the mouse being an artefact of transmural conduction patterns, when analysis area is restricted to near the apical pacing site (where conduction is assumed to be more parallel to the epicardial surface), guinea pig CV is more closely matched to the mouse at 68.0±2.1cm/s, (Fig 2e-f), although remains quicker.

Code Availability

All code used for analysis of the data are freely available at: https://github.com/CXO531/ElectroMap.

Acknowledgements

This work was funded by the Wellcome Trust (Sir Henry Wellcome Fellowship 221650/Z/20/Z to COS, Seed Award Grant 109604/Z/15/Z to DP), EPSRC (Sci-Phy-4-Health Centre for Doctoral Training studentship L016346 to DP, KR and LF) and the British Heart Foundation (PG/17/55/33087, RG/17/15/33106 to DP, PG/17/30/32961 to AH, Accelerator Award AA/18/2/34218 to Institute of Cardiovascular Sciences).

Author contributions

COS, JW, SNK, MOR, SW, LCS collected experimental data. COS, JC, APH, LF, KR and DP designed and developed analysis software. COS and OB analysed data for validation studies. COS collected, organised, and uploaded data. COS and DP produced figures. JW, ML, PK, APH, LF, KR and DP designed the research projects for which these data were collected. All authors contributed to the final manuscript.

Competing interests

There are no competing interests

References

1. Roth, G. A. *et al.* Global, Regional, and National Burden of Cardiovascular Diseases for 10 Causes, 1990 to 2015. *J. Am. Coll. Cardiol.* **70**, 1–25 (2017).
2. Atienza, F., Martins, R. P. & Jalife, J. Translational research in atrial fibrillation: A quest for mechanistically based diagnosis and therapy. *Circ. Arrhythmia Electrophysiol.* **5**, 1207–1215 (2012).
3. Salama, G. & Morad, M. Merocyanine 540 as an optical probe of transmembrane electrical activity in the heart. *Science (80-.).* **191**, 485–487 (1976).
4. Berenfeld, O. & Efimov, I. Optical Mapping. *Cardiac Electrophysiology Clinics* vol. 11 495–510 (2019).
5. O'Shea, C. *et al.* Cardiac optical mapping – State-of-the-art and future challenges. *Int. J. Biochem. Cell Biol.* **126**, 105804 (2020).
6. Wen, Q. *et al.* Transverse cardiac slicing and optical imaging for analysis of transmural gradients in membrane potential and Ca2+ transients in murine heart. *J. Physiol.* **596**, 3951–3965 (2018).
7. Chen, S. *et al.* A conductive cell-delivery construct as a bioengineered patch that can improve electrical propagation and synchronize cardiomyocyte contraction for heart repair. *J. Control. Release* **320**, 73–82 (2020).
8. Mendonca Costa, C. *et al.* The amplitude-normalised area of a bipolar electrograms as a measure of local conduction delay in the heart. *Front. Physiol.* **11**, (2020).
9. Boukens, B. J. & Efimov, I. R. A century of optocardiography. *IEEE Rev. Biomed. Eng.* **7**, 115–125 (2014).
10. Wang, L., Myles, R. C., Lee, I.-J., Bers, D. M. & Ripplinger, C. M. Role of Reduced Sarco-Endoplasmic Reticulum Ca2+-ATPase Function on Sarcoplasmic Reticulum Ca2+ Alternans in the Intact Rabbit Heart. *Front. Physiol.* **12**, 656516 (2021).
11. Winter, J. *et al.* Sympathetic nervous regulation of cardiac alternans in the intact heart. *Front. Physiol.* **9**, 1–12 (2018).
12. Kappadan, V., Telele, S., Uzelac, I., Fenton, F. & Parlitz, U. High-Resolution Optical Measurement of Cardiac Restitution , Contraction , and Fibrillation Dynamics in Beating vs . Blebbistatin-Uncoupled Isolated Rabbit Hearts. *Front. Physiol.* **11**, 1–18 (2020).
13. O'Shea, C. *et al.* ElectroMap: High-throughput open-source software for analysis and mapping of cardiac electrophysiology. *Sci. Rep.* **9**, 1–13 (2019).
14. Gloschat, C. *et al.* RHYTHM: An Open Source Imaging Toolkit for Cardiac Panoramic Optical Mapping. *Sci. Rep.* **8**, 1–12 (2018).
15. Tomek, J., Burton, R. A. B. & Bub, G. Ccoffinn: Automated Wave Tracking in Cultured Cardiac Monolayers. *Biophys. J.* **111**, 1595–1599 (2016).
16. Laughner, J. I., Ng, F. S. F. S., Sulkin, M. S., Arthur, R. M. & Efimov, I. R. Processing and

analysis of cardiac optical mapping data obtained with potentiometric dyes. *AJP Hear. Circ. Physiol.* **303**, H753-65 (2012).

17. Doshi, A. N. *et al.* Feasibility of a semi-automated method for cardiac conduction velocity analysis of high-resolution activation maps. *Comput. Biol. Med.* **65**, 177–183 (2015).

18. Li, X. *et al.* Standardised Framework for Quantitative Analysis of Fibrillation Dynamics. *Sci. Rep.* **9**, 1–10 (2019).

19. Tomek, J., Wang, Z. J., Burton, R. A. B., Herring, N. & Bub, G. COSMAS: a lightweight toolbox for cardiac optical mapping analysis. *Sci. Rep.* **11**, 1–17 (2021).

20. Ng, G. A., Brack, K. E. & Coote, J. H. Effects of direct sympathetic and vagus nerve stimulation on the physiology of the whole heart - A novel model of isolated Langendorff perfused rabbit heart with intact dual autonomic innervation. *Exp. Physiol.* **86**, 319–329 (2001).

21. O'Shea, C. *et al.* Temporal irregularity quantification and mapping of optical action potentials using wave morphology similarity. *Prog. Biophys. Mol. Biol.* **157**, 84–93 (2020).

22. O'Shea, C., Pavlovic, D., Rajpoot, K. & Winter, J. Examination of the effects of conduction slowing on the upstroke of the optically-recorded action potentials. *Front. Physiol.* **10**, 1–11 (2019).

23. O'Shea, C. *et al.* 135 Development and validation of high-throughput processing and analysis software platform for cardiac optical mapping. *Heart* **104**, A98 LP-A98 (2018).

24. Holmes, A. P. *et al.* A Regional Reduction in Ito and IKACh in the Murine Posterior Left Atrial Myocardium Is Associated with Action Potential Prolongation and Increased Ectopic Activity. *PLoS One* **11**, e0154077 (2016).

25. Syeda, F. *et al.* PITX2 Modulates Atrial Membrane Potential and the Antiarrhythmic Effects of Sodium-Channel Blockers. *J. Am. Coll. Cardiol.* **68**, 1881–1894 (2016).

26. O'Reilly, M. *et al.* Increased early sodium current provokes familial atrial fibrillation and reduces effectiveness of sodium channel block. *bioRxiv* 1–28 (2022) doi:doi.org/10.1101/2022.01.18.476646.

27. O'Shea, C. *et al.* High-Throughput Analysis of Optical Mapping Data Using ElectroMap. *J. Vis. Exp.* 1–10 (2019) doi:10.3791/59663.

28. Yu, T. Y. *et al.* An automated system using spatial oversampling for optical mapping in murine atria. Development and validation with monophasic and transmembrane action potentials. *Prog. Biophys. Mol. Biol.* **115**, 340–348 (2014).

29. Bayly, P. V *et al.* Estimation of Conduction Velocity Vector Fields from Epicardial Mapping Data. **45**, 563–571 (1998).

30. Li, X. *et al.* An interactive platform to guide catheter ablation in human persistent atrial fibrillation using dominant frequency, organization and phase mapping. *Comput. Methods Programs Biomed.* **141**, 83–92 (2017).

31. O'Shea, C. *et al.* High resolution optical mapping of cardiac electrophysiology in pre-

clinical models. *figshare* (2022).

32. Shattock, M. J. *et al.* Restitution slope is principally determined by steady-state action potential duration. *Cardiovasc. Res.* **113**, 817–828 (2017).

33. Weber, F. M. *et al.* Conduction velocity restitution of the human atriuman-An efficient measurement protocol for clinical electrophysiological studies. *IEEE Trans. Biomed. Eng.* **58**, 2648–2655 (2011).

34. Mironov, S., Jalife, J. & Tolkacheva, E. G. Role of conduction velocity restitution and short-term memory in the development of action potential duration alternans in isolated rabbit hearts. *Circulation* **118**, 17–25 (2008).

35. Murray, K. T. Ibutilide. *Circulation* **97**, 493–497 (1998).

36. Tapa, S. *et al.* Adrenergic supersensitivity and impaired neural control of cardiac electrophysiology following regional cardiac sympathetic nerve loss. *Sci. Rep.* **10**, 1–12 (2020).

37. Echt, D. S. & Ruskin, J. N. Use of Flecainide for the Treatment of Atrial Fibrillation. *Am. J. Cardiol.* **125**, 1123–1133 (2020).

38. Kirchhof, P. *et al.* Early Rhythm-Control Therapy in Patients with Atrial Fibrillation. *N. Engl. J. Med.* **383**, 1305–1316 (2020).

39. Dhillon, P. S. *et al.* Relationship between gap-junctional conductance and conduction velocity in mammalian myocardium. *Circ. Arrhythmia Electrophysiol.* **6**, 1208–1214 (2013).

40. Klabunde, R. E. Cardiac electrophysiology: Normal and ischemic ionic currents and the ECG. *Adv. Physiol. Educ.* **41**, 29–37 (2017).

41. Laughner, J. I., Ng, F. S., Sulkin, M. S., Arthur, R. M. & Efimov, I. R. Processing and analysis of cardiac optical mapping data obtained with potentiometric dyes. *AJP Hear. Circ. Physiol.* **303**, H753–H765 (2012).

42. Cooper, B. L. *et al.* KairoSight: Open-Source Software for the Analysis of Cardiac Optical Data Collected From Multiple Species. *Front. Physiol.* **12**, 1–13 (2021).

43. Garrott, K. *et al.* KATP channel inhibition blunts electromechanical decline during hypoxia in left ventricular working rabbit hearts. *J. Physiol.* **595**, 3799–3813 (2017).

44. Christoph, J. *et al.* Electromechanical vortex filaments during cardiac fibrillation. *Nature* **555**, 667–672 (2018).

45. Reed, A., Kohl, P. & Peyronnet, R. Molecular candidates for cardiac stretch-activated ion channels. *Glob. Cardiol. Sci. Pract.* **2014**, 19 (2014).

46. Brack, K. E., Narang, R., Winter, J. & Andr, G. The mechanical uncoupler blebbistatin is associated with significant electrophysiological effects in the isolated rabbit heart. **5**, 1009–1027 (2013).

47. Fedorov, V. V. *et al.* Application of blebbistatin as an excitation-contraction uncoupler for electrophysiologic study of rat and rabbit hearts. *Hear. Rhythm* **4**, 619–626 (2007).

48. Larsen, A. P., Sciuto, K. J., Moreno, A. P. & Poelzing, S. The voltage-sensitive dye di-4-

ANEPPS slows conduction velocity in isolated guinea pig hearts. *Heart Rhythm* **9**, 1493–500 (2012).

49. Bishop, M. J., Gavaghan, D. J., Trayanova, N. A. & Rodriguez, B. Photon Scattering Effects in Optical Mapping of Propagation and Arrhythmogenesis in the Heart. *J. Electrocardiol.* **40**, 75–80 (2007).

50. Hyatt, C. J., Mironov, S. F., Vetter, F. J., Zemlin, C. W. & Pertsov, A. M. Optical action potential upstroke morphology reveals near-surface transmural propagation direction. *Circ. Res.* **97**, 277–284 (2005).

51. Zemlin, C. W., Bernus, O., Matiukas, A., Hyatt, C. J. & Pertsov, A. M. Extracting intramural wavefront orientation from optical upstroke shapes in whole hearts. *Biophys. J.* **95**, 942–950 (2008).

52. Glukhov, A. V. *et al.* Transmural dispersion of repolarization in failing and nonfailing human ventricle. *Circ. Res.* **106**, 981–991 (2010).

53. Walton, R. D. *et al.* Extracting surface activation time from the optically recorded action potential in three-dimensional myocardium. *Biophys. J.* **102**, 30–38 (2012).

Tables

Table 1: Summary of data records available at (https://figshare.com/s/9b7ddd01cb76dc56d341).
***For mouse atrial files, pixel count varies between experiments**

Datatype	*Number of experiments*	*Pixel Size (μM)*	*Sampling Rate (kHz)*	*Pacing cycle lengths (ms)*	*Recording duration (s)*	*Pixel count (x,y)*	*Intervention(s)*
Mouse whole heart	12	156	1	110	5	51x51	Ischemia-Reperfusion (n=12) Flecainide, 1,2,3μM (n=6) Carbenoxolone, 10,30,50μM (n=6)
Mouse Atria	10	71.4	0.987	120-80	30-60	45x45 *	Time control, 35minutes (n=5) Flecainide 1,5μM (n=5)
Guinea Pig Whole heart	23	320	0.5	170-80	60	64x64	Sympathetic Nervous Simulation (n=23) Ibutilide 100nM (n=5) Cyclopiazonic acid 10μM (n=4) HMR 1556 2μM (n=4) Noradrenaline 200nM (n=4)

5 Chapter V - Methods: JavaCyte, a novel open-source tool for automated quantification of key hallmarks of cardiac structural remodeling

Publication 3. This research was originally published in Scientific Reports.

JavaCyte, a novel open-source tool for automated quantification of key hallmarks of cardiac structural remodelling.

Winters J, von Braunmuhl ME, Zeemering S, Gilbers M, Brink TT, Scaf B, Guasch E, Mont L, Batlle M, Sinner M, Hatem S, Mansour MK, Fabritz L, **Sommerfeld LC**, Kirchhof P, Isaacs A, Stoll M, Schotten U, Verheule S. *Sci Rep. 2020 Nov 18;10(1):20074. doi: 10.1038/s41598-020-76932-3.*

Author contributions in publication 3

I tested the tool and the script and gave feedback upon validation of the initial script for the tool and revised the manuscript. I applied the tool for murine atrial tissue analysis described in this methods chapter as described in preprint 1 and 2, Chapters VI and VII.

JavaCyte, a novel open-source tool for automated quantification of key hallmarks of cardiac structural remodeling

Authors: Winters J.[1], Edler von Braunmuhl M.[1], Zeemering S.[1], Gilbers M.[1], Ten Brink T.[1], Scaf B.[1], Guasch E.[2-4], Mont L.[2-4], Batlle M.[2], Sinner M.[10], Hatem S.[5], Mansour MK.[6], Fabritz L.[7,8], Sommerfeld LC.[7], Kirchhof P.[7-10], Isaacs A.[1], Stoll M.[11], Schotten U.[1], Verheule S.[1]

1 Department of Physiology, Cardiovascular Research Institute Maastricht, Maastricht, The Netherlands.
2 Cardiovascular Institute, Hospital Clinic de Barcelona Spain
3 Institut d'Investigacions Biomédiques, August Pi I Sunver (IDIBAPS), Barcelona, Spain
4 CIBERCV, Madrid, Spain
5 INSERM UMRS1166, ICAN - Institute of CardioMetabolism and Nutrition, Sorbonne Université, Institut de Cardiologie, Hôpital Pitié-Salpêtrière, Paris, France
6 Hôpital Necker Enfants Malades, Paris, France
7 Institute of Cardiovascular Sciences, College of Medical and Dental Sciences, Medical School, University of Birmingham, Edgbaston, Birmingham UK
8 Departments of Cardiology, UHB NHS Trusts, Birmingham, UK
9 Department of Cardiology, SWBH NHS Trust, Birmingham, UK
10 University Heart and Vascular Center, UKE Hamburg, Hamburg, Germany and German Centre for Cardiovascular Research (DZHK), partner site: Hamburg, Germany
11 Department of Biochemistry, Cardiovascular Research Institute Maastricht, Maastricht, The Netherlands

Corresponding author:
Sander Verheule, PhD
Department of Physiology, Universiteitssingel 50, P.O. Box 616, 6200 MD, Maastricht, The Netherlands
E-mail: [redacted]

Abstract

Background: Many cardiac pathologies involve changes in tissue structure. Conventional analysis of structural features is extremely time-consuming and subject to observer bias. The possibility to determine spatial interrelations between these features is often not fully exploited.

Methods: We developed a staining protocol and an ImageJ-based tool (JavaCyte) for automated histological analysis of cardiac structure, including quantification of cardiomyocyte size, overall and endomysial fibrosis, spatial patterns of endomysial fibrosis, fibroblast density, capillary density and capillary size. This automated analysis was compared to manual quantification in several well-characterized goat models of atrial fibrillation (AF). In addition, we tested inter-observer variability in atrial biopsies from the CATCH-ME consortium atrial tissue bank, with patients stratified by their cardiovascular risk profile for structural remodeling.

Results: We were able to reproduce previous manually derived histological findings in goat models for AF and AV block (AVB) using JavaCyte. Furthermore, strong correlation was found between manual and automated observations for myocyte count ($r=0.94$, $p<0.001$), myocyte diameter ($r=0.97$, $p<0.001$), endomysial fibrosis ($r=0.98$, $p<0.001$) and capillary count ($r=0.95$, $p<0.001$) in human biopsies. No significant variation between observers was observed ($ICC=0.89$, $p < 0.001$).

Discussion: We developed and validated an open-source tool for high-throughput, automated histological analysis of cardiac tissue properties. JavaCyte was as accurate as manual measurements, with less inter-observer variability and faster throughput.

Introduction

The progression of multiple cardiac diseases causes, or is associated with, gradual changes of cardiac tissue structure. These structural alterations alter the passive mechanical properties of the myocardium, contractility, electrical propagation, tissue perfusion and energetics. Quantification and comparison of cardiac tissue structure normally relies on manual inspection and measurements by researchers, making the process time-consuming and subject to inter-observer variability. Therefore, we developed a suite of algorithms for automated quantification of structural features in myocardial tissue.

A key factor in myocardial remodeling is fibrosis, an increase in the amount of fibrous tissue with age that is accelerated by the presence of chronic cardiovascular diseases. Increased fibrosis has been reported in left ventricular failure [2], right ventricular dysfunction [3], and atrial fibrillation (AF)[4], among other conditions. Seminal work by Weber and co-workers described several distinct types of fibrosis, which are caused by different disease processes [5, 6]. Reparative fibrosis, also called replacement fibrosis, occurs in reaction to myocyte death, e.g. after myocardial infarction, typically leading to larger areas of fibrous tissue deposition. By contrast, reactive fibrosis, also called interstitial fibrosis, occurs in reaction to increased stretch, pressure or volume overload or neurohumoral activation. Interstitial fibrosis can lead to thickening of collagen septa around bundles of myocytes (perimysial fibrosis) and between myocytes within bundles (endomysial fibrosis). Endomysial fibrosis leads to increased cell-to-cell distances between myocytes and can thereby impair electrical propagation . In a goat model, we previously demonstrated that 6 months of AF does not lead to an increase of overall fibrosis but does result in endomysial fibrosis in the epicardial layer of the atria, impairing transverse propagation [8, 9]. In the ventricles, increased endomysial fibrosis is viewed as a key determinant of increased ventricular stiffness leading to diastolic heart failure . Assessment of fibrosis is commonly performed in histological sections by quantifying the relative area occupied by fibrous tissue in Sirius Red or Masson's Trichrome staining, irrespective of the particular type of fibrosis. This usually involves setting a subjective color threshold by the operator to distinguish fibrous tissue from myocytes. However, as is apparent in Fig. 1, there is considerable overlap in the RGB values of myocytes and fibrous tissue, both in Sirius Red and Trichrome staining. As a result, the quantification is sensitive to inhomogeneous illumination (i.e. shading artefacts) and observer bias. Reported values for the percentage of fibrosis in normal, healthy atria vary widely, also within the same species Moreover, whereas larger areas of fibrosis are clearly stained, endomysial septa are not. An alternative for specifically quantifying endomysial fibrosis, the manual measurement of cell-to-cell distances, is extremely time-consuming [11]. In the context of fibrosis, the density of fibroblasts is also relevant [12], both because they are responsible for excess extracellular matrix ECM formation, and because fibroblasts may couple to myocytes electrically, thereby affecting conduction through electrotonic interactions.

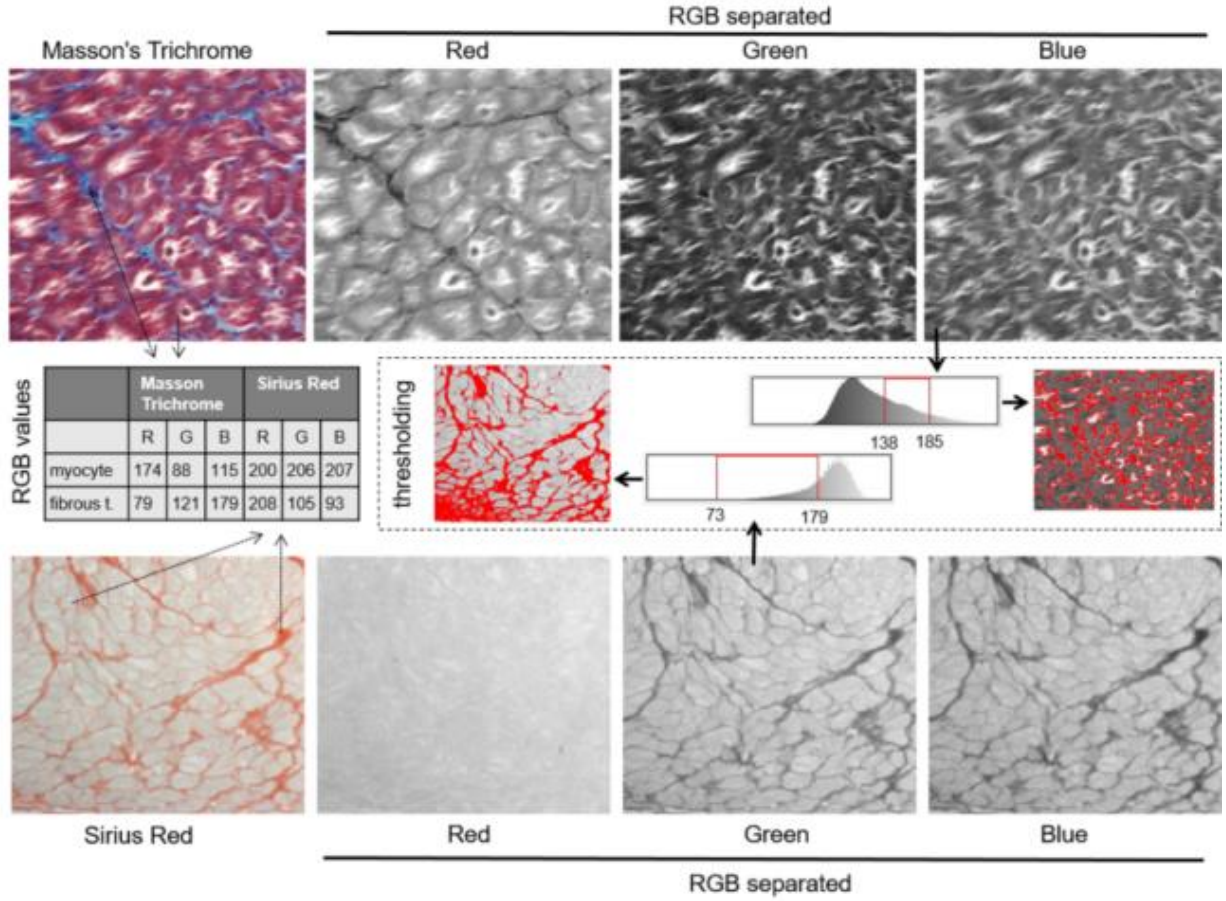


Fig.1 Disadvantages of automated analysis of Sirius red and Masson's Trichrome staining. Similarity in RGB values for myocytes and fibrous tissue following Sirius red staining complicate automated analysis. Manual thresholding is slow, inaccurate and prone to observer bias. Endomysial septa are poorly visibile in both staining approaches. Co-localization of other important markers of structural remodeling is not possible.

Another hallmark of structural remodeling is myocyte hypertrophy. Increased myocyte size relates to increased wall thickness and chamber dilatation macroscopically, and can also alter electrical propagation, both in the ventricles [11, 14] and in the atria . Again, manually measuring myocyte dimensions in histological or immunohistochemical staining is time-intensive and prone to observer bias.

Capillary rarefaction has also been linked to myocardial dysfunction, such as in heart failure with preserved ejection fraction (HFpEF) and AF . Capillary density is often reported as the number of capillaries per unit of surface area. Although this is a relevant correlate of oxygen diffusion distances, it does not accurately reflect the loss or gain in number of capillaries in settings with concomitant myocyte hypertrophy. In those circumstances, the number of capillaries per myocyte is needed to assess the degree of capillary rarefaction or angiogenesis.

We developed a fluorescent triple staining method and an integrated suite of algorithms for the automated quantification of all of the aforementioned structural features. Wheat Germ Agglutinin (WGA) was used to visualize the extracellular matrix (ECM) [15], yielding the number and size of myocytes, overall fibrosis and myocyte-to-myocyte distances as a measure for endomysial fibrosis. Capillaries were stained with the biotinylated isolectin Griffonia Simplifolia (GS-IB4) in animal tissues and CD31 in human biopsies, providing the size and number of capillaries. Fibroblasts were stained with anti-vimentin antibody, yielding the size and distribution of fibroblasts. From these data, the number of capillaries or fibroblasts can be calculated in a simple manner. Because the positions of all recognized structures are stored, this method also allows analysis of the spatial correlation between various parameters. This method was successfully tested in atrial tissue samples from goats, pigs, horses and humans. Here, we present the validation of the method in several goat models of AF that were previously characterized extensively by manual analysis. In addition, we analyzed biopsies from selected patient populations. In general, the extent of atrial pathology is far larger in patient samples than in animal models of heart disease. For this reason, we analyzed the degree of inter-observer variability in these human biopsies as a test case. For these data, we also extended our analysis to spatial heterogeneity in the distribution of endomysial fibrosis, thereby providing an example of the potential for further development.

Materials and Methods

Tissue sampling

Collections of atrial tissue biopsies from several previously described and characterized goat models were used: sham-operated goats (n=6), goats with AF maintained by burst pacing for 3 weeks (short term, ST, n=7) and 6 months (long term, LT, n=6) [16] and goats with atrial dilatation as a result of His bundle ablation (AV block, AVB, n=6) [17]. All animal experiments were approved by the ethical board for animal experimentation 'Centrale Commissie Dierproeven (CCD)' and were in compliance with the European directive 2010/63/EU on the protection of animals used for scientific purposes. All research on human atrial tissue samples was performed in accordance with relevant guidelines, as approved by the ethical committee "METC academic hospital Maastricht/university Maastricht". Informed consent was obtained from all participants.

Human atrial samples (n=14 left atrial appendages, LAA, and n=8 right atrial appendages, RAA) were collected from the CATCH-ME atrial tissue biobank from patients undergoing coronary artery bypass grafting (CABG), valvular surgery or heart transplant surgery (table 1). Patients were stratified based on the expected risk for the presence of atrial structural remodeling associated with their clinical profile. Cardiovascular risk profile positive patients (CVRP+, n=11) were all diagnosed with both heart failure and persistent AF. Tissue from all but one of the patients in this group was obtained during a heart transplant xenograft surgery. The remaining patient was diagnosed with grade III mitral valve regurgitation. Most (n=6) of the CVRP+ patients had an underlying valvular cardiomyopathy, predominantly resulting from the mitral valve. In two other CVRP+ patients, the cardiomyopathy was ischemic. None of the patients had a known genetic basis for cardiomyopathy, long QT syndrome or Brugada syndrome. Two CVRP+ patients, however, were diagnosed with an idiopathic non-obstructive cardiomyopathy. As a whole, ejection fractions were significantly lower in the CVRP+ group, resulting in a higher NYHA classification. Cardiovascular risk profile negative patients (CVRP-, n=11) had no history of either AF or heart failure. In seven CVRP- patients, the primary indication for surgery was coronary artery bypass grafting (CABG). Three others had grade I or II mitral valve regurgitation, requiring mitral valve repair. One tissue sample was collected from a vegetative donor. Patients from the CVRP+ group were matched to CVRP- patients based on sampling side (LAA/RAA), gender (exactly matched) and age (+/-5y).

Triple staining

A complete and detailed protocol for the staining method is provided in supplement 1. All atrial tissues were excised rapidly, snap frozen and stored at -80°C. Cryosections of 6µm were made at -22°C and stored at -80°C. Antigen fixation was performed by submerging slides in ice-cold acetone for 10 minutes. Nonspecific binding sites were blocked for 60min with a blocking solution consisting

of 2 m/v % fraction V BSA and 0.3M glycine dissolved in PBS. Fibroblasts were visualized with an overnight stain using a mouse monoclonal anti-vimentin antibody at a concentration of 1/150. In human samples endothelial cells were stained overnight at room temperature with a monoclonal anti-human CD31 antibody at a concentration of 1/50. The next morning, sections were incubated for 120 minutes at room temperature with appropriate fluorescent secondary antibodies at a concentration of 1/200 (Fig. 2). Cell membranes were stained at room temperature using WGA lectin conjugated to an Alexa 594 fluorophore at a 1/200 dilution. In animal tissue, capillaries were labeled with the biotinylated GS-IB4 conjugated to Alexa Fluor 488 at a dilution of 1/200, for a duration of 120min. Coverslips were mounted with 'Prolong Gold Antifade' mounting medium (ThermoFisher Scientific). Stained sections were stored at 4°C prior to microscopy.

Target	Primary AB/lectin	[X],t	Secondary AB	[X],t
Collagen type I,III	Wheat germ agglutinin (WGA)	NA	None	1/200, 2h
CD31 (endothelium)	Mouse monoclonal anti-CD31	1/50, O/N	Goat anti-mouse 488	1/200, 2h
Vimentin (fibroblast)	Rabbi monoclonal anti-vimentin	1/150, O/N	Goat anti-rabbit 405	1/200, 2h

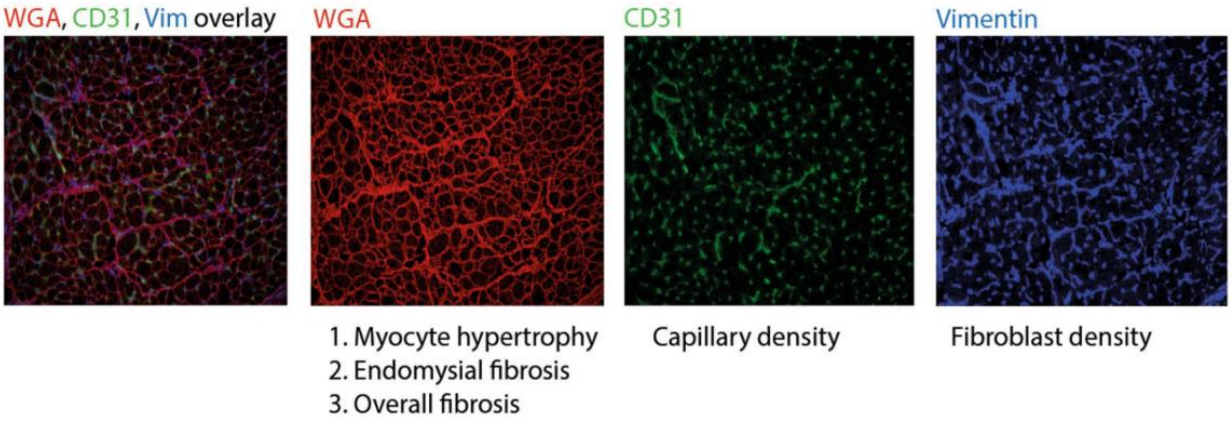


Fig. 2 Triple immunohistochemical staining for the visualization of fibrous structures, endothelial cells and fibroblasts. Optimal contrast between three fluorescent components allows to study the spatial correlation between fibrous tissue (red, WGA), endothelial cells (green, CD31/GSI-B4) and fibroblasts (vimentin).

Microscopy

Sections were imaged using a Leica DM4B microscope with a Leica MC170 HD camera. WGA, GS-IB4/ CD31 and vimentin were visualized using Leica filter cubes A (bandpass, BP, 340-380nm), N2.1 (BP515-560nm) and I3 (BP450-490nm), respectively. Only areas where myocytes were sectioned approximately transversely were selected and photographed for further analysis.

Automated quantification

To perform a standardized, automated analysis of structural remodeling, JavaCyte was developed for the public domain image analysis platform Fiji (www.fiji.sc), an extended version of ImageJ. Output files with the position and dimensions of all structures recognized by the algorithms are stored as comma separated value (csv) files, compatible with most statistical packages, for further analysis. The code of JavaCyte will be made available as an open source at GitHub.

Fibrosis, myocyte size and myocyte dissociation index, clustering coefficient

A Phansalkar's algorithm for automatic local thresholding was used to delineate WGA-positive pixels (Fig. 3a,b). The total area of fibrosis was calculated as the fraction of WGA-positive pixels to the total pixel count. Next, the original WGA-images were filtered using a Gaussian blur function to reduce noise. For each image, the average contrast between WGA-positive and -negative pixels was used to obtain the 'optimal prominence' setting for cardiomyocyte detection using Fiji's built-in 'segment particles' function to determine local minima in fluorescence. Most of the recognized local minima are myocytes, but some local minima represent small dark patches within larger regions of fibrosis. To reduce the number of false positive structures, the pixel intensity directly surrounding local minima was determined. Local minima for which the surrounding pixel values where in the red spectrum were rejected as a cardiomyocyte and were masked. For the remaining local minima, Voronoi watershedding and particle analysis was applied. Myocyte size for each object was calculated as the minimal Feret diameter. For each detected myocyte, all directly neighboring myocytes were defined. A profile plot of the line selection between the local minima of each pair of neighboring myocytes was generated. The thickness of the ECM in between myocytes (i.e. endomysial collagen septa) was calculated as a measure of endomysial fibrosis (Fig. 3c-e).

As an extension of the method in human samples, a cardiomyocyte dissociation index (CDI) was obtained for each cell by determining the fraction of inter-cardiomyocyte distances that exceeded the mean value measured in CVRP- patients with an indication for CABG surgery, i.e. the 'healthiest' patients in our study population, by more than two standard deviations. Distribution of CDI was visualized for each image as a heat map (white cells are closely apposed to neighbors while dark red cells are isolated from neighbors, Fig. 3f). Furthermore, clustering of enhanced inter-myocyte distances was tested in analogy with the local clustering coefficient, as described in graph theory. Myocytes separated by a larger than normal area of endomysial fibrosis are connected in a clique. The

clustering coefficient of myocytes in a clique is enhanced. The impact of augmented clustering coefficients in a clique directly corresponds to the size of the clique. The average clustering coefficient of all myocytes in an image was measured using Matlab. Permutation testing was applied to calculate the expected clustering coefficient in the case of a completely random distribution of inter-myocyte distances measured in the image. The mean of 1000 permutations defined the expected clustering coefficient. Furthermore, the proportion of permuted clustering coefficients smaller than the observed clustering coefficient was defined.

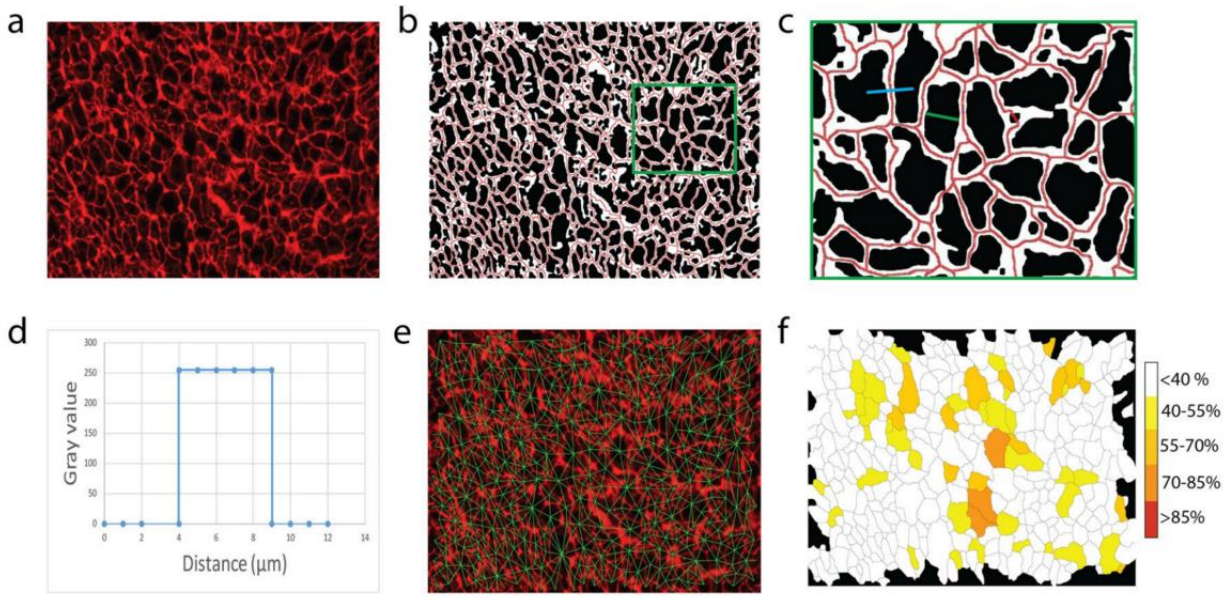


Fig. 3 Analysis pipeline of WGA images applying JavaCyte. a) Original image following WGA staining. b) Phansalkar thresholding of a WGA image. ECM is represented in white, cardiomyocytes in black. c) For each cardiomyocyte, minimal Feret diameter (green) is determined as a measure for size. Neighbors are detected. Local minima of neighboring cells are connected with a line selection (yellow). d) Pixel values across the line selection are plotted. The width of the profile plot corresponds to the width of the endomysial septum between two neighboring cardiomyocytes. e) A control image is generated for visual inspection of accuracy. f) For each cell, cardiomyocyte dissociation index (CDI) is visualized as a measure for fibrosis surrounding the cell.

Capillary density and size

The number of capillaries was obtained by counting CD31 or GSIB4-positive structures using a particle analysis function after applying a Gaussian blur and Landini's [14] Hue-Saturation-Brightness (HSB)-based color threshold. A minimal size threshold of 1.5µm² was used to reduce noise. For each image, capillary density was calculated as the number of capillaries per myocyte. For the

determination of capillary size, a circularity filter of 0.35 was used to select transversely cut capillaries prior to calculations of the minimal Feret diameter (Fig. 4).

Fibroblast density

Vimentin positive objects were selected applying Landini's color threshold [13]. Vimentin shows some cross-reactivity to endothelial cells [18], which was confirmed by overlaying thresholded GS-I4B/ CD31 and vimentin images. For analysis of fibroblast density, we therefore subtracted the thresholded GS-I4B/ CD31 images from the thresholded vimentin images. For each image, the number of fibroblasts per myocyte was calculated as a measure for fibroblast density (Fig. 4).

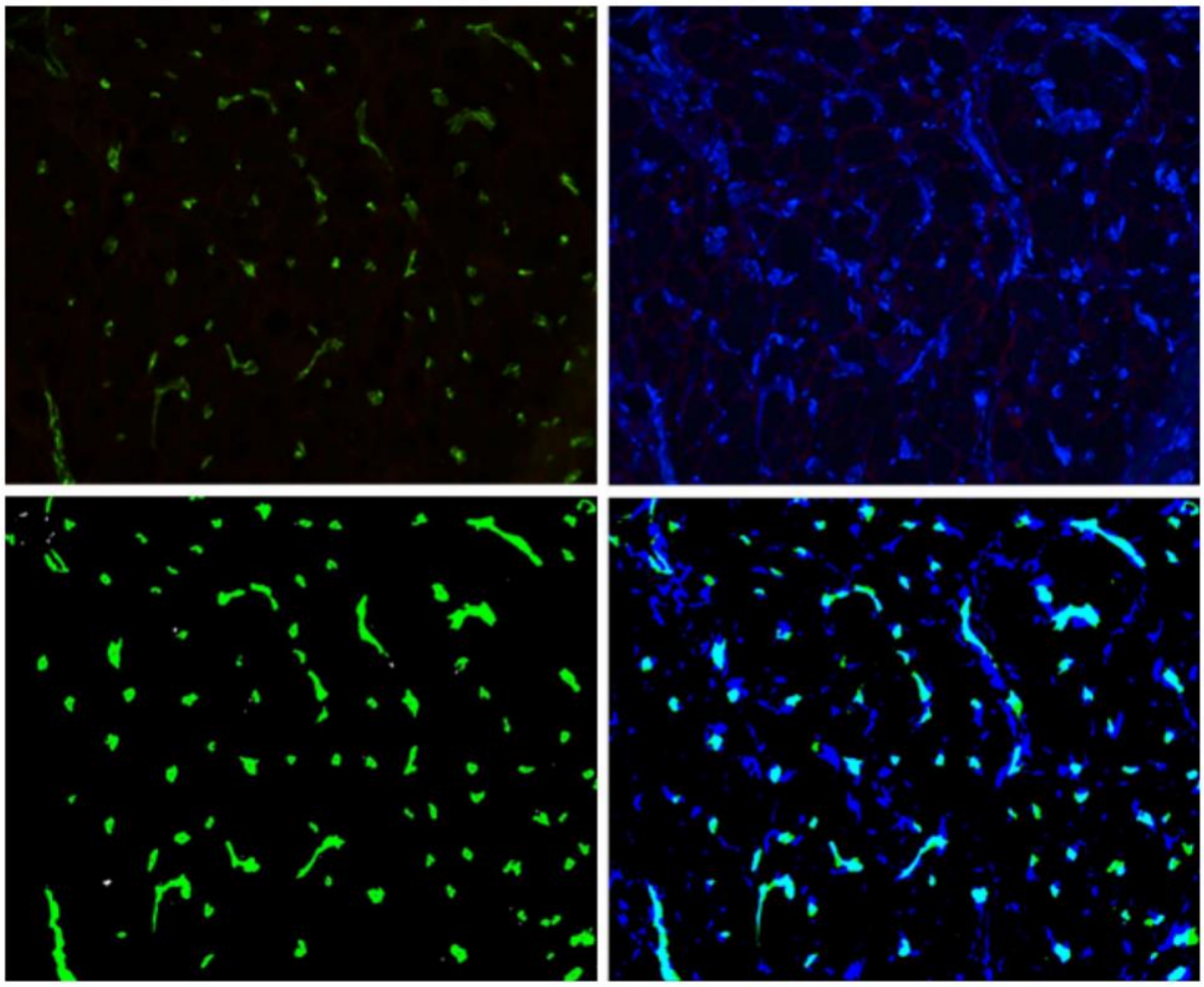


Fig. 4 Analysis pipeline of CD31/GSI-B4 and vimentin images applying JavaCyte. CD31/GSI-B4 positive objects (top left) and vimentin positive objects (top right) are segmented (bottom left and bottom right) according to Landini's algorithm for HSB thresholding. Capillary count is determined. Capillary size is obtained for objects that meet circularity requirements. Non-circular objects are ignored in size measurements, but are counted for determination of the total number. Fibroblast count is obtained after correction for cross-reactive endothelial vimentin staining.

Validation and performance measures

Performance measures were obtained by comparing automated results to data obtained through manual segmentation and measurement. In a first stage, object recognition was tested by quantifying the number of true positive (TP), false positive (FP) and false negative (FN) objects in human atrial samples. True positive denotes the number of manually identified myocytes or capillaries that were recognized by the algorithm. False negative depicts the number of manually identified structures that were not recognized by the algorithm. Performance was analyzed by calculation of sensitivity, precision, false negative rate (FNR) and F1 score, defined by the following formulas:

$$\text{Sensitivity} = \frac{\text{TP}}{\text{TP} + \text{FN}}$$

$$\text{Precision} = \frac{TP}{TP + FP}$$

$$FNR = \frac{FN}{FN + TP}$$

$$F1 = \frac{2TP}{2TP + FP + FN}$$

Normal distribution of count data was confirmed with a Shapiro-Wilk's test. The assumption of homoscedasticity was tested by obtaining a spread-versus-level plot in the statistical program R. Next, correlation between the manually obtained and automated count for myocytes and capillaries was tested applying Pearson's correlation test. Further validation of optimal object recognition included a second stage where area and minimal Feret diameter of matched truly positive objects was compared. Each manually detected myocyte was assigned to an automatically detected myocyte based on the minimal distance between centroids (analogous to maximal matching described by graph theory), as measured by the following formula:

$$d = \sqrt{\Delta Cx^2 + \Delta Cy^2}$$

The percentage of deviation of the area and minimal Feret values of automatically recognized objects from manually obtained measurements was calculated and plotted in a Bland-Altman curve. Once optimal myocyte recognition had been achieved, correlation between median inter-myocyte distances obtained manually and by applying the algorithm was tested.

Inter-observer variation

Sampling variation between two observers was quantified by independently taking 10 photographs per cardiac sample of 10 unique patients. Further analysis was carried out using JavaCyte. Variation in inter-myocyte distance was visualized per sample. To compare observers, a two-way mixed, absolute agreement intra-class correlation test was performed.

Statistics

The open source software environment for statistical computing, 'R' (www.r-project.org), was used for all statistical analysis. For each tissue sample, a minimum of three independent images was obtained, while the operator was blinded to the experimental group or patient group. For analysis of endomysial fibrosis, cardiomyocyte size, CDI and capillary size, the median value per image was calculated. Differences were tested using a mixed-effects model. For analysis of goat samples, the models contained the fixed-effect variables 'sublayer (endocardium/epicardium)', 'group (Sham/ST-AF/LT-AF/AVB)' and the interaction term 'sublayer*group'. The factor 'goat study number' was included as a random-effect variable. For analysis in human samples the models included the fixed-effect factor 'group (CVRP+/CVRP-)' and the random-effect 'matched pair_ID' to identify matched patients.

Results

Workflow

We developed a suite of algorithms for the automated analysis of the previously described features of myocardial tissue structure, JavaCyte, as a plug-in tool for the commonly used image analysis environment Fiji. We recommend that images for analysis are taken at the same magnification (100 to 400x) and with similar illumination and exposure, preferably using the same microscope and camera for all images. The program has been successfully tested for jpg, tiff and bmp image formats, but will work in principle for all standard image formats that can be imported into ImageJ. At the start of image analysis, the user is prompted to enter the resolution (in pixels per millimeter). The user can specify entire folders of images to be analyzed per 'image color' (red for WGA, green for CD31/GSIB4, blue for vimentin), and one output folder per analyzed parameter. After specification of the desired analysis, quantification of endomysial fibrosis, CDI, total ECM content, myocyte size and count, capillary size and count, and fibroblast count can be performed simultaneously. The program will produce feedback throughout the analysis phase regarding the percentage of images analyzed. As no manual input is needed during the automated analysis phase, the program can run unattended.

In the output folders, one output image is stored for each original image showing thresholded images of the recognized structures (figure 3E). For WGA images, the locations where myocyte size and myocyte-to-myocyte distances were measured are indicated. This allows the user to inspect each analyzed image in order to detect potential recognition problems. In addition, numerical data is written to .csv files, with individual measurements of the location and size of the recognized structures. These files can be directly imported for further statistical analysis in e.g. R or SPSS.

Inter-myocyte distance and myocyte size in goat models of AF

Structural parameters in the epicardial and endocardial layer from the LA free wall of ST-AF (n=7), LT-AF (n=6), AVB (n=6) and sham-operated (n=6) goats were studied. In agreement with our earlier quantification in the same model [19], no significant differences in total ECM content were observed between groups in either of the layers (Fig. 5a). Inter-myocyte distances were analyzed as a measure for endomysial fibrosis. In the epicardial layer, there was significantly more endomysial fibrosis in LT-AF goats than in ST-AF goats (+0.42µm, $p=0.01$) or Sham-operated goats (+0.74 µm, $p<0.001$). Endomysial fibrosis was increased in AVB goats compared to Sham-operated goats (+0.37µm, $p=0.02$), and in LT-AF goats compared toAVB goats (+0.37µm, $p=0.03$).
In addition, bigger myocytes were observed in ST-AF goats (+2.14µm, $p=0.03$) and in LT-AF goats (+2.36µm, $p=0.02$) compared to Sham-operated goats. As expected [18], myocyte diameter was increased in AVB goats compared to Sham-operated goats (+3.47µm, $p<0.001$).

In the endocardial layer, no changes in inter-myocyte distance (Fig. 5b) or minimal Feret diameters were determined, despite the presence of a trend (Fig. 5c). No changes were observed in capillary density or size in either layer (Fig.5d), although the number of capillaries per surface area decreased in the endocardium of LT-AF goats compared to sham-operated goats (-42, p=0.04, results not shown). Fibroblast density was not quantified for these samples. For all parameters analyzed, the direction of change and effect size agreed well between manual and automated quantification (table 2).

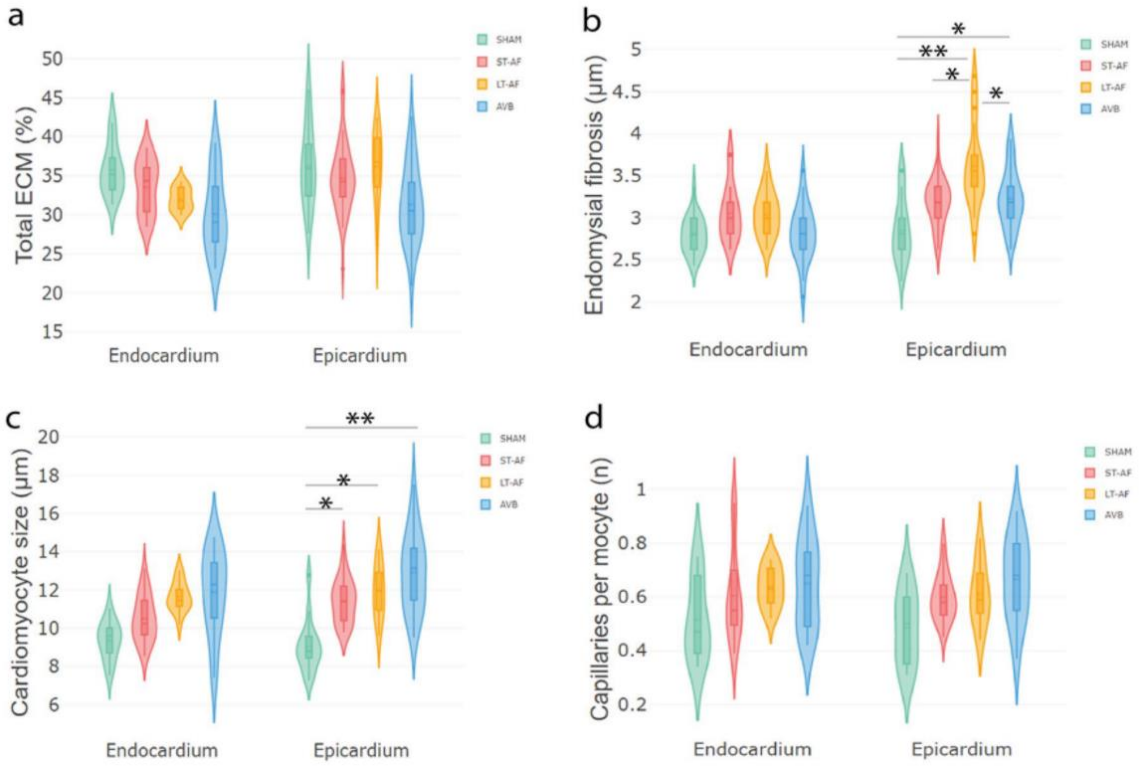


Fig. 5 Increased inter-myocyte distance in LT-AF goats and myocyte hypertrophy in LT-AF goats and AVB goats. a) Total ECM content is similar in Sham-operated goats and goats in ST-AF, LT-AF and AVB. b) Significantly more endomysial fibrosis is observed in the epicardial layer in LT-AF goats (3.61±0.10 µm) than in ST-AF goats (3.19±0.08, p=0.01 µm) or Sham-operated goats (2.87±0.10 µm, p<0.001). There is more endomysial fibrosis in AVB goats (3.24±0.09 µm) than Sham-operated goats (2.87±0.10 µm, p=0.02), and more endomysial fibrosis in LT-AF goats (3.61±0.10 µm) than AVB goats (3.24±0.09 µm, p=0.03). These differences are not present in the endocardium. c) Cardiomyocytes are larger in ST-AF goats (11.50±0.48 µm, p=0.03), LT-AF goats (11.72±0.55 µm, p=0.02) and AVB goats (12.83±0.52 µm, p<0.001) compared to Sham-operated goats (9.36±0.57 µm). d) Capillary density or size did not differ.

Validation of myocyte recognition, myocyte diameter, inter-myocyte distance and capillary count

To validate automated quantification, we compared it to manual quantification of the same images. Pearson's correlation coefficients were calculated to assess the correlation between automated cardiomyocyte count and manually obtained cardiomyocyte counts from human (n=10) atrial samples (Fig 6a,b). A strong positive correlation between both counts was observed ($r=0.94$, $n=10$, $p<0.001$). To further evaluate the accuracy of myocyte recognition in human atrial samples, measures of sensitivity (93.9%±5.5%), precision (95.4%±4.5%), FNR (6.1%±5.5%) and F1-score (94.5%±3.5%) were calculated. These results show high precision in myocyte detection, while maintaining sensitivity. Next, automatically detected cells were matched with manually recognized cells. Minimal Feret diameter of matched truly positive objects was compared (Fig 6b). The mean difference between matched manually and automatically obtained cardiomyocyte diameters situates in the 95% confidence interval [-2.82%, -1.08%], as shown in a Bland-Altman plot (Fig 6b). Furthermore, a positive correlation was observed between median (Fig 6c) inter-myocyte distances measured by the algorithm and manually in human samples ($R=0.98$, $n=10$, $p<0.001$). Comparison of the number of capillaries was studied in CD31 images. A Pearson's correlation coefficient was computed to test the correlation between automated and manually obtained capillary counts, where we also observed a high correlation ($R=0.95$; $n=10$; $p<0.001$). Performance measurements in human atrial samples demonstrated high precision (95.3 ± 3.7%) while maintaining considerable sensitivity (92.0 ± 5.2%). Moreover, JavaCyte showed great time-efficiency as manual measurements for total ECM content, inter-myocyte distance, CDI, cardiomyocyte size and count take up to 2 hours per image for a trained analyst, while JavaCyte functions independently and analysed 141 images in the same time frame on a standard device with an Intel i7 processor and 32GB RAM.

The inter-observer effect related to area selection for imaging was quantified. An intra-class correlation test demonstrated reproducibility between both observers (Fig. 6d). A high degree of reliability was found between both observers (ICC=0.89, n=10, p=0.001).

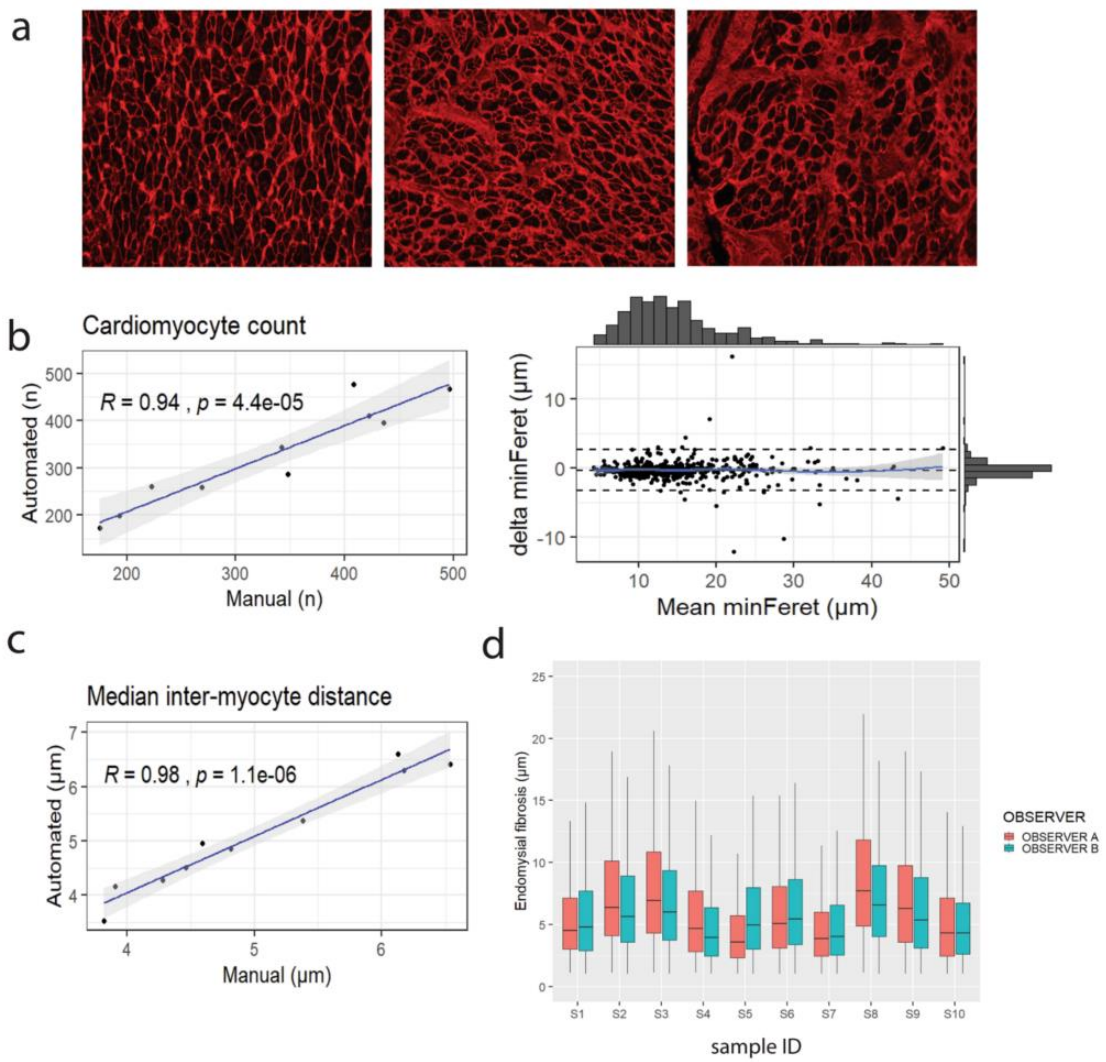


Fig. 6 Two-step validation of JavaCyte algorithm. a) Human tissue is typically more heterogeneous resulting from (unknown) comorbidities. b) Manual observations for myocyte count (R=0.94), correlated strongly to automated results applying JavaCyte. The mean difference in minimal Feret diameter of matched cardiomyocytes is small. c) Manual Median inter-cardiomyocyte distances correlates strongly with measurements made applying JavaCyte. d) Intra-class correlation testing showed no difference between two independent, blinded observers who each acquired 10 unique images per sample of 10 patients (ICC=0.89).

Cardiovascular risk profile as a determinant of atrial tissue structure in patients

Structural characteristics of cardiac tissue samples of matched patients in the CVRP+ and CVRP- groups were compared. No change in total ECM content was observed (Fig. 7a), in contrast to a significant increase in inter-myocyte distance (Fig. 7b) in the CVRP+ group compared to the CVRP- group (+1.90µm, $p<0.001$). Furthermore, myocytes were bigger in CVRP+ patients compared to CVRP- patients (+1.60µm, $p=0.02$) (Fig. 7d). On average, a higher CDI was measured in CVRP+ patients (+9.40 %, $p<0.001$). Moreover, the fraction of cells that was at least 50% dissociated is also higher (fig. 7c) in CVRP+ than CVRP- patients (+12.60 %, $p<0.001$). This expansion of endomysial fibrosis was accompanied by an increase in fibroblast density (+9.20%, $p=0.003$) (Fig. 7f). No change in capillary density (-3.70% $p=0.44$) was observed (Fig. 7e), although absolute capillary counts were lower in CVRP+ patients (-15% , $p=0.04$).

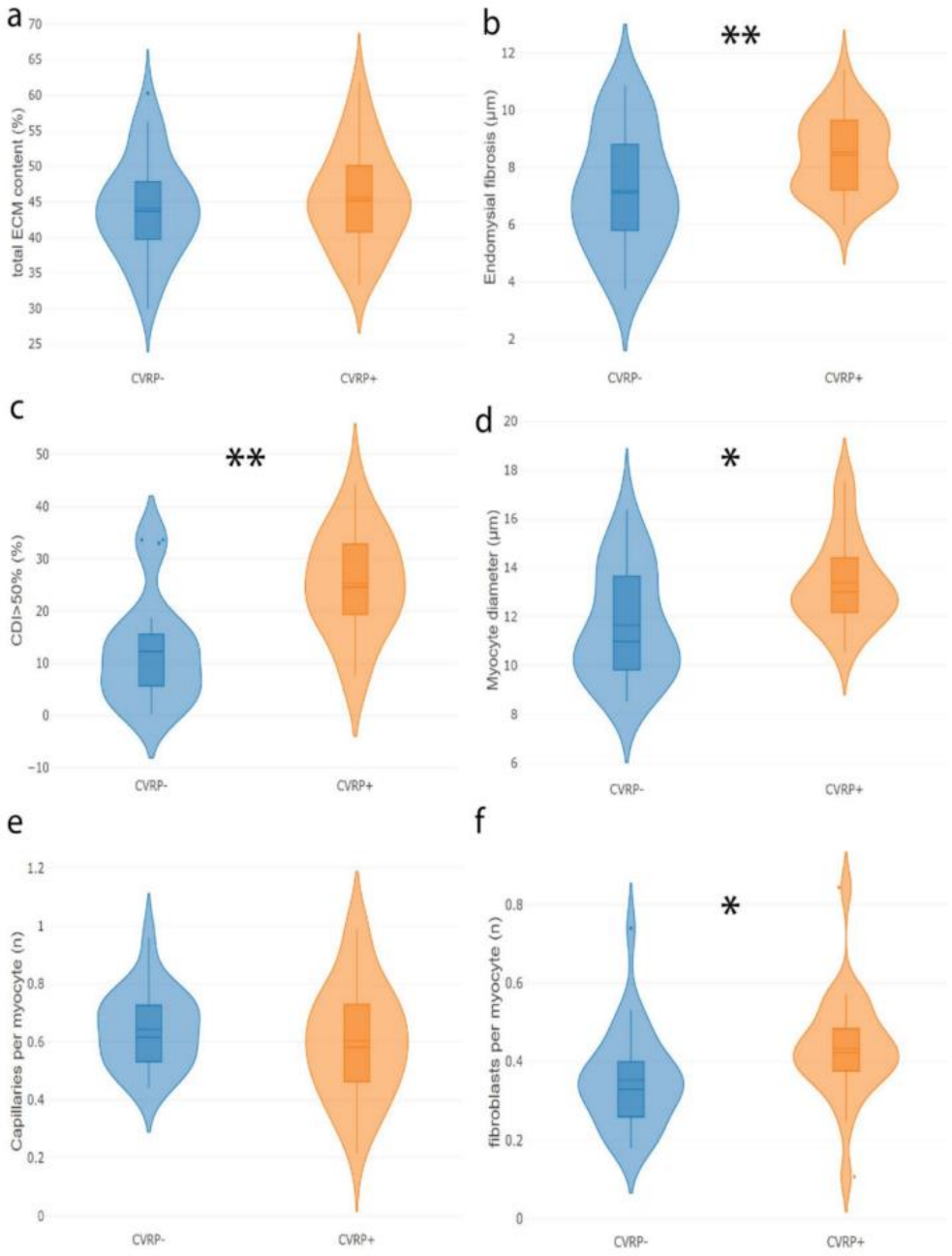


Fig. 7 Features of structural remodeling in CVRP+ compared to CVRP- patients. 22 patients were matched and stratified into two equal groups based on their cardiovascular risk profile (CVRP). a) Total ECM content is similar between the 2 groups. b) Endomysial fibrosis is significantly more present in atrial tissue of CVRP+ patients (+1.90 µm, $p<0.001$). c) The fraction of cells that is at least 50% dissociated from its neighbors (CDI > 50%) is larger in the CVRP+ group (+12.6%, $p<0.001$). d) Tissue of CVRP+ patients shows signs of myocyte hypertrophy compared to CVPR- patients (+1.6 µm, $p=0.02$). e) The number of capillaries per myocyte was similar between both groups. f) The fibroblast-to-myocyte ratio is enhanced in CVRP+ patients compared to CVRP- patients (+9.2%, $p=0.003$).

Clustering of endomysial fibrosis in patients.

Visually, the spatial distribution of fibrous tissue suggested clustering of higher inter-myocyte distances, i.e endomysial fibrosis (Fig. 8a). As an extension of the automated quantification, the degree of clustering of enhanced inter-myocyte distances was studied in both patient groups. The fraction of expected clustering coefficients that was smaller than the observed clustering coefficient was high in the CVRP- (96.5±1.50%) and the CVRP+ (95.7±1.44%) group. This indicates that high values of endomysial fibrosis appear in clusters, regardless of the phenotype of the patient. However, the relative increase of observed clustering coefficients compared to expected values of clustering (Fig. 8b,c) was larger in the CVRP+ group (+14.3 ±1.26%) than in the CVRP- group (+10.0±1.32%, p=0.02), confirming the larger degree of spatial heterogeneity in transverse myocyte separation.

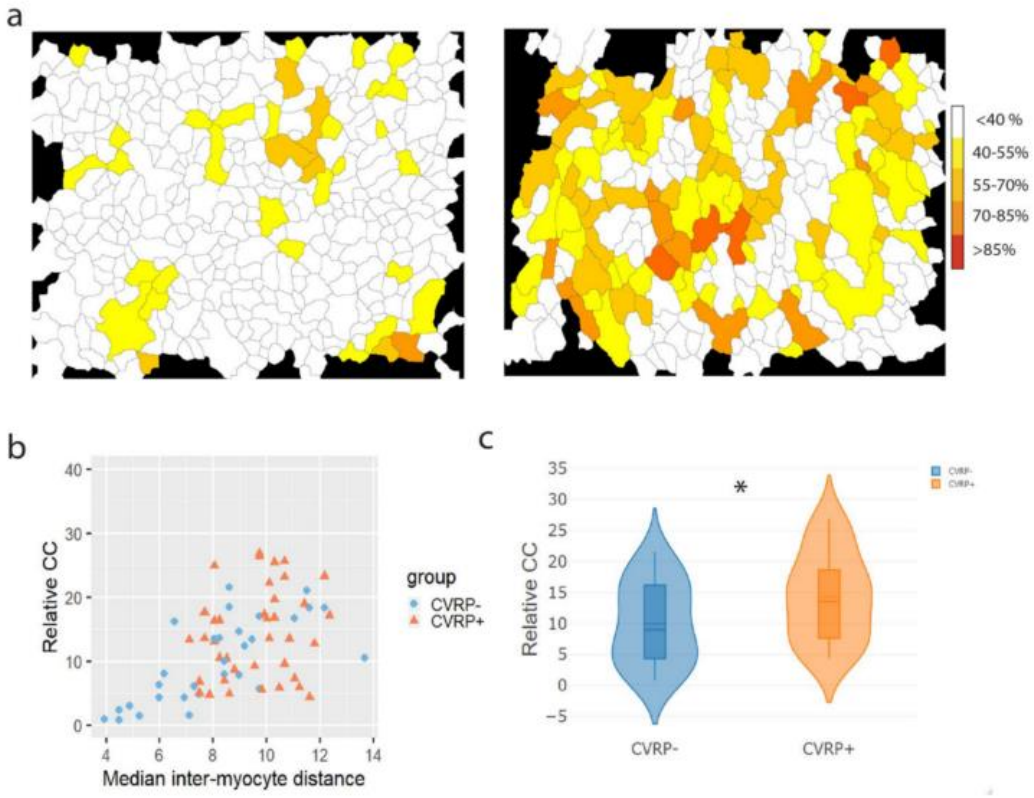


Fig. 8 Clustering of enhanced endomysial fibrosis in CVRP- and CVRP+ patients. a) Heat maps showing spatial distribution of CDI for each cardiomyocyte in an image, representing the degree of surrounding fibrosis. b) Relative deviation in clustering coefficient (CC) from the expected clustering coefficient based on permutation testing. More clustering than expected in CVRP- (p-score=0.965) and CVRP+ (p-score= 0.957) patients. c) The observed CC deviates more relative to the expected CC in CVRP+ patients than in CVRP- patients (+4.3 %, p=0.02).

Discussion

In the present study, simultaneous visualization and automated analysis of multiple features of structural remodeling was successfully applied. Accurate detection of cardiomyocytes and capillaries was confirmed by evaluating performance metrics. Moreover, JavaCyte offers a much faster alternative to characterize myocardial structure objectively, as it no user input is required once it started. In a validation study on goat atrial biopsies, structural properties were visualized in experimental goat models for ST-AF, LT-AF and AV-block. Inter-myocyte distance and myocyte size were increased in LT-AF, validating earlier findings in these goat models [14]. In the AV-block model, an expected increase in myocyte size was observed [20]. Outcomes from the automated quantification agreed well with manual quantification of the same sections.

In addition, applying JavaCyte, no significant inter-observer variability in providing input for automated analysis was detected in a study on human biopsies, which show more heterogeneity in tissue structure than biopsies from the goat models. Application of this novel automated analysis made it possible to compare atrial tissue from patients whose clinical profile suggested an increased risk of atrial remodeling and those whose clinical profile did not. Alterations in atrial tissue structure were detected, including more, and more clustered, endomysial fibrosis, more dissociated cardiomyocytes, proliferation of fibroblasts and cellular hypertrophy. Each of these factors has been proposed to contribute to AF progression. By contrast, similar degrees of overall fibrosis were observed in both groups.

Advantages over traditional methods and validation in animal models

Fluorescent staining and automated analysis using JavaCyte offers several advantages over traditional approaches which apply a multi-step process involving subjective detection thresholds. Poor color contrast in conventional histology between myocytes and particularly endomysial fibrosis limits digital thresholding of images, complicating automated analysis strategies. Manual quantification of fibrosis is slow and more sensitive to larger areas of fibrosis rather than endomysial fibrosis. As a result, reports on the level of fibrosis in animal studies vary widely between and within species. In this study, fibrotic structures were visualized using WGA, a lectin that binds to sialic acid and N-acetylglucosaminyl residues in the cell membrane. WGA was previously described as a tool to stain cardiac sarcolemma and fibrotic structures [21-23], as well as connective tissue and ECM. Many glycosaminoglycans in the ECM contain N-acetylglucosamin, a target of WGA . This staining enabled the detection of increased endomysial fibrosis in LT-AF goats compared to ST-AF goats, particularly in the epicardium [25], which may have been missed using Sirius Red or Trichrome staining. In prior studies using optical mapping, observations of enhanced endomysial fibrosis in LT-AF goats were linked to impaired epicardial wavefront expansion in LT-AF goats compared to ST-AF goats (7). Applying JavaCyte, we have confirmed our earlier findings of increased endomysial thickness in LT-AF goats compared to sham-operated and ST-AF goats in the epicardial layer.

Furthermore, the presence of myocyte hypertrophy was confirmed in LT-AF and AV-block goats compared to Sham-operated animals.

This approach to quantifying myocyte size and the distribution of fibrous tissue is fast, relatively inexpensive, reproducible, suitable for cryosections and allows for the simultaneous visualization of additional structures. Conventional fluorescence microscopy is limited to the detection of three different fluorescent labels at sufficiently distinct wavelengths. We used WGA in combination with staining of capillaries and fibroblasts. However, with minor modifications in the staining protocol and analysis algorithms, this method is also suitable for the quantification of other discrete structures and cell types, such as macrophages, smooth muscle cells and myofibroblasts with the appropriate fluorescent labels. The size and positions of all recognized structures is automatically stored, allowing further statistical analysis of the spatial intercorrelations between different structures.

Part of this potential was employed here by normalizing capillary and fibroblast counts to the number of myocytes in an image. Capillary rarefaction, i.e. a loss of the number of capillaries has been implicated in various disease processes. While a reduced capillary count per unit of surface area implies longer diffusion distances, it is an unreliable indicator for capillary rarefaction with concomitant myocyte hypertrophy. Normalization of capillary counts for the number of myocytes therefore provides important additional information on rarefaction/ angiogenesis. Furthermore, it is possible to study inter-capillary distance to investigate oxygen diffusion distances. This parameter was not analyzed in the current manuscript, but it could be calculated in a straightforward manner from the JavaCyte output files.

Moreover, fibroblasts were visualized applying an antibody directed to vimentin, the major protein in the cytoskeleton of mesenchymal cells. Vimentin-positive structures were corrected for cross-reaction with endothelial cells [26] by subtraction. The application of a myofibroblast-specific marker such as alpha smooth muscle actin was outside the scope of this article, but could be useful to study the degree of fibroblast differentiation.

Initially, the algorithm was validated by comparing the number of automatically identified cardiomyocytes and capillaries to manual counts. The sensitivity, precision, false negative rate and F1 score were calculated as measures of precision. JavaCyte was very sensitive in recognizing cardiomyocytes and capillaries, while maintaining precision. Additionally, cardiomyocyte size and median inter-myocyte distance correlated strongly with manual measurements.

Structural remodeling in patient biopsies

Following validation of JavaCyte in previously characterized goat models, the algorithm was applied to a clinical test case. As a result of multiple underlying comorbidities of unknown, varying durations, atrial tissue structure in patients tends to be more variable and extensive, affording a challenge to test the performance of automated quantification. One of the most important attributes of JavaCyte is standardization and reproducibility of data, independent of the operator. This quality was confirmed

by studying inter-observer variation between 2 individual observers who individually took 10 photographs per sample of 10 unique patients. The images were then analyzed using JavaCyte, eliminating inter-observer variation in the data analysis phase. In this way, the impact of potential bias in area selection during microscopy and photographing of the tissue was assessed. A high degree of similarity between both analysts was observed. Moreover, JavaCyte is capable of analyzing hundreds of images per hour, making it ideally suited for high throughput analysis in large, multi-center trials in a cost-effective and reproducible manner.

In summary, cardiomyocyte size was increased in CVRP+ patients. Enhanced deposition of ECM in between cardiomyocytes was observed in patients with concomitant cardiac conditions that are believed to accelerate structural remodeling of the heart. Organized and accurate quantification of inter-myocyte distance between each pair of myocytes makes it possible to study the spatial distribution of enhanced endomysial fibrosis. In this study, the degree of dissociation of each myocyte from its neighbors was calculated (CDI), reflecting the local amount of surrounding fibrosis. A higher CDI indicated that myocytes are surrounded by more extreme endomysial fibrosis and are thus more isolated from their neighbors. The substantial rise in CDI observed in CVRP+ patients suggests that the observed increase in median inter-myocyte distance results from regions with more extreme endomysial fibrosis, rather than a mild homogenous increase of endomysial fibrosis throughout the tissue. Such a loss of inter-myocyte connections could produce zigzag conduction patterns and promote microreentry [27]. Such patterns of conduction have also previously been associated with aging [28-31]. Following these observations, the degree of clustering of large inter-myocyte distances was calculated. In both patient groups, large values of endomysial fibrosis clustered more often than can be expected by chance, suggesting that extensive endomysial fibrosis tends to localize in clusters. The relative degree in observed clustering compared to expected clustering of endomysial fibrosis was higher in the CVRP+ group than the CVRP- group.

Moreover, a higher fibroblast/myocyte ratio was observed in CVRP+ patients, which could imply more opportunities for electrotonic interaction between these cell types. Although a smaller number of capillaries was observed in atrial appendages of CVRP+ patients compared to CVRP- patients, the number of capillaries per myocyte and the size of these capillaries did not differ. This suggests that, although oxygen diffusion distances may have increased, capillary rarefaction does not occur under these circumstances.

Conclusion

Here, we provide a flexible and expandable, open source tool that is well-suited for the accurate characterization of myocardial structure including the quantification of fibrous tissue distribution, myocyte hypertrophy, fibroblast density, capillary density and size, and the spatial interrelations between these features. Compared to conventional analysis, our method is highly time- and cost-efficient, and largely eliminates observer bias and inter-observer variability.

Limitations

The analysis algorithms were developed for the quantification of structural features in regions where myocytes and capillaries are sectioned transversely. Although conduction is most rapid in the longitudinal direction of myocyte bundles, longitudinal conduction is affected less by structural remodeling. Several studies have highlighted the importance of transverse electrical uncoupling resulting from endomysial fibrosis to the discontinuous conduction and microreentry . In addition, interstitial/ endomysial fibrosis is a major determinant for decreased myocardial compliance and diastolic dysfunction .

Within the regions used for analysis, myocytes and capillaries were approximately, rather than exactly, transversely sectioned. For these structures, using the maximal width would represent a variable and potentially large overestimation of size. To minimize this inaccuracy, the algorithm uses the minimal Feret diameter as a measure for myocyte and capillary size. This results in a systematic but small underestimation of actual myocyte and capillary sizes, which should be similar between study groups.

Here, we have tested the method in atrial biopsies from diverse animal models (goats, pigs and horses) and human patients, but we expect that the validity and performance will be similar in transversely sectioned tissue from ventricular and skeletal muscle.

CVRP+ patients were diagnosed with both persistent AF and heart failure. The pathologies responsible for heart failure in these patients were variable. It is not possible to disentangle whether the differences in tissue structure compared to CVRP- patients can be attributed to the effects associated with (end-stage) heart failure, underlying pathologies inducing heart failure, AF, or a combined synergistic effect. The impact of varying clinical profiles in distinct groups of patients should be studied in a larger, more extensively subclassified and phenotyped cohort of patients. Furthermore, the tool provided here could be used to study pathogenesis of pro-fibrotic remodeling in such a study, for example by linking histological features to mRNA and protein expression profiles.

Competing interests

The author(s) declare no competing interests.

Acknowledgments/Funding

This study was supported by a Grant from the Netherlands Heart Foundation (CVON2014-09, RACE V: Reappraisal of Atrial Fibrillation: Interaction between hypercoagulability, Electrical remodeling, and Vascular Destabilisation in the Progression of AF) and a Grant from the EU (CATCH ME Horizon 2020, EU-H2020-PHC-RIA (633196)).

Tables

Table 1

	CVRP-	CVRP+	p-value
Age (yrs)	64 (±7.6)	63 (±5.8)	0.66
Sex (F/M)	1/10	1/10	1.00
BMI	26 (±3.7)	27 (±3.8)	0.54
Rhythm (pers. AF)	0 (0%)	11 (100%)	<0.001
Heart Failure	0 (0%)	11 (100%)	<0.001
EF (%)	61 (±10)	30 (±12)	< 0.001
NYHA	1.3 (±1.2)	2.8 (±1.3)	0.01
Indication for surgery			<0.001
• CABG	7 (64%)	0 (0%)	
• Donor	1 (9%)	0 (0%)	
• HTX	0 (0%)	10 (46 %)	
• MVD	3 (27%)	1 (9. %)	
Hypertension	6 (55%)	6 (55%)	1.00
Location (LAA/RAA)	7 (64%) / 4 (36%)	7 (64%) / 4 (36%)	1.00

Distribution of clinical parameters of patients with and without a cardiovascular risk profile for structural remodeling (CVRP). A chi-square test of independence is used for categorical variables, and a t-test for continuous variables. BMI body mass index, EF ejection fraction, CABG coronary artery bypass graft, HTX heart transplant xenograft, MVD mitral valve disease, LAA/RAA lef/right atrial appendage.

Table 2

	Cardiomyocyte diameter		Inter-myocyte distance		Capillary density	
	Manual (µm)	JavaCyte (µm)	Manual (µm)	JavaCyte (µm)	Manual	JavaCyte
SHAM	9.69±1.70	9.36±0.57	2.54±0.47	2.87±0.10	0.48±0.13	0.47±0.06
ST-AF	11.83±1.53	11.50±0.48	2.72±0.62	3.19±0.08	0.57±0.02	0.59±0.04
LT-AF	12.65±2.98	11.72±0.55	3.64±0.45	3.61±0.11	0.67±0.02	0.60±0.05
AVB	13.98±1.97	12.83±0.52	3.12±0.39	3.24±0.09	0.68±0.04	0.65±0.04

Manual and automated analysis of cardiomyocyte diameter, inter-myocyte distance and capillary density in goat models for AF and AV block (AVB). Values are represented as mean ± SD in µm. ST-AF short term AF. LT-AF long term AF.

References

1. Piek A, Sillje HHW, de Boer RA. The vicious cycle of arrhythmia and myocardial fibrosis. Eur J Heart Fail. 2019;21(4):492-4.
2. Frangogiannis NG. Cardiac fibrosis: Cell biological mechanisms, molecular pathways and therapeutic opportunities. Mol Aspects Med. 2019;65:70-99.
3. Burstein B, Nattel S. Atrial fibrosis: mechanisms and clinical relevance in atrial fibrillation. J Am Coll Cardiol. 2008;51(8):802-9.
4. Weber KT, Pick R, Jalil JE, Janicki JS, Carroll EP. Patterns of myocardial fibrosis. J Mol Cell Cardiol. 1989;21 Suppl 5:121-31.
5. Kawara T, Derksen R, de Groot JR, Coronel R, Tasseron S, Linnenbank AC, et al. Activation delay after premature stimulation in chronically diseased human myocardium relates to the architecture of interstitial fibrosis. Circulation. 2001;104(25):3069-75.
6. Verheule S, Tuyls E, Gharaviri A, Hulsmans S, van Hunnik A, Kuiper M, et al. Loss of continuity in the thin epicardial layer because of endomysial fibrosis increases the complexity of atrial fibrillatory conduction. Circ Arrhythm Electrophysiol. 2013;6(1):202-11.
7. Chen W, Frangogiannis NG. The role of inflammatory and fibrogenic pathways in heart failure associated with aging. Heart Fail Rev. 2010;15(5):415-22.
8. Bench T, Burkhoff D, O'Connell JB, Costanzo MR, Abraham WT, St John Sutton M, et al. Heart failure with normal ejection fraction: consideration of mechanisms other than diastolic dysfunction. Curr Heart Fail Rep. 2009;6(1):57-64.
9. Krul SP, Berger WR, Smit NW, van Amersfoorth SC, Driessen AH, van Boven WJ, et al. Atrial fibrosis and conduction slowing in the left atrial appendage of patients undergoing thoracoscopic surgical pulmonary vein isolation for atrial fibrillation. Circ Arrhythm Electrophysiol. 2015;8(2):288-95.
10. Kohl P, Camelliti P, Burton FL, Smith GL. Electrical coupling of fibroblasts and myocytes: relevance for cardiac propagation. J Electrocardiol. 2005;38(4 Suppl):45-50.
11. Quinn TA, Camelliti P, Rog-Zielinska EA, Siedlecka U, Poggioli T, O'Toole ET, et al. Electrotonic coupling of excitable and nonexcitable cells in the heart revealed by optogenetics. Proc Natl Acad Sci U S A. 2016;113(51):14852-7.
12. Wiegerinck RF, Verkerk AO, Belterman CN, van Veen TA, Baartscheer A, Opthof T, et al. Larger cell size in rabbits with heart failure increases myocardial conduction velocity and QRS duration. Circulation. 2006;113(6):806-13.
13. Spach MS, Heidlage JF, Barr RC, Dolber PC. Cell size and communication: role in structural and electrical development and remodeling of the heart. Heart Rhythm. 2004;1(4):500-15.
14. Spach MS, Heidlage JF, Dolber PC, Barr RC. Electrophysiological effects of remodeling cardiac gap junctions and cell size: experimental and model studies of normal cardiac growth. Circ Res. 2000;86(3):302-11.
15. Opacic D, van Bragt KA, Nasrallah HM, Schotten U, Verheule S. Atrial metabolism and tissue perfusion as determinants of electrical and structural remodelling in atrial fibrillation. Cardiovasc Res. 2016;109(4):527-41.
16. D'Amario D, Migliaro S, Borovac JA, Restivo A, Vergallo R, Galli M, et al. Microvascular Dysfunction in Heart Failure With Preserved Ejection Fraction. Front Physiol. 2019;10:1347.
17. Emde B, Heinen A, Godecke A, Bottermann K. Wheat germ agglutinin staining as a suitable method for detection and quantification of fibrosis in cardiac tissue after myocardial infarction. Eur J Histochem. 2014;58(4):2448.
18. Verheule S, Tuyls E, van Hunnik A, Kuiper M, Schotten U, Allessie M. Fibrillatory conduction in the atrial free walls of goats in persistent and permanent atrial fibrillation. Circ Arrhythm Electrophysiol. 2010;3(6):590-9.

19. Neuberger HR, Schotten U, Verheule S, Eijsbouts S, Blaauw Y, van Hunnik A, et al. Development of a substrate of atrial fibrillation during chronic atrioventricular block in the goat. Circulation. 2005;111(1):30-7.
20. Landini G, Randell DA, Fouad S, Galton A. Automatic thresholding from the gradients of region boundaries. J Microsc. 2017;265(2):185-95.
21. Franke WW, Schmid E, Osborn M, Weber K. Different intermediate-sized filaments distinguished by immunofluorescence microscopy. Proc Natl Acad Sci U S A. 1978;75(10):5034-8.
22. Kostrominova TY. Application of WGA lectin staining for visualization of the connective tissue in skeletal muscle, bone, and ligament/tendon studies. Microsc Res Tech. 2011;74(1):18-22.
23. Ohno J, Tajima Y, Utsumi N. Binding of wheat germ agglutinin in the matrix of rat tracheal cartilage. Histochem J. 1986;18(10):537-40.
24. Soderstrom KO. Lectin binding to collagen strands in histologic tissue sections. Histochemistry. 1987;87(6):557-60.
25. Spach MS, Boineau JP. Microfibrosis produces electrical load variations due to loss of side-to-side cell connections: a major mechanism of structural heart disease arrhythmias. Pacing Clin Electrophysiol. 1997;20(2 Pt 2):397-413.
26. Spach MS, Dolber PC. Relating extracellular potentials and their derivatives to anisotropic propagation at a microscopic level in human cardiac muscle. Evidence for electrical uncoupling of side-to-side fiber connections with increasing age. Circ Res. 1986;58(3):356-71.
27. Koura T, Hara M, Takeuchi S, Ota K, Okada Y, Miyoshi S, et al. Anisotropic conduction properties in canine atria analyzed by high-resolution optical mapping: preferential direction of conduction block changes from longitudinal to transverse with increasing age. Circulation. 2002;105(17):2092-8.

6 Chapter VI - Results: Male sex hormone and reduced plakoglobin jointly impair atrial conduction and cardiac sodium currents

Preprint 1. This preprint is available on biorXiv.

Male sex hormone and reduced plakoglobin jointly impair atrial conduction and cardiac sodium currents.

Sommerfeld LC, Holmes AP, Yu TY, O'Shea C, Kavanagh DM, Pike JM, Wright T, Syeda F, Aljehani A, Kew T, Cardoso VR, Kabir SN, Hepburn C, Menon PM, Broadway-Stringer S, O'Reilly M, Witten A, Fortmueller L, Lutz S, Kulle A, Gkoutos GV, Pavlovic D, Arlt W, Lavery GG, Steeds R, Gehmlich K, Stoll M, Kirchhof P, Fabritz L. *biorXiv. 2022, doi: 10.1101/2022.06.03.494748*

Author contributions in preprint 1

I performed murine in vivo experiments (Echocardiography and ECG), super-resolution microscopy (dSTORM) experiments in atrial cardiomyocytes and cluster analysis with a custom-designed script, gravimetry of the mice and hearts and atrial histology analysis, RNAseq analysis visualization, P wave analysis in human ECGs from ARVC patients and unaffected controls and wrote the manuscript together with co-authors.

Male sex hormone and reduced plakoglobin jointly impair atrial conduction and cardiac sodium currents

Laura C. Sommerfeld[1,2,3], Andrew P. Holmes[1,4], Ting Y. Yu[1,5], Christopher O'Shea[1,5], Deirdre M. Kavanagh[1,6], Jeremy M. Pike[1,6], Thomas Wright[1], Fahima Syeda[1], Areej Aljehani[1], Tania Kew[1], Victor R. Cardoso[1,7], S. Nashitha Kabir[1], Claire Hepburn[1], Priyanka M. Menon[1], Sophie Broadway-Stringer[1], Molly O'Reilly[1], Anika Witten[8,9], Lisa Fortmueller[2,3], Susanne Lutz[11], Alexandra Kulle[12], Georgios V. Gkoutos[7,13,14], Davor Pavlovic[1], Wiebke Arlt[15], Gareth G. Lavery[15], Richard Steeds[1,16], Katja Gehmlich[1], Monika Stoll[8,9,10], Paulus Kirchhof[1,3,17], & Larissa Fabritz[1,2,3]

[1]Institute of Cardiovascular Sciences, University of Birmingham, UK

[2]University Center of Cardiovascular Science, University Heart and Vascular Center, UKE Hamburg, Germany

[3]German Center for Cardiovascular Research (DZHK), Standort Hamburg/Kiel/Lübeck, Germany

[4]School of Biomedical Sciences, Institute of Clinical Sciences, University of Birmingham, UK

[5]Research and Training Centre in Physical Sciences for Health, Birmingham, UK

[6]Centre of Membrane Proteins and Receptors (COMPARE), University of Birmingham, UK

[7]Institute of Cancer and Genomic Sciences, University of Birmingham, UK

[8]Genetic Epidemiology, Institute for Human Genetics, University of Münster, Germany

[9]Core Facility Genomics of the Medical Faculty, University of Münster, Germany

[10]Cardiovascular Research Institute Maastricht, Department of Biochemistry, Maastricht University, The Netherlands

[11]Institute of Pharmacology and Toxicology, University Medical Center Göttingen, Germany

[12]Division of Paediatric Endocrinology and Diabetes, University Hospital Schleswig-Holstein, Campus Kiel, Germany

[13]Institute of Translational Medicine, University Hospitals Birmingham NHS Foundation Trust, Birmingham, UK

[14]MRC Health Data Research UK (HDR), Midlands Site, UK

[15]Institute of Metabolism and Systems Research (IMSR) University of Birmingham, UK & Centre for Endocrinology, Diabetes and Metabolism (CEDAM), Birmingham Health Partners

[16]Department of Cardiology, University Hospitals Birmingham NHS Foundation Trust, Birmingham, UK

[17]Department of Cardiology, University Heart & Vascular Center Hamburg, University Medical Center Hamburg-Eppendorf, Hamburg, Germany

Corresponding author:

Professor Larissa Fabritz

University Center of Cardiovascular Science

University Heart and Vascular Center, UKE Hamburg

Hamburg, Germany

Conflicts of interest

The authors have declared no direct conflict of interest in regards to the manuscript.

L.F. has received institutional research grants from governmental and charity funding agencies and several biomedical companies.

P.K. has received research support from several drug and device companies active in atrial fibrillation and has received honoraria from several such companies in the past.

L.F. and P.K. are listed as inventors on two patents held by University of Birmingham (Atrial Fibrillation Therapy WO 015140571, Markers for Atrial Fibrillation WO 2016012783).

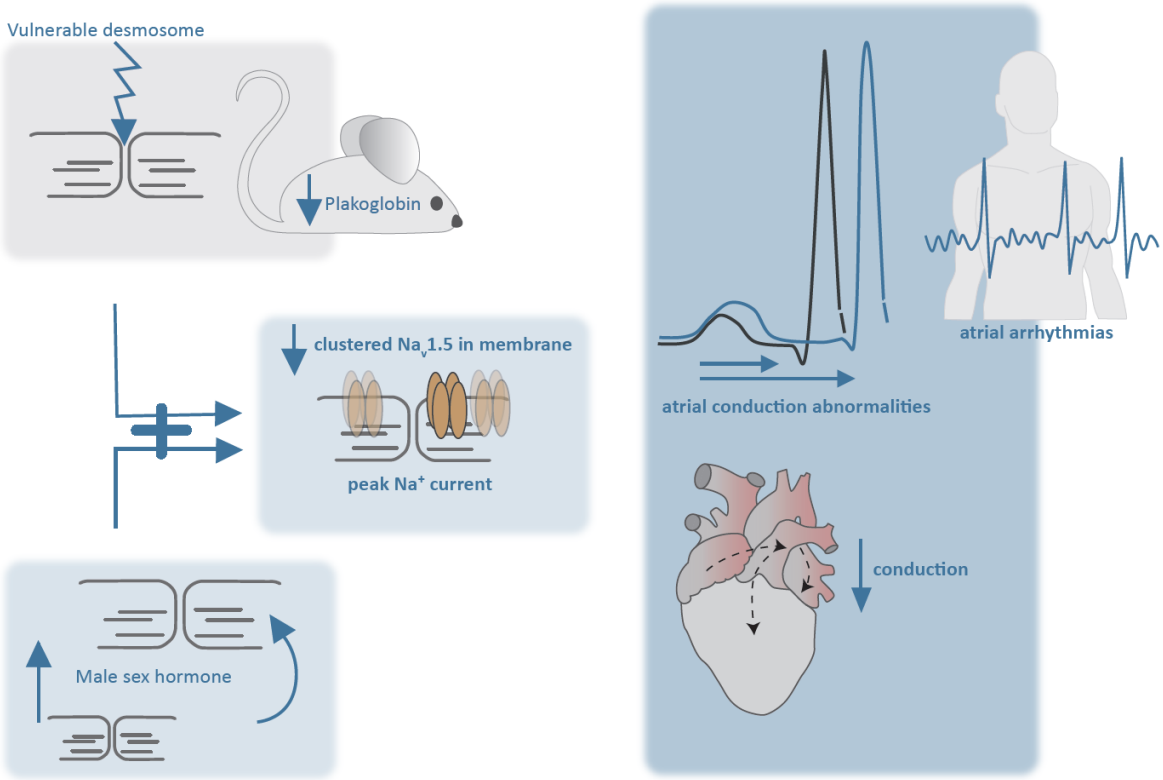
Word count: 11425 (all text inclusive of title page, full text, references, figure legends and tables)

Abstract

Androgenic anabolic steroids (AAS) are commonly abused by young men. Male sex associates with earlier manifestation of common and rare cardiac conditions including atrial fibrillation and arrhythmogenic right ventricular cardiomyopathy (ARVC). Clinical data suggest an atrial involvement in ARVC. The disease is caused by desmosomal gene defects such as reduced plakoglobin expression. Analysis of clinical records from 146 ARVC patients identified male preponderance and increased prevalence of atrial arrhythmias in definite vs non-definite cases. Definite patients displayed ECG changes suggesting atrial remodelling. To study mechanisms of atrial remodelling due to desmosomal vulnerability and AAS, young adult male mice, heterozygously deficient for plakoglobin ($Plako^{+/-}$) and wildtype (WT) littermates, were chronically exposed to 5α-dihydrotestosterone (DHT) or placebo. DHT increased atrial expression of pro-hypertrophic, fibrotic and inflammatory transcripts. DHT caused conduction slowing, decreased peak sodium current density, reduced action potential amplitude and lowered the peak depolarisation rate in $Plako^{+/-}$ but not WT left atria. Super-resolution microscopy revealed a reduction in $Na_v1.5$ clustering in $Plako^{+/-}$ atrial cardiomyocytes following DHT exposure. These data reveal that AAS combined with plakoglobin deficiency cause pathological atrial electrical remodelling in young male hearts. AAS abuse may increase the risk of atrial myopathy in males with desmosomal gene variants.

Key words: desmosome, testosterone, cardiac atria, conduction velocity, $Na_v1.5$, ARVC

Graphical abstract



Introduction

Several inherited arrhythmia syndromes develop more severe phenotypes in men carrying pathogenic variants, e.g. Brugada syndrome or Arrhythmogenic Right Ventricular Cardiomyopathy (ARVC) (1). Male sex also associates with greater incidence of atrial arrhythmias, both in the general population and in rare conditions (2-7). Effects mediated by anabolic androgenic steroids (AAS) such as testosterone and the most potent androgen, 5α-dihydrotestosterone (DHT), could contribute. Abuse of AAS is an emerging global health concern, not restricted to elite athletes but common in the general population, with reports indicating a 3.3% lifetime prevalence worldwide (8). AAS are abused predominately by men to increase muscle mass, improve athletic performance and alter appearance (8). However, AAS can cause cardiac pathology, including hypertrophy and electrophysiological changes (9-14). Atrial arrhythmias have recently been associated with elevated total plasma testosterone levels in men (15) and observed in patients known to take AAS devoid of a clinical indication (16-18). Despite these observations, the mechanisms underpinning cardiac electrical remodelling in response to higher levels of AAS are largely unknown.

ARVC has recently been reported to show more adverse outcomes in men (19) related to sex hormone levels (20). Emerging evidence suggests increased incidence of atrial arrhythmias in cardiomyopathies (21). ARVC is often caused by variants in desmosomal genes including plakoglobin (22-25). Plakoglobin is located in desmosomal junctional complexes where it stabilizes cell-cell contacts (26), thereby maintaining mechanical and electrical integrity of the myocardium.

We hypothesized that a substantial proportion of ARVC patients is suffering from clinically relevant atrial arrhythmias and that vulnerability of the desmosome, caused by e.g. plakoglobin reduction, may increase the risk of male sex hormone-induced atrial electrical remodelling.

To test this hypothesis, we screened patient records for atrial arrhythmias from definite and non-definite ARVC patients seen at a tertiary center inherited cardiac conditions clinic. We

furthermore employed a murine ARVC model to study the effects of chronically elevated AAS levels in male mice with heterozygous plakoglobin (gamma-catenin) deficiency (Plako$^{+/-}$) (27) and their wildtype (WT) littermates.

Results

Atrial arrhythmias and ECG changes in definite ARVC patients

The clinical cohort studied comprised of 146 patients with suspected cardiomyopathy; 97 were identified as “Non-definite” ARVC cases and 49 as “Definite” ARVC, i.e. presenting with a complete phenotype according to 2010 Task Force Criteria (1). Mean age of the patients at time of ECG analyses was not different between the groups (42 ± 18 years for non-definite vs 43 ± 18 years for definite). 24% of definite ARVC patients experienced atrial fibrillation and/or flutter compared to 3% of the non-definite ARVC patients (Table 1). There was a significant association between sex and ARVC diagnosis type (Table 1, 43% male amongst non-definite vs. 73% male amongst definite patients). Semi-automated analysis of digital ECG lead II recordings focussing on atrial parameters (Figure 1A) showed PR interval prolongation in advanced, definite disease stage (Figure 1B). P wave duration and P wave area were also significantly increased in definite compared to non-definite patients. Non-definite ARVC patients exhibited no difference in the analyzed P wave parameters compared to unaffected control subjects. Results of a meta-analysis of clinical observational studies are presented in the discussion.

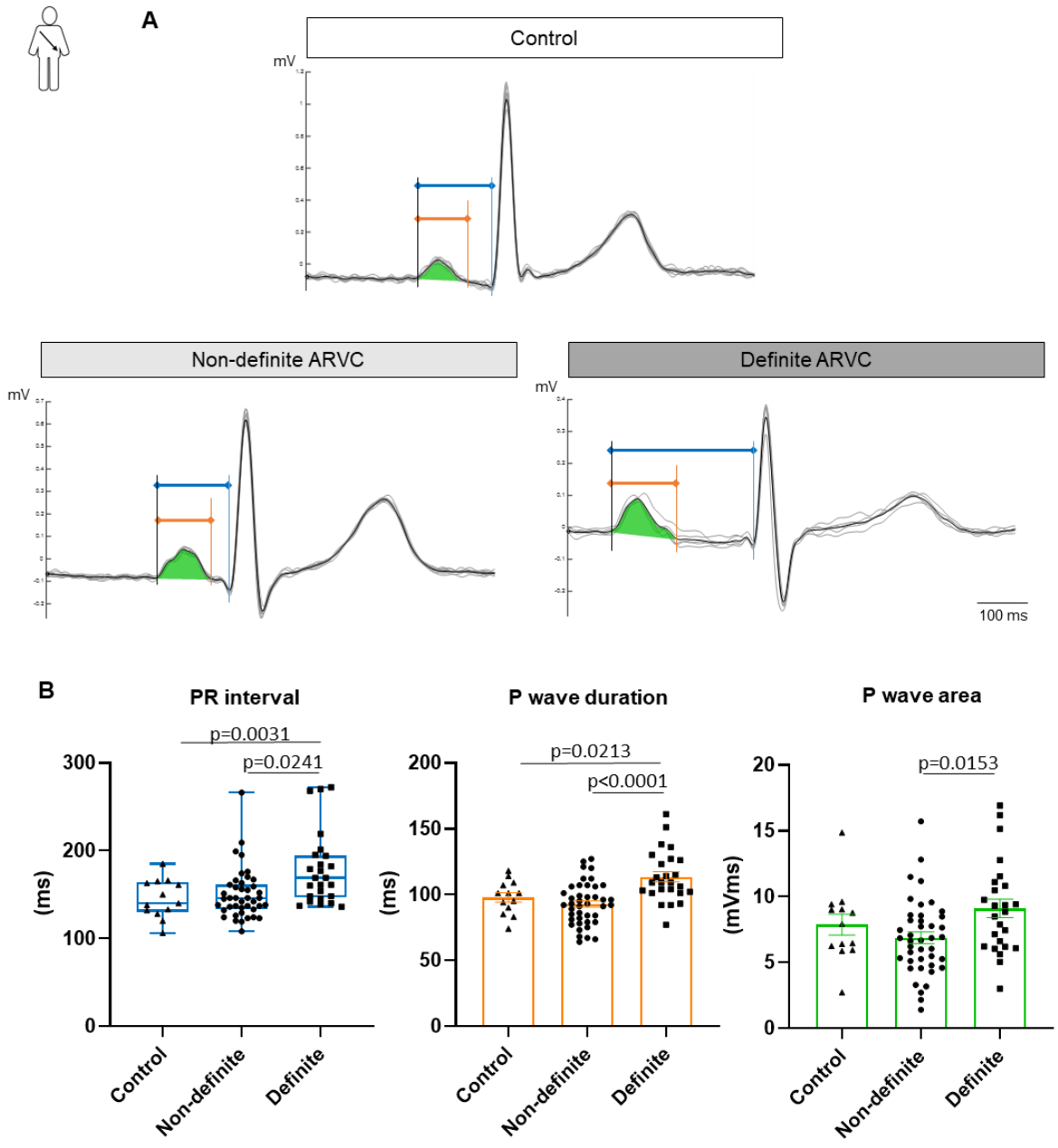
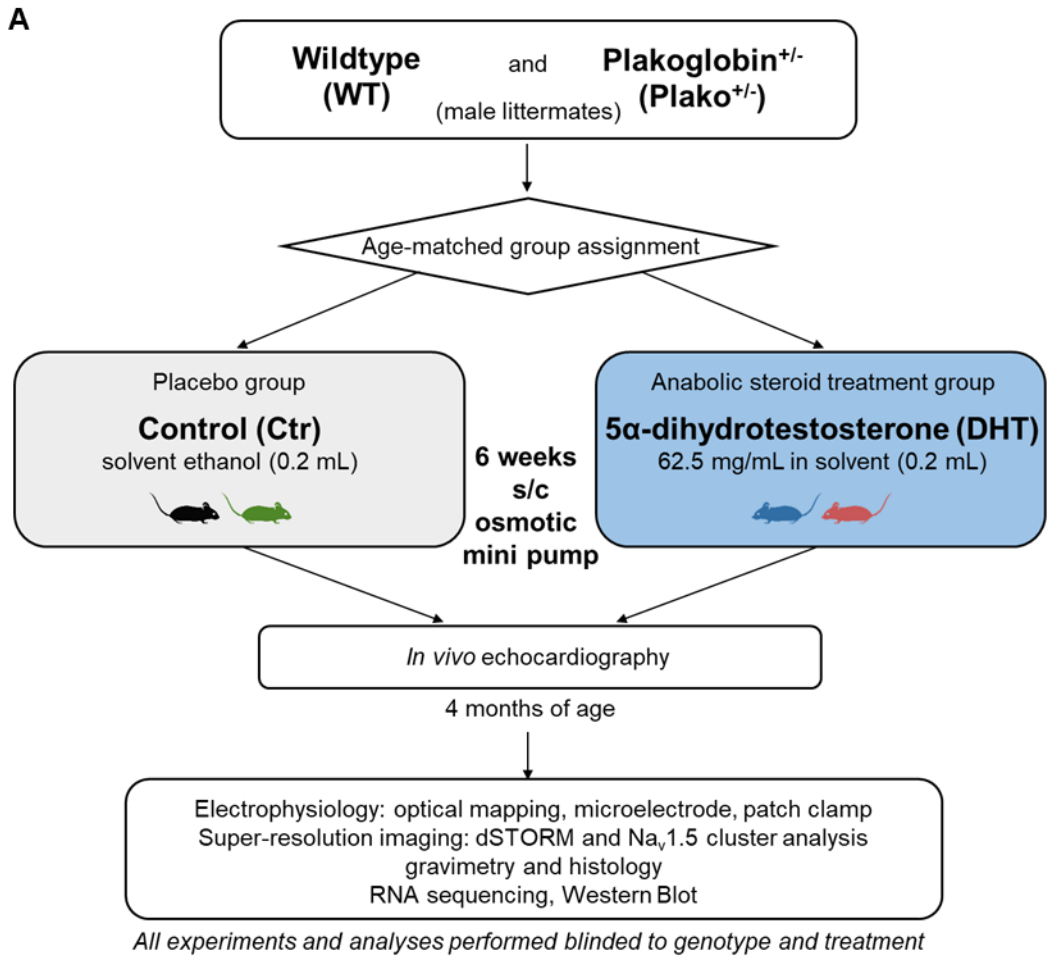


Figure 1 - Arrhythmogenic Right Ventricular Cardiomyopathy (ARVC) patients' and control individuals' P wave characteristics derived from digital ECG analysis

(**A**) Lead II ECG recordings from an unaffected (control) as well as a non-definite and definite ARVC patient. Individual cardiac cycles over a duration of 10 sec (grey traces) are overlaid by detected R waves and averaged (black trace). PR interval (blue), P wave duration (orange) and P wave area (green) are marked. (**B**) PR interval and P wave characteristics obtained from semi-automated analysis of the averaged ECG. All parameters are derived from lead II recordings. Mean heart rate ± SEM: Control: 73 ± 3 bpm ; Non-definite ARVC: 75 ± 2 bpm; Definite ARVC: 60 ± 3 bpm. P-values from post hoc tests are reported on the graphs (Kruskal-Wallis ($p<0.05$) with Dunn's post hoc test for PR interval; one-way ANOVA ($p<0.05$) with Bonferroni post hoc test for P wave duration and area). n (number of patients) = Control: 13, Non-definite ARVC: 42, Definite ARVC: 25

5α-dihydrotestosterone (DHT) causes general and cardiac growth response in mice

To study increased androgen exposure and desmosomal instability jointly in atria, Plako$^{+/-}$ mice, an established animal model of ARVC (28) and wildtype (WT) littermates were subjected to chronic DHT treatment over 6 weeks (please refer to Figure 2A for an overview scheme). Treatment led to a 3-4-fold increase in serum DHT concentration in both genotypes compared to controls (Ctr) (Figure 2B). Moreover, it increased body weight, seminal vesicle mass/tibia length ratio and atrial weight/tibia length ratio as well as causing left ventricular hypertrophy in Plako$^{+/-}$ animals (Figure 2C, Supplementary Figure 1).



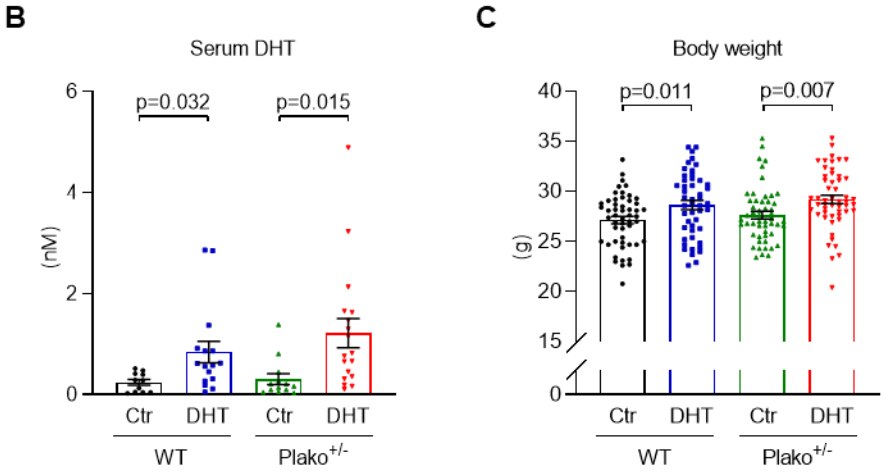


Figure 2 - Study design for murine experiments

(**A**) Experimental timeline and methods used in the underlying murine study. All results described were obtained in male WT or Plako$^{+/-}$ mice at 4 months of age, at the end point of the protocol, i.e. after exposure to either 5α-dihydrotestosterone (DHT) or placebo control (Ctr) for 6 weeks. (**B**) Serum DHT concentration (n=11-18 mice/group) and (**C**) body weight (n=48-54 mice/group) are increased following DHT treatment.

DHT induces ARVC-like atrial ECG changes in plakoglobin-deficient mice

To check whether atrial ECG changes observed in definite ARVC patients are similarly present in the murine model, ECGs were recorded from conscious mice following DHT treatment. Both PR interval as well as P wave duration were prolonged in Plako$^{+/-}$ animals exposed to DHT compared to WT littermates exposed to DHT (Figure 3).

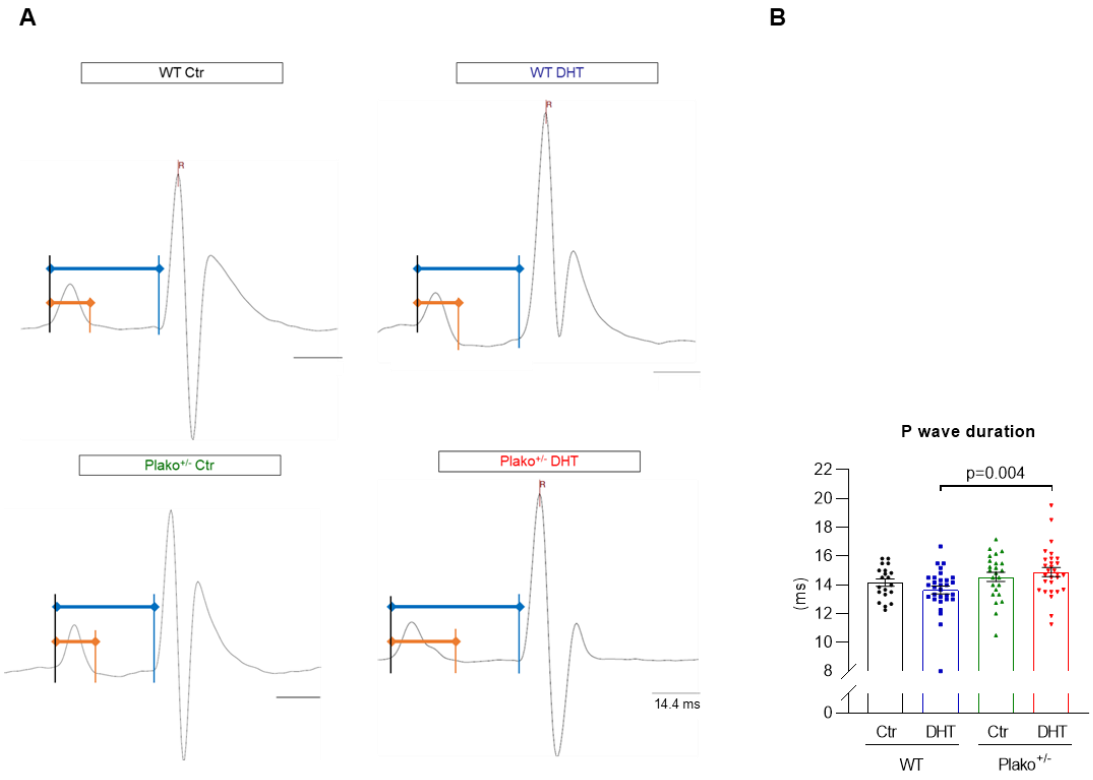


Figure 3 - Murine awake ECGs after 6 week chronic control or DHT treatment

(**A**) Exemplary ECG recordings in conscious mice. Shown are compound potentials averaged from 20 subsequent cardiac cycles. PR interval (blue) and monophasic part of P wave (orange) are marked. (**B**) PR interval (n=30-34 mice/group) and P wave duration (n=20-30 mice/group) are prolonged in Plako$^{+/-}$ DHT compared to WT DHT (Two-way ANOVA $p<0.05$ with post-hoc t-test; p-values are indicated on graphs).

DHT causes atrial unfolded area dilation and atrial conduction slowing in heterozygous plakoglobin-deficient hearts

Left atrial unfolded area was increased in Plako$^{+/-}$ DHT compared to Plako$^{+/-}$ Ctr (Figure 4A&B), but not in WT left atria after DHT exposure. Chronic DHT exposure slowed conduction in Plako$^{+/-}$ but not WT atria (Figure 4C&D). The reduction in conduction velocity in Plako$^{+/-}$ DHT left atria was more pronounced at higher pacing frequencies. The Plako$^{+/-}$ left atria exposed to DHT exhibited an overall prolongation of 95% left atrial activation times and increased beat-to-beat activation variability compared to WT Ctr and Plako$^{+/-}$ Ctr (Figure 5). Connexin expression was not impaired (Supplementary Figure 2).

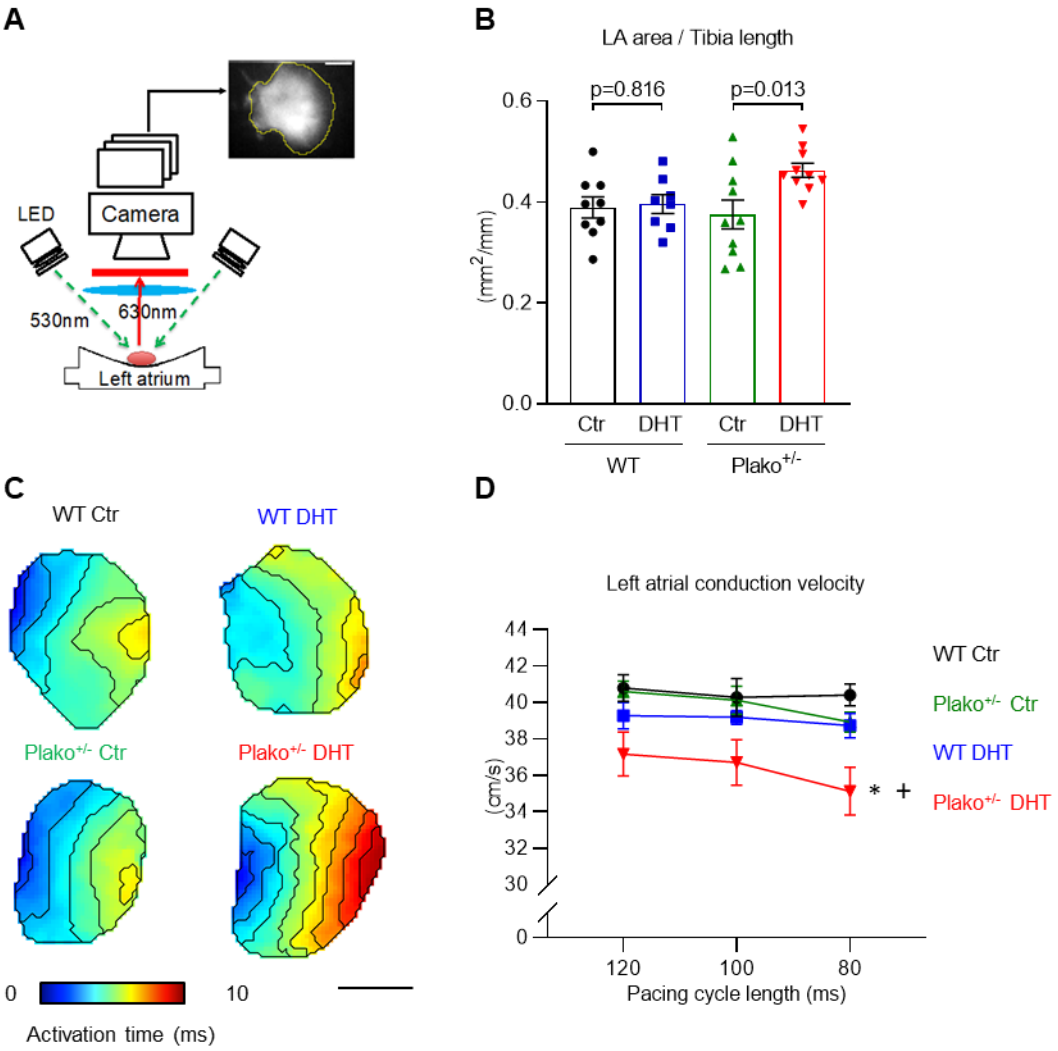


Figure 4 - Left atrial (LA) area and conduction

(**A**) Experimental setup for optical mapping of isolated LA, scale bar 1 mm. DHT exposure has a significant effect on (**B**) LA unfolded area ($p<0.05$, 2-way ANOVA) measured from optical mapping raw images and area is significantly increased in Plako$^{+/-}$ left atria subjected to DHT (post hoc unpaired t-test, p-values indicated on graph, n=8-10 LA per group). (**C**) Exemplary isochronal activation maps of LA at 100 ms pacing cycle length (averaged, scale bar 1 mm). Both, heterozygous deletion of plakoglobin and DHT exposure have a significant effect on (**D**) LA conduction velocity ($p<0.05$, 2-way repeated measures ANOVA), but it is only significantly decreased in LA of Plako$^{+/-}$ DHT animals (Bonferroni-adjusted post hoc test, $+p_{adj}<0.05$ vs Plako$^{+/-}$ Ctr; $*p_{adj}<0.05$ vs WT Ctr, across all cycle lengths, n=8-9 LA per group). Data plotted as mean ± SEM.

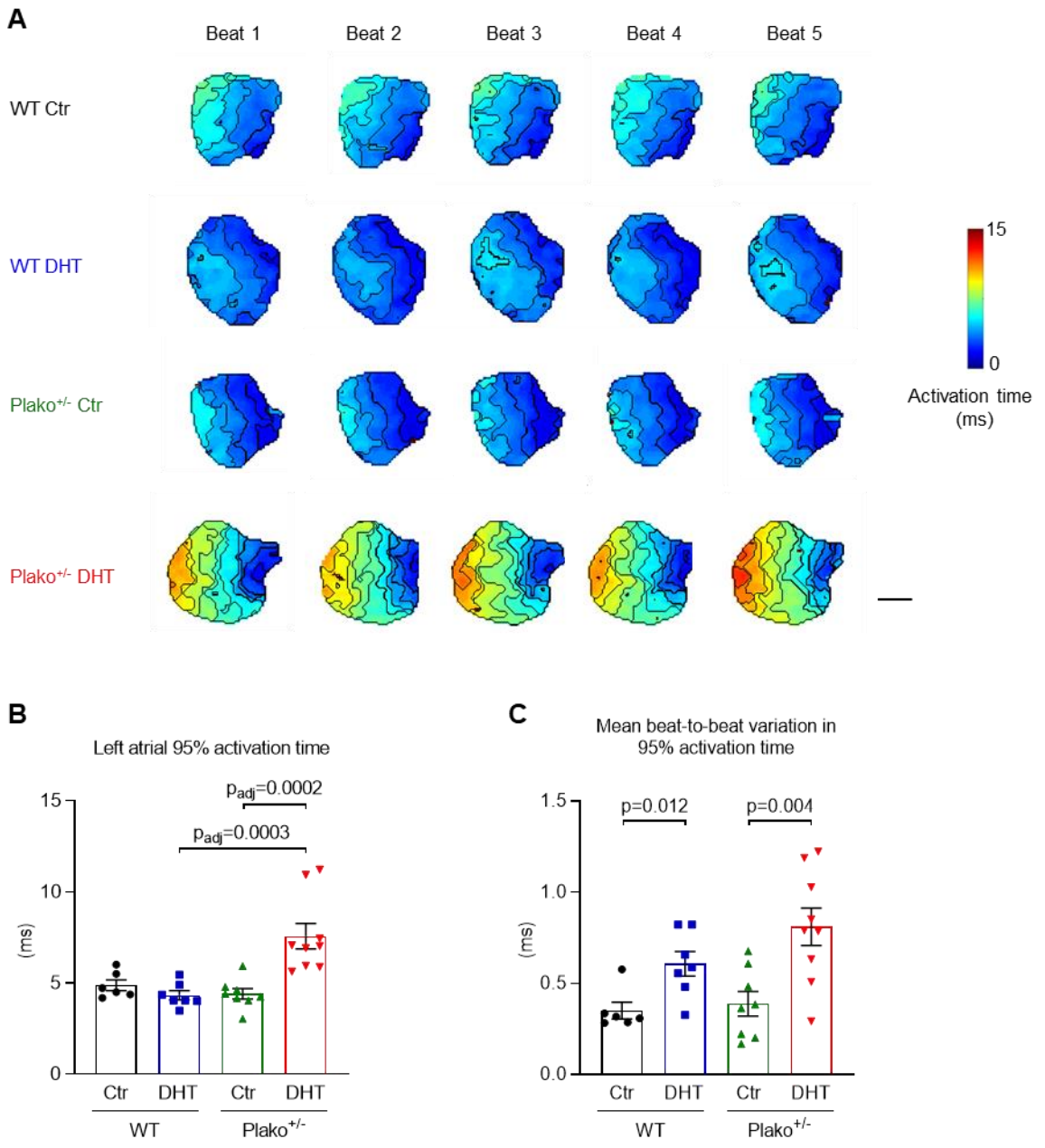


Figure 5 - Left atrial activation time and beat-to-beat variation

(**A**) Example individual activation maps taken from the final 5 beats of a train of 50 pulses at 80 ms pacing cycle length (CL). DHT exposure has a significant effect on (**B**) beat averaged 95% left atrial activation times. Both genotype and DHT treatment have a significant effect on (**C**) mean beat-to-beat variation in 95% activation times calculated from the final 10 beats of a train of 50 pulses at 80 ms CL (2-way ANOVA with post-hoc analysis as appropriate, p-values indicated). Individual data points denote single left atria (LA). N = WT Control: 6 LA, WT DHT: 7 LA, Plako$^{+/-}$ Control: 8 LA, Plako$^{+/-}$ DHT: 9 LA. Scale bar in (A) indicates 1 mm.

DHT induces atrial expression of gene profiles implicated in ARVC

Exploratory RNA sequencing analysis confirmed approximately 50% reduction in atrial plakoglobin (*Jup*) expression in Plako$^{+/-}$ compared to WT animals (Figure 6B). In control hearts, gene expression patterns did not markedly differ between genotypes (data not shown). Chronic DHT exposure resulted in significant transcriptional changes in atria of both, WT and Plako$^{+/-}$ mice (Figure 6A&C). DHT activated expression of genes associated with muscle growth (e.g. *Igf1*, *Mtpn, Myocd*), but additionally also immune (e.g. *C7*, *Tlr3, Tlr4*) and pro-fibrotic response genes (e.g. *Col1a1*, *Col3a1, Srf, Lox)* (Figure 6C). Before-mentioned transcriptional changes were similarly induced in left and right atria (Supplementary Figure 3). However, atrial cardiac myocyte diameter and endomysial collagen deposition was not significantly different between genotypes after DHT treatment, as quantified in semi-automated histology analysis (Supplementary Figure 5).

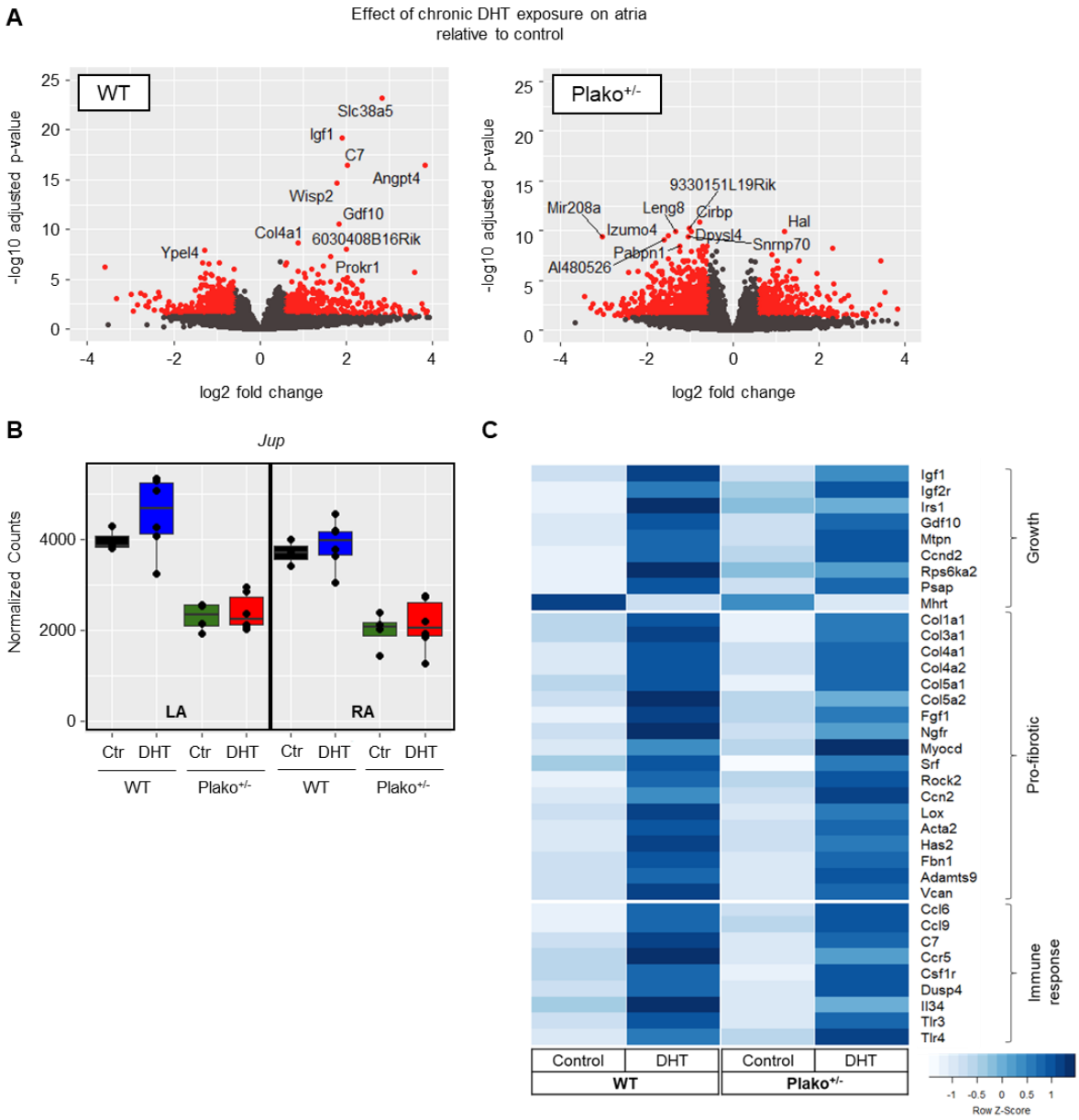


Figure 6 - Atrial gene expression profiles. Confirmation of Jup deficiency and growth response.

(**A**) Volcano plot illustrating the effect of DHT treatment, comparing gene expression of WT DHT atria to WT Ctr. Significantly differentially expressed genes at a fold change ≥|0.5| (adjusted p value from DESeq2 < 0.05) are highlighted in red, top 10 hits are labelled. (**B**) Normalized read counts of plakoglobin gene Jup from RNA sequencing analysis from all groups, confirming ~50% reduction of expression in heterozygous knock-out animals (Plako$^{+/-}$) in both left (LA) and right atria (RA) (FDR from DESeq2 WT vs Plako$^{+/-}$ <0.05 for both treatment groups). (**C**) Selected genes significantly regulated (adjusted p value from DESeq2 < 0.05) by DHT exposure in at least one of the genotypes. DHT treatment leads to atrial growth, pro-fibrotic and immune response gene expression.

n= WT Ctr: 3 LA + 3 RA; WT DHT: 6 LA + 6 RA; Plako$^{+/-}$ Ctr: 4 LA + 4 RA; Plako$^{+/-}$ DHT: 6 LA + 6 RA. Ccnd2, cyclin D2; Gdf10, growth differentiation factor; Igf1, insulin-like growth factor 1; Igf2r, insulin-like growth factor 2 receptor; Irs1, insulin receptor substrate 1; Mhrt, myosin heavy chain associated RNA transcript; Mtpn, myotrophin; Psap, prosaposin; Acta2, smooth muscle (α)-2 actin; Adamts9, ADAM metallopeptidase with thrombospondin type 1 motif 9; Ccn2, connective tissue growth factor; Col1a1/3a1/4a1/4a2/5a1, collagen type 1 alpha 1/3 alpha 1/4 alpha 1/4 alpha 2/5 alpha 1; Fbn1,

fibrillin 1; Fgf1, fibroblast growth factor 1; Has2, hyaluronan synthase 2; Lox, lysyl oxidase; Myocd, myocardin; Ngfr, nerve growth factor receptor; Rock2, rho associated coiled-coil containing protein kinase 2; C7, complement C7; Cd, cluster of differentiation 6; Cd9, tetraspanin CD9; Ccr5, C-C motif chemokine receptor 5; Csf1r, colony stimulating factor 1 receptor; Dusp4, dual specificity phosphatase 4; Il34, interleukin 34; Tlr3, toll like receptor 3; Tlr4, toll like receptor 4

DHT reduces action potential amplitude and rate of depolarisation in heterozygous plakoglobin-deficient left atria

The intracellular microelectrode technique was used to record transmembrane action potentials (TAPs) from paced, superfused left atria (Figure 7). Paced left atria isolated from Plako$^{+/-}$ DHT mice showed longer activation times compared to all other groups (Figure 7C, Supplementary Table 1). Action potential amplitude (APA) was reduced in Plako$^{+/-}$ DHT left atria, as well as the peak rate of depolarisation (dV dt^{-1} max) (e.g. 120 ms pacing cycle length WT Ctr: 118±5 V/s; WT DHT: 120±7 V/s; Plako$^{+/-}$ Ctr: 116±4 V/s; Plako$^{+/-}$ DHT: 89±5 V/s) (Figure 7D&E, Supplementary Table 1), both indicative of sodium current impairments. The Plako$^{+/-}$ DHT left atrial cells had a more positive resting membrane potential than WT Ctr (Supplementary Table 1). Chronic DHT exposure did not modify action potential duration (APD) in either genotype (Supplementary Table 1). Beat-averaged left atrial optical APD90, as well as beat-to-beat APD90 variability were similar between all four groups (Supplementary Table 2).

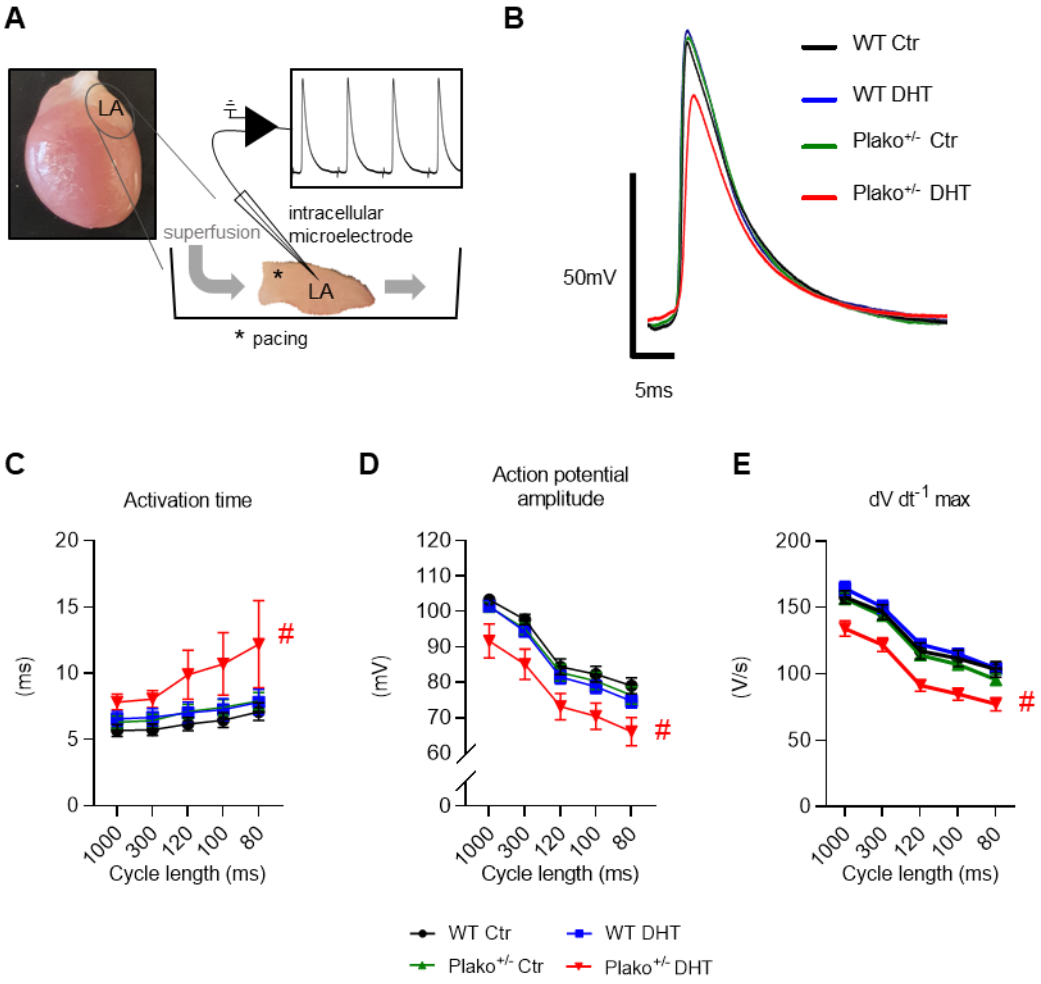


Figure 7 - Left atrial (LA) activation time and action potential characteristics
(**A**) Experimental setup for intracellular microelectrode measurements in paced LA to record transmembrane action potentials. Representative examples obtained at 100 ms pacing cycle length are shown in (**B**). Both, heterozygous plakoglobin deletion and DHT exposure have a significant effect on mean (**C**) LA activation time, (**D**) action potential amplitude (APA) and (**E**) maximum upstroke velocity (dV dt^{-1} max) (2-way repeated measures ANOVA, $p<0.05$). WT Ctr (n=21 cells, N=7 LA), WT DHT (n=13 cells, N=5 LA), Plako$^{+/-}$ Ctr (n=20 cells, N=7 LA) and Plako$^{+/-}$ DHT LA (n=23 cells, N=8 LA). Plako$^{+/-}$ DHT LA have longer activation times, decreased APA and reduced dV dt^{-1} max (Bonferroni-adjusted post hoc analysis: #padj<0.05 vs all other groups, across all cycle lengths). Data averaged per atrium before performing statistical analysis and plotted as mean ± SEM.

DHT decreases peak sodium current density in heterozygous plakoglobin-deficient left atrial cardiac myocytes

To examine mechanisms underlying alterations in action potential morphology and conduction in the Plako$^{+/-}$ DHT left atria, whole-cell patch clamp experiments were performed monitoring peak sodium current (I_{Na}) amplitude and kinetics. Peak whole-cell I_{Na} density was

decreased by approximately 20% in Plako$^{+/-}$ left atrial cells following DHT exposure (Figure 8A&B). Activation kinetics were consistent between all groups (V_{50} activation, WT Ctr: -43±1 mV; WT DHT: -46±1 mV; Plako$^{+/-}$ Ctr: -46±1 mV; Plako$^{+/-}$ DHT: -46±2 mV). DHT exposure tended to cause a left shift in steady-state inactivation kinetics in both WT and Plako$^{+/-}$, being statistically significant in Plako$^{+/-}$ (Supplementary Figure 5A). The 50% recovery time (P_{50}) from inactivation was significantly longer in the Plako$^{+/-}$ DHT, suggestive of a delayed rate of sodium channel recovery (Supplementary Figure 5B&C).

Left atrial cell capacitance was elevated by DHT exposure in both WT and Plako$^{+/-}$, but not significantly different between the genotypes (Figure 8C). Of note, there was a considerable spread of individual cell capacitance in DHT-exposed groups, indicative of variable degrees of hypertrophy (Figure 8C). I_{Na} density was negatively correlated against cell capacitance in Plako$^{+/-}$ left atria cardiac myocytes following DHT treatment (Figure 8D). This negative correlation was not detected in the WT DHT group. These data suggest that a hypertrophic response in the Plako$^{+/-}$ DHT left atrial cardiac myocytes was not matched by a rise in I_{Na}, leading to an overall depletion of I_{Na} density. In contrast, hypertrophy in the WT DHT left atria was matched by an increase in I_{Na}, so that I_{Na} density was preserved.

Whole left atrial tissue RNA expression of sodium voltage gated channel 5 (*Scn5a*) was neither significantly affected by genotype, or DHT exposure (Figure 8E).

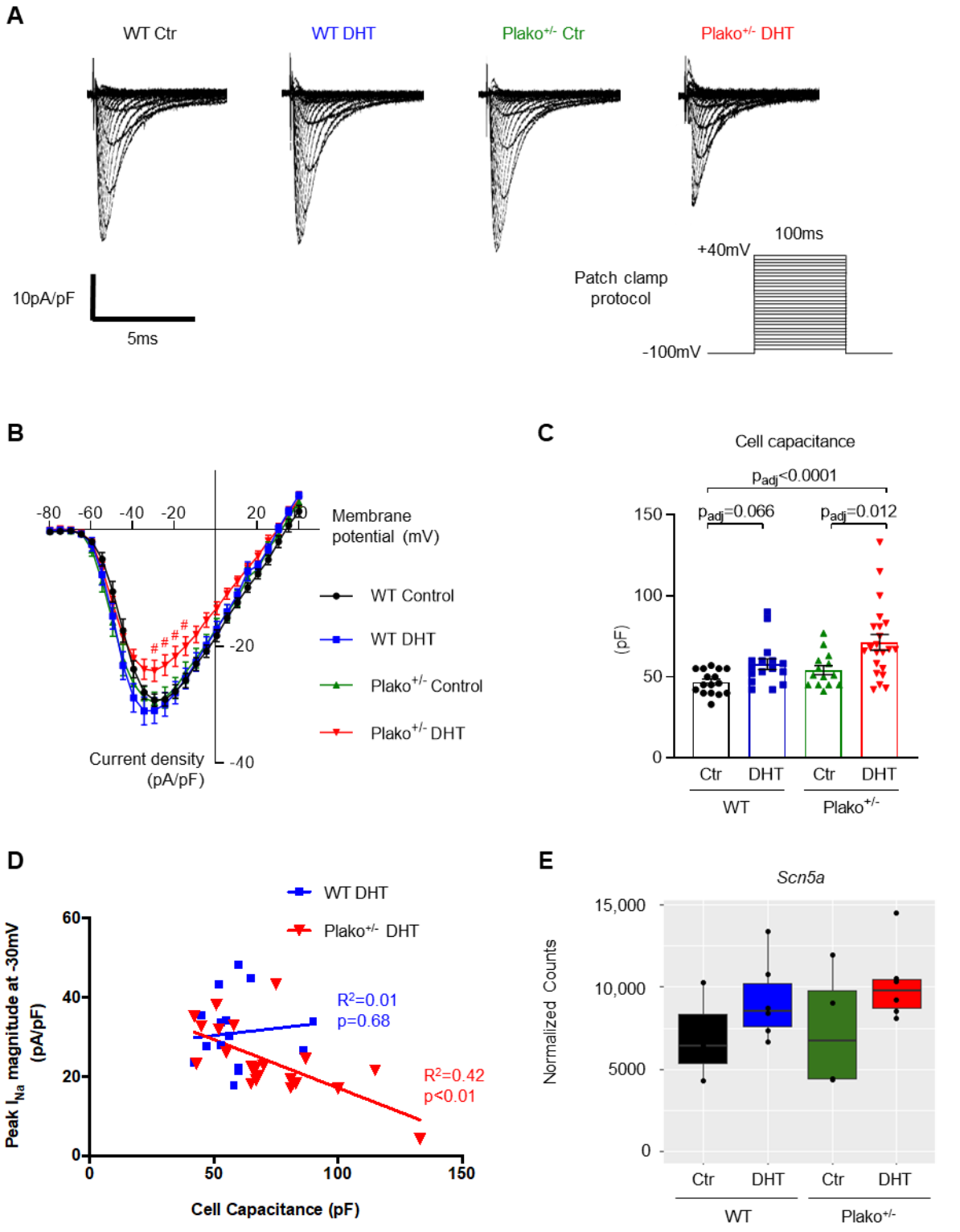


Figure 8 - Left atrial (LA) cardiomyocyte sodium current, cell capacitance and sodium channel expression

(A) Representative LA whole cell peak Na^+ current (I_{Na}) traces measured at test potentials -100 to +40 mV. (**B**) Mean current-voltage relationships for WT Ctr, WT DHT, Plako$^{+/-}$ Ctr and Plako$^{+/-}$ DHT. Plako$^{+/-}$ DHT LA cells have reduced I_{Na} density (2-way repeated measures ANOVA with Bonferroni post hoc analysis: #padj<0.05 vs all other groups at the respective test potential). Data plotted as

mean ± SEM. Both genotype and DHT treatment show a significant effect on (**C**) individual cell capacitance (2-way ANOVA, $p<0.05$) as measured in WT Ctr (n=14 cells, N=5 LA), WT DHT (n=16 cells, N=5 LA), Plako$^{+/-}$ Ctr (n=11 cells, N=4 LA) and Plako$^{+/-}$ DHT (n=21 cells, N=5 LA). Data points shown individually and plotted as mean ± SEM. Bonferroni-corrected post hoc analysis shows a significant increase in cell capacity by DHT compared to Ctr in both genotypes. Cell capacitance is highest in LA cardiomyocytes from Plako$^{+/-}$ DHT. (**D**) Scatter plots of individual LA cell capacitance against peak I_{Na} density for WT Ctr (n=14 cells, N=5 LA), WT DHT (n=16 cells, N=5 LA), Plako$^{+/-}$ Ctr (n=11 cells, N=4 LA) and Plako$^{+/-}$ DHT (n=21 cells, N=5 LA). There is a significant negative correlation of peak I_{Na} density against cell capacitance for Plako$^{+/-}$ but not WT LA cells after DHT treatment; linear regression analysis. (**E**) Normalized read counts of sodium channel transcript *Scn5a* in LA obtained from RNA sequencing analysis (n=3-6 LA per group). Data points shown individually and box whiskers denote IQR, max-min and median.

$Na_v1.5$ cluster depletion in Plako$^{+/-}$ left atrial cardiac myocytes following DHT exposure

To define a molecular cause of I_{Na} density depletion in Plako$^{+/-}$ DHT left atrial cardiac myocytes, we examined $Na_v1.5$ organisation at super-resolution level using direct Stochastic Optical Reconstruction Microscopy (dSTORM, workflow see Supplementary Figure 6). Due to the high variability in T-tubule density between different atrial cells, we focused on $Na_v1.5$ channels located within ca. 200 nm of the contact cell surface membrane by using TIRF/HILO. Exemplary super-resolution images of $Na_v1.5$ detections, as well as characteristic cluster maps are shown in Figure 9A.

Characteristics of identified $Na_v1.5$ clusters, i.e. cluster density and cluster area, were similar in all 4 groups (Supplementary Figure 7A&B). The 95% confidence intervals generated from our murine WT Ctr left atria experiments suggest a range of 3-4x10^{-3} $Na_v1.5$ channels per nm^2 cluster (Supplementary Figure 7C, both mean and median at 3x10^{-3} channels per nm^2 cluster), resulting in an estimated nearest-neighbour distance of 20 nm.

At the Plako$^{+/-}$ DHT left atrial cardiac myocyte membranes, fewer $Na_v1.5$ detections were observed compared to WT DHT (Figure 9B). Of the total detections, the proportion present in distinct $Na_v1.5$ clusters was significantly lower in the Plako$^{+/-}$ DHT compared to WT DHT cardiac myocytes (Figure 9C).

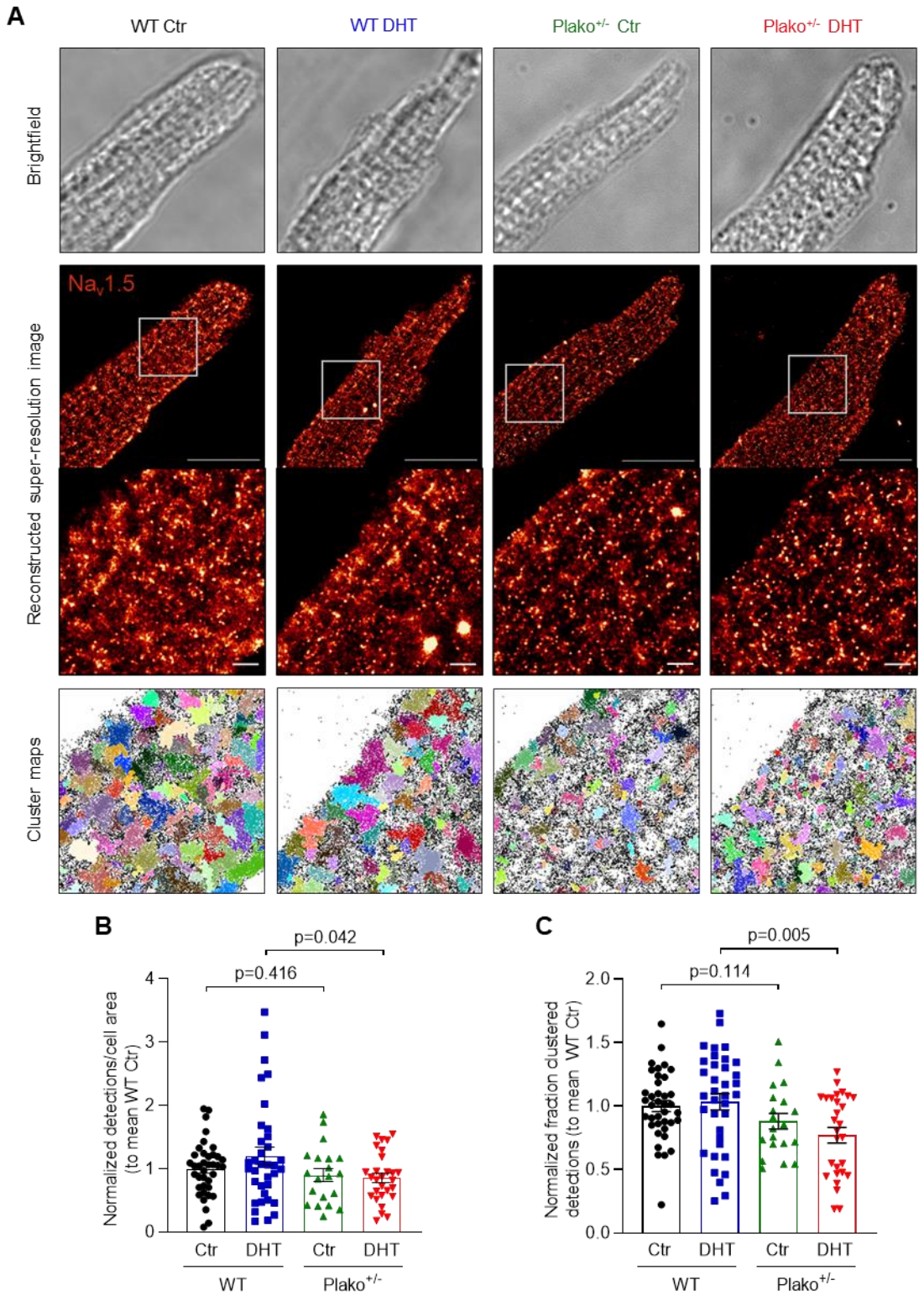


Figure 9 - Sodium channel clustering analysis in left atrial (LA) cardiomyocyte dSTORM images

(**A**) Brightfield images of fixed LA cardiomyocytes prior to dSTORM recording (top lane), reconstructed super-resolution images of membrane $Na_v1.5$ and zoom-ins of the indicated area (middle lanes) as well as corresponding cluster maps generated from binary images (bottom lane).

Detections allocated to a cluster appear in (arbitrary) colour, non-clustered detections remain black. Scale bar 20 µm and 1.5 µm for zoom-in images, respectively. Genotype has a significant effect on (**B**) number of $Na_v1.5$ detections at the LA cardiomyocyte membrane and (**C**) fraction of $Na_v1.5$ detections allocated to a cluster (2-way ANOVA, $p<0.05$). Both number and fraction of clustered membrane $Na_v1.5$ is significantly reduced in cardiomyocytes from $Plako^{+/-}$ DHT. Results from post-hoc t-tests are reported on the graphs. For (B) and (C): WT Ctr (n=38 cells, N=7 LA), WT DHT (n=35/36 cells, N=11 LA), $Plako^{+/-}$ Ctr (n=20 cells, N=5 LA) and $Plako^{+/-}$ DHT (n=28 cells, N=6 LA). Data points were normalized to the mean of the respective WT Ctr group on the same imaging session and are shown individually and plotted as mean ± SEM.

Discussion

Main findings

- Atrial arrhythmias and P wave changes represent a common clinical observation in patients with a full ARVC phenotype. The cohort studied here presents with a male preponderance amongst definite ARVC patients.
- Exposure to the potent androgen 5α-dihydrotestosterone leads to pro-hypertrophic, pro-fibrotic and inflammatory transcriptional signatures in murine atria.
- Chronic 5α-dihydrotestosterone exposure in mice heterozygously deficient for plakoglobin induces atrial changes on ECG as observed in definite ARVC patients.
- Increased 5α-dihydrotestosterone concentrations interact with plakoglobin to decrease the number of membrane-localized $Na_v1.5$ clusters, reducing atrial sodium current density and causing atrial conduction slowing.

We report that definite ARVC patients exhibit increased P wave area and prolonged PR interval as well as P wave duration on ECG. A phenocopy of these ECG changes is observed in plakoglobin-deficient mice exposed to supraphysiological 5α-dihydrotestosterone (DHT) concentrations. Heterozygous plakoglobin deficiency predisposes cardiac atrial tissue to hypertrophy and a reduction in sodium current density after six weeks of exposure to elevated concentrations of DHT, resulting in a decrease in the peak upstroke velocity of the atrial action potential ($dV\ dt^{-1}$ max), left atrial conduction slowing and increased electrical beat-to-beat variability. Super-resolution microscopy, dSTORM, identified a depletion of $Na_v1.5$ channels and clusters at left atrial cardiac myocyte membranes isolated from $Plako^{+/-}$ DHT-treated mice. This was accompanied by the functional electrophysiological modifications of reduced atrial $Na_v1.5$ current density and impaired atrial conduction.

The results underpin a role of plakoglobin in regulating $Na_v1.5$ channel cellular localization in the left atrium and in preserving left atrial electrical integrity in response to stressors such as pro-hypertrophic DHT exposure.

Patients in the definite ARVC disease stage display a high prevalence of atrial arrhythmias, P wave changes on ECG and preponderance of male sex

A quarter (24%) of the patients with definite ARVC had atrial arrhythmias in our cohort. Meta-analysis of published studies (between 1991 and 2021) revealed a weighted mean atrial arrhythmia prevalence of 15% amongst a total of 1915 ARVC patients (Table 3). Over 99% of the reported patients were diagnosed with “definite” ARVC. Male preponderance has been a common feature of all described ARVC patient cohorts. Definite ARVC patients were also more likely to be male in the here described cohort.

Several P wave indices were found to be changed amongst in the ARVC patients in the definite disease stage. P wave duration was prolonged and P wave area increased in those patients compared to controls or non-definite patients, suggesting pathophysiological remodelling of the atria. Both, P wave prolongation and increased P wave area have been associated with atrial fibrillation (AF) or increased AF recurrence (29-32). Furthermore, definite ARVC patients displayed longer PR intervals compared to non-definite patients and controls, suggesting attenuated conduction of the atrioventricular node in late disease stages. In line with our results, Baturova and colleagues recntly found evidence for ARVC disease progression to be paralleled by changes in P wave area (33). Generally, this study supports the notion progressive atrial conduction disturbances with progression of ARVC.

DHT exposure interacts with plakoglobin deficiency leading to atrial electrical dysfunction

Although commonly performed in doping, systematic observation of androgen level elevation is difficult due to not being disclosed. Murine models however represent a unique tool to understand molecular mechanisms of elevated androgen levels in desmosomal vulnerability. They allow for the study of early stages of the disease, i.e. even before a clinical phenotype manifests.

We show that chronic DHT exposure prolongs PR interval and P wave duration and slows conduction in the murine Plako$^{+/-}$ left atrium. Conduction slowing is a common feature of heart rhythm disorders including AF, and acts by permitting the development and maintenance of both micro and macro re-entry (34).

As no reduction in connexin expression could be observed, conduction slowing caused by DHT was likely mediated by locally reduced availability of sodium channels. A key determinant of conduction velocity is the magnitude of depolarising current, primarily carried by Na^+ through $Na_v1.5$ channels (35). The reduction in the atrial action potential amplitude and upstroke velocity (APA and dV dt^{-1} max) suggests that sodium current decrease is sufficient to lower both the magnitude and rate of depolarisation, key contributors to cardiac conduction velocity. A delay of sodium current recovery times, as observed in Plako$^{+/-}$ DHT-treated cardiomyocytes, becomes more physiologically relevant at higher pacing frequencies. The reduced availability of $Na_v1.5$ channels in cells already operating without a sufficient "conduction reserve" (36, 37), is likely to cause more pronounced conduction slowing and beat-to-beat variability as observed at the higher pacing frequencies in our experiments.

Supraphysiological DHT concentrations increased atrial expression of genes related to immune response and fibrotic remodelling. Both processes contribute to the pathophysiology of ARVC as well as AF (38-46) and are likely intertwined. Lysyl oxidase (*Lox*), which we here report to be upregulated in atria in response to DHT, mediates cross-linking of collagen I and collagen III fibrils. Both collagen isoforms, amongst others, were also upregulated in DHT-exposed atria in our study, indicating remodelling of the extracellular matrix (ECM). Lox overexpression in mice was also found to accelerate the inflammatory response during angiotensin II (AngII)-induced cardiac hypertrophy, including increased cytokine levels (47).

Among the immune-response genes increased in atrial expression upon DHT treatment were the Toll-like receptor 3 (*Tlr3*) and the Toll-like receptor 4 (*Tlr4*) in our study. Silencing or deficiency of these receptors has been demonstrated to improve cardiac function post myocardial infarction in rodent models by attenuating inflammatory cytokine production and fibrotic scar formation (48, 49). Toll-like receptors can be activated by endogenous ligands, including components of the extracellular matrix (50), and have been associated with matrix turn-over.

Excessive ECM deposition is another pathological driver of conduction defects (51, 52) and increased perivascular fibrosis has been observed in the ventricular myocardium of male rats, in response to 20 days of testosterone administration (53). Rho associated coiled-coil containing protein kinase 2 (*Rock2*)-dependent pathways, implicated in cardiac fibroblast activation, can regulate expression of ECM component levels, including CTGF (*Ccn2*) and α-smooth muscle actin (*Acta2*) (54). Indeed, the expression of *Rock2, Ccn2,* as well as *Acta2* transcript, was upregulated in atria after chronic DHT exposure. *Ccn2* expression, in response to the pro-hypertrophic stimulus AngII, has previously been shown to be mediated via the transcription factor serum response factor (*Srf*) in cardiac fibroblasts (55), which we also found to be upregulated in atria subjected to high concentrations of DHT.

Transcriptional changes did not yet translate to structural changes other than atrial area dilation, e.g. excessive ECM deposition in atria in our murine study. Hence, we were likely able to capture early responses to chronic DHT exposure.

In the scope of this study, we were able to demonstrate that the combination of a pro-inflammatory/fibrotic environment, caused by DHT, plus the selective reduction in I_{Na} in Plako$^{+/-}$ cardiomyocytes is sufficient to induce conduction slowing and increased beat-to-beat heterogeneity in these vulnerable atria.

While this is the first study showing the molecular effect on *atria*, it has been previously demonstrated that androgens, including DHT, induce a hypertrophic response in *ventricular* cardiomyocytes (12). One of the genes consistently elevated in atrial expression after DHT exposure was insulin growth factor 1 (*Igf1*), a known driver of (cardiac) muscle growth (56, 57). *Igf1* mRNA expression was also found to contribute to atrial fibrotic remodelling and AF inducibility in a rodent model (58). *IGF1*, containing an androgen response element within its promoter region (59), is a well-established target of androgen-receptor mediated gene activation. To our knowledge, we are the first to show that supraphysiological plasma DHT concentration can induce upregulation of *Igf1* transcript levels in atria. Further evidence of the pro-hypertrophic atrial gene response to DHT exposure can be based on the downregulation of the lncRNA Myosin heavy chain associated RNA transcript (*Mhrt*). Repression of *Mhrt* expression has previously been established as a prerequisite for stress-induced, pathological cardiac hypertrophy and restoring *Mhrt* expression levels protected murine hearts from pressure overload-induced hypertrophy (60). Mhrt has been shown to inhibit expression of the transcription factor myocardin (*Myocd*) (61) and increased *Myocd* expression in peripheral blood cells of patients has been associated with increased ventricular mass (62). In accordance with this, down-regulation of *Mhrt* expression upon DHT exposure was paralleled by upregulation of *Myocd* expression compared to control groups. Since we were not able to demonstrate a significant increase in atrial cell diameter in histology at the investigated time point, but were able to demonstrate increased cell capacitance in atrial cardiomyocytes on single cell level as well as atrial area dilation, we propose that the seen atrial hypertrophic growth response to DHT is of an eccentric nature.

Reduced plakoglobin decreases left atrial $Na_v1.5$ cluster availability at the membrane in response to pro-hypertrophic DHT exposure

Super-resolution imaging and electrophysiological techniques suggest that $Na_v1.5$ spatial sarcolemmal localization is not random, but rather characterized by formation of distinct clusters (63, 64). To our knowledge, this the first study to evaluate the molecular arrangement of sarcolemma-localized $Na_v1.5$ channels in atria through the use of dSTORM

to allow for visualisation at nanometer resolution (localisation accuracy estimated to be within 20-30 nm). This confirmed that the mismatch between cell size and I_{Na} density following DHT exposure in Plako$^{+/-}$ left atria was due to reduced membrane $Na_v1.5$ channel number and/or defective cluster availability. Interestingly, the values we can estimate for next-neighbour distance, calculated from cluster density in WT cells, are slightly lower than those reported employing similar super-resolution methods in ventricular cardiac myocytes (64), suggesting slightly higher cluster densities in atrial cardiomyocytes.

The number of plasma membrane-localized $Na_v1.5$ detections was reduced in left atrial cardiomyocytes obtained from Plako$^{+/-}$ DHT and showed a similar trend in Plako$^{+/-}$ control. A link between plakoglobin and $Na_v1.5$ channel incorporation/trafficking into the cell membrane at the intercalated disc has been reported in ventricles (65, 66). Interactions of desmosomal and intercalated disc proteins with sodium channel complex have been demonstrated in ventricles previously (67) and loss or mutations of the desmosomal components plakophilin-2 and desmoglein-2 were associated with reduced sodium current in different cell and murine models (67-69). A mismatch in cell size and $Na_v1.5$ cluster availability could have implications for other cardiomyopathies and pathological hypertrophy (70, 71). Understanding the role of ion channel cluster properties is in its infancy, but our observations are consistent with other recent studies reporting a reduced I_{Na} in response to changes in single-molecule $Na_v1.5$ organisation (72, 73).

Implications for patients and athletes

Our results show that atrial arrhythmias are an important clinical feature of ARVC and confirm male patients are more likely to show a full ARVC phenotype. We demonstrate a previously unknown interaction between defective desmosomal gene expression and exposure to androgenic anabolic steroids (AAS) in atria. This may partially explain the occurrence of atrial conduction slowing and arrhythmias (74-76) in athletes abusing AAS to enhance their performance. Based on our results, searching for desmosomal gene defects in

steroid abusers with atrial arrhythmias seems warranted. Such analyses may add to a better understanding of the cardiac damage observed in some of these patients.

Our data, gained from well-controlled murine experiments, demonstrate that reduced expression of plakoglobin, as commonly observed in cardiac tissue of patients with pathogenic mutations in a variety of desmosomal genes (77), renders atria susceptible to AAS-induced pathology. Prevention of atrial arrhythmias in arrhythmogenic cardiomyopathies is of interest also because they can give rise to inappropriate defibrillator shocks in affected patients (4, 78) and compromise right heart function.

We here add exposure to DHT to the list of stimuli aggravating pro-arrhythmic phenotypes in carriers of desmosomal mutations and demonstrate that this affects atrial electrical function. Our data also provide an explanation for the stronger phenotypic expression in male gene carriers with desmosomal mutations and the observed worsened clinical outcome in ARVC patients with high physiological testosterone levels (20, 22-25).

Methods

See supplement for full methods.

Patient record screening for atrial arrhythmias and semi-automated analysis of digital electrocardiograms (ECGs) from ARVC patients

Adult ARVC patients (>18 years of age) seen at a specialty clinic at a tertiary centre between 2010 and 2021 were classified into two disease severity groups: non-definite and definite cases based on 2010 ARVC Task Force Criteria (TFC) (1).

Clinical records were retrospectively reviewed to obtain information from several modalities including imaging, electrophysiology, histopathology, genetic testing and family history, to cumulatively fulfil a diagnostic classification. Patients exhibiting signs of confirmed disease based on specific combinations of minor or major criteria were classified as the “definite” group. Individuals exhibiting signs on diagnostic investigation congruous with the 2010 TFC as “borderline” or “possible” ARVC were cumulatively considered as the “non-definite” group, as they do not confer a confirmed diagnosis of ARVC. Non-definite cases were included in the analysis to represent individuals in the earlier phases of disease, with a less severe profile of phenotypic expression. Atrial fibrillation and flutter status was extracted from previous electrocardiograms (ECG) and clinical letters.

Digital ECG recordings (10 seconds, sampling frequency 500 Hz) from the most recent follow-up in Inherited Cardiac Conditions Clinic were collated and analyzed using Matlab and BioSigKit (https://doi.org/10.21105/joss.00671). To discern the extent of atrial involvement in definite ARVC patients in comparison with non-definite patients as well as controls, family members of index patients without meeting TFC and/or exclusion of ARVC pathogenic variants attained from targeted gene panel testing, were additionally included (“Control”). Digital ECG analysis was performed by multiple independent observers in recordings displaying sinus rhythm applying a custom-designed, semi-automated algorithm. ECGs were digitally filtered between 0.5 and 50 Hz and using a Chebyshev type II filter. The R wave was

automatically identified, and all complexes within the recording were averaged to improve signal quality. The isoelectric line was defined from P wave start to end.

Animal husbandry

Wildtype (WT) and plakoglobin deficient (Plako$^{+/-}$) littermate male mice (28), 129/Sv background, were housed in individually ventilated cages, (2-7 mice/ cage), monitored daily under standard conditions: 12 h light/dark cycle, 22±2 °C and 55±10% humidity. Food and water were available *ad libitum*.

Chronic DHT exposure in the murine model and experimental timeline

Young adult male mice (8-11 weeks) were assigned to either DHT or placebo/control treatment groups in mixed cages and were fitted with subcutaneous osmotic mini-pumps (Alzet 2006), containing either DHT (62.5 mg/mL in ethanol), or solvent alone (Control, Ctr), for 6 weeks (Figure 2). Age and DHT exposure time were matched for all groups. At least 40 minutes before pump implantation, mice were subcutaneously injected with 0.05 mL of Buprenorphine. Pump implant was performed under anaesthesia with isoflurane inhalation (max. 4%) in O_2 with a flow rate of 1-2 L/min. Animal handling staff and investigators were blinded to genotype and treatment. Echocardiography was performed at 6 weeks exposure. Murine hearts were then extracted by thoracotomy under deep terminal anaesthesia (4-5% isoflurane in O_2, flow rate 1-2 L/min,), and used for *in organ* and *in vitro* experimental analysis.

Anabolic androgenic steroid measurements

Murine serum DHT concentrations were determined by ultra-performance liquid chromatography-tandem mass spectrometry (LC-MS/MS) (Waters, Milford, MA, USA) as described before (79).

Murine conscious ECG measurements

Murine ECGs were recorded from conscious mice using a tunnel system (ecgTunnel, EMKA Technologies, France) as reported previously (80). Analyses were performed manually on compound potentials averaged from 20 beats taken at three time-points throughout a 4-min

recording with comparable heart rates between groups. Obtained values were then averaged per animal. For P-wave duration the monophasic part of the P-wave was only taken from ECGs displaying a stable isoelectric line.

Optical mapping of murine left atria

Activation and action potential duration (APD) maps were generated from isolated left atria loaded with the voltage-sensitive dye Di-4-ANEPPS (17.5 µM; Cambridge Bioscience, CA, USA), paced over a range of 120-80 ms cycle length (CL) as described (81-83). To analyze conduction changes in more detail, beat-to-beat variability in whole tissue activation times was evaluated during rapid physiological pacing. To do this, 10 individual activation maps were compared from the final 10 beats of a train of 50 pulses at 80 ms CL (84).

Murine echocardiography

Echocardiography was performed with a dedicated small animal system (Vevo 2100; Visualsonics Fujifilm, Toronto, Ont, Canada) under light anaesthesia (0.5-2% isoflurane in O_2) at a target heart rate of 390-440 bpm (27, 85-87). The investigators were blinded to intervention and genotype. Images were analyzed by a second blinded observer.

Transmembrane action potential recordings

Transmembrane action potentials were recorded from isolated, superfused murine left atria as described previously (81-83, 88).

Cellular electrophysiology

Individual murine left atrial cardiac myocytes were isolated by perfusion with a Tyrode's enzyme solution containing 20 µg/mL Liberase™ (Roche, Indianapolis, IN) or a collagenase+protease mix, 20 mM taurine and 30 µM $CaCl_2$, via Langendorff over a period of 10-15 min (81, 83). I_{Na} were evoked in voltage-clamp mode using standard protocols and low Na^+ solution (89). All currents were normalized to cell capacitance.

Murine atrial fiber size and collagen composition

10 μm left atrial transverse sections were stained with FITC-conjugated wheat germ agglutinin (lectin) and cell diameter as well as endomysial fibrosis were quantified using an automated analysis tool (90).

Super-resolution microscopy and $Na_v1.5$ cluster analysis

Freshly isolated murine left atrial cardiac myocytes were plated on 10mm diameter laminin-coated coverslips (Mattek, 35 mm dish, 1.5# coverglass), fixed, permeabilized and blocked. Cells were stained with primary rabbit anti-$Na_v1.5$ antibody (ASC-005, 1:50, Alomone Laboratories, Jerusalem, Israel) and after additional washing and blocking they were incubated in secondary antibody (F(ab')2- Goat anti-Rabbit IgG, Alexa Fluor 647, A212-56, 1:1000, ThermoFisher Scientific, Waltham, MA, USA). Direct stochastic optical reconstruction microscopy (dSTORM) (91) experiments were performed on a NIKON Eclipse Ti inverted N-STORM microscope equipped with a NIKON APO 100 x 1.49 NA total internal reflection fluorescence (TIRF) oil immersion objective. Immunolabelled samples were imaged in 0.5 mg/mL glucose oxidase, 40 μg/mL catalase, 10% wt/vol glucose and 100 mM MEA in PBS, pH 7.4 to induce Alexa 647 blinking. During dSTORM acquisition, the sample was continuously illuminated at 640 nm for 20,000 frames. Final rendered images of the localized molecules were generated using ThunderSTORM (92) and false coloured in FIJI. Final detections were subjected to a segmentation protocol, using a persistence-based clustering approach (93).

RNA sequencing of murine left atria

Poly(A) mRNA-enriched libraries were sequenced 75 cycles in a single read mode on the NextSeq-500 System (v2.5 Chemistry, Illumina). Acquired data was trimmed and FASTQ files were aligned using HISAT2 (version 2.1.0; ref Pertea) and the reference genome Ensembl Mus Musculus GRCm38. Differential expression analysis were performed in R (http://www.R-project.org/, R 3.4.1) using the DESeq2 package (94). Differential expression with a false discovery rate <0.05 was deemed significant. Results were visualized using R.

Statistics

All experiments and analyses were performed blinded to genotype and treatment. Data from murine studies was first subjected to outlier analysis, ROUT method, based around a false discovery rate, where α = 0.01 and outliers were removed (Prism v8, GraphPad Software, La Jolla, CA, USA). Associations between categorical variables were analyzed by Fisher´s exact test. Significance between groups for normally distributed data was taken as $p<0.05$, ordinary one-way or two-way (repeated) measures ANOVA, with Bonferroni's post hoc test, as appropriate. Non-normally distributed data was subjected to Kruskal-Wallis with significance level of $p<0.05$ and Dunn's post hoc test (Prism v8, GraphPad Software, La Jolla, CA, USA).

Study approval

Ethical approval for analysis of clinical data from Inherited Cardiac Conditions clinic at the University Hospital Queen Elisabeth, Birmingham, was granted by the local department of research ethics at the QE Hospital (Audit number CARMS-16044).

All animal procedures were approved by the UK Home Office (PPL number 30/2967 and PFDAAF77F) and by the institutional review board of University of Birmingham, UK. All animal procedures conformed to the guidelines from Directive 2010/63/EU of the European Parliament on the protection of animals used for scientific purposes.

Author contributions

LCS performed murine *in vivo* experiments, dSTORM experiments and analysis, gravimetry and histology analysis, RNAseq analysis, P wave analysis in human ECGs and wrote the manuscript. APH performed and analyzed microelectrode, optical mapping, patchclamp and dSTORM studies, performed gravimetry analysis and wrote the manuscript. TYY and COS set up and performed and analyzed optical mapping experiments. DMK designed dSTORM experiments and trained LCS and APH. JMP generated cluster analysis workflows.TW and PMM performed histology. FS codesigned experiments and trained TW, TYY, SNK. AA and TK screened clinical records according to Task Force Criteria. LCS, TK and COS performed semi-automated patient ECG analysis. CH prepared RNA samples and co-supervised PMM. VRC and GVG analyzed RNAseq. MS and AW performed and analyzed RNAseq. SNK and SBS performed *in vivo* experiments and gravimetry. MOR co-supervised TK. LFo analyzed *in vivo* experiments. SL trained LCS and co-supervised PMM. AK performed mass spectrometry of serum DHT concentrations. WA and GGL advised on AAS experimental design, DP co-supervised COS, RS co-supervised AA, KG co-supervised LCS. PK provided input throughout and co-supervised APH, FS, CH, VRC. LFa (co)-supervised LCS, APH, TYY, COS, TW, FS, AA, TK,VRC, SNK, CH, PMM, SBS, MOR, LFo, designed and coordinated the study and wrote the manuscript. All authors reviewed the results, revised the manuscript and approved the final version of it.

Acknowledgements

We thank Clara Apicella, Olivia Grech, Pushpa Patel, Genna Riley, and staff of BMSU Birmingham for expert support. We thankfully acknowledge the Centre of Membrane Proteins and Receptors COMPARE (www.birmingham-nottingham.ac.uk/compare) for both their expertise and infrastructure. We thank the Core Facility Genomics of the Medical Faculty Münster, University of Muenster. We thank all members of the Translational Research in Heart Failure and Arrhythmias Cluster for discussion.

This work was partially supported by European Union (grant agreement No 633196 [CATCH ME] to PK and LF), European Union BigData@Heart (grant agreement EU IMI 116074), British Heart Foundation (FS/13/43/30324 to PK and LF; PG/17/30/32961 to PK and APH, PG/20/22/35093 to PK; AA/18/2/34218 to PK and LF; FS/12/40/29712 to KG), German Centre for Cardiovascular Research supported by the German Ministry of Education and Research (DZHK to PK); Leducq Foundation to PK; UOB research development fund (LF). TYY studentship was supported by PSIBS to LF. Funding from the Wellcome Trust was received by KG (201543/B/16/Z) and WA (WT209492/Z/17/Z). KG is also funded by the MRC (MR/V009540/1). The Institute of Cardiovascular Sciences is a recipient of a BHF Accelerator Award (AA/18/2/34218).

GVG acknowledges support from the NIHR Birmingham ECMC, NIHR Birmingham SRMRC, Nanocommons H2020-EU (731032) and the MRC Heath Data Research UK (HDRUK/CFC/01), an initiative funded by UK Research and Innovation, Department of Health and Social Care (England) and the devolved administrations, and leading medical research charities. GVG and WA receive support from the NIHR Birmingham Biomedical Research Centre. The views expressed in this publication are those of the authors and not necessarily those of the NHS, the National Institute for Health and Care Research, the Medical Research Council or the Department of Health.

References

1. Marcus FI, McKenna WJ, Sherrill D, Basso C, Bauce B, Bluemke DA, et al. Diagnosis of arrhythmogenic right ventricular cardiomyopathy/dysplasia: proposed modification of the Task Force Criteria. *European heart journal.* 2010;31(7):806-14.

2. Morita H, Kusano-Fukushima K, Nagase S, Fujimoto Y, Hisamatsu K, Fujio H, et al. Atrial fibrillation and atrial vulnerability in patients with Brugada syndrome. *J Am Coll Cardiol.* 2002;40(8):1437-44.

3. Tonet JL, Castro-Miranda R, Iwa T, Poulain F, Frank R, and Fontaine GH. Frequency of supraventricular tachyarrhythmias in arrhythmogenic right ventricular dysplasia. *The American journal of cardiology.* 1991;67(13):1153.

4. Camm CF, James CA, Tichnell C, Murray B, Bhonsale A, te Riele AS, et al. Prevalence of atrial arrhythmias in arrhythmogenic right ventricular dysplasia/cardiomyopathy. *Heart rhythm.* 2013;10(11):1661-8.

5. Chu AF, Zado E, and Marchlinski FE. Atrial arrhythmias in patients with arrhythmogenic right ventricular cardiomyopathy/dysplasia and ventricular tachycardia. *The American journal of cardiology.* 2010;106(5):720-2.

6. Baturova MA, Haugaa KH, Jensen HK, Svensson A, Gilljam T, Bundgaard H, et al. Atrial fibrillation as a clinical characteristic of arrhythmogenic right ventricular cardiomyopathy: Experience from the Nordic ARVC Registry. *Int J Cardiol.* 2020;298:39-43.

7. Priori SG, Blomstrom-Lundqvist C, Mazzanti A, Blom N, Borggrefe M, Camm J, et al. 2015 ESC Guidelines for the management of patients with ventricular arrhythmias and the prevention of sudden cardiac death: The Task Force for the Management of Patients with Ventricular Arrhythmias and the Prevention of Sudden Cardiac Death of the European Society of Cardiology (ESC). Endorsed by: Association for European Paediatric and Congenital Cardiology (AEPC). *European heart journal.* 2015;36(41):2793-867.

8. Sagoe D, Molde H, Andreassen CS, Torsheim T, and Pallesen S. The global epidemiology of anabolic-androgenic steroid use: a meta-analysis and meta-regression analysis. *Annals of Epidemiology.* 2014;24(5):383-98.

9. Urhausen A, Albers T, and Kindermann W. Are the cardiac effects of anabolic steroid abuse in strength athletes reversible? *Heart.* 2004;90(5):496-501.

10. Luijkx T, Velthuis BK, Backx FJG, Buckens CFM, Prakken NHJ, Rienks R, et al. Anabolic androgenic steroid use is associated with ventricular dysfunction on cardiac MRI in strength trained athletes. *International journal of cardiology.* 2013;167(3):664-8.

11. Alizade E, Avci A, Fidan S, Tabakci M, Bulut M, Zehir R, et al. The Effect of Chronic Anabolic-Androgenic Steroid Use on Tp-E Interval, Tp-E/Qt Ratio, and Tp-E/Qtc Ratio in Male Bodybuilders. *Ann Noninvasive Electrocardiol.* 2015;20(6):592-600.

12. Marsh JD, Lehmann MH, Ritchie RH, Gwathmey JK, Green GE, and Schiebinger RJ. Androgen receptors mediate hypertrophy in cardiac myocytes. *Circulation.* 1998;98(3):256-61.

13. Medei E, Marocolo M, Rodrigues DD, Arantes PC, Takiya CM, Silva J, et al. Chronic treatment with anabolic steroids induces ventricular repolarization disturbances: Cellular, ionic and molecular mechanism. *Journal of molecular and cellular cardiology.* 2010;49(2):165-75.

14. Pirompol P, Teekabut V, Weerachatyanukul W, Bupha-Intr T, and Wattanapermpool J. Supra-physiological dose of testosterone induces pathological cardiac hypertrophy. *J Endocrinol.* 2016;229(1):13-23.

15. Berger D, Folsom AR, Schreiner PJ, Chen LY, Michos ED, O'Neal WT, et al. Plasma total testosterone and risk of incident atrial fibrillation: The Atherosclerosis Risk in Communities (ARIC) study. *Maturitas.* 2019;125:5-10.

16. Sullivan ML, Martinez CM, and Gallagher EJ. Atrial fibrillation and anabolic steroids. *J Emerg Med.* 1999;17(5):851-7.

17. Tsai WC, Lee TI, Chen YC, Kao YH, Lu YY, Lin YK, et al. Testosterone replacement increases aged pulmonary vein and left atrium arrhythmogenesis with enhanced adrenergic activity. *International journal of cardiology.* 2014;176(1):110-8.

18. Lau DH, Stiles MK, John B, Shashidhar, Young GD, and Sanders P. Atrial fibrillation and anabolic steroid abuse. *Int J Cardiol.* 2007;117(2):e86-7.

19. Rootwelt-Norberg C, Lie OH, Chivulescu M, Castrini AI, Sarvari SI, Lyseggen E, et al. Sex differences in disease progression and arrhythmic risk in patients with arrhythmogenic cardiomyopathy. *Europace : European pacing, arrhythmias, and cardiac electrophysiology : journal of the working groups on cardiac pacing, arrhythmias, and cardiac cellular electrophysiology of the European Society of Cardiology.* 2021;23(7):1084-91.

20. Akdis D, Saguner AM, Shah K, Wei C, Medeiros-Domingo A, von Eckardstein A, et al. Sex hormones affect outcome in arrhythmogenic right ventricular cardiomyopathy/dysplasia: from a stem cell derived cardiomyocyte-based model to clinical biomarkers of disease outcome. *Eur Heart J.* 2017.

21. Wilde AAM, Semsarian C, Marquez MF, Sepehri Shamloo A, Ackerman MJ, Ashley EA, et al. European Heart Rhythm Association (EHRA)/Heart Rhythm Society (HRS)/Asia Pacific Heart Rhythm Society (APHRS)/Latin American Heart Rhythm Society (LAHRS) Expert Consensus Statement on the State of Genetic Testing for Cardiac Diseases. *Heart rhythm.* 2022.

22. Asimaki A, Syrris P, Wichter T, Matthias P, Saffitz JE, and McKenna WJ. A novel dominant mutation in plakoglobin causes Arrhythmogenic right ventricular cardiomyopathy. *American journal of human genetics.* 2007;81(5):964-73.

23. Protonotarios N, Tsatsopoulou A, Anastasakis A, Sevdalis E, McKoy G, Stratos K, et al. Genotype-phenotype assessment in autosomal recessive arrhythmogenic right ventricular cardiomyopathy (Naxos disease) caused by a deletion in plakoglobin. *Journal of the American College of Cardiology.* 2001;38(5):1477-84.

24. Antoniades L, Tsatsopoulou A, Anastasakis A, Syrris P, Asimaki A, Panagiotakos D, et al. Arrhythmogenic right ventricular cardiomyopathy caused by deletions in plakophilin-2 and plakoglobin (Naxos disease) in families from Greece and Cyprus: genotype-phenotype relations, diagnostic features and prognosis. *European heart journal.* 2006;27(18):2208-16.

25. McKoy G, Protonotarios N, Crosby A, Tsatsopoulou A, Anastasakis A, Coonar A, et al. Identification of a deletion in plakoglobin in arrhythmogenic right ventricular cardiomyopathy with palmoplantar keratoderma and woolly hair (Naxos disease). *Lancet (London, England).* 2000;355(9221):2119-24.

26. Li J, Swope D, Raess N, Cheng L, Muller EJ, and Radice GL. Cardiac tissue-restricted deletion of plakoglobin results in progressive cardiomyopathy and activation of {beta}-catenin signaling. *Mol Cell Biol.* 2011;31(6):1134-44.

27. Fabritz L, Hoogendijk MG, Scicluna BP, van Amersfoorth SC, Fortmueller L, Wolf S, et al. Load-reducing therapy prevents development of arrhythmogenic right ventricular cardiomyopathy in plakoglobin-deficient mice. *J Am Coll Cardiol.* 2011;57(6):740-50.

28. Kirchhof P, Fabritz L, Zwiener M, Witt H, Schafers M, Zellerhoff S, et al. Age- and training-dependent development of arrhythmogenic right ventricular cardiomyopathy in heterozygous plakoglobin-deficient mice. *Circulation.* 2006;114(17):1799-806.

29. Weinsaft JW, Kochav JD, Kim J, Gurevich S, Volo SC, Afroz A, et al. P wave area for quantitative electrocardiographic assessment of left atrial remodeling. *PLoS One.* 2014;9(6):e99178.

30. Magnani JW, Zhu L, Lopez F, Pencina MJ, Agarwal SK, Soliman EZ, et al. P-wave indices and atrial fibrillation: cross-cohort assessments from the Framingham Heart Study (FHS) and Atherosclerosis Risk in Communities (ARIC) study. *Am Heart J.* 2015;169(1):53-61 e1.

31. Soliman EZ, Prineas RJ, Case LD, Zhang ZM, and Goff DC, Jr. Ethnic distribution of ECG predictors of atrial fibrillation and its impact on understanding the ethnic distribution of ischemic stroke in the Atherosclerosis Risk in Communities (ARIC) study. *Stroke; a journal of cerebral circulation.* 2009;40(4):1204-11.

32. Gorenek B, Birdane A, Kudaiberdieva G, Goktekin O, Cavusoglu Y, Unalir A, et al. P wave amplitude and duration may predict immediate recurrence of atrial fibrillation after internal cardioversion. *Ann Noninvasive Electrocardiol.* 2003;8(3):215-8.

33. Baturova MA, Svensson A, Aneq MA, Svendsen JH, Risum N, Sherina V, et al. Evolution of P-wave indices during long-term follow-up as markers of atrial substrate progression in arrhythmogenic right ventricular cardiomyopathy. *Europace : European pacing, arrhythmias, and cardiac electrophysiology : journal of the working groups on cardiac pacing, arrhythmias, and cardiac cellular electrophysiology of the European Society of Cardiology.* 2021;23(23 Suppl 1):i29-i37.

34. Kirchhof P. The future of atrial fibrillation management: integrated care and stratified therapy. *Lancet.* 2017;390(10105):1873-87.

35. Heijman J, Guichard JB, Dobrev D, and Nattel S. Translational Challenges in Atrial Fibrillation. *Circulation research.* 2018;122(5):752-73.

36. van Rijen HV, and de Bakker JM. Penetrance of monogenetic cardiac conduction diseases. A matter of conduction reserve? *Cardiovasc Res.* 2007;76(3):379-80.

37. van Rijen HV, de Bakker JM, and van Veen TA. Hypoxia, electrical uncoupling, and conduction slowing: Role of conduction reserve. *Cardiovasc Res.* 2005;66(1):9-11.

38. Campian ME, Verberne HJ, Hardziyenka M, de Groot EA, van Moerkerken AF, van Eck-Smit BL, et al. Assessment of inflammation in patients with arrhythmogenic right ventricular cardiomyopathy/dysplasia. *Eur J Nucl Med Mol Imaging.* 2010;37(11):2079-85.

39. Chelko SP, Asimaki A, Lowenthal J, Bueno-Beti C, Bedja D, Scalco A, et al. Therapeutic Modulation of the Immune Response in Arrhythmogenic Cardiomyopathy. *Circulation.* 2019.

40. Frustaci A, Chimenti C, Bellocci F, Morgante E, Russo MA, and Maseri A. Histological substrate of atrial biopsies in patients with lone atrial fibrillation. *Circulation.* 1997;96(4):1180-4.

41. Chung MK, Martin DO, Sprecher D, Wazni O, Kanderian A, Carnes CA, et al. C-reactive protein elevation in patients with atrial arrhythmias: inflammatory mechanisms and persistence of atrial fibrillation. *Circulation.* 2001;104(24):2886-91.

42. Aviles RJ, Martin DO, Apperson-Hansen C, Houghtaling PL, Rautaharju P, Kronmal RA, et al. Inflammation as a risk factor for atrial fibrillation. *Circulation.* 2003;108(24):3006-10.

43. Xu J, Cui G, Esmailian F, Plunkett M, Marelli D, Ardehali A, et al. Atrial extracellular matrix remodeling and the maintenance of atrial fibrillation. *Circulation.* 2004;109(3):363-8.

44. Boldt A, Wetzel U, Lauschke J, Weigl J, Gummert J, Hindricks G, et al. Fibrosis in left atrial tissue of patients with atrial fibrillation with and without underlying mitral valve disease. *Heart.* 2004;90(4):400-5.

45. Marcus FI, Fontaine GH, Guiraudon G, Frank R, Laurenceau JL, Malergue C, et al. Right ventricular dysplasia: a report of 24 adult cases. *Circulation.* 1982;65(2):384-98.

46. Thiene G, Corrado D, Nava A, Rossi L, Poletti A, Boffa GM, et al. Right ventricular cardiomyopathy: is there evidence of an inflammatory aetiology? *European heart journal.* 1991;12 Suppl D:22-5.

47. Galan M, Varona S, Guadall A, Orriols M, Navas M, Aguilo S, et al. Lysyl oxidase overexpression accelerates cardiac remodeling and aggravates angiotensin II-induced hypertrophy. *FASEB J.* 2017;31(9):3787-99.

48. Lu C, Ren D, Wang X, Ha T, Liu L, Lee EJ, et al. Toll-like receptor 3 plays a role in myocardial infarction and ischemia/reperfusion injury. *Biochimica et biophysica acta.* 2014;1842(1):22-31.

49. Liu L, Wang Y, Cao ZY, Wang MM, Liu XM, Gao T, et al. Up-regulated TLR4 in cardiomyocytes exacerbates heart failure after long-term myocardial infarction. *J Cell Mol Med.* 2015;19(12):2728-40.

50. Okamura Y, Watari M, Jerud ES, Young DW, Ishizaka ST, Rose J, et al. The extra domain A of fibronectin activates Toll-like receptor 4. *J Biol Chem.* 2001;276(13):10229-33.

51. Verheule S, Sato T, Everett T, Engle SK, Otten D, von der Lohe MR, et al. Increased vulnerability to atrial fibrillation in transgenic mice with selective atrial fibrosis caused by overexpression of TGF-beta 1. *Circulation research.* 2004;94(11):1458-65.

52. Fabritz L, and Kirchhof P. Selective atrial profibrotic signalling in mice and man. *Cardiovasc Res.* 2013;99(4):592-4.

53. Papamitsou T, Barlagiannis D, Papaliagkas V, Kotanidou E, and Dermentzopoulou-Theodoridou M. Testosterone-induced hypertrophy, fibrosis and apoptosis of cardiac cells--an ultrastructural and immunohistochemical study. *Med Sci Monit.* 2011;17(9):BR266-73.

54. Akhmetshina A, Dees C, Pileckyte M, Szucs G, Spriewald BM, Zwerina J, et al. Rho-associated kinases are crucial for myofibroblast differentiation and production of extracellular matrix in scleroderma fibroblasts. *Arthritis Rheum.* 2008;58(8):2553-64.

55. Ongherth A, Pasch S, Wuertz CM, Nowak K, Kittana N, Weis CA, et al. p63RhoGEF regulates auto- and paracrine signaling in cardiac fibroblasts. *J Mol Cell Cardiol.* 2015;88:39-54.

56. Kim J, Wende AR, Sena S, Theobald HA, Soto J, Sloan C, et al. Insulin-like growth factor I receptor signaling is required for exercise-induced cardiac hypertrophy. *Mol Endocrinol.* 2008;22(11):2531-43.

57. Weeks KL, Bernardo BC, Ooi JYY, Patterson NL, and McMullen JR. The IGF1-PI3K-Akt Signaling Pathway in Mediating Exercise-Induced Cardiac Hypertrophy and Protection. *Adv Exp Med Biol.* 2017;1000:187-210.

58. Wang J, Li Z, Du J, Li J, Zhang Y, Liu J, et al. The expression profile analysis of atrial mRNA in rats with atrial fibrillation: the role of IGF1 in atrial fibrosis. *BMC Cardiovasc Disord.* 2019;19(1):40.

59. Wu Y, Zhao W, Zhao J, Pan J, Wu Q, Zhang Y, et al. Identification of androgen response elements in the insulin-like growth factor I upstream promoter. *Endocrinology.* 2007;148(6):2984-93.

60. Han P, Li W, Lin CH, Yang J, Shang C, Nuernberg ST, et al. A long noncoding RNA protects the heart from pathological hypertrophy. *Nature.* 2014;514(7520):102-6.

61. Luo Y, Xu Y, Liang C, Xing W, and Zhang T. The mechanism of myocardial hypertrophy regulated by the interaction between mhrt and myocardin. *Cell Signal.* 2018;43:11-20.

62. Kontaraki JE, Parthenakis FI, Patrianakos AP, Karalis IK, and Vardas PE. Altered expression of early cardiac marker genes in circulating cells of patients with hypertrophic cardiomyopathy. *Cardiovasc Pathol.* 2007;16(6):329-35.

63. Bhargava A, Lin XM, Novak P, Mehta K, Korchev Y, Delmar M, et al. Super-resolution Scanning Patch Clamp Reveals Clustering of Functional Ion Channels in Adult Ventricular Myocyte. *Circulation research.* 2013;112(8):1112-+.

64. Leo-Macias A, Agullo-Pascual E, Sanchez-Alonso JL, Keegan S, Lin XM, Arcos T, et al. Nanoscale visualization of functional adhesion/excitability nodes at the intercalated disc. *Nature communications.* 2016;7:11.

65. Asimaki A, Kapoor S, Plovie E, Arndt AK, Adams E, Liu ZZ, et al. Identification of a New Modulator of the Intercalated Disc in a Zebrafish Model of Arrhythmogenic Cardiomyopathy. *Sci Transl Med.* 2014;6(240):15.

66. Noorman M, Hakim S, Kessler E, Groeneweg JA, Cox M, Asimaki A, et al. Remodeling of the cardiac sodium channel, connexin43, and plakoglobin at the intercalated disk in patients with arrhythmogenic cardiomyopathy. *Heart rhythm : the official journal of the Heart Rhythm Society.* 2013;10(3):412-9.

67. Rizzo S, Lodder EM, Verkerk AO, Wolswinkel R, Beekman L, Pilichou K, et al. Intercalated disc abnormalities, reduced Na(+) current density, and conduction slowing in desmoglein-2 mutant mice prior to cardiomyopathic changes. *Cardiovascular research.* 2012;95(4):409-18.

68. Sato PY, Musa H, Coombs W, Guerrero-Serna G, Patino GA, Taffet SM, et al. Loss of plakophilin-2 expression leads to decreased sodium current and slower conduction velocity in cultured cardiac myocytes. *Circ Res.* 2009;105(6):523-6.

69. Cerrone M, Lin X, Zhang M, Agullo-Pascual E, Pfenniger A, Chkourko Gusky H, et al. Missense mutations in plakophilin-2 cause sodium current deficit and associate with a Brugada syndrome phenotype. *Circulation.* 2014;129(10):1092-103.

70. Hofmann F, Fabritz L, Stieber J, Schmitt J, Kirchhof P, Ludwig A, et al. Ventricular HCN channels decrease the repolarization reserve in the hypertrophic heart. *Cardiovasc Res.* 2012;95(3):317-26.

71. Wagner S, Dybkova N, Rasenack EC, Jacobshagen C, Fabritz L, Kirchhof P, et al. Ca2+/calmodulin-dependent protein kinase II regulates cardiac Na+ channels. *J Clin Invest.* 2006;116(12):3127-38.

72. Agullo-Pascual E, Lin XM, Leo-Macias A, Zhang ML, Liang FX, Li Z, et al. Super-resolution imaging reveals that loss of the C-terminus of connexin43 limits microtubule plus-end capture and Na(V)1.5 localization at the intercalated disc. *Cardiovascular research.* 2014;104(2):371-81.

73. te Riele A, Agullo-Pascual E, James CA, Leo-Macias A, Cerrone M, Zhang ML, et al. Multilevel analyses of SCN5A mutations in arrhythmogenic right ventricular dysplasia/cardiomyopathy suggest non-canonical mechanisms for disease pathogenesis. *Cardiovascular research.* 2017;113(1):102-11.

74. Furlanello F, Serdoz LV, Cappato R, and De Ambroggi L. Illicit drugs and cardiac arrhythmias in athletes. *Eur J Cardiovasc Prev Rehabil.* 2007;14(4):487-94.

75. Akcakoyun M, Alizade E, Gundogdu R, Bulut M, Tabakci MM, Acar G, et al. Long-term anabolic androgenic steroid use is associated with increased atrial electromechanical delay in male bodybuilders. *Biomed Res Int.* 2014;2014:451520.

76. Nieschlag E, and Vorona E. Doping with anabolic androgenic steroids (AAS): Adverse effects on non-reproductive organs and functions. *Rev Endocr Metab Disord.* 2015;16(3):199-211.

77. Asimaki A, Tandri H, Huang H, Halushka MK, Gautam S, Basso C, et al. A new diagnostic test for arrhythmogenic right ventricular cardiomyopathy. *N Engl J Med.* 2009;360(11):1075-84.

78. Takehara N, Makita N, Kawabe J, Sato N, Kawamura Y, Kitabatake A, et al. A cardiac sodium channel mutation identified in Brugada syndrome associated with atrial standstill. *J Intern Med.* 2004;255(1):137-42.

79. Kulle AE, Riepe FG, Melchior D, Hiort O, and Holterhus PM. A novel ultrapressure liquid chromatography tandem mass spectrometry method for the simultaneous determination of androstenedione, testosterone, and dihydrotestosterone in pediatric blood samples: age- and sex-specific reference data. *J Clin Endocrinol Metab.* 2010;95(5):2399-409.

80. Silbernagel N, Walecki M, Schafer MK, Kessler M, Zobeiri M, Rinne S, et al. The VAMP-associated protein VAPB is required for cardiac and neuronal pacemaker channel function. *FASEB J.* 2018;32(11):6159-73.

81. Holmes AP, Yu TY, Tull S, Syeda F, Kuhlmann SM, O'Brien S-M, et al. A Regional Reduction in Ito and IKACh in the Murine Posterior Left Atrial Myocardium Is Associated with Action Potential Prolongation and Increased Ectopic Activity. *PloS one.* 2016;11(5):e0154077.

82. Yu TY, Syeda F, Holmes AP, Osborne B, Dehghani H, Brain KL, et al. An automated system using spatial oversampling for optical mapping in murine atria. Development and validation with monophasic and transmembrane action potentials. *Progress in biophysics and molecular biology.* 2014.

83. Syeda F, Holmes AP, Yu TY, Tull S, Kuhlmann SM, Pavlovic D, et al. PITX2 Modulates Atrial Membrane Potential and the Antiarrhythmic Effects of Sodium-Channel Blockers. *J Am Coll Cardiol.* 2016;68(17):1881-94.

84. O'Shea C, Holmes AP, Yu TY, Winter J, Wells SP, Correia J, et al. ElectroMap: High-throughput open-source software for analysis and mapping of cardiac electrophysiology. *Scientific reports.* 2019;9(1):1389.

85. Kirchhof P, Kahr PC, Kaese S, Piccini I, Vokshi I, Scheld HH, et al. PITX2c is expressed in the adult left atrium, and reducing Pitx2c expression promotes atrial fibrillation inducibility and complex changes in gene expression. *Circ Cardiovasc Genet.* 2011;4(2):123-33.

86. Blana A, Kaese S, Fortmuller L, Laakmann S, Damke D, van Bragt K, et al. Knock-in gain-of-function sodium channel mutation prolongs atrial action potentials and alters atrial vulnerability. *Heart Rhythm.* 2010;7(12):1862-9.

87. Fabritz L, Kirchhof P, Fortmuller L, Auchampach JA, Baba HA, Breithardt G, et al. Gene dose-dependent atrial arrhythmias, heart block, and brady-cardiomyopathy in mice overexpressing A(3) adenosine receptors. *Cardiovasc Res.* 2004;62(3):500-8.

88. Lemoine MD, Duverger JE, Naud P, Chartier D, Qi XY, Comtois P, et al. Arrhythmogenic left atrial cellular electrophysiology in a murine genetic long QT syndrome model. *Cardiovasc Res.* 2011;92(1):67-74.

89. S OB, Holmes AP, Johnson DM, Kabir SN, C OS, M OR, et al. Increased atrial effectiveness of flecainide conferred by altered biophysical properties of sodium channels. *J Mol Cell Cardiol.* 2022;166:23-35.

90. Winters J, von Braunmuhl ME, Zeemering S, Gilbers M, Brink TT, Scaf B, et al. JavaCyte, a novel open-source tool for automated quantification of key hallmarks of cardiac structural remodeling. *Scientific reports.* 2020;10(1):20074.

91. Kavanagh DM, Smyth AM, Martin KJ, Dun A, Brown ER, Gordon S, et al. A molecular toggle after exocytosis sequesters the presynaptic syntaxin1a molecules involved in prior vesicle fusion. *Nature communications.* 2014;5:14.

92. Ovesny M, Krizek P, Borkovec J, Svindrych ZK, and Hagen GM. ThunderSTORM: a comprehensive ImageJ plug-in for PALM and STORM data analysis and super-resolution imaging. *Bioinformatics.* 2014;30(16):2389-90.

93. Pike JA, Khan AO, Pallini C, Thomas SG, Mund M, Ries J, et al. Topological data analysis quantifies biological nano-structure from single molecule localization microscopy. *Bioinformatics (Oxford, England).* 2020;36(5):1614-21.

94. Love MI, Huber W, and Anders S. Moderated estimation of fold change and dispersion for RNA-seq data with DESeq2. *Genome Biol.* 2014;15(12):550.

95. Jaoude SA, Leclercq JF, and Coumel P. Progressive ECG changes in arrhythmogenic right ventricular disease. Evidence for an evolving disease. *European heart journal.* 1996;17(11):1717-22.

96. Brembilla-Perrot B, Jacquemin L, Houplon P, Houriez P, Beurrier D, Berder V, et al. Increased atrial vulnerability in arrhythmogenic right ventricular disease. *Am Heart J.* 1998;135(5 Pt 1):748-54.

97. Peters S, Trummel M, and Meyners W. Prevalence of right ventricular dysplasia-cardiomyopathy in a non-referral hospital. *Int J Cardiol.* 2004;97(3):499-501.

98. Saguner AM, Ganahl S, Kraus A, Baldinger SH, Medeiros-Domingo A, Saguner AR, et al. Clinical role of atrial arrhythmias in patients with arrhythmogenic right ventricular dysplasia. *Circulation journal : official journal of the Japanese Circulation Society.* 2014;78(12):2854-61.

99. Wu L, Guo J, Zheng L, Chen G, Ding L, Qiao Y, et al. Atrial Remodeling and Atrial Tachyarrhythmias in Arrhythmogenic Right Ventricular Cardiomyopathy. *The American journal of cardiology.* 2016;118(5):750-3.

100. Bourfiss M, Te Riele AS, Mast TP, Cramer MJ, JF VDH, TA VANV, et al. Influence of Genotype on Structural Atrial Abnormalities and Atrial Fibrillation or Flutter in Arrhythmogenic Right Ventricular Dysplasia/Cardiomyopathy. *J Cardiovasc Electrophysiol.* 2016;27(12):1420-8.

101. Mazzanti A, Ng K, Faragli A, Maragna R, Chiodaroli E, Orphanou N, et al. Arrhythmogenic Right Ventricular Cardiomyopathy: Clinical Course and Predictors of Arrhythmic Risk. *J Am Coll Cardiol.* 2016;68(23):2540-50.

102. Gilljam T, Haugaa KH, Jensen HK, Svensson A, Bundgaard H, Hansen J, et al. Heart transplantation in arrhythmogenic right ventricular cardiomyopathy - Experience from the Nordic ARVC Registry. *Int J Cardiol.* 2018;250:201-6.

103. Wu L, Bao J, Liang E, Fan S, Zheng L, Du Z, et al. Atrial involvement in arrhythmogenic right ventricular cardiomyopathy patients referred for ventricular arrhythmias ablation. *J Cardiovasc Electrophysiol.* 2018;29(10):1388-95.

104. Mussigbrodt A, Knopp H, Efimova E, Weber A, Bertagnolli L, Hilbert S, et al. Supraventricular arrhythmias in patients with arrhythmogenic right ventricular dysplasia/cardiomyopathy associate with long-term outcome after catheter ablation of ventricular tachycardias. *Europace : European pacing, arrhythmias, and cardiac electrophysiology : journal of the working groups on cardiac pacing, arrhythmias, and cardiac cellular electrophysiology of the European Society of Cardiology.* 2018;20(7):1182-7.

105. Cardona-Guarache R, Astrom-Aneq M, Oesterle A, Asirvatham R, Svetlichnaya J, Marcus GM, et al. Atrial arrhythmias in patients with arrhythmogenic right ventricular cardiomyopathy: Prevalence, echocardiographic predictors, and treatment. *J Cardiovasc Electrophysiol.* 2019;30(10):1801-10.

106. Kikuchi N, Shiga T, Suzuki A, and Hagiwara N. Atrial tachyarrhythmias and heart failure events in patients with arrhythmogenic right ventricular cardiomyopathy. *Int J Cardiol Heart Vasc.* 2020;31:100669.

Tables

Table 1 - ARVC patient characteristics

Patient characteristics	Non-definite n=97	Definite n=49	p value
Age at last follow-up, mean ± std (years)	42 ± 18	43 ± 16	0.743
Male, n (%)	42 (43)	36 (73)	**0.0008**
Atrial fibrillation/flutter, n (%)	3 (3)	12 (24)	**0.0001**

Table 2 - Phenotypic characteristics of the murine model

	WT control	WT DHT	Plako$^{+/-}$ control	Plako$^{+/-}$ DHT
Age at terminal experiment (weeks) (n=59-67)	16.5 ± 0.2	16.7 ± 0.2	16.0 ± 0.2	16.6 ± 0.2
Body weight (g) (n=59-65)	27.9 ± 0.4	29.4 ± 0.4*	27.9 ± 0.4	29.2 ± 0.4^{+}
Serum DHT (nM) (n=11-18)	0.25 ± 0.06	0.85 ± 0.21*	0.31 ± 0.11	1.22 ± 0.29^{+}
Left atrial weight:tibia length (mg mm^{-1}) (n=29-32)	0.23 ± 0.01	0.24 ± 0.01	0.22 ± 0.01	0.28 ± 0.02^{+}
Right atrial weight:tibia length (mg mm^{-1}) (n=28-32)	0.25 ± 0.01	0.29 ± 0.01*	0.26 ± 0.02	0.30 ± 0.03
Seminal vesicle weight:tibia length (mg mm^{-1}) (n=39-45)	6.0 ± 0.4	6.0 ± 0.3	5.5 ± 0.2	6.5 ± 0.3^{+}
Murine echocardiography (light anaesthesia, mean heart rate 390-440 bpm)				
Heart rate (bpm) (n=18-28)	411 ± 3	415 ± 3	413 ± 3	414 ± 3
Left atrial diameter:tibia length (mm mm^{-1}) (n=15-23)	0.130 ± 0.005	0.140 ± 0.007	0.138 ± 0.006	0.144 ± 0.007
Left ventricular mass:tibia length (mg mm^{-1}) (n=18-28)	5.4 ± 0.3	5.5 ± 0.3	4.9 ± 0.2	6.0 ± 0.3^{+}
Left ventricular ejection fraction (%) (n=18-28)	43 ± 3	50 ± 3	47 ± 2	45 ± 3

Data presented as mean ± SEM, n=number of animals per group, *p<0.05 vs WT control (post-hoc t-test, 2-way ANOVA p<0.05 for DHT treatment), $^{+}$p<0.05 vs Plako$^{+/-}$ control (post-hoc t-test, 2-way ANOVA p<0.05 for DHT treatment)

Table 3 - Prevalence of Atrial fibrillation/flutter (Atrial Arrhythmia, AA) in ARVC patients

Study [First author]	Year	Number of patients	Mean age [years, ± SD / (range)]	**AA prevalence [%]**	Patients with AA; male [%]	Patients without AA; male [%]
Tonet (3)	1991	72	38 (16-73)	**24**	n.r.	n.r.
Jaoude (95)	1996	74	37.2 ± 13.5 (11-68)	**4**	n.r.	n.r.
Brembilla-Perot (96)	1998	47	44 ± 18 (17-72)	**17**	63	n.r.
Peters (97)	2004	80	45.9 (22-91)	**30**	n.r.	n.r.
Chu (5)	2010	36	47 (17-80)	**42**	80	76
Camm (4)	2013	248	41.6 ± 14	**14**	69	50
Saguner (98)	2014	90	49.7 ± 14.6	**20**	61	64
Wu (99)	2016	294	37.7 ± 14.8	**13**	62	77
Bourfiss (100)	2016	66	46.4 ± 15.8	**21**	79	50
Mazzanti (101)	2016	301	38 ± 18	**4**	n.r.	n.r.
Gilljam (102)	2018	183	Median 46 (14-65)	**9**	n.r.	n.r.
Wu (103)	2018	100	37.1 ± 12.1	**9**	n.r.	n.r.
Müssigbrodt (104)	2018	70	53.2 ± 14.0	**37**	62	73
Cardona-Guarache (105)	2019	117	52 ± 14	**22**	69	57
Kikuchi (106)	2020	90	44 ± 15	**36**	78	76
Baturova (33)	2021	100	41 (30-55)	**28**	n.r.	n.r.
		∑ 1915		**Weighted mean: 15%**		
Present study: ARVC diagnosis						
Non-definite		97	42 ± 18	**3**	67	43
Definite		49	43 ± 16	**24**	67	73

SD = standard deviation, n.r. = not reported

Supplement to

Male sex hormone and reduced plakoglobin jointly impair atrial conduction and cardiac sodium currents

Full methods

Ethical statement

All animal procedures were approved by the UK Home Office (PPL number 30/2967 and PFDAAF77F) and by the institutional review board of University of Birmingham. All animal procedures conformed to the guidelines from Directive 2010/63/EU of the European Parliament on the protection of animals used for scientific purposes. Wildtype (WT) and plakoglobin deficient (Plako$^{+/-}$) male 129/Sv mice (1) were housed in individually ventilated cages, (2-7 mice/ cage), under standard conditions: 12 h light/dark circle, 22 °C and 55% humidity. Food and water were available *ad libitum*. The general health status of all mice (bearing, grooming, behaviour) used in the study was monitored daily and immediately prior all animal procedures.

Chronic 5α-dihydrotestosterone (DHT) exposure and experimental timeline

Mice were age and weight matched and assigned to either DHT or placebo/control treatment groups. At 8-10 weeks of age, they were fitted with a subcutaneous osmotic mini-pump (Alzet, Cupertino, CA, US) containing either DHT (62.5 mg/mL in ethanol), or ethanol alone (Control - Ctr). At least 40 minutes before pump implantation, mice were subcutaneously injected with 0.05 mL of Buprenorphine. Pump implant was performed under anaesthesia with isoflurane inhalation in O_2. After implant, mice were subcutaneously injected with 0.5 mL of glucose saline. An echocardiogram was performed at 6 weeks exposure. At 4 months of age, following the 6 weeks DHT or control treatment, mouse hearts were extracted by thoracotomy under deep terminal anaesthesia (4-5% isoflurane inhalation in O_2), and used for *in vitro* experimental analysis, as summarised in Figure 2.

Murine conscious ECG measurements

Murine surface six lead ECGs were recorded from conscious mice using a tunnel system (ecgTunnel, EMKA Technologies, France) with contact electrodes installed in the tunnel

floor. ECG recording started after a short adaptation period. All measurements were conducted during daytime. Mean ECG recording time was approximately 4 minutes (3.64 ± 0.13 min) using the IOX software (EMKA Technologies, France).

The analysis of ECG recordings was performed blinded to genotype and group (placebo, DHT). All parameters were measured from lead II. Mean heart rate was measured by using the ecgAUTO software (EMKA Technologies). Detected heart beats were checked for ECG quality including a stable isoelectric line and ECG recordings were also scanned manually for arrhythmias and abnormalities by the blinded observer.

Two types of P-wave morphology, monophasic and biphasic, were detected. Automatic analysis approaches by the software were not able to distinguish between the two types. Hence, biphasic P-waves would have been at risk of being underestimated in duration. Therefore, the software was used for creating compound potentials of 20 single beats delivering very clear ECG waves. Signals were chosen for similar P-wave morphology and heart rate (to exclude heart rate-dependent effects). For each animal, three of those compound potentials were analyzed manually for P-wave duration, PR-, QRS-, and QT-interval and averaged.

Murine echocardiography

Echocardiography was performed as previously described (2, 3) with a dedicated small animal system (Vevo 2100; Visual Sonics, Toronto, Ont, Canada, now Fujifilm) under light anaesthesia (0.5-2% isoflurane in O_2) in a warm environment to keep body temperature stable. Cardiac dimensions and function were assessed in long and short parasternal axis and apical views. Mean values taken from at least 3 images in 2D and M-Mode. Experiment and analysis were performed in a blinded fashion and the analysis was performed by a second blinded observer.

Steroid measurements

Serum DHT was determined by ultra-performance liquid chromatography-tandem mass spectrometry (LC-MS/MS) as described (4). In brief, aliquots of samples, calibrator and

controls were combined with the internal standard mixture to monitor recovery. All samples were extracted using Oasis MAX SPE system Plates (Waters, Milford, MA, USA). The chromatographic separation was carried out using an ultra performance liquid chromatography (UPLC) system, which is connected to a Quattro Premier/XE triple Quad mass spectrometer (Waters, Milford, MA). A Waters Acquity UPLC BEH C18 column (1.7 µm, 100 x 2.1) was used at a flow rate of 0.4 mL/min at 50C. Water and acetonitril with 0.01% formic acid were used as mobile phase. Two mass transitions were monitored. The following optimized voltages were used: capillary voltage, 3.5 kV, cone voltage 28-33 V, collision energy 18-25 eV, dwell time 0.01-0.08 s depending on the steroid, source temperature 120 °C, desolvation temperature 450 °C. Argon was used as collision gas. Data were acquired with MassLynx 4.1 software and quantification was performed by TargetLynx software (Waters, Milford, MA). During all analyses the ambient temperature was kept at 21°C by air conditioning. Limit of detection: 0.054 nmol/L; Limit of quantification: 0.1 nmol/L, coefficient of variation inter-assay: 4-8% for 0.75 nmol/L and 7.5 nmol/L and intra-assay between 2-3%.

Left atrial optical mapping

Murine hearts were mounted on a vertical Langendorff apparatus (Hugo Sachs, March-Hugstetten, Germany) and the aorta was retrogradely perfused at 36-37°C, pH 7.4 with Krebs-Henseleit (KH) solution plus Di-4-ANEPPS (17.5 µM; Cambridge Bioscience, CA, USA). The left atrium (LA) was removed and pinned out in a recording chamber with the superior surface exposed (6, 7). The LA was continuously superfused with a KH solution containing in mM: NaCl 118; $NaHCO_3$ 24.88; KH_2PO_4 1.18; Glucose 5.55; $MgSO_4$ 0.83; $CaCl_2$ 1.8; KCl 3.52, equilibrated with 95% O_2/5% CO_2, pH 7.4. Blebbistatin (10 µM; Cayman Chemical, Michigan, USA) was added to the superfusate to prevent contraction artefacts. After 15 minutes equilibration, the LA was paced (2 ms duration pulses, 2x diastolic voltage threshold) at 120-80 ms cycle length (CL) using bipolar platinum electrodes and constant voltage stimulator (Digitimer, Welwyn Garden City, UK). Di-4-ANEPPS was excited at

530 nm by four LEDs (Cairn Research, Kent, UK) and fluorescence was captured at 630±20 nm using a second generation, high spatial resolution CMOS ORCA flash 4.0 camera (Hamamatsu Photonics, Japan). Images were captured at a sampling rate of 0.987 kHz (128 x 2048 pixels) and digitised using WinFluor V3.4.9 (Dr John Dempster, University of Strathclyde, UK).

Raw images were used to manually measure LA unfolded area in FIJI. Activation maps, conduction velocity vectors and optical action potentials were generated using MATLAB algorithms as described previously (6-9). Individual beat activation times were calculated from activation maps constructed by measuring the depolarisation midpoint (time of 50% upstroke amplitude) of the optical action potential at each pixel. Percentage tissue activation was then measured as a function of time, with time to 95% activation compared between the individual beats.

Left atrial transmembrane action potential analysis

Transmembrane action potentials (TAPs) were recorded from isolated, superfused LA using floating glass microelectrodes (resistance 15-30 MΩ) filled with 3 M KCl (6-8). Preparations were paced incremental from 1000 ms to 80 ms. Voltage was digitised at 20 kHz and was unfiltered. TAPs used for analysis were following 200 stimulations to allow for sufficient rate adaptation.

RNA isolation, sequencing and analysis

Left and right atria tissue samples were collected from excised hearts after quick perfusion to rinse out remaining blood. Total RNA was extracted using Direct-zol RNA MiniPrep kit (Zymo Research, Irvine, U.S.A.). RIN values (>7) were checked using the Bioanalyzer RNA 6000 Nano Kit (Agilent, Santa Clara, U.S.A.). mRNA enrichment and subsequent cDNA NGS library preparation was completed using a NEBNext Poly(A) mRNA Magnetic Isolation Module and Ultra II Directional RNA Library Prep Kit for Illumina (New England BioLabs, Hitchin, U.K). NGS library size distribution was determined by use of the Bioanalyzer High Sensitivity DNA Kit (Agilent, Santa Clara, U.S.A.) and quantified using the KAPA Library

Quantification Kit (Roche, Basel, Switzerland). Equimolar pooled libraries were sequenced 75 cycles in a single read mode on the NextSeq 500 System (v2.5 Chemistry, Illumina). RNA-seq FASTQ files were aligned on HISAT2 (version 2.1.0) using Ensembl Mus Musculus reference GRCm38 (10, 11). Aligned reads were counted using HTseq version 0.11.2 (12). Required transformations through different RNA-seq analysis steps were done using Samtools version 1.4 (13). Differential expression was obtained using DESeq2 in R (14) (http://www.R-project.org/, R 3.4.1). Ensembl IDs were transformed to gene symbols using BioTools (https://www.biotools.fr/mouse/ensembl_symbol_converter, accessed: 28/02/2020).

Upon publication, data will be made publically available at https://www.ncbi.nlm.nih.gov/geo/.

Protein quantification

Snap-frozen left ventricles were homogenized and resuspended in lysis buffer. 50 µg whole cell lysate per sample were used for SDS-PAGE and semi-dry blotting. Membranes were blocked in 10% milk in TBS-Tween and antibodies (GAPDH, Santa Cruz, sc-365062, 1:300; Connexin 43, Thermo Scientific, 13-8300, 1:250) were diluted in 4% milk in TBS-Tween. Protein-Antibody-HRP complexes were visualized using ECL substrates on a ChemiDoc Imaging System (Bio-Rad, Hercules, California, USA).

Left atrial cardiomyocyte cell isolation

Hearts were mounted onto a Langendorff apparatus and perfused with the following three solutions, equilibrated with 100% O_2: (i) HEPES-buffered modified Tyrode's solution containing in mM: NaCl 145, KCl 5.4, $CaCl_2$ 1.8, $MgSO_4$ 0.83, Na_2HPO_4 0.33, HEPES 5, and glucose 11 (pH 7.4, NaOH) x 5 min; (ii) Ca^{2+}-free Tyrode's solution × 5 min; (iii) Tyrode's enzyme solution containing 20 µg/mL Liberase™ (Roche, Indianapolis, IN) or a collagenase/protease mix (640 µg/mL collagenase type II, 600 µg/mL collagenase type IV and 50 µg/mL protease (Worthington, Lakewood, NJ)), 20 mM taurine and 30 µM $CaCl_2$ × 15-20 min. The LA was removed and placed into a high-K^+ modified Kraft-Bruhe (KB) solution containing in mM: DL-potassium aspartate 10, L-potassium glutamate 100, KCl 25,

KH_2PO_4 10, $MgSO_4$ 2, taurine 20, creatine 5, EGTA 0.5, HEPES 5, 0.1% bovine serum albumin (BSA, Sigma), and glucose 20 (pH 7.2, KOH). The LA was dissected into small strips and then cells were released by gentle trituration with fire-polished glass pipettes (1-2 mm diameter). Cells to be used for patch clamp experiments were gradually reintroduced to Ca^{2+} over a period of 2 hours to reach a final concentration of 1.8 mM. All experiments were performed within 4-8 hours of isolation.

Sodium current recordings

Isolated atrial cells were plated on laminin coated coverslips and superfused at 3-4 mL/min at 22±0.5 °C with a low sodium external solution containing in mM: NaCl 10, $C_5H_{14}ClNO$ 130, HEPES 10, $CaCl_2$ 1.8, MgCl 1.2, $NiCl_2$ 2, glucose 10, pH 7.4 (CsOH). Peak I_{Na} was recorded in voltage clamp mode using borosilicate glass pipettes (tip resistance 1.5–2.5 MΩ). The internal pipette solution contained in mM: NaCl 5, CsCl 115, HEPES 10, EGTA 10, MgATP 5, $MgCl_2$ 0.5 and TEA 20, pH 7.2 (CsOH). Currents were digitised at 50 kHz and low pass filtered at 20 kHz. Series resistance was compensated between 60 and 80%. Experiments were terminated if series resistance increased abruptly or was greater than 10 MΩ (usually 4-8 MΩ). Current-voltage relationships were examined using 100 ms step depolarisations over test potentials ranging from -95 mV to +40 mV, in 5 mV increments, from a holding potential of -100 mV. I/V curves were fitted using the modified Boltzmann equation: $I_{Na} = G_{max}(V_m - V_{rev})/(1+Exp[(_{V0.5}-V_m)/k])$, where I_{Na} is the current density at an equivalent test potential (V_m), G_{max} is the peak conductance (nS), V_{rev} is the reverse potential, $V_{0.5}$ is the membrane potential at 50% current activation and k is the slope constant (15) (16). Time dependent peak I_{Na} recovery kinetics were evaluated using standard 20 ms P1-P2 pulse protocols (-100 mV to -30 mV) with increasing time delay ranging from 1 to 100 ms. Measurements of steady state inactivation of I_{Na}, were made by applying 500 ms pre-pulses ranging from -120 mV to -40 mV in 5 mV increments prior to the test potential (-30 mV for 100 ms). Individual atrial cell capacitance was calculated by

integrating the cellular capacitance current elicited by 10 mV depolarisation from a holding potential of -80 mV.

Atrial fiber size and extracellular matrix composition analysis

Hearts were isolated and coronary arteries cleared with blood using KH buffer, before being snap-frozen in optimal cutting compound (OCT). For fiber size analysis, 10 µm atrial sections were stained with FITC-conjugated wheat germ agglutinin WGA (1:1000) and imaged on Leica DM6000 B fully automated fluorescence microscope (Leica Microsystems, Wetzlar, Germany) with a 40 x objective. Scaled images were extracted using LASX (Leica Application Suite X, Leica Microsystems, Wetzlar, Geramany) imaging suite and cell diameter and endomysial fibrosis were quantified from sections using the JavaCyte ImageJ plugin (17).

Super-resolution microscopy and $Na_v1.5$ cluster analysis

LA cells were plated on 10 mm diameter laminin coated coverslips (Mattek, 35 mm dish, 1.5# coverglass) and then fixed in 4% paraformaldehyde for 90 minutes to ensure maximal immobilization of cellular proteins. Cells were permeabilised with a 0.1% Triton in PBS solution for 5 minutes and blocked in a 5% BSA in PBS solution for 60 minutes. The primary polyclonal rabbit anti-Nav1.5 antibody (ASC-005, Alomone Laboratories, Jerusalem, Israel) (1:50) was diluted in blocking solution and incubated overnight at 4°C. Cells were washed three times in PBS, blocked again for 30 minutes and then incubated in secondary antibody fragment (F(ab')2- Goat anti-Rabbit IgG, Alexa Fluor 647, A212-56, 1:1000, ThermoFisher Scientific, Waltham, MA, USA) for 90 minutes at room temperature. Direct stochastic optical reconstruction microscopy (dSTORM) experiments were performed on a NIKON Eclipse Ti inverted N-STORM microscope equipped with a NIKON APO 100 x 1.49 NA total internal reflection fluorescence (TIRF) oil immersion objective. Laser illumination was provided using 405 nm (20 mW), 491 nm (100 mW), 561 mW (100 mW) and 640 nm (200 mW) solid-state lasers. A NIKON Perfect Focus System (PFS) ensured minimal lateral drift during acquisition. Immunolabelled samples were imaged in 0.5 mg/mL glucose oxidase, 40 µg/mL

catalase, 10% wt/vol glucose and 100 mM MEA in PBS, pH 7.4 to induce Alexa 647 blinking. During dSTORM acquisition, the sample was continuously illuminated at 640 nm for 20,000 frames, fluorescence emission was filtered through a single band far red emission filter (MBE47200 N-STORM cube) and detected using an Andor iXon Ultra DU897 EMCCD camera (256 x 256 pixels, 160 nm effective pixel size, 9.2 ms exposure time). the angle of illumination as well as the z-depth were kept as consistent as possible across different samples. Samples were maintained in an OKO environmental chamber at 27 ^{o}C for maximum system stability during imaging. Immunolabelled samples were imaged in 0.5 mg/mL glucose oxidase, 40 µg/mL catalase, 10% wt/vol glucose and 100 mM MEA in PBS, pH 7.4 to induce Alexa 647 blinking.

Fluorescence detections were localised in ThunderSTORM (18) using default settings for the localisation step. Post-localisation the samples were subjected to drift correction (cross correlation), filtering for localizations with a spatial uncertainty below 40 nm, duplicate removal (distance threshold 75 nm) and merging (performed with a maximum distance of 75 nm, maximum off frames 1, maximum frames per molecule 0).

Depending on the overall number of blinking events in a sample, either 20,000 or 5,000 of the post-processed images were subjected to cluster analysis. Due to variability in blinking events across different imaging sessions, resulting cluster parameters from each group were normalised to the mean of the wildtype control group, acquired during the same imaging session.

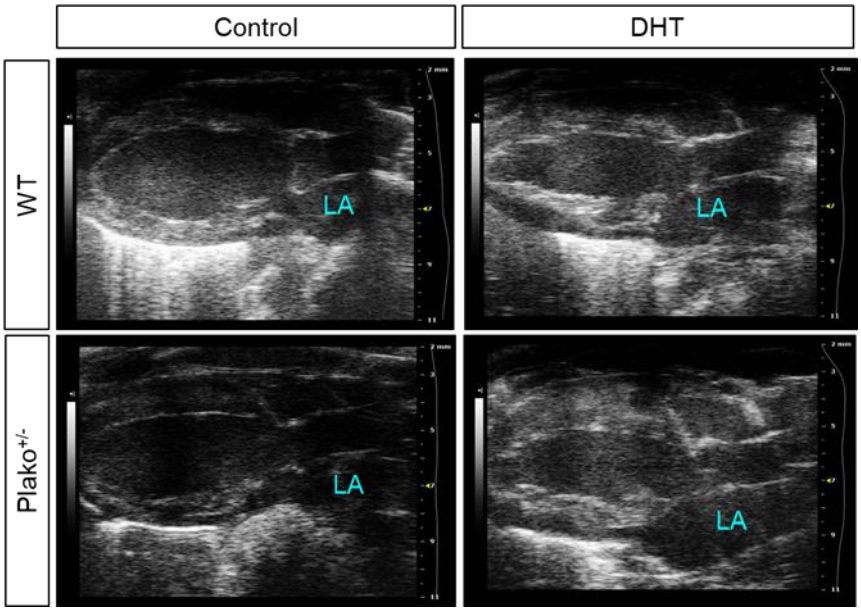
For cluster analysis, we used a topological analysis tool (5), with codes customized to cardiomyocyte images in an R environment and the following set parameters: r=40 nm, Threshold=10, minimal number of detections per cluster = 10. Prior to cluster analysis, only data points within the cell area were selected using the normalized Ripley's K-function (H-function, $H(r) = L(r)-r$ with a set linking distance of r = 1 µm and only points with $H(r) > 0$, indicating a non-dispersed spatial distribution, were included (background will be randomly distributed and hence $H(r) < 0$). The minimum area to be detected as 'cell' was set to

15 μm^2. Final super-resolution rendered images were achieved by applying a normalised Gaussian with magnification 50 and the lateral uncertainty set to the calculated uncertainty of the localisation for each blink (20 nm). Cell area selection and cluster map images for visualization were generated using MATLAB.

Statistics

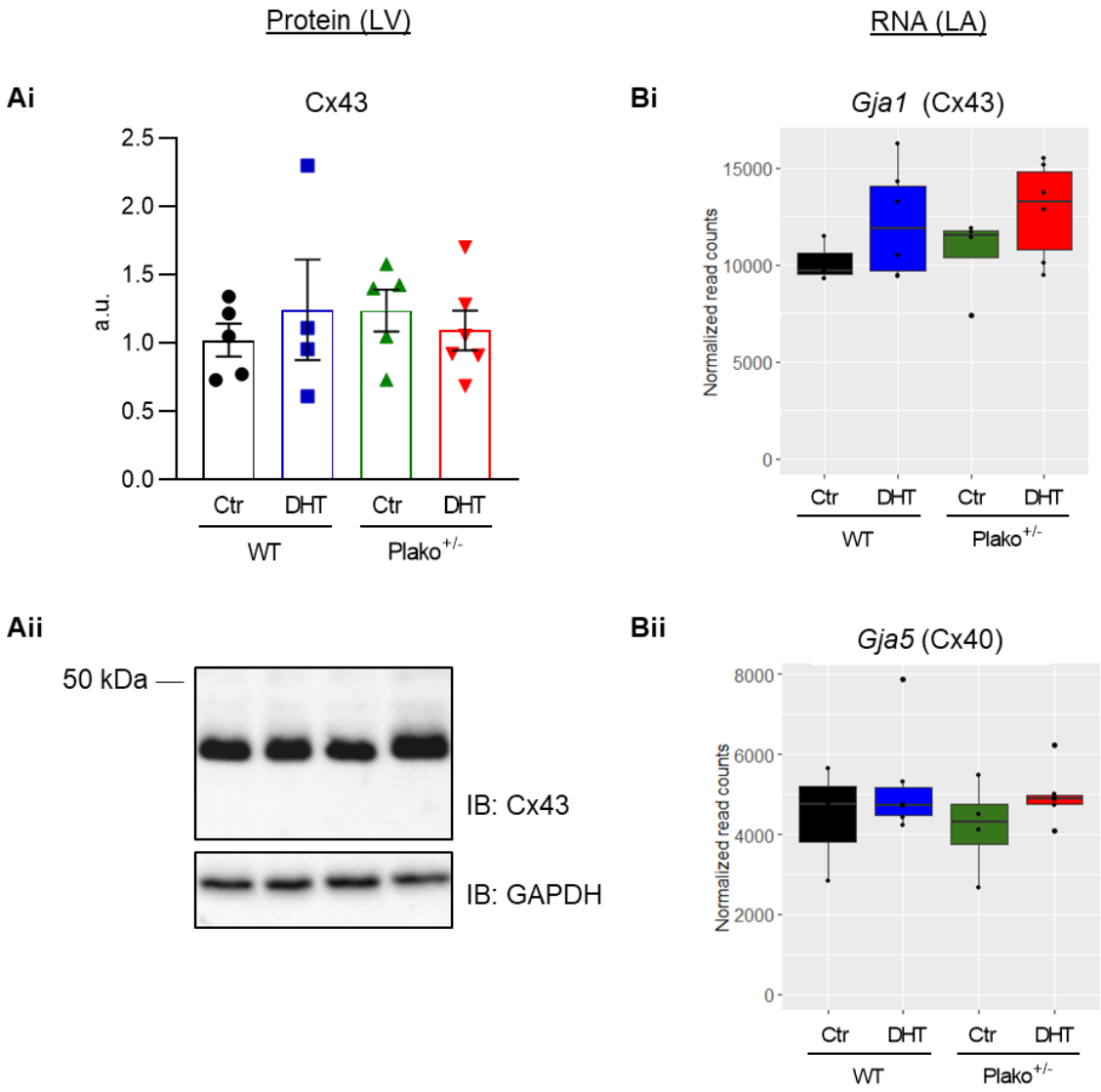
Data was first subjected to outlier analysis, ROUT method, based around a false discovery rate, where $\alpha = 0.01$ and outliers were removed (Prism v8, GraphPad Software, La Jolla, CA, USA). Significance was taken at $p<0.05$, applying two-way or two-way repeated measures ANOVA with post hoc t-tests or Bonferroni correction, as appropriate (Prism v8, GraphPad Software, La Jolla, CA, USA). All experiments and analyses were performed blinded to genotype and treatment.

Supplementary Figures and Tables



Supplementary Figure 1 - Echocardiographic assessment of murine hearts

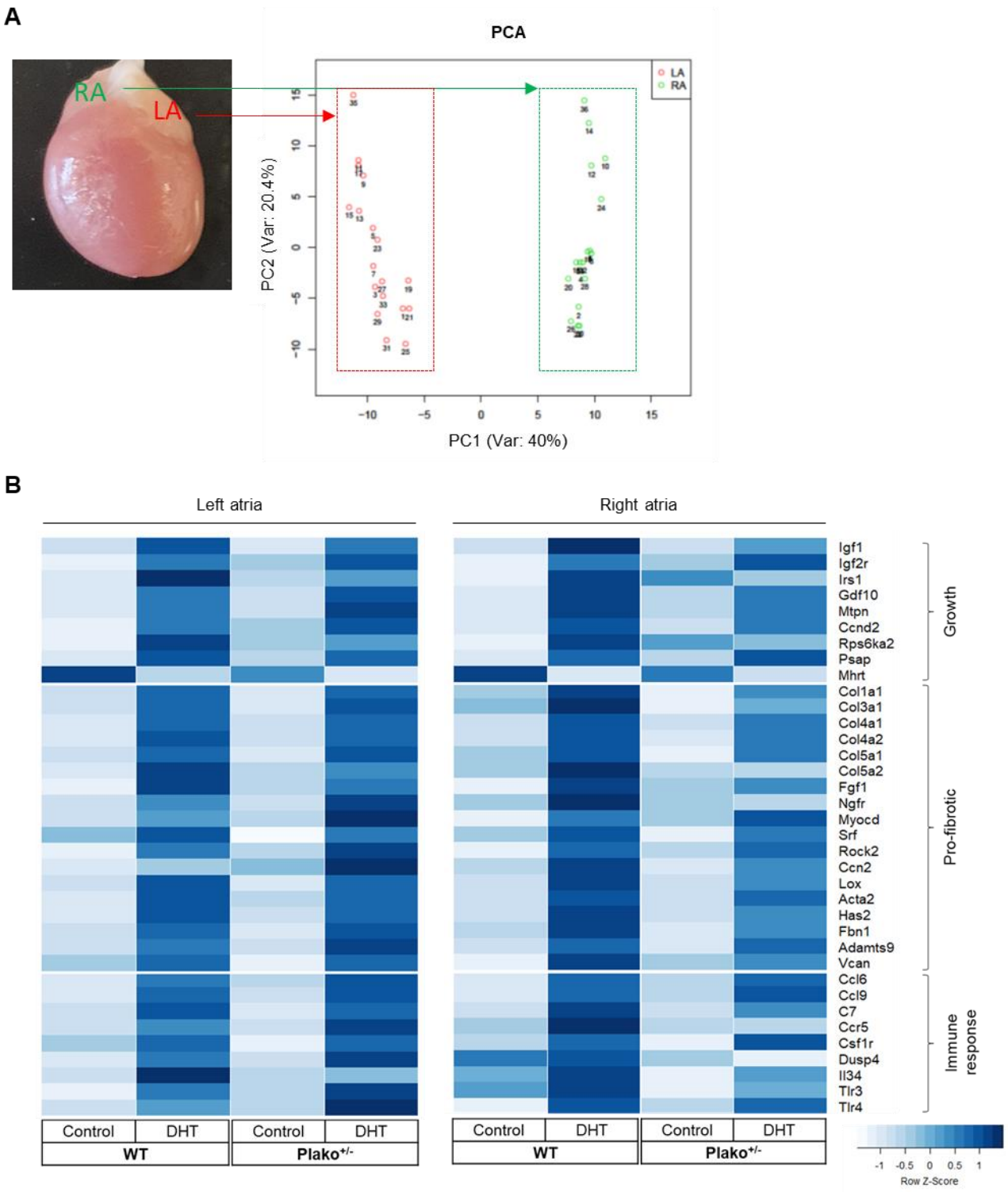
Example echocardiographic images obtained in parasternal long axis view, displayed during systole (atrial diastole).



Supplementary Figure 2 - Expression levels of Connexins

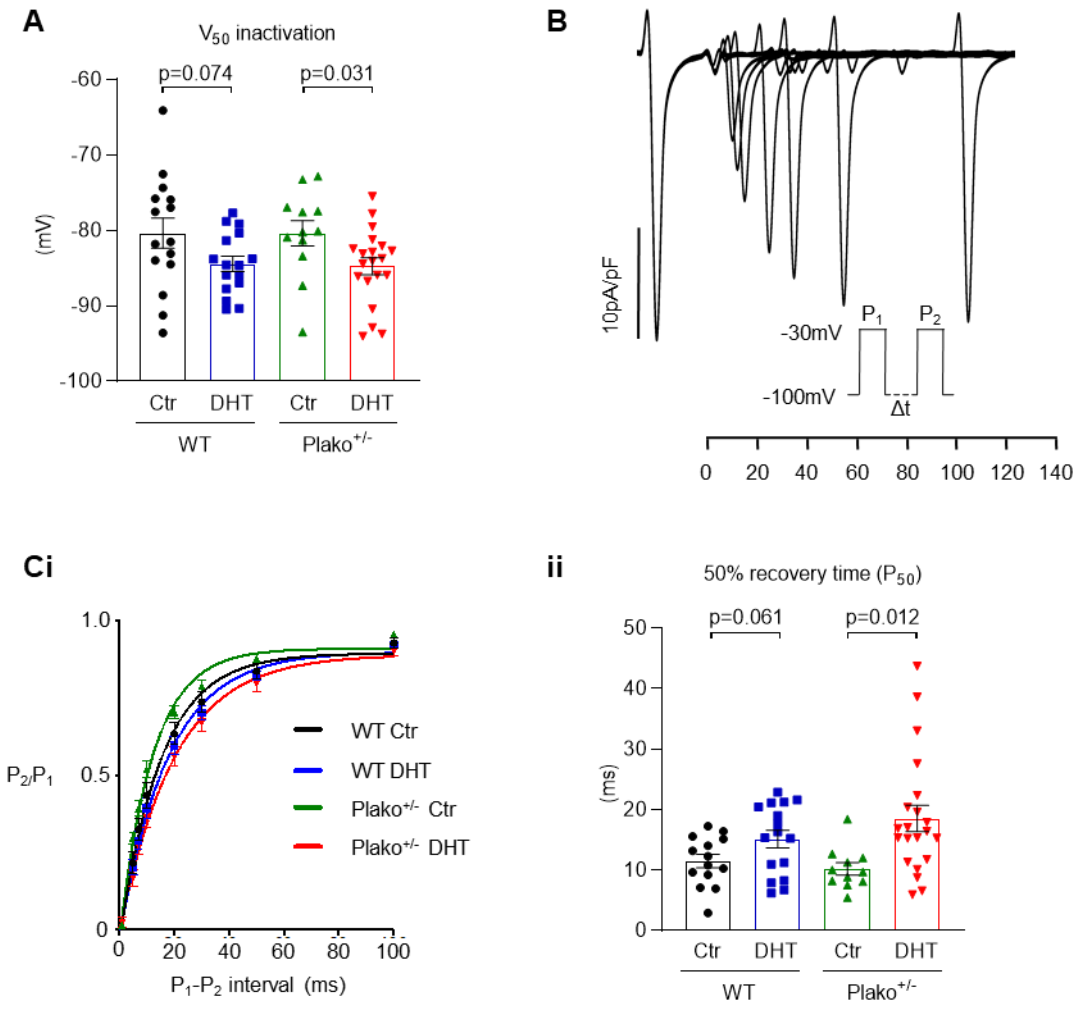
(**Ai**) Quantification of Cx43 protein expression in LV normalized to the housekeeping protein GAPDH and given as a fraction of the mean expression value in WT Ctr tissue. (**Aii**) Representative Western blot of Connexin 43 (Cx43) in murine left ventricular (LV) tissue.

(**Bi**) Left atrial (LA) RNA expression levels of Gja1, encoding for Connexin 43, Cx43 and of (**Bii**) Gja5, encoding for Connexin 40, Cx40.



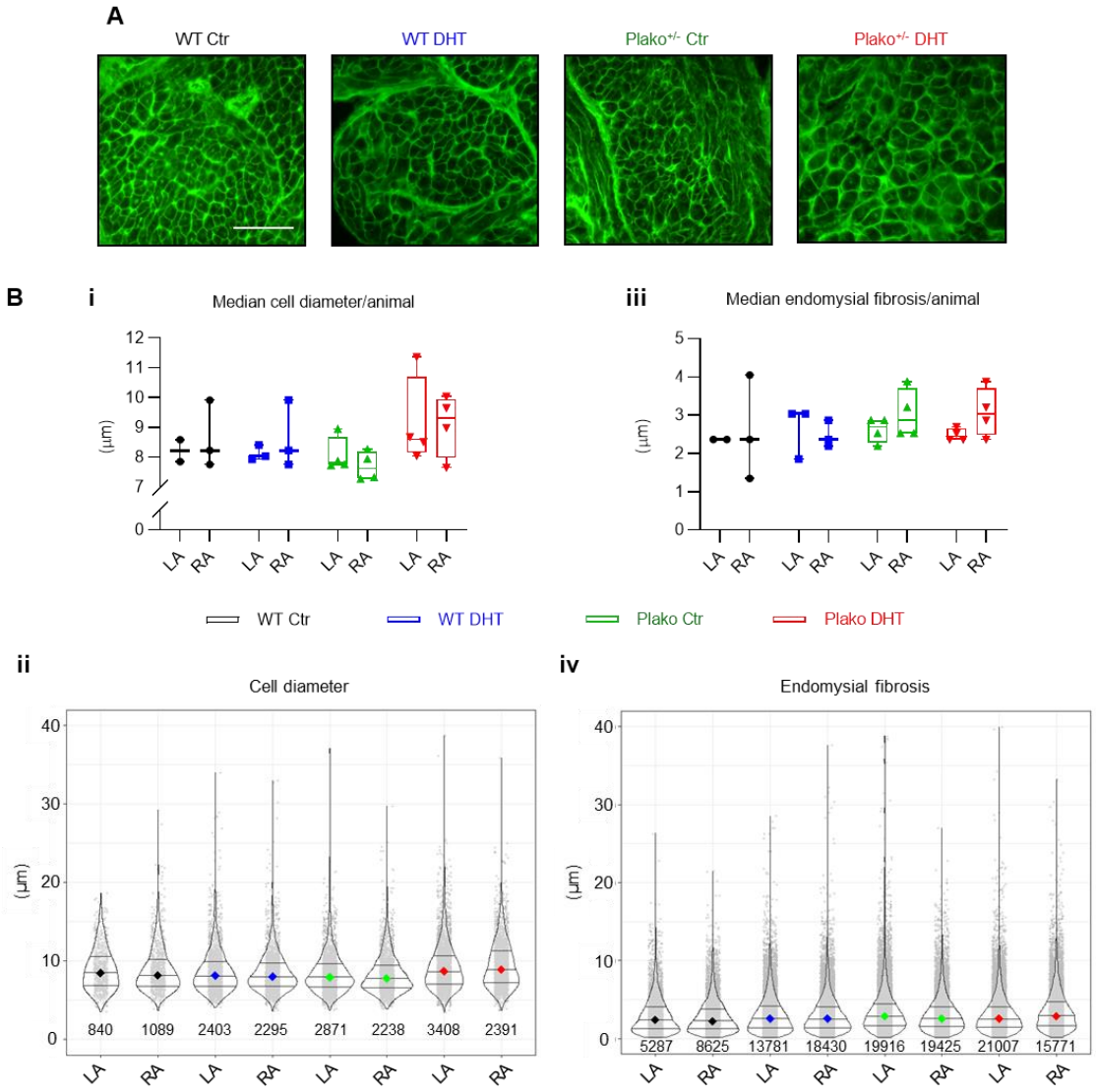
Supplementary Figure 3 - Atrial RNA expression

(**A**) Principal component analysis (PCA) plot of all atrial samples (LA, left atria, red; RA, right atria, green) used for RNA sequencing analysis. The PCA was generated using the top 250 transcripts obtained from the "variance stabilizing transformation" of DESeq2. Range of unique mapped reads/sample across all samples: 16592072 to 22124528. Read length = 75 bp (**B**) Heat map illustrating differential expression of selected genes in LA and RA resulting from RNA sequencing analysis. n= WT Control: 3 LA / 3 RA; WT DHT: 6 LA / 6 RA; Plako$^{+/-}$ Control: 4 LA / 4 RA; Plako$^{+/-}$ DHT: 6 LA / 6 RA



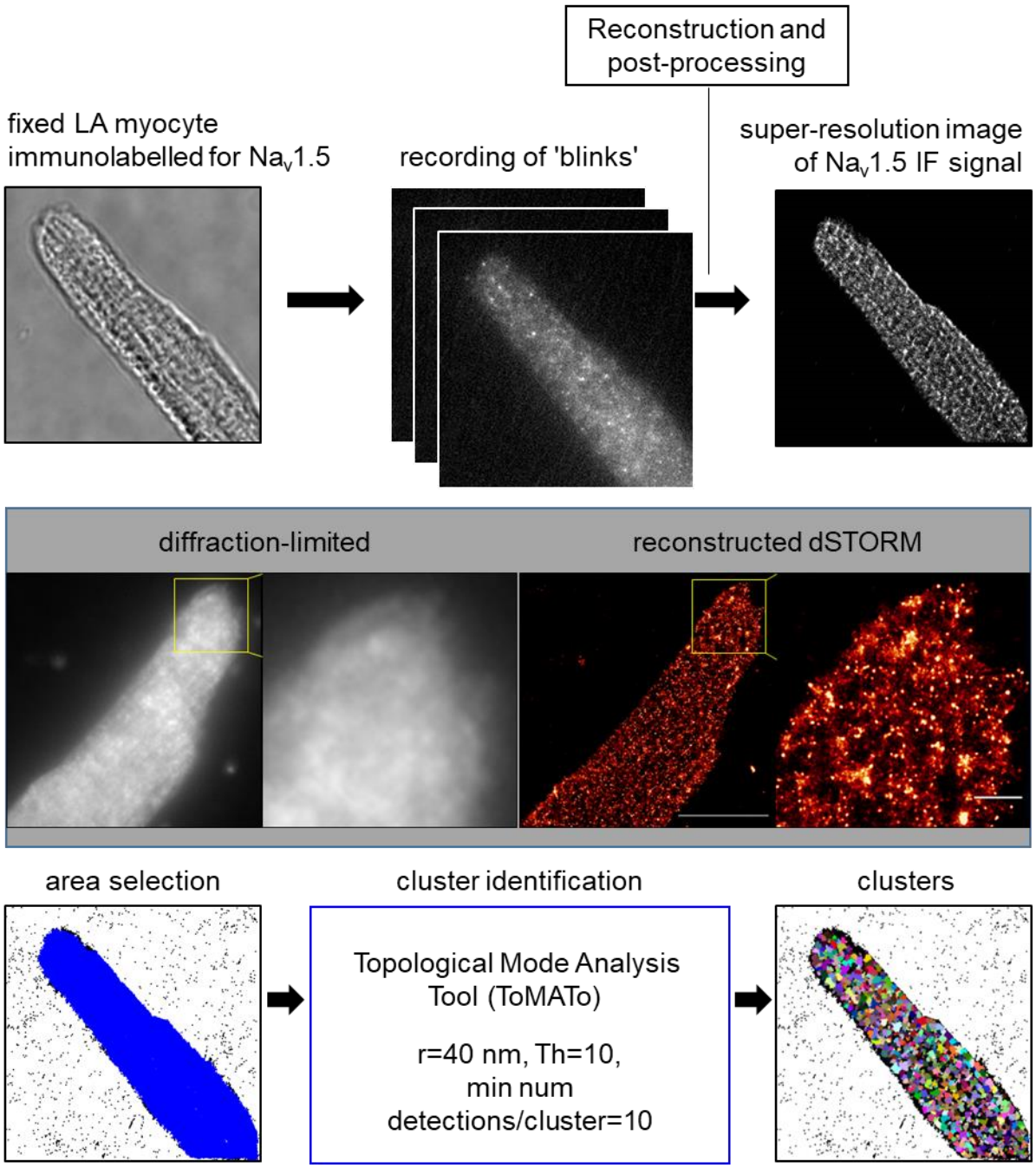
Supplementary Figure 4 - Sodium channel kinetics

Exposure to DHT has a significant effect on (**A**) Mean V50 values for steady state inactivation of sodium channels (2-way ANOVA, $p<0.05$). Results of post hoc t-test are indicated on the graph. All data points are shown as well as mean ± SEM (**B**) Example trace showing time dependent sodium channel recovery. (**Ci**) Mean curves showing recovery times. Data plotted as mean ± SEM. DHT treatment has a significant effect on (**Cii**) 50% sodium channel recovery times (P_{50}) for each group (two-way ANOVA, $p<0.05$). Results of post hoc t-test are indicated on the graph. Plako$^{+/-}$ LA DHT-treated cells have delayed recovery. All data points are shown as well as mean ± SEM. For C: WT Ctr (n=14 cells, N=5 LA), WT DHT (n=16 cells, N=5 LA), Plako$^{+/-}$ Ctr (n=11 cells, N=4 LA) and Plako$^{+/-}$ DHT (n=21 cells, N=5 LA).



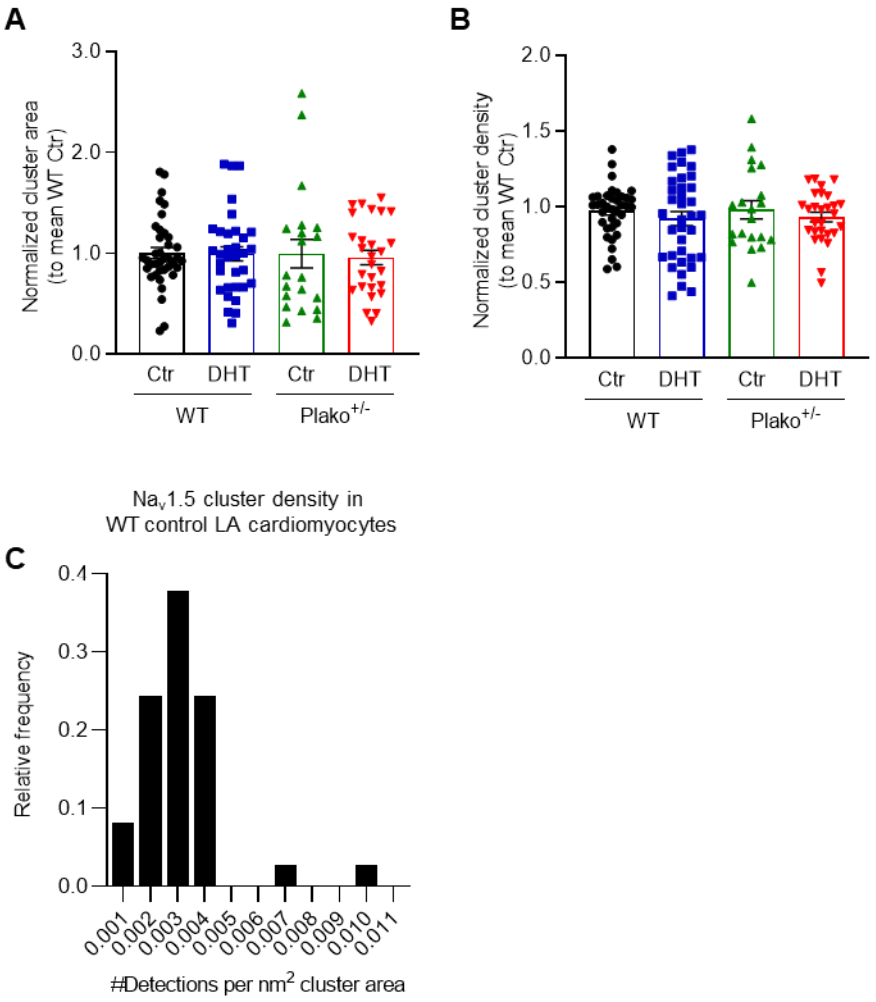
Supplementary Figure 5 - Histological analysis of atria

(**A**) Example left atrial (LA) sections stained with FITC-conjugated wheat germ agglutinin (lectin, 400 x magnification) for automated quantification of (**Bi&ii**) cell diameter and (**Biii&iv**) endomysial fibrosis (cell-cell-distance) in both, LA and right atria (RA). Scale bar 20 µm
(Bi and Biii) Single data points denote medians of individual measurements per atrium
(Bii and Biv) individual measurements data points (light grey) with violin plots including medians (color-coded per group) and IQR. (Bii) IQR (µm) are as follows: WT Placebo LA: 3.678, WT Placebo RA: 3.248, WT DHT LA: 3.1375, WT DHT RA: 2.89, Plako$^{+/-}$ Placebo LA: 2.8395, Plako$^{+/-}$ Placebo RA: 2.8545, Plako$^{+/-}$ DHT LA: 3.5878, Plako$^{+/-}$ DHT RA: 4.071 (Biv) WT Placebo LA: 2.867, WT Placebo RA: 2.53, WT DHT LA: 2.698, WT DHT RA: 2.698, Plako$^{+/-}$ Placebo LA: 2.698, Plako$^{+/-}$ Placebo RA: 2.529, Plako$^{+/-}$ DHT LA: 2.529, Plako$^{+/-}$ DHT RA: 3.036. Number of cell diameters / distances measured for each group is reported in the respective column of the graphs. Linear mixed modelling revealed no significant differences between genotype or treatment groups.



Supplementary Figure 6 - Workflow for direct stochastic optical reconstruction microscopy (dSTORM) and subsequent clustering analysis in left atrial (LA) cardiomyocytes

Fixed LA cardiomyocytes were immunolabelled for $Na_v1.5$ and blinking events (blinks) in STORM buffer were recorded. Recordings over time were then post-processed and super-resolution images were reconstructed and false-coloured. Increase in resolution over the diffraction-limited image is depicted in the middle panel. The cell area was selected (blue) and contained detections were subjected to clustering analysis, using a topological approach (5). Proposed clusters are depicted in arbitrary colours, detections not allocated to any cluster remain black.



Supplementary Figure 7 - Sodium channel cluster characteristics

Neither plakoglobin heterozygous knockout nor exposure to DHT have an effect on (**A**) normalized $Na_v1.5$ cluster area and (**B**) cluster density. (**C**) Relative frequency of $Na_v1.5$ cluster densities (number of detections per nm^2 cluster area in WT control left atrial cardiomyocytes (n=38 cells, N=7 LA)).

Supplementary Table 1 - Transmembrane action potential analysis

	WT Control (n=21, N=7)			WT DHT (n=13, N=5)			Plako$^{+/-}$ Control (n=20, N=7)			Plako$^{+/-}$ DHT (n=23, N=8)		
Pacing CL (ms)	**120**	**100**	**80**	**120**	**100**	**80**	**120**	**100**	**80**	**120**	**100**	**80**
RMP (mV)	-72 ±1	-71 ±1	-70 ±1	-71 ±1	-70 ±1	-69 ±1	-71 ±1	-70 ±1	-69 ±1	-69 ±1*	-68 ±1*	-67 ±1*
APA (mV)	84 ±1	82 ±1	79 ±1	82 ±2	79 ±2	75 ±2	82 ±2	80 ±2	76 ±2	74 ±2*#+	71 ±2*#+	67 ±2*#+
dV dt^{-1} peak (V/s)	118 ±5	112 ±5	104 ±5	120 ±7	113 ±7	103 ±6	116 ±4	109 ±4	98 ±4	89 ±5*#+	83 ±5*#+	74 ±5*#+
APD50 (ms)	7.1 ±0.4	6.8 ±0.4	6.4 ±0.4	6.5 ±0.3	6.1 ±0.3	5.7 ±0.4	7.2 ±0.4	6.8 ±0.4	6.5 ±0.4	6.8 ±0.2	6.6 ±0.2	6.3 ±0.2
APD70 (ms)	10.8 ±0.6	10.2 ±0.5	9.6 ±0.5	9.9 ±0.6	9.2 ±0.5	8.5 ±0.4	11.2 ±0.8	10.6 ±0.7	9.9 ±0.6	10.5 ±0.4	10.0 ±0.4	9.5 ±0.4
APD90 (ms)	20.5 ±1.0	19.2 ±0.8	17.9 ±0.8	19.2 ±1.0	17.7 ±0.9	15.9 ±0.8	21.4 ±1.4	20.0 ±1.3	18.5 ±1.1	20.2 ±0.7	19.1 ±0.6	17.6 ±0.6
AT (ms)	6 ±0.3	7 ±0.4	7 ±0.4	7 ±0.5	7 ±0.5	8 ±0.6	7 ±0.3	8 ±0.4	8 ±0.4	9 ±0.8 *#+	10 ±1.0 *#+	11 ±1.4 *#+

Action potentials from microelectrode recordings in paced, superfused left atria. WT, wildtype; DHT, 5α-dihydrotestosterone; CL, cycle length; RMP, resting membrane potential; APA, action potential amplitude; APD50-90, action potential duration at 50-90% repolarisation; AT, activation time. Data presented as mean ±SEM. *p<0.05 vs WT Control, #p<0.05 vs WT DHT, +p<0.05 vs Plako$^{+/-}$ Control; two-way ANOVA with Bonferroni post-hoc analysis. n=number of measurements, N=number of left atria

Supplementary Table 2 - Optical action potential analysis

	WT Control (N=6)	WT DHT (N=7)	Plako$^{+/-}$ Control (N=8)	Plako$^{+/-}$ DHT (N=9)
Pacing CL (ms)	**80**	**80**	**80**	**80**
APD90 (ms)	20.7 ±0.9	22.5 ±1.4	21.7 ±1.1	22.8 ±1.4
B-to-b Δ APD90 (ms)	1.6 ±0.3	3.2 ±0.7	1.9 ±0.2	1.3 ±0.4

Action potentials recorded optically from paced, superfused left atria (LA). WT, wildtype; DHT, 5α-dihydrotestosterone; CL, cycle length; APD90, action potential duration at 90% repolarisation; B-to-b Δ APD90, Beat-to-beat difference in APD90. Data presented as mean ±SEM. N=number of LA

Supplementary References

1. Kirchhof P, et al. Age- and training-dependent development of arrhythmogenic right ventricular cardiomyopathy in heterozygous plakoglobin-deficient mice. *Circulation.* 2006;114(17):1799-806.
2. Fabritz L, et al. Load-reducing therapy prevents development of arrhythmogenic right ventricular cardiomyopathy in plakoglobin-deficient mice. *Journal of the American College of Cardiology.* 2011;57(6):740-50.
3. Kirchhof P, et al. PITX2c is expressed in the adult left atrium, and reducing Pitx2c expression promotes atrial fibrillation inducibility and complex changes in gene expression. *Circulation Cardiovascular genetics.* 2011;4(2):123-33.
4. Kulle AE, et al. A novel ultrapressure liquid chromatography tandem mass spectrometry method for the simultaneous determination of androstenedione, testosterone, and dihydrotestosterone in pediatric blood samples: age- and sex-specific reference data. *J Clin Endocrinol Metab.* 2010;95(5):2399-409.
5. Pike JA, et al. Topological data analysis quantifies biological nano-structure from single molecule localization microscopy. *Bioinformatics (Oxford, England).* 2020;36(5):1614-21.
6. Yu TY, et al. An automated system using spatial oversampling for optical mapping in murine atria. Development and validation with monophasic and transmembrane action potentials. *Progress in biophysics and molecular biology.* 2014.
7. Holmes AP, et al. A Regional Reduction in Ito and IKACh in the Murine Posterior Left Atrial Myocardium Is Associated with Action Potential Prolongation and Increased Ectopic Activity. *PloS one.* 2016;11(5):e0154077.
8. Syeda F, et al. PITX2 Modulates Atrial Membrane Potential and the Antiarrhythmic Effects of Sodium-Channel Blockers. *Journal of the American College of Cardiology.* 2016;68(17):1881-94.
9. O'Shea C, et al. ElectroMap: High-throughput open-source software for analysis and mapping of cardiac electrophysiology. *Scientific reports.* 2019;9(1):1389.
10. Kim D, et al. Graph-based genome alignment and genotyping with HISAT2 and HISAT-genotype. *Nat Biotechnol.* 2019;37(8):907-15.
11. Zerbino DR, et al. Ensembl 2018. *Nucleic Acids Res.* 2018;46(D1):D754-D61.
12. Anders S, et al. HTSeq--a Python framework to work with high-throughput sequencing data. *Bioinformatics (Oxford, England).* 2015;31(2):166-9.
13. Li H, et al. The Sequence Alignment/Map format and SAMtools. *Bioinformatics (Oxford, England).* 2009;25(16):2078-9.
14. Love MI, et al. Moderated estimation of fold change and dispersion for RNA-seq data with DESeq2. *Genome Biol.* 2014;15(12):550.
15. Spencer CI, et al. Actions of pyrethroid insecticides on sodium currents, action potentials, and contractile rhythm in isolated mammalian ventricular myocytes and perfused hearts. *J Pharmacol Exp Ther.* 2001;298(3):1067-82.

16. Ackers-Johnson M, et al. A Simplified, Langendorff-Free Method for Concomitant Isolation of Viable Cardiac Myocytes and Non-Myocytes from the Adult Mouse Heart. *Circulation research.* 2016.

17. Winters J, et al. JavaCyte, a novel open-source tool for automated quantification of key hallmarks of cardiac structural remodeling. *Scientific reports.* 2020;10(1):20074.

18. Ovesny M, et al. ThunderSTORM: a comprehensive ImageJ plug-in for PALM and STORM data analysis and super-resolution imaging. *Bioinformatics (Oxford, England).* 2014;30(16):2389-90.

7 Chapter VII - Results: Familial atrial fibrillation mutation M1875T-SCN5A increases early sodium current and dampens the effect of flecainide

Preprint 2. This preprint is available on biorXiv and currently under revision.

Familial atrial fibrillation mutation M1875T-SCN5A increases early sodium current and dampens the effect of flecainide.

O'Reilly M*, **Sommerfeld LC***, O'Shea C, Broadway-Stringer S, Andaleeb S, Reyat JS, Kabir SN, Stastny D, Malinova A, Delbue D, Fortmueller L, Gehmlich K, Pavlovic D, Skryabin BV, Holmes AP, Kirchhof P, Fabritz L. *biorXiv. 2022, doi: 10.1101/2022.01.18.476646*

*These authors share first authorship

Author contributions in preprint 2

I, alongside co-authors, performed in vivo experiments and gravimetry of mice and optical mapping experiments. I revised the genotyping protocol for the model and conducted offspring analysis in regards to genotype and sex distribution and supervised cardiac histological analysis and protein quantification protocols. I furthermore designed figures and the graphical abstract and wrote the manuscript together with co-authors.

Familial atrial fibrillation mutation M1875T-SCN5A increases early sodium current and dampens the effect of flecainide

O'Reilly M[1,2*], Sommerfeld LC[1,3,4*], O'Shea C[1], Broadway-Stringer S[1], Andaleeb S[1], Reyat JS[1], Kabir SN[1], Stastny D[3], Malinova A[1], Delbue D[3,4], Fortmueller L[3,4], Gehmlich K[1,6], Pavlovic D[1], Skryabin BV[7], Holmes AP[1,8], Kirchhof P[1,4,5], Fabritz L[1,3,4,5]

[1]*Institute of Cardiovascular Sciences, University of Birmingham, UK*

[2]*Department of Experimental Cardiology, Academic Medical Center, The Netherlands*

[3]*University Center of Cardiovascular Science, University Heart and Vascular Center Hamburg, UKE Hamburg, Germany*

[4]*DZHK Standort Hamburg/Kiel/Luebeck, Germany*

[5]*Department of Cardiology, University Heart and Vascular Center UKE Hamburg, Germany*

[6]*Division of Cardiovascular Medicine, Radcliffe Department of Medicine and British Heart Foundation Centre of Research Excellence Oxford, University of Oxford, UK*

[7]*Medical Faculty, Core Facility Transgenic animal and genetic engineering Models (TRAM), University of Muenster, Germany*

[8]*Institute of Clinical Sciences, University of Birmingham, UK*

*equal contribution

Word count (excl. references and figure legends): 4759

Corresponding author:

Professor Larissa Fabritz
University Center of Cardiovascular Science
University Heart and Vascular Center, UKE Hamburg
Hamburg, Germany
E-Mail: [redacted]

Abstract

Aims

Atrial fibrillation (AF) is the most common cardiac arrhythmia. Pathogenic variants in genes encoding ion channels are associated with familial AF. The point mutation M1875T in the *SCN5A* gene, which encodes the α-subunit of the cardiac sodium channel $Na_v1.5$, has been associated with increased atrial excitability and familial AF in patients.

Methods

We designed a new murine model carrying the *Scn5a*-M1875T mutation enabling us to study the effects of the $Na_v1.5$ mutation in detail *in vivo* and *in vitro* using patch clamp and microelectrode recording of atrial cardiomyocytes, optical mapping, ECG, echocardiography, gravimetry, histology and biochemistry.

Results

Atrial cardiomyocytes from newly generated adult *Scn5a*-M1875T$^{+/-}$ mice showed a selective increase in the early (peak) cardiac sodium current, larger action potential amplitude and a faster peak upstroke velocity. Conduction slowing caused by the sodium channel blocker flecainide was less pronounced in *Scn5a*-M1875T$^{+/-}$ compared to wildtype atria. Overt hypertrophy or heart failure in *Scn5a*-M1875T$^{+/-}$ mice could be excluded.

Conclusion

The *Scn5a*-M1875T point mutation causes gain-of-function of the cardiac sodium channel. Our results suggest increased atrial peak sodium current as a potential trigger for increased atrial excitability.

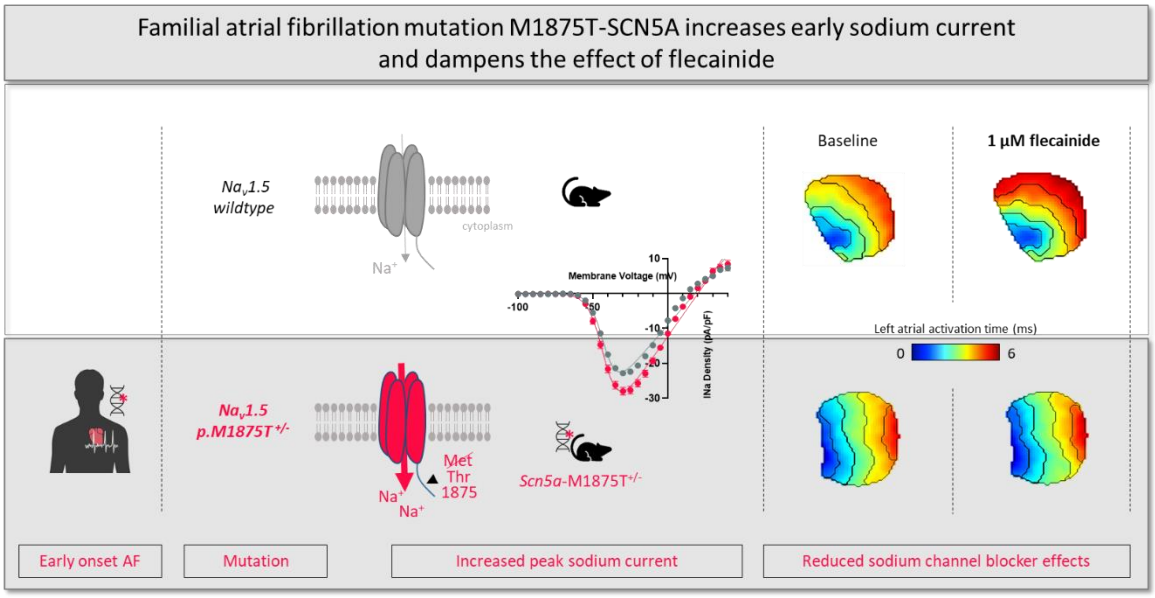
Keywords

Sodium channel, channelopathy, atrial electrophysiology, sodium channel blocker

What's new

- The point mutation M1875T in the C-terminal domain of the cardiac sodium channel $Na_v1.5$ causes an increase in early peak sodium current in atrial cardiomyocytes.
- The observed changes induced by this point mutation suggest an increase in peak sodium current as an electrophysiological substrate for the familial atrial fibrillation (AF) seen in patients.
- Our findings provide a possible explanation for the variable effectiveness of sodium channel blockers in patients with AF. Carriers of such sodium channel gain-of-function mutations may benefit more from tailored treatments.

Graphical abstract



Introduction

Atrial fibrillation (AF), the most common cardiac arrhythmia, is characterised by episodes of irregular and uncoordinated atrial electrical activity. It is associated with ischaemic stroke, cardiovascular death and frequent hospitalisations [1]. A range of different common factors, such as heart failure, diabetes and increased formation of fibrosis, can damage the atria, contributing to AF [2]. These factors interact with a pre-existent, potentially inherited substrate to result in AF [2]. Inherited forms are characterised by early onset of the condition. Pathogenic variants in several genes associated with cardiomyopathies have been identified in familial AF, including variants in sarcomeric and cell-cell contact genes, and others [3]. Within the group of ion channel genes, variants leading to dysfunction of the cardiac sodium channel ($Na_v1.5$) are associated with familial AF [3, 4]. The pore-forming α-subunit of the $Na_v1.5$ is encoded by the *SCN5A* gene. Variants in *SCN5A* have been linked to several cardiac conditions, including AF [4].

A missense *SCN5A* point mutation, Met1875Thr (M1875T), located in the C-terminus of the channel protein, was linked to autosomal dominant familial AF that spanned three generations [5]. Atrial ectopy was evident in mutation carriers in adolescence, and persistent AF occurred as early as 27 years of age. Analyses in the human cell line HEK293 heterologous expression system [5] suggested an enhanced function of the mutated $Na_v1.5$ channel.

To investigate the impact of the M1875T mutation in the heart and atria, we generated and characterised a novel knock-in murine model (*Scn5a*-M1875T$^{+/-}$). Mice that were heterozygous for the M1875T mutation were viable and studied herein. We investigated hearts of these mice from the whole organ *in vivo* to the level of the single cardiac cell *ex vivo*.

Methods

Generation and sequencing of the *Scn5a*-M1875T murine model

Mice heterozygous for the knock-in mutation M1875T in the *Scn5a* gene (*Scn5a*-M1875T$^{+/-}$) were generated by T-C point-mutating exon 28 of the cardiac sodium channel *SCN5A* gene using pSCN5a_targ3 targeting vector and CRISPR/Cas9 system in murine embryonic stem (ES) cells (Figure 1a). Mutation-harboring ES cells were characterised using Southern blot analysis and sequenced to exclude genomic rearrangements (Figure 1b) [6], and injected into B6D2F1 mouse blastocysts. Sequencing analysis of the mutation-containing region using DNA from adult wildtype (WT) and heterozygous *Scn5a*-M1875T$^{+/-}$ mice on C57Bl/6J x 129sv hybrid genetic background are shown in Figure 1c. Detailed steps of the generation are further explained in the supplement.

Methionine at position 1875 of the human $Na_v1.5$ protein sequence corresponds to position 1877 of the murine sequence. The latter is therefore point-mutated in this model. However, to underpin the bedside-to-bench nature of this investigation, we use the human annotation and refer to it as "Scn5a-M187**5**T" throughout this manuscript.

Mice were bred on an FVB or 129/sv genetic background and housed in individually ventilated cages with sex-matched littermates (2-5 mice/cage), under standard conditions: 12 hours light/dark circle, 22°C and 55% humidity. Food and water were available *ad libitum*. The health status of mice used in the study was monitored daily and prior to experiments.

Functional experiments were conducted on hearts of male and female young adult mice of pure background (8-20 weeks), heterozygous for the knock-in mutation M1875T in the *Scn5a* gene *(Scn5a*-M1875T$^{+/-}$) and their WT littermates. Mice of both sexes and background were used evenly and analysed jointly, to make the data more widely applicable.

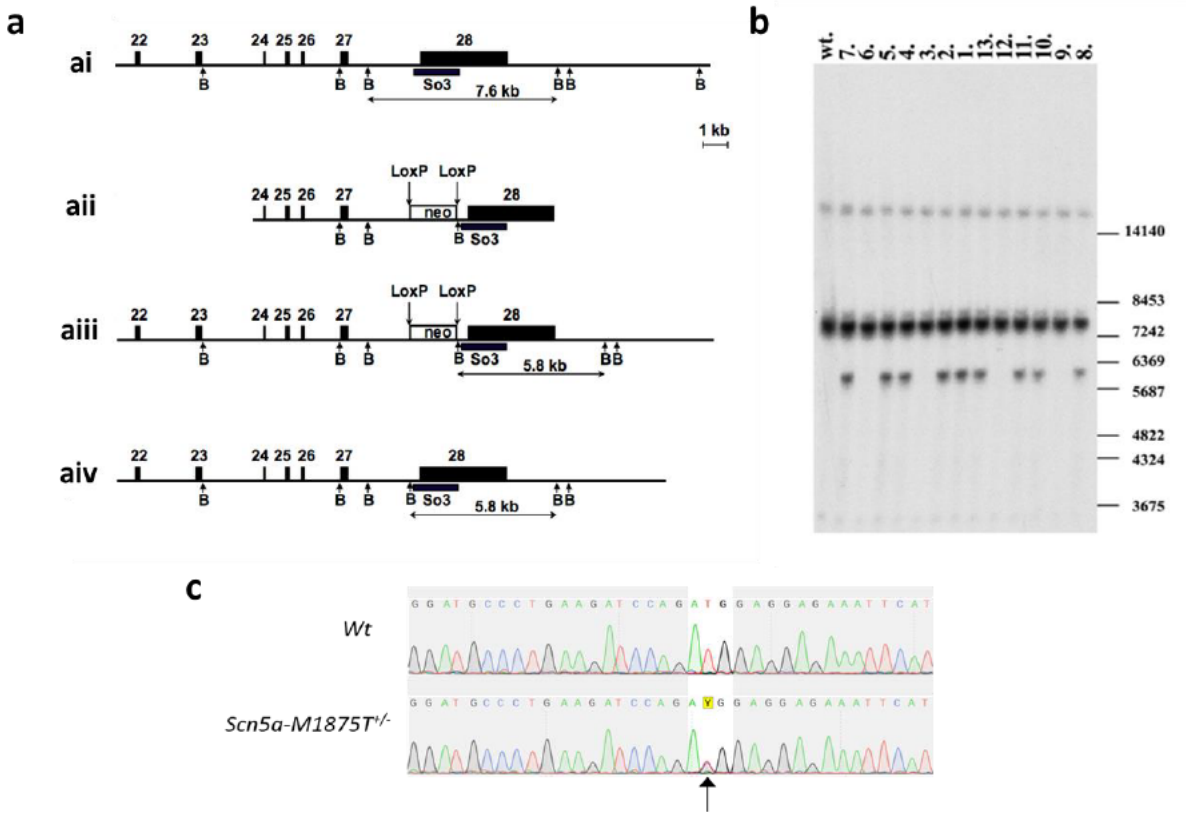


Figure 16 Targeting of exon 28 of the mouse *Scn5a* gene in order to introduce the M1875T coding mutation, and sequencing confirmation of its presence

a) The intronic and intergenic regions are shown as lines, exons are shown as filled boxes. The empty box corresponds to the neomycin resistance cassette (neo) flanked by the LoxP sites (vertical arrows). Exon numeration is shown above. The arrows below are corresponding to BamHI restriction endonuclease sites (B). The black box corresponds to Southern probe sequences (So3). The expected sizes of restriction DNA fragments are indicated below in kb. **ai)** Wildtype (WT) locus. **aii)** Targeted vector structure (without negative selection marker and plasmid backbone). **aiii)** Genomic locus after the homologous recombination. The neomycin cassette is present in intron 27 and flanked by two LoxP sites. **aiv)** Genomic locus after the CRE-mediated neo cassette deletion. **b)** Southern blot analysis of DNA isolated from mouse tail biopsy of the F1 offspring (1-13) and hybridized with the So3 probe. With help of the BamHI enzymatic digestion, we detect the WT allele 7.6 kb and targeted allele 5.8 kb. DNA samples 1, 2, 4, 5, 7, 8, 10, 11, and 13 contain correctly targeted *Scn5a* gene (Scn5a-M1875T$^{+/-}$). Positions of the size marker (in bp) are shown on the right. The WT control animal is labeled "wt". **c)** Sequencing analysis of the *Scn5a* gene region containing the mutation site in back-crossed adult mice (on pure genetic background). The T-C mutation on one allele causing the methionine-threonine exchange at position 1875 (1877) is indicated by an arrow.

Study approval

All procedures were performed in compliance with the guidelines from Directive 2010/63/EU of the European Parliament on the protection of animals used for scientific purposes and conducted in accordance with rules and regulations for experiments with animals and approved by the UK Home Office (PPL number 30/2967) and by the institutional review board of University of Birmingham.

ECG recordings *in vivo*

Non-invasive electrocardiograms (ECG) were recorded in conscious young adult mice (8-19 weeks) using a tunnel system for gentle restraint (ecgTunnel, EMKA Technologies, Paris, France) [7]. ECG recordings were analysed using ECGauto software (EMKA Technologies, Paris, France). ECGs were also recorded in isoflurane-sedated mice during echocardiography as below.

Echocardiography *in vivo*

Echocardiography was performed in sedated mice (0.5-2% isoflurane, supplemented with 100% O_2) using Vevo® 2100 system (VisualSonics, Amsterdam, Netherlands) as reported previously [8]. Heart rate was maintained at 450 ± 70 bpm. Left atria (LA) were visualised in the parasternal long axis view in the plane of the aortic root. LA area and diameter were measured during pre-atrial contraction, using the P-wave of the limb ECG trace as a guide.

Histological analysis

Hearts were fixed in formalin and paraffin-embedded tissues were cut into slices of 4 µm. Sections were dewaxed, stained with hematoxylin and eosin for overviews and subsequently dehydrated, embedded and imaged on a NanoZoomer 2.0-HAT (Hamamatsu).

Slides used for quantitative analysis were cooked in citrate buffer for antigen retrieval. Autofluorescence was quenched with a 0.25% Sudan black solution for 30 min and samples were blocked with 2% BSA/2.2% Glycine for 1 h at room temperature (RT). Wheat germ agglutinin (WGA) with Alexa Fluor™ 488 Conjugate (1:200, W11261, Invitrogen) was applied for 2 h at RT.

Images of WGA-stained cardiac tissue were obtained with a confocal microscope equipped with an Aurox Clarity (Aurox Ltd.) spinning disc unit and a 20x EC Plan-Neofluar objective (420353-9900-000, Zeiss, NA=0.5) run with Aurox Visionary (Aurox Ltd.) software.

Quantitative analysis of WGA-stained area and cardiac cell diameters was carried out using a published ImageJ plugin for atrial histological analysis (JavaCyte [9]), with minor adjustments.

Atrial cardiomyocyte isolation

Murine hearts were excised under deep terminal anaesthesia (4% isoflurane inhalation in O_2, 1.5 L/min) and perfused at 4 mL.min^{-1} at 37°C on a vertical Langendorff apparatus with the following solutions, equilibrated with 100% O_2: (i) HEPES-buffered, Ca^{2+}-free, modified Tyrode's solution containing in mM: NaCl 145, KCl 5.4, $MgSO_4$ 0.83, Na_2HPO_4 0.33, HEPES 5, and glucose 11 (pH 7.4, NaOH) x 5 min; (ii) Tyrode's enzyme solution containing 640 µg/mL collagenase type II (270 U/mg), 600 µg/ml collagenase type IV (270 U/mg) and 50 µg/mL protease (Worthington, Lakewood, NJ), 20 mM taurine and 3 µM $CaCl_2$ × 8-12 min [10]. The heart was removed from the Langendorff setup and

perfused with 5 mL of modified Kraftbruhe (KB) solution containing in mM: DL-potassium aspartate 10, L-potassium glutamate 100, KCl 25, KH_2PO_4 10, $MgSO_4$ 2, taurine 20, creatine 5, EGTA 0.5, HEPES 5, 0.1% BSA, and glucose 20 (pH 7.2, KOH).

The LA was dissected free and cardiomyocytes were dissociated gently with fire-polished glass pipettes (2 to 1 mm diameter in sequence). Cells were re-suspended in 2 mL KB buffer and Ca^{2+} was gradually reintroduced to the cell suspension incrementally over a period of 2 hours to reach a final concentration of 1 mM. All experiments were performed within 8 hours of isolation.

Whole-cell patch clamp electrophysiology of isolated atrial cardiomyocytes

Dissociated murine LA cardiomyocytes were plated on, and allowed to adhere to, laminin-coated coverslips (10 mm diameter) for at least 20 minutes. Coverslips were transferred to a recording chamber and were continually superfused at 3 $mL.min^{-1}$, with a low Na^+ external solution containing in mM; NaCl 10, KCl 4.5, $C_5H_{14}ClNO$ 130, $CaCl_2$ 1, $MgCl_2$ 1.2, HEPES 10 and glucose 10 (pH 7.4 with CsOH). To block L-type Ca^{2+} currents, 2 mM $NiCl_2$ was added to the superfusate. Experiments were performed at 22 ± 0.5°C. Whole-cell patch clamp recordings were obtained in voltage-clamp mode using borosilicate glass pipettes (tip resistances 1.5-3 MΩ).

For Na^+ current recordings, the pipette solution contained in mM: CsCl 115, NaCl 5, EGTA 10, HEPES 10, MgATP 5, TEACl 20 and $MgCl_2$ 0.5 (pH 7.2, KOH). Voltage-dependent Na^+ currents were evoked by 5 mV step depolarisations (100 ms) from a holding potential of -100 mV to test potentials ranging from -95 mV to +40 mV. Cells were excluded from analysis if there was no reversal of the sodium current by +40mV. To investigate $Na_v1.5$ voltage-dependent inactivation kinetics, cells were subject to 500 ms pre-pulses ranging from -120 mV to -40 mV, followed by a 100 ms step to -30 mV. For $Na_v1.5$ time-dependent recovery kinetics, a standard two pulse protocol was used (-120 mV to -30 mV, 20 ms), with the time between the two pulses incrementally varying between 5 and 950 ms.

All recordings and analysis protocols were performed using an Axopatch 200B amplifier (Molecular Devices, USA) and digitized at 50 kHz using a CED micro1401 driven by Signal v6 software (Cambridge Electronic Design, Cambridge, UK). Series resistance was compensated, ranging between 60-100% for all cells. Experiments were terminated if series resistance abruptly changed or was above 10 MΩ.

Atrial microelectrode recordings

As previously described [11, 12], following isolation the LA was immediately transferred into a dissecting chamber and continuously superfused at 10 $mL.min^{-1}$ with a bicarbonate buffered Krebs-Henseleit (KH) solution containing in mM: NaCl 118; $NaHCO_3$ 24.88; KH_2PO_4 1.18; Glucose 11; $MgSO_4$ 0.83; $CaCl_2$ 1.8; KCl 3.52, equilibrated with 95% O_2/5% CO_2, 36-37°C, pH 7.4. Micro-dissection and pinning out of

the LA was performed using a dissection microscope (Stemi SV 11, Zeiss, Germany). The LA was paced at 1–10 Hz via bipolar platinum electrodes. Action potentials (APs) were recorded from freely contracting LA using custom made glass floating microelectrodes containing 3 M KCl, (resistance 15-30 MΩ). Voltage signals were amplified and digitised at 20 kHz and were unfiltered (Axoclamp 2B; Molecular Devices, California, USA; Spike2 software Cambridge Electronic Design, Cambridge, UK). Measured parameters included the resting membrane potential (RMP), action potential amplitude (APA), peak depolarisation rate (dV/dt) and action potential duration (APD) at 30-90% repolarisation. APs were only analysed following sufficient rate adaptation achieved after at least 50 stimulated APs at each frequency.

Atrial optical mapping

Optical mapping of the LA was conducted as previously described [13]. Isolated whole hearts were loaded on to a vertical Langendorff apparatus and perfused with a standard KH solution. Hearts were perfused at 4 mL.min^{-1} (equilibrated with 95%O_2/5%CO_2 and heated to 36-37°C, pH 7.4). Hearts were loaded with 25 µL of voltage sensitive dye Di-4-ANEPPS at a concentration of 5 mg/mL, diluted in 1 mL of KH solution and delivered via bolus port injection over 3-5 minutes. The LA was then isolated and pinned in a superfusion chamber containing 37°C KH solution for transfer to the optical mapping setup, anterior surface facing up.

In the optical mapping system, atria were superfused with KH solution (95%O_2/5%CO_2, 36-37°C) containing contraction uncoupler Blebbistatin (35 µM). For imaging, atria were illuminated by two dual LEDs at 530 nm. A 630 nm long-pass filter was used to separate emitted fluorescence, imaged using an ORCA flash 4.0 CMOS camera (Hamamatsu, Japan). Images were acquired at a framerate 0.987 kHz and pixel size of 71 µm/pixel^2. Atria were paced using bipolar platinum electrodes delivering 2 ms pulses at twice diastolic threshold (minimum voltage required to elicit APs).

One-minute baseline recording was taken following a 10 minute equilibration period to ensure contraction uncoupling and temperature re-stabilisation. During imaging, atria were initially paced at 330 ms pacing cycle length (PCL). A 'ramp' pacing protocol was then initiated, in which the atria were paced at 120 ms PCL for 100 stimuli and then PCL was reduced from 120 ms to 80 ms in 10 ms intervals every 20 stimuli. After taking baseline recordings, LED illumination was switched off and the superfusion solution replaced with an identical solution containing flecainide, a clinically-used sodium channel blocker [14] at a concentration of 1 µM and then 5 µM (or control solution without flecainide for time control experiments).

Subsequent recordings were then made as described above after 20 minutes superfusion with 1 µM flecainide solution, and then further 15 minutes with 5 µM flecainide solution. Atria were paced at 330 ms PCL continuously in dark conditions between recordings.

From these recordings, APD and conduction velocity (CV) were mapped across the LA using ElectroMap software [13]. Atria were removed from analysis at a given PCL if loss of 1:1 capture ratio with pacing stimuli (i.e. missed beats) was observed.

Statistics

For all murine experiments presented herein, experimenters were blinded to the genotype of the littermate pairs during data collection and analysis. Student t-tests were used for singular comparisons for normally distributed data. A hierarchical nested t-test (Figure 3) and Mann-Whitney test (Table S3) were used where appropriate. Multiple comparisons were made using 2-way ANOVA with Bonferroni's post-hoc tests. For current-voltage graphs (Figure 3b), a Boltzmann curve was fit to the data, using the modified Boltzmann equation: $I_{Na} = G_{max}(V_m - V_{rev})/(1+Exp[(V_{0.5}-V_m)/k])$, where I_{Na} is the current density at an equivalent test potential (V_m), $_{Gmax}$ is the peak conductance (nS), V_{rev} is the reverse potential, $V_{0.5}$ is the membrane potential at 50% current activation, and k is the slope constant . All graphical representations display individual measurements. Means are quoted and shown in Figures ± SEM unless stated otherwise. Level of statistical significance is shown in Figures as follows: *p<0.05; **p<0.01; ***p<0.001; ****p<0.0001. Statistics and Figures were created using Prism 8 (GraphPad Software, San Diego, California).

Results

Viable heterozygous *Scn5a*-M1875T$^{+/-}$ mice show normal cardiac size, structure and basic function

The point mutation previously identified in patients with early familial AF was successfully introduced to exon 28 of the mouse *Scn5a* gene via homologous recombination of a targeting vector. The vector contained the T-C point mutation (CRISPR/cas9-mediated) resulting in methionine-threonine exchange in the $Na_v1.5$ protein (Figure 1, Figure S1a). Offspring from both WT x heterozygote (=*Scn5a*-M1875T$^{+/-}$) and heterozygote x heterozygote pairings were viable. No homozygous *Scn5a*-M1875T$^{-/-}$ offspring were born (Figure S1b), suggesting embryonic lethality, as previously reported for other *Scn5a* mutations [15]. Accordingly, the ratio of WT and heterozygous animals shifted from 1:2 (expected) to approximately 1:3 when heterozygous animals were crossed (Figure S1b). The ratio of male:female sex in offspring approximated 1:1 as expected (Figure S1c).

Age-matched young adult WT and *Scn5a*-M1875T$^{+/-}$ mice displayed similar heart rate, PR-, QRS- and QT- interval in electrocardiograms recorded awake (Table S1) and during sedation (Table S2). Echocardiography and histological examination excluded overt differences in structure (Table S3, Figure 2a). Neither atrial extracellular matrix content nor atrial cardiomyocyte cell diameter were affected by the mutation (Figure 2b and c, Figure S2a). Accordingly, pro atrial natriuretic peptide protein expression (proANP) was detected in right atria as expected but was not elevated in ventricles (Figure S2b).

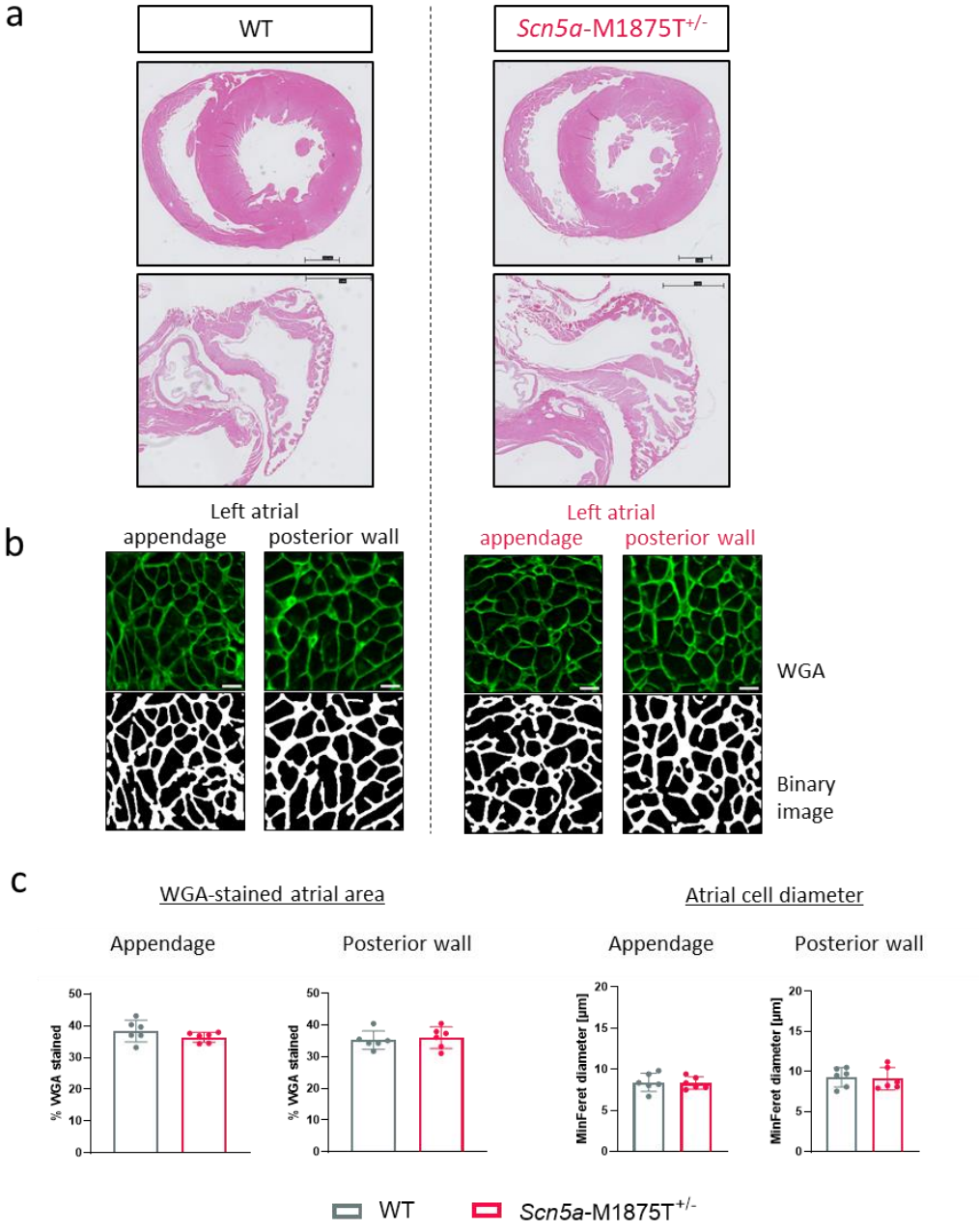


Figure 2 Unaltered atrial amount of extracellular matrix content and myocyte diameter

a) Hematoxylin and eosin-stained sections of wildtype (WT) and *Scn5a*-M1875T$^{+/-}$ litter pair hearts (ventricles, upper panel; left atria, lower panel). Scale bars represent 1 mm. There were no obvious differences between genotypes. **b)** Exemplary immunofluorescence images from atrial regions of interest (ROI) of wheat germ agglutinin (WGA, green) staining and corresponding binary images for quantification in left atrial (LA) appendage and LA posterior wall from WT and *Scn5a*-M1875T$^{+/-}$ hearts. Scale bars represent 10 µm. **c)** Quantification of WGA-stained atrial area and atrial cell diameters from transverse sections as depicted in b). Neither parameter was affected by the point mutation (WGA-stained atrial area quantified from LA appendage: N=6 hearts and 65/67 individual ROI per group; LA posterior wall N=6 hearts and 26/29 ROI per group. Atrial cell diameter quantified from LA appendage: N=6 hearts and 14563/13368 individual cells per group; LA posterior wall and 8283/8384 individual cells per group). Data are presented as mean ± SD.

Atrial *Scn5a*-M1875T$^{+/-}$ cardiomyocytes have an augmented peak sodium current density

To determine the impact of the M1875T point mutation on peak I_{Na} amplitude and $Na_v1.5$ channel gating properties, left atrial cardiomyocytes from WT and *Scn5a*-M1875T$^{+/-}$ mice (8-13 weeks) were isolated and whole-cell patch clamp recordings were performed.

The M1875T variant increased I_{Na} over test potentials ranging from –100 to +40 mV (Figure 3a and b). At a peak test potential of -30 mV, mean left atrial cardiomyocyte I_{Na} density was higher in *Scn5a*-M1875T$^{+/-}$ (-28.0 ± 1.1 pA/pF, n=107 cells) than in WT littermates (-22.8 ± 0.7 pA/pF, n=109 cells, p<0.0001, Figure 3ci). The elevation in I_{Na} was also apparent when recordings were grouped by heart

(*Scn5a*-M1875T$^{+/-}$ -29.1 ± 2.2 pA/pF, N=14 vs WT -22.3 ± 0.9 pA/pF, N=15, p=0.0075, Figure 3cii) and after applying hierarchical analysis (*Scn5a*-M1875T$^{+/-}$ -29.1 ± 1.1 pA/pF, n=107 cells, N=14 mice vs WT -22.3 ± 0.9 pA/pF, n=109 cells, N=15 mice, p=0.0093).

Capacitance measurements were not different between genotypes, indicative of similar cell size of atrial cardiomyocytes (Figure S3a).

Whole-cell I_{Na} voltage-dependent inactivation and time-dependent recovery kinetics were not altered in *Scn5a*-M1875T$^{+/-}$ cardiomyocytes compared to WT (Figure S3b and c). $Na_v1.5$ expression in hearts of *Scn5a*-M1875T$^{+/-}$ mice at the mRNA and the protein level revealed no difference at either the whole cell or isolated membrane fraction level (Figure S4).

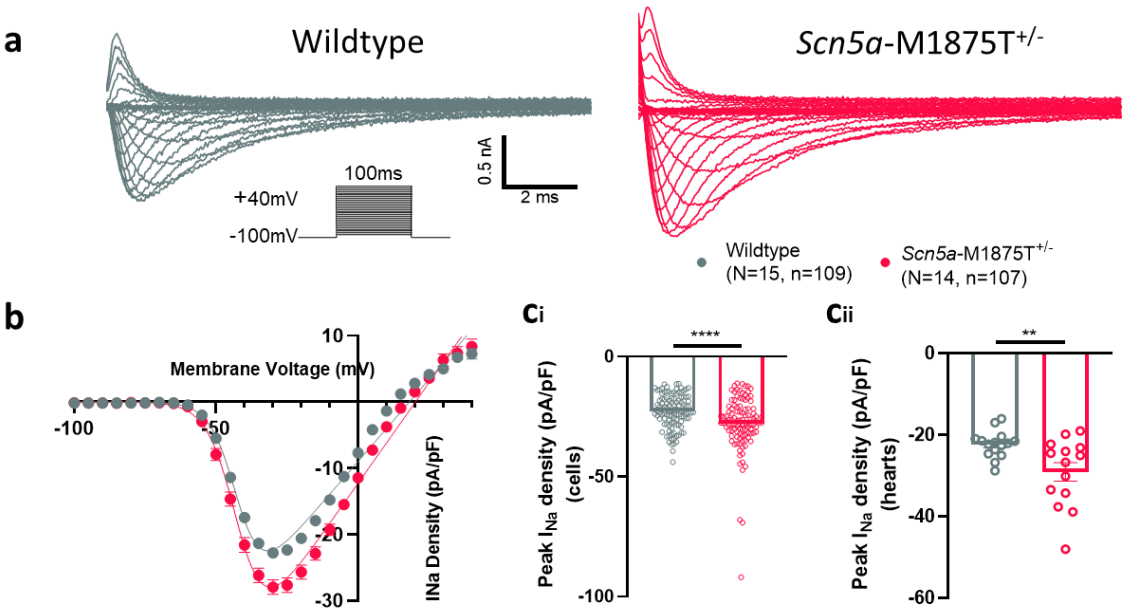


Figure 3 Isolated atrial cardiomyocytes with the *Scn5a*-M1875T$^{+/-}$ mutation have a larger sodium current than wildtypes when measured with whole-cell patch clamp electrophysiology
a) Representative sodium current (I_{Na}) traces from whole-cell voltage clamp recording of isolated left atrial (LA) cardiomyocytes from wildtype (WT) (grey) and *Scn5a*-M1875T$^{+/-}$ (red) hearts. **b)** Normalised grouped data revealed that the *Scn5a*-M1875T$^{+/-}$ mutation increases peak I_{Na} in LA cardiomyocytes over test potentials ranging from –100 to +40 mV. **c)** At the peak I_{Na} test potential of -30 mV, *Scn5a*-M1875T$^{+/-}$ cardiomyocytes had a significantly larger I_{Na} than WTs, both when comparing individual cells (n=109 WT, n=107 *Scn5a*-M1875T$^{+/-}$) **(ci)** and hearts (N=15 WT, N=14 *Scn5a*-M1875T$^{+/-}$) **(cii)**. Data are presented as the mean ± SEM.

Action potentials from *Scn5a*-M1875T$^{+/-}$ atria have a larger amplitude and faster peak upstroke velocity

Action potentials (APs) were measured in whole left atrial tissue isolated from WT and *Scn5a*-M1875T$^{+/-}$ mice (9-13 weeks) using sharp microelectrodes.

Action potential amplitude was significantly larger in *Scn5a*-M1875T$^{+/-}$ murine left atria at all PCLs tested and this effect was more pronounced at shorter cycle lengths (N=8, n=24-25, Figure 4a). The variant resulted in a faster peak upstroke velocity (dV/dt), especially at the shorter cycle lengths (100 ms PCL: WT 128.0 ± 3.3, n=24; *Scn5a*-M1875T$^{+/-}$ 142.8 ± 4.0 mV/ms, n=25, p=0.0282, Figure 4b, representative traces Figure 4c).

The resting membrane potential was not different between genotypes (100 ms PCL: WT -72.4 ± 0.6; *Scn5a*-M1875T$^{+/-}$ -73.1 ± 0.6 mV). Atrial activation times were also similar (100 ms PCL: WT 4.9 ± 0.2; *Scn5a*-M1875T+/- 4.9 ± 0.2 ms) (Table S4). Only at the long PCL of 1000 ms, the AP duration (APD) at 50 and 90% repolarisation was shorter in *Scn5a*-M1875T$^{+/-}$ left atria than in WT (Figure 4d-f), while the APD at 30 and 70% repolarisation was not significantly different (Table S4). Similarly, optical mapping data showed no APD differences at PCLs tested. We performed analyses of APD restitution (Figure S5, which suggest that an effect of the M1875T mutation may be a blunting of APD restitution.

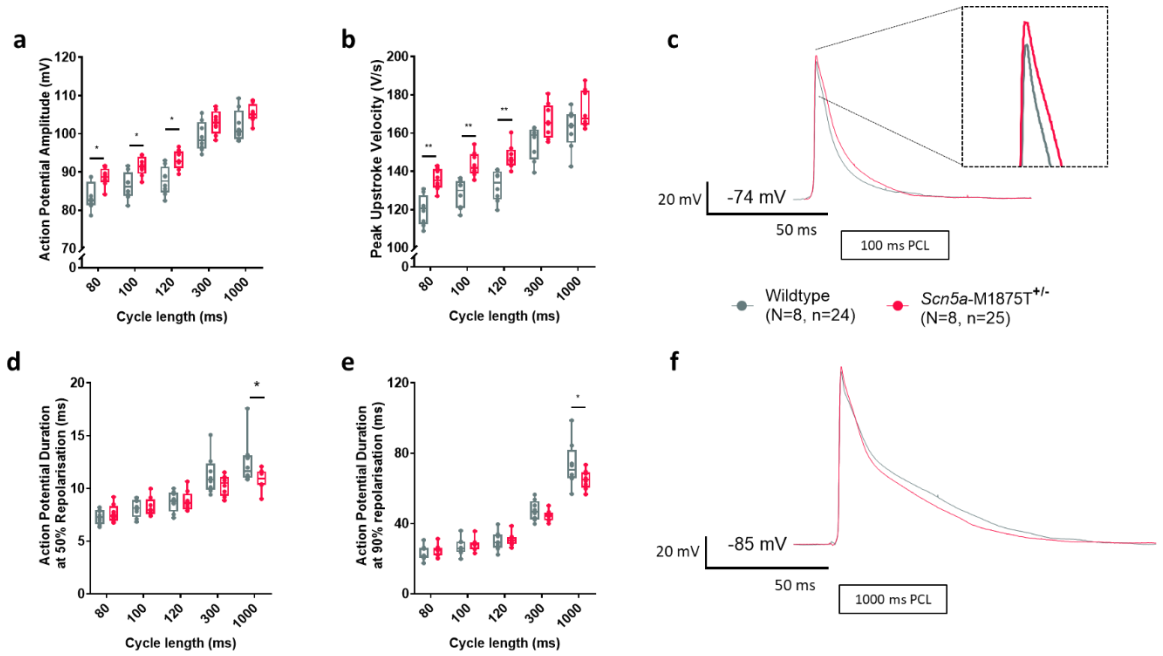


Figure 4 Action potentials from atria with the *Scn5a*-M1875T$^{+/-}$ mutation have a larger action potential amplitude and a faster peak upstroke velocity when measured with the sharp microelectrode technique

a) *Scn5a*-M1875T$^{+/-}$ left atria (LA) had a significantly larger action potential (AP) amplitude at shorter pacing cycle lengths (PCLs) of 80-120 ms ($p<0.05$) and **b)** a significantly faster peak upstroke velocity (dV/dt). **c)** Representative AP traces from WT (grey) and *Scn5a*-M1875T$^{+/-}$ (red) LA stimulated at 100 ms PCL. **d-f)** When paced at 1000 ms PCL, *Scn5a*-M1875T$^{+/-}$ LA had a significantly shorter AP duration (APD) when measured at 50% (APD50) **(d)** and 90% (APD90) **(e)** repolarisation. *$p<0.05$, **$p<0.01$, wildtype (WT) vs *Scn5a*-M1875T$^{+/-}$, N=8 per group, n=24 WT, n=25 *Scn5a*-M1875T$^{+/-}$; ANOVA statistics. **f)** Representative AP traces from WT (grey) and *Scn5a*-M1875T$^{+/-}$ (red) LA stimulated at 1000 ms PCL. Data in a, b, d and e are presented as box-whiskers with box limits denoting the IQR and the whiskers projecting to the outliers.

Flecainide-induced atrial conduction slowing and post-repolarisation refractoriness is less pronounced in *Scn5a*-M1875T$^{+/-}$ atria

Optical mapping of WT and *Scn5a*-M1875T$^{+/-}$ whole left atrial tissue was performed to test effects of the heterozygous *Scn5a*-M1875T mutation on atrial conduction. Left atria were superfused with the open channel sodium channel blocker flecainide (1 µM, clinically used concentration) to determine the response of *Scn5a*-M1875T$^{+/-}$ and WT left atria. While conduction velocity was unchanged at baseline, flecainide slowed conduction less in *Scn5a*-M1875T$^{+/-}$ left atria (conduction velocity difference at 100 ms PCL -6 ± 1 cm/s, n=12, p=0.0357) than in WTs (conduction velocity difference at 100 ms PCL -10 ± 1 cm/s, n=12, p=0.0357, Figure 5a and b, Figure S6).

We also investigated flecainide-induced changes in left atrial refractoriness as it is known that flecainide induces post-repolarisation refractoriness using rapid atrial pacing. Representative optical

AP recordings show 1:1 capture in the *Scn5a*-M1875T$^{+/-}$ left atria with flecainide, while several stimuli in the WT left atria did not elicit APs (Figure 5c). All time-controlled left atria (no flecainide, same experimental duration) were successfully paced with 1:1 capture down to 80 ms PCL. Loss of 1:1 capture began at longer PCLs in WT (7/12 atria lost 1:1 capture at PCLs ≤ 120 ms, Figure 5d) compared to *Scn5a*-M1875T$^{+/-}$ (1/12 atria lost 1:1 capture at PCLs ≤ 120 ms, p=0.0185) left atria. The diastolic pacing threshold remained consistent throughout experiments. Thus, flecainide induced less pronounced post-repolarisation refractoriness in the *Scn5a*-M1875T$^{+/-}$ left atria.

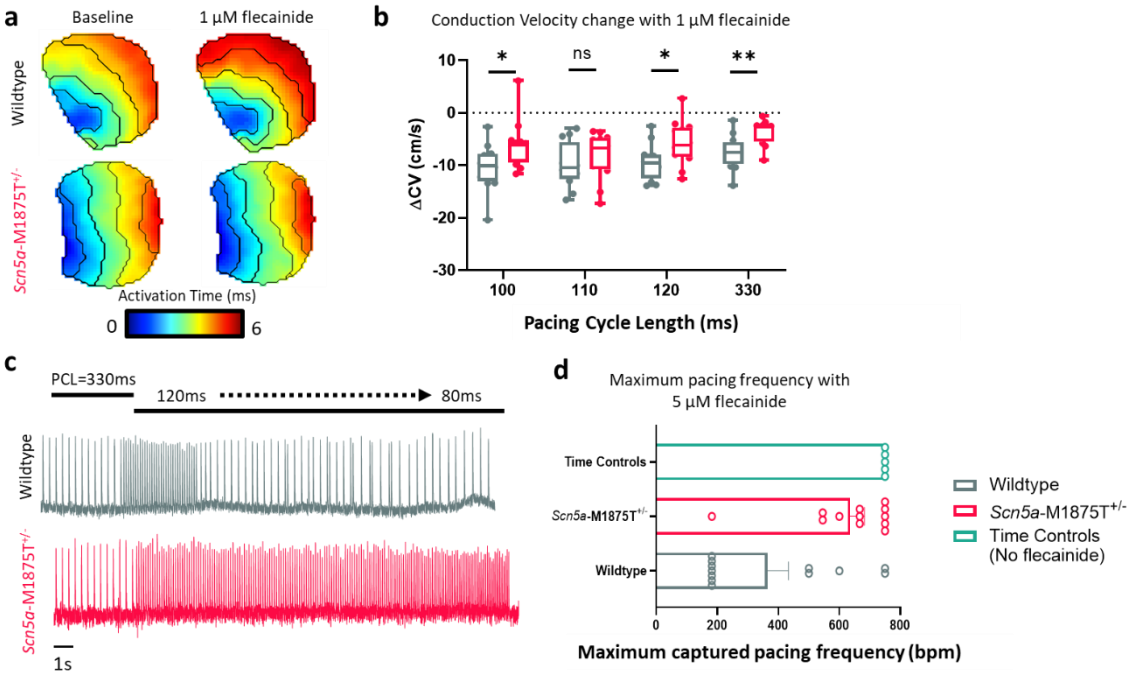


Figure 5 The response to the anti-arrhythmic agent flecainide is reduced in *Scn5a*-M1875T$^{+/-}$ atria in optical mapping

a) Example left atrial (LA) activation maps from wildtype (WT, top panels) and *Scn5a*-M1875T$^{+/-}$ (bottom panels) mice. Left panels show activation maps at baseline, right panels show activation of the same atria following exposure to 1 µM flecainide for 20 minutes. **b)** Grouped data showing change in conduction velocity (ΔCV) following exposure to 1 µM flecainide in WT (grey) and *Scn5a*-M1875T$^{+/-}$ (red) LA for 20 mins at different pacing cycle lengths. **c)** Example traces of optical action potentials (APs) recorded following further treatment of WT (top, grey) and *Scn5a*-M1875T$^{+/-}$ (bottom, red) LA with 5 µM flecainide for 15 mins while reducing pacing cycle length (increasing pacing frequency). **d)** Grouped data showing minimum pacing frequency in beats per minute (bpm) at which 1:1 stimulus capture was maintained in WT (grey) and *Scn5a*-M1875T$^{+/-}$ (red) LA following exposure to 5 µM flecainide. Time control data (green) shows minimum PCL at which 1:1 stimulus capture was maintained in atria that were not exposed to flecainide but had been under experiment conditions for the same time period (35 mins from baseline recording). N=12 per group at 330 ms-100 ms PCL. Atria were excluded from further analysis at shorter PCLs if 1:1 capture was lost, only data in steady state was used. N=5 for time control experiments. *p<0.05, **p<0.01, WT vs *Scn5a*-M1875T$^{+/-}$; ANOVA statistics. Data are represented as box-whiskers with box limits denoting the IQR and the whiskers projecting to min and max values (b) or as as the mean ± SEM (d).

Discussion

Main findings

Our study describes the effects of the familial atrial fibrillation (AF) mutation *Scn5a*-M1875T$^{+/-}$ in a newly generated murine model. Key findings are that the M1875T *Scn5a* mutation leads to an increased atrial action potential upstroke velocity and amplitude, and a selective increase in the early cardiac sodium current (I_{Na}). Atrial cardiomyocyte capacitance and size, as well as cardiac size and function, are preserved. The effect of the sodium channel blocker flecainide is dampened in *Scn5a*-M1875T$^{+/-}$ atria. Our measurements in this new murine model confirm that a selective increase of I_{Na} may lead to familial AF as observed in the family affected, and suggest that commonly used concentrations of sodium channel blockers may be less effective in familial forms of AF with a selective increase in I_{Na} than in other types.

Gain-of-function properties of *Scn5a*-M1875T$^{+/-}$ sodium channels in the murine atrium

Our data show a gain-of-function variant, namely an increased early sodium current as evidenced by an augmented action potential amplitude and upstroke velocity, and larger I_{Na} in hearts with a *Scn5a*-M1875T$^{+/-}$ variant.

In contrast to findings in HEK293 cells [5], there was no depolarising shift of $Na_v1.5$ channel inactivation in murine left atrial cardiomyocytes observed. Instead, we show a similarly augmented I_{Na} without alterations in channel gating properties. Generation of the murine mutant model allowed us to study mutated sodium channels in cardiac tissue within the presence of the greater protein complex including α- and β- subunits and other membrane proteins, a complete cardiomyocyte contractile apparatus and all other cardiac cell types.

SCN5A genetic variants reported show various underlying mechanisms mainly linked to channel dysfunction, defective channel trafficking or protein complex formation [16]. Cardiac sodium channels have been observed to form dimers and different regions of the channel protein have been implicated in dimerization [17]. Structural analysis following the hypothesis of $Na_v1.5$ dimerization via C-terminal interaction reveals that the surface of residue Met1875 of one $Na_v1.5$ cytosolic C-terminus will interact with Ala1924 of a second $Na_v1.5$ [17]. This prediction suggests that the location site containing the mutation in our model could provide a structural basis for altered $Na_v1.5$-$Na_v1.5$ channel interaction further to be investigated.

It is unlikely that the M1875T mutation increases the *late* sodium current ($I_{Na,l}$), as action potentials (APs) we measured were not prolonged by the mutation, in line with the initial report of the mutation

in HEK cells [5]. A lack of AP prolongation clearly differs to findings in the gain-of-function mutation *ΔKPQ-Scn5a*$^{+/-}$ mutant murine model which shows an increase in $I_{Na,l}$ [11] with prolonged atrial and ventricular AP duration, especially at longer pacing cycle lengths. This suggests that the M1875T mutation acts differently to, and is distinct from, *SCN5A* gain-of-function mutations leading to prolonged repolarisation and long QT syndrome, in concordance with the broad spectrum of phenotypic outcomes resulting from mutations in the same ion channel gene [18].

It could be of interest to model the effects of the increased I_{Na} including effects on restitution and on human atrial AP models, e.g. higher amplitude and upstroke velocity at fast rates, while a slight APD shortening was only seen at slower rates.

Effect of *Scn5a*-M1875T$^{+/-}$ on conduction and refractoriness

While defects in the cardiac sodium channel can also cause conduction disturbances [16, 18], this variant shows a dampened response to flecainide both on conduction and post-repolarisation refractoriness. Flecainide is a clinically used sodium channel blocker that inhibits cardiac I_{Na} via blocking the pores of open $Na_v1.5$ channels [10, 14]. The differential response to flecainide is likely due to the increased early sodium influx through the mutated $Na_v1.5$ channels, enabling preservation of conduction and activation properties in atrial cardiomyocytes when sodium channels are inhibited, leading to an enhanced activation reserve.

Limitations

This study primarily investigated which alteration in sodium channels is the basis for the clinically observed AF in the family carrying the mutation. Spontaneous AF was not observed during the single time point ECG. Detailed investigation of the arrhythmia trigger and pro-arrhythmic effects in the model, e.g. using telemetry and electrophysiological studies, are warranted in the future. It would also be of interest to systematically investigate the effect of the mutation on ventricular I_{Na}.

Murine models have limitations due to differences between mice and human, but due to consistency in sodium currents have been useful in characterising sodium channel mutations [8, 11, 15]. Identified mutation-induced changes at the cellular and organ level in this model appear sufficient to explain AF in the original family. Studies in human cardiomyocytes and in atrial engineered heart tissue would be desirable to assess the effect of the M1875T mutation in human models in the future.

Conclusion

The *Scn5a*-M1875T$^{+/-}$ variant causes a selective increase in the early cardiac sodium current, leading to an increased activation reserve and reduced refractoriness, whilst structure and contractile function are preserved. These findings can explain the familial occurrence of atrial ectopy and atrial fibrillation in the absence of reported severe heart disease. More widely they suggest a mechanism by which altered cardiomyocyte sodium current can predispose to atrial fibrillation. Our data also show that the M1875T gain-of-function mutation decreases the effectiveness of sodium channel blockers such as flecainide, which may have implications for treatment.

Data Availability Statement

The datasets generated during the current study are available from the corresponding author on reasonable request.

Author Contribution Statement

LF and PK designed the research; BVS generated the mouse model in TRAM upon request by PK and LF;

MO, LCS, CO, SBS, SA, JSR, SNK, AM, DD, LFo, LF and APH conducted experiments, analysed data and performed statistical analysis;

KG, DP, APH, PK, LF supervised experiments and analysis.

MO, LCS, CO, SBS and LF wrote the manuscript together with all co-authors. All co-authors critically reviewed the manuscript.

Declaration of Interests

The authors have declared no direct conflict of interest in regards to the manuscript.

L.F. has received institutional research grants from governmental and charity funding agencies and several biomedical companies.

P.K. has received research support from several drug and device companies active in atrial fibrillation and has received honoraria from several such companies in the past.

L.F. and P.K. are listed as inventors on two patents held by University of Birmingham (Atrial Fibrillation Therapy WO 015140571, Markers for Atrial Fibrillation WO 2016012783).

Funding

This work was partially supported by the Leducq Foundation, British Heart Foundation ((FS/12/40/29712); FS/13/43/30324; PG/17/30/32961; PG/20/22/35093; AA/18/2/34218), EU Horizon 2020 CATCH ME (grant agreement number 633196) and MAESTRIA (grant agreement number 965286), AFFECT EU (grant agreement number 847770); European Union BigData@Heart (grant agreement EU IMI 116074), German Centre for Cardiovascular Research supported by the German Ministry of Education and Research (DZHK), Medical Research Council (MR/V009540/1), and the Wellcome Trust (201543/B/16/Z; 221650/Z/20/Z).

Acknowledgments

We thank Hartwig Wieboldt, Clara Apicella and Olivia Grech for technical assistance and acknowledge UoB Biomedical Services Unit (BMSU) and the UKE Microscopy Imaging Facility (UMIF) for expert support.

References

[1] Fabritz L, Crijns H, Guasch E, Goette A, Hausler KG, Kotecha D, et al. Dynamic risk assessment to improve quality of care in patients with atrial fibrillation: the 7th AFNET/EHRA Consensus Conference. *Europace* 2021; **23**: 329-344.

[2] Fabritz L, Guasch E, Antoniades C, Bardinet I, Benninger G, Betts TR, et al. Expert consensus document: Defining the major health modifiers causing atrial fibrillation: a roadmap to underpin personalized prevention and treatment. *Nat Rev Cardiol* 2016; **13**: 230-237.

[3] Yoneda ZT, Anderson KC, Quintana JA, O'Neill MJ, Sims RA, Glazer AM, et al. Early-Onset Atrial Fibrillation and the Prevalence of Rare Variants in Cardiomyopathy and Arrhythmia Genes. *JAMA Cardiol* 2021; **6**: 1371-1379.

[4] Darbar D, Kannankeril PJ, Donahue BS, Kucera G, Stubblefield T, Haines JL, et al. Cardiac sodium channel (SCN5A) variants associated with atrial fibrillation. *Circulation* 2008; **117**: 1927-1935.

[5] Makiyama T, Akao M, Shizuta S, Doi T, Nishiyama K, Oka Y, et al. A novel SCN5A gain-of-function mutation M1875T associated with familial atrial fibrillation. *J Am Coll Cardiol* 2008; **52**: 1326-1334.

[6] Skryabin BV, Kummerfeld DM, Gubar L, Seeger B, Kaiser H, Stegemann A, et al. Pervasive head-to-tail insertions of DNA templates mask desired CRISPR-Cas9-mediated genome editing events. *Sci Adv* 2020; **6**: eaax2941.

[7] Silbernagel N, Walecki M, Schafer MK, Kessler M, Zobeiri M, Rinne S, et al. The VAMP-associated protein VAPB is required for cardiac and neuronal pacemaker channel function. *FASEB J* 2018; **32**: 6159-6173.

[8] Blana A, Kaese S, Fortmüller L, Laakmann S, Damke D, van Bragt K, et al. Knock-in gain-of-function sodium channel mutation prolongs atrial action potentials and alters atrial vulnerability. *Heart Rhythm* 2010; **7**: 1862-1869.

[9] Winters J, von Braunmuhl ME, Zeemering S, Gilbers M, Brink TT, Scaf B, et al. JavaCyte, a novel open-source tool for automated quantification of key hallmarks of cardiac structural remodeling. *Scientific reports* 2020; **10**: 20074.

[10] S OB, Holmes AP, Johnson DM, Kabir SN, C OS, M OR, et al. Increased atrial effectiveness of flecainide conferred by altered biophysical properties of sodium channels. *J Mol Cell Cardiol* 2022; **166**: 23-35.

[11] Lemoine MD, Duverger JE, Naud P, Chartier D, Qi XY, Comtois P, et al. Arrhythmogenic left atrial cellular electrophysiology in a murine genetic long QT syndrome model. *Cardiovascular research* 2011; **92**: 67-74.

[12] Holmes AP, Yu TY, Tull S, Syeda F, Kuhlmann SM, O'Brien SM, et al. A Regional Reduction in Ito and IKACh in the Murine Posterior Left Atrial Myocardium Is Associated with Action Potential Prolongation and Increased Ectopic Activity. *PLoS One* 2016; **11**: e0154077.

[13] O'Shea C, Holmes AP, Yu TY, Winter J, Wells SP, Correia J, et al. ElectroMap: High-throughput open-source software for analysis and mapping of cardiac electrophysiology. *Sci Rep* 2019; **9**: 1389.

[14] Ramos E, O'Leary M E. State-dependent trapping of flecainide in the cardiac sodium channel. *J Physiol* 2004; **560**: 37-49.

[15] Remme CA, Verkerk AO, Nuyens D, van Ginneken AC, van Brunschot S, Belterman CN, et al. Overlap syndrome of cardiac sodium channel disease in mice carrying the equivalent mutation of human SCN5A-1795insD. *Circulation* 2006; **114**: 2584-2594.

[16] Clerx M, Heijman J, Collins P, Volders PGA. Predicting changes to INa from missense mutations in human SCN5A. *Scientific reports* 2018; **8**: 12797.

[17] Nathan S, Gabelli SB, Yoder JB, Srinivasan L, Aldrich RW, Tomaselli GF, et al. Structural basis of cytoplasmic NaV1.5 and NaV1.4 regulation. *J Gen Physiol* 2021; **153**.

[18] Remme CA, Bezzina CR. Sodium channel (dys)function and cardiac arrhythmias. *Cardiovasc Ther* 2010; **28**: 287-294.

Supplement to: Familial atrial fibrillation mutation M1875T-SCN5A increases early sodium current and dampens the effect of flecainide

Supplemental Figures

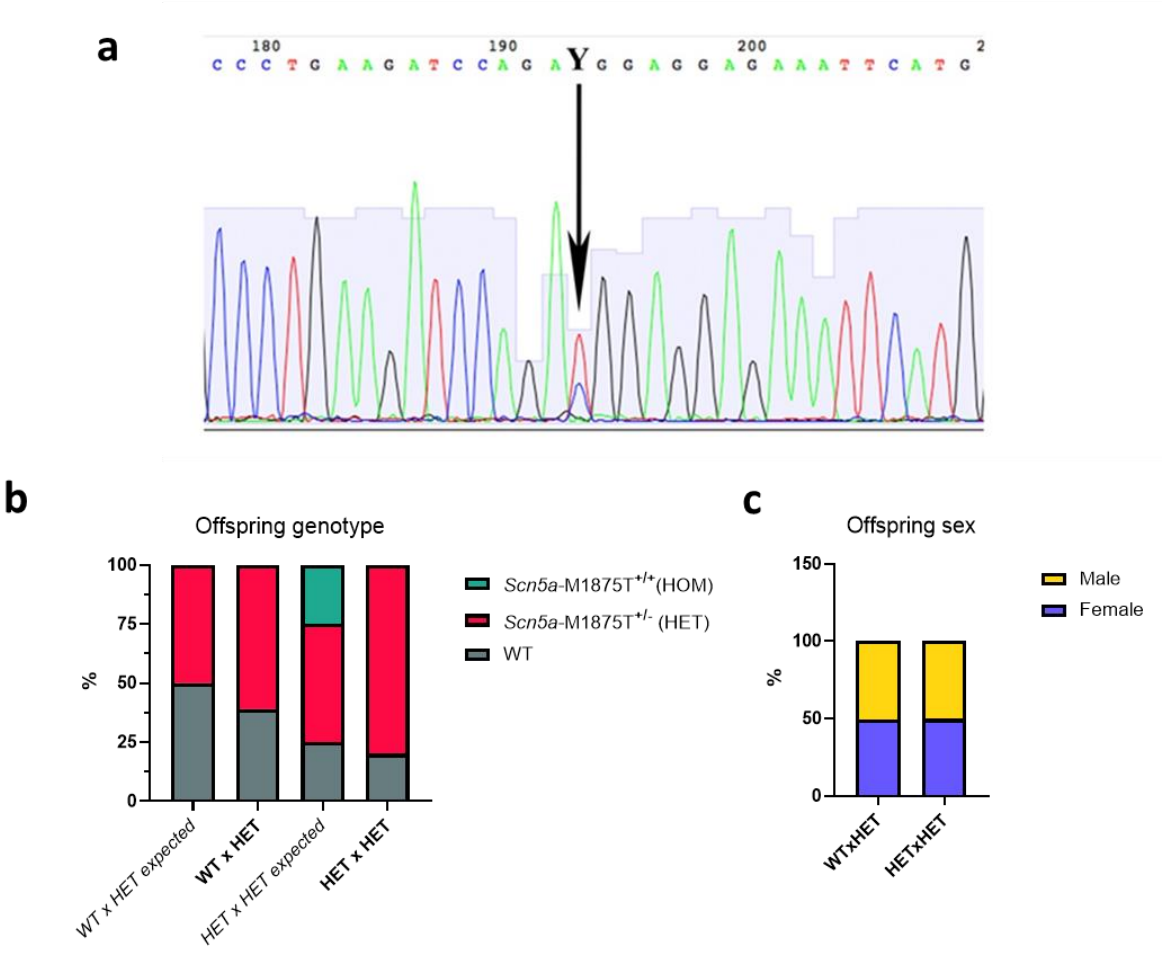


Figure S1: Sequencing analysis of F1 offspring, and subsequent offspring genotype and sex ratios. **a)** Sequencing analysis of the heterozygous F1 offspring animal number 8 (Figure 1b). Position of the T-C mutation, which corresponds to M1875(7)T amino acid exchange in the protein sequence, is labeled by an arrow. **b)** Observed offspring genotype and **c)** sex distribution, analysed from 90 litters (901 animals in total), pairing with WTxHET or HETxHET animals. WT, wildtype; HET, heterozygous; HOM, homozygous.

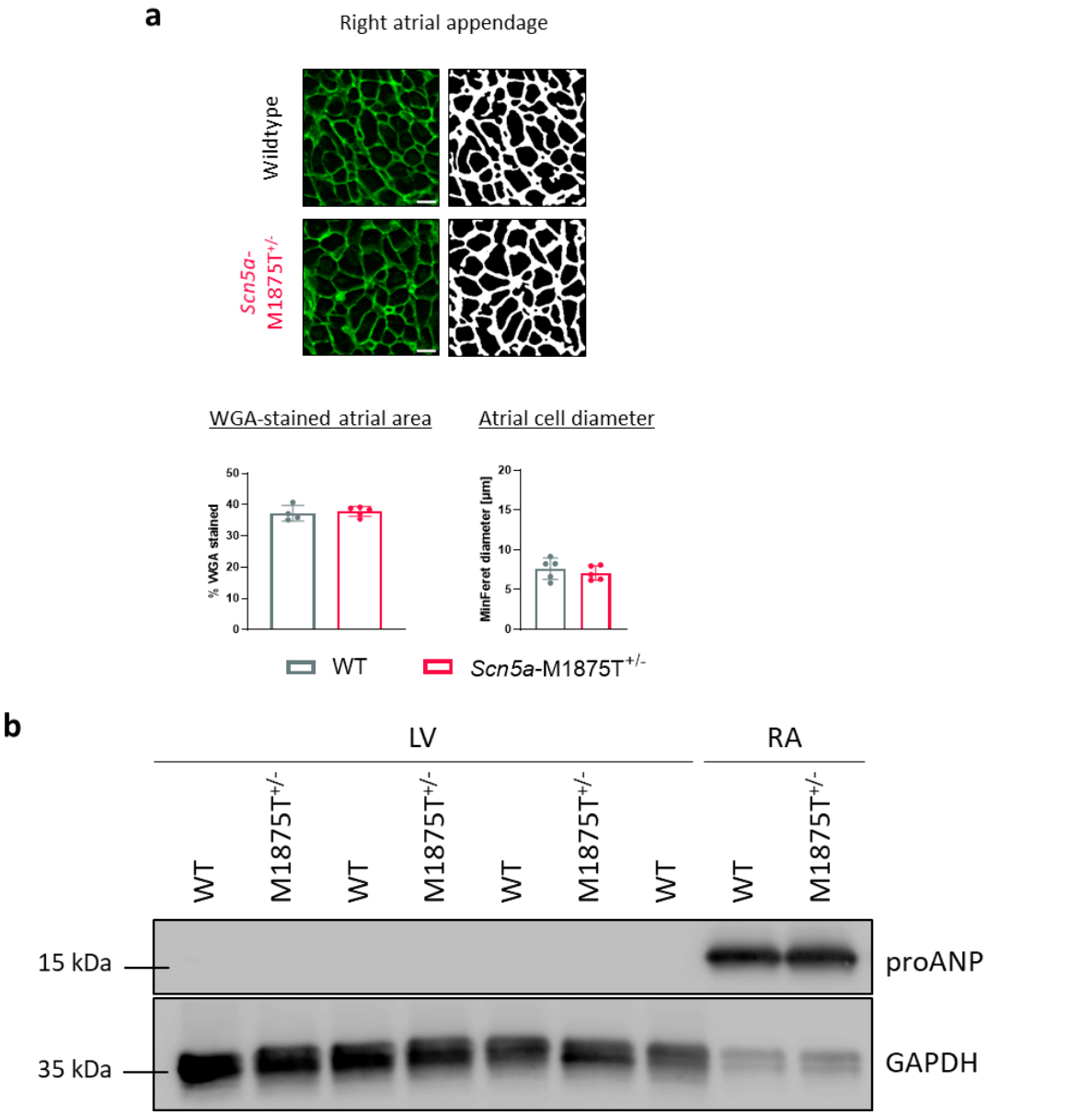


Figure S2: Histological phenotyping of wildtype and *Scn5a*-M1875T$^{+/-}$ right atria and ventriclular and right atrial proANP protein level assessment

a) Exemplary immunofluorescence images from atrial regions of interest (ROI) of wheat germ agglutinin (WGA, green) staining and corresponding binary images for quantification in left atrial (LA) appendage and LA posterior wall from wildtype (WT, left) and *Scn5a*-M1875T$^{+/-}$ (right) mice. Scale bars represent 10 µm. Graphs show quantification of WGA-stained atrial area and atrial cell diameters from transverse sections as depicted above. Neither parameter was affected by the point mutation at young adult age (WGA-stained atrial area quantified from LA appendage: N=6 hearts and 22/21 individual ROI per group; Atrial cell diameter quantified from N=6 hearts and 8548/11883 individual cells per group. Data are presented as mean ± SD. **b)** Immunoblot probing for pro-ANP in left ventricular (LV) as well as right atrial (RA) tissue. GAPDH expression serves as loading reference with reduced loading for the atrial samples. There was no ventricular signal for proANP, excluding overt heart failure.

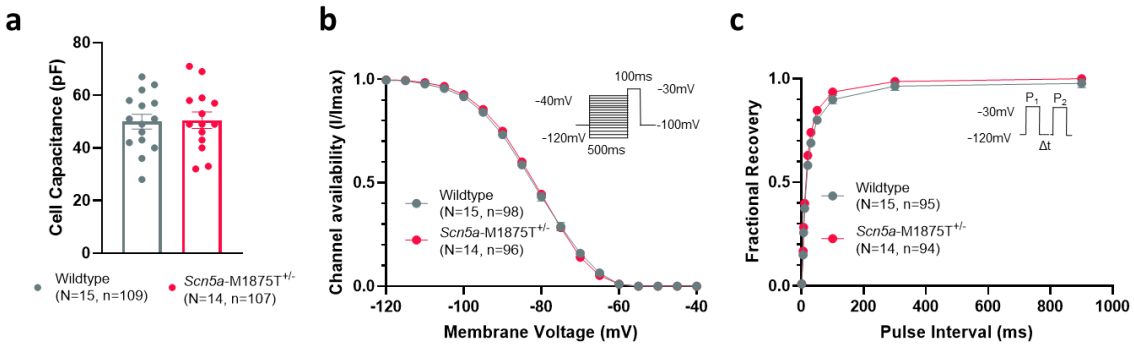


Figure S3: Measurements of cell capacitance, voltage-dependent inactivation and time-dependent recovery kinetics of I_{Na} using patch clamp electrophysiology. a) Cell capacitance measurements exclude overt hypertrophy, **b)** voltage-dependent inactivation and **c)** time-dependent recovery kinetics of I_{Na} in isolated left atrial cardiomyocytes from wildtype and *Scn5a*-M1875T$^{+/-}$ mice.

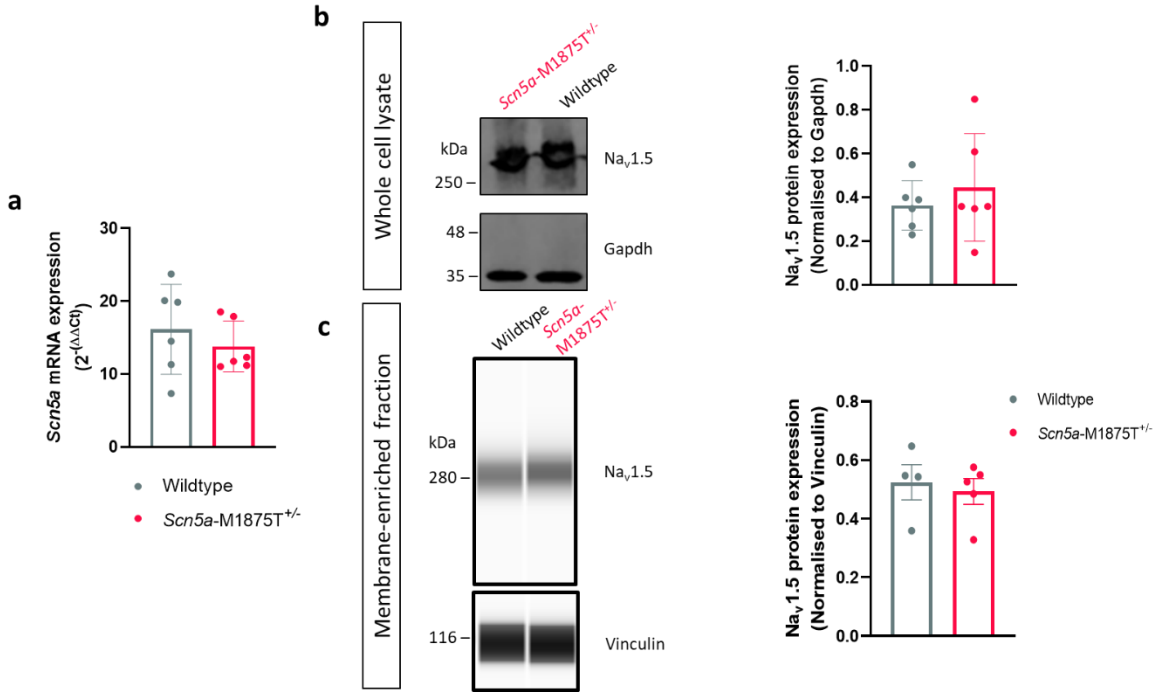


Figure S4: Quantification of *Scn5a* mRNA and $Na_v1.5$ protein expression in the *Scn5a*-M1875T$^{+/-}$ and wildtype mouse hearts, when measured at the whole cell and isolated membrane fraction level. a) *Scn5a* mRNA quantification of LA tissue samples from *Scn5a*-M1875T$^{+/-}$ as well as WT mice measured using RT-qPCR. Expression levels were normalised against GAPDH (n=6 per group).

b) $Na_v1.5$ protein expression levels in left atrial (LA) tissue samples from *Scn5a*-M1875T$^{+/-}$ and wildtype mice were measured using western blotting. GAPDH was used as a loading control. A representative blot is shown (left) with band quantification (right) (n=6 per group). **c)** $Na_v1.5$ protein quantification in membrane-enriched fractions of LA tissue samples from *Scn5a*-M1875T$^{+/-}$ (n=4) and WT (n=5) mice using capillary-based automated western blotting. Vinculin was used as a loading control. The detected protein amount is visualised (left) and area under peak was quantified (right). There were no obvious changes between genotypes.

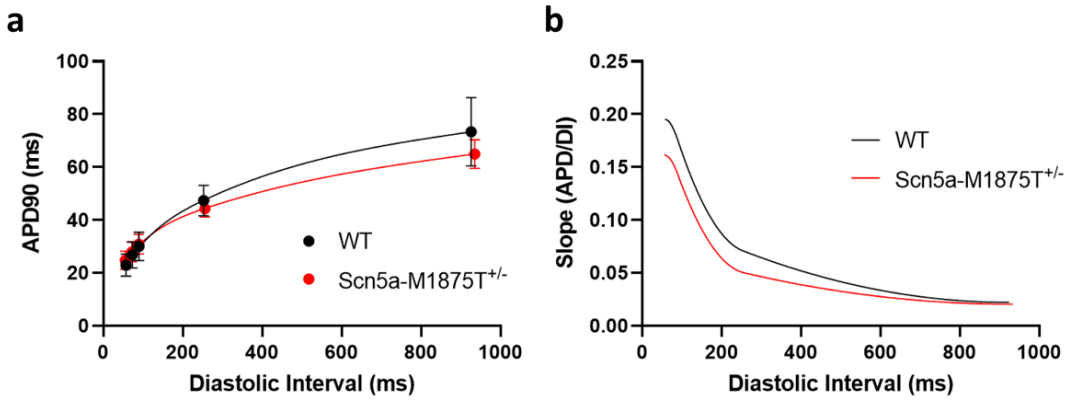


Figure S5: APD restitution analysis from microelectrode experiments in left atria.

Restitution curve (a) and derivative (b) of APD90 as a function of diastolic interval in WT and *Scn5a*-M1875T$^{+/-}$ left atria illustrates a visually more pronounced effect of the M1875T mutation on APD slope at short diastolic intervals (short cycle lengths, high pacing frequencies).

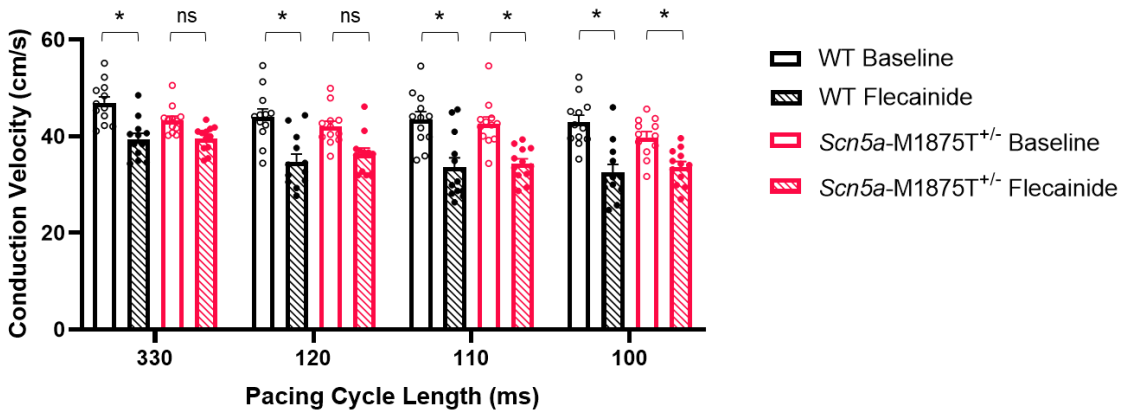


Figure S6: Conduction velocity in left atria from optical mapping experiments at baseline and after addition of 1 µM flecainide at different pacing cycle lengths. Means + SEM are shown. (12 atria per genotype group; ANOVA revealed no significant effect of genotype. ns non-significant; * $p_{adj} < 0.05$; Tukey-corrected post-hoc analysis)

This figure provides additional information to data presented in Figure 5 of the main manuscript.

Supplemental Tables

Parameters	Wildtype	*Scn5a*-M1875T$^{+/-}$	P value
n	19	19	NA
Age (weeks)	16 ± 0.5 (12-18)	15 ± 0.5 (12-18)	0.12
Heart rate (beats/min)	681 ± 7.0 (610-727)	691 ± 6.3 (655-755)	0.30
RR interval (ms)	88 ± 1.0 (83-99)	87 ± 0.8 (80-92)	0.28
P duration (ms)	13 ± 0.4 (9.8-16.5)	13 ± 0.6 (7.3-18.0)	0.23
PR duration (ms)	30 ± 0.7 (26-36)	30 ± 0.6 (26-36)	0.57
QRS duration (ms)	14 ± 0.3 (12-17)	13 ± 0.2 (12-15)	0.28
QT duration (ms)	46 ± 1.1 (40-53)	47 ± 1.0 (39-53)	0.55
R amplitude (mV)	0.35 ± 0.04 (0.10-0.76)	0.37 ± 0.04 (0.11-0.78)	0.74

Table S1: Electrocardiogram (ECG) characteristics of conscious wildtype and *Scn5a*-M1875T$^{+/-}$ mice. Data are expressed as mean ± SEM (range).

Parameters	Wildtype	*Scn5a*-M1875T$^{+/-}$	P value
n	23	21	NA
Age (weeks)	14 ± 0.7 (9-20)	14 ± 0.6 (10-20)	0.95
Heart rate (beats/min)	433 ± 8.2 (388-494)	423 ± 5.3 (393-467)	0.30
RR interval (ms)	139 ± 2.7 (110-155)	142 ± 1.8 (129-153)	0.26
P duration (ms)	16 ± 1.2 (10-25)	15 ± 1.3 (11-25)	0.70
PR duration (ms)	38 ± 1.1 (24-47)	38 ± 1.3 (24-49)	0.83
QRS duration (ms)	15 ± 0.8 (10-23)	16 ± 0.9 (12-25)	0.88

Table S2: Electrocardiogram (ECG) characteristics of unconscious wildtype and *Scn5a*-M1875T$^{+/-}$ mice. Data are expressed as mean ± SEM (range).

Parameter	Wildtype	*Scn5a*-M1875T$^{+/-}$	P value
n	21	26	N/A
Age (weeks)	15 ± 0.6 (9-18)	14 ± 0.6 (9-20)	0.30
Body weight (g)	28 ± 1.2 (19-42)	28 ± 0.8 (23-38)	0.84
Heart rate (beats/min)	438 ± 7.5 (382-501)	427 ± 6.4 (380-499)	0.29
LA diameter (mm)	2.2 ± 0.1 (1.6-2.7)	2.3 ± 0.1 (1.6-2.7)	0.35
LA area (mm^2)	9.7 ± 0.3 (7.1-12.7)	9.4 ± 0.3 (6.6-11.9)	0.54
IVS, d (mm)	0.8 ± 0.03 (0.5-1.1)	0.9 ± 0.02 (0.7-1.1)	0.16
IVS, s (mm)	1.1 ± 0.05 (0.7-1.5)	1.1 ± 0.04 (0.8-1.5)	0.46
LVID, d (mm)	3.9 ± 0.1 (3.0-4.7)	3.9 ± 0.1 (3.2-4.4)	0.88
LVID, s (mm)	2.9 ± 0.1 (1.7-3.6)	2.8 ± 0.1 (1.7-3.5)	0.62
LVPW, d (mm)	0.9 ± 0.04 (0.6-1.2)	0.9 ± 0.04 (0.7-1.3)	0.57
LVPW, s (mm)	1.1 ± 0.1 (0.8-1.6)	1.2 ± 0.1 (0.8-1.5)	0.44
LVEF (%)	52 ± 3.0 (29-82)	53 ± 2.2 (39-83)	0.62
LVFS (%)	25 ± 2.0 (10-49)	28 ± 1.6 (19-51)	0.34
LV mass (mg)	97 ± 5.0 (66-137)	104 ± 4.0 (70-144)	0.32
LV mass/BW	3.5 ± 0.1 (2.7-4.6)	3.7 ± 0.1 (2.8-4.8)	0.16
RVID, d (mm)	1.7 ± 0.07 (1.3-2.2)	1.7 ± 0.04 (1.4-1.9)	0.82

Table S3: Echocardiographic measurements of wildtype and *Scn5a*-M1875T$^{+/-}$ mice. Values are mean ± SEM (range). Mann-Whitney test used for statistical analysis; IVS, interventricular septum; LVID, left ventricular internal diameter; LVPW, left ventricular posterior wall; LVEF, left ventricular ejection fraction; LVFS, left ventricular fractional shortening; LV mass, left ventricular mass; BW, body weight: LA diameter, left atrial diameter; LA area, left atrial area; RVID, right ventricle internal diameter; d, diastole; s, systole.

	Wildtype					*Scn5a*-M1875T$^{+/-}$				
	Pacing cycle length (ms)					Pacing cycle length (ms)				
	1000.00	300.00	120.00	100.00	80.00	1000.00	300.00	120.00	100.00	80.00
APD30	6.3 ±0.2	6.5 ±0.2	5.5 ±0.1	5.3 ±0.1	4.8 ±0.1	5.7 ±0.1	6.0 ±0.1	5.6 ±0.1	5.3 ±0.1	5.0 ±0.1
APD50	12.5 ±0.5	11.3 ±0.4	8.8 ±0.2	8.1 ±0.2	7.3 ±0.1	10.8* ±0.2	10.3 ±0.2	8.8 ±0.2	8.3 ±0.2	7.6 ±0.2
APD70	38 ±1.9	24 ±0.9	15 ±0.5	13 ±0.4	12 ±0.3	31 ±0.8	21 ±0.4	15 ±0.4	14 ±0.4	12 ±0.3
APD90	73 ±2.6	47 ±1.2	30 ±1.1	27 ±1.0	23 ±0.8	65* ±1.1	44 ±0.6	31 ±0.7	28 ±0.8	25 ±0.7
APA (mV)	102 ±0.8	99 ±0.8	88 ±0.7	86 ±0.7	84 ±0.7	105 ±0.5	103 ±0.6	93* ±0.5	91* ±0.5	88* ±0.5
dV/dt (mV/ms)	162 ±2.1	154 ±1.8	132 ±1.6	128 ±1.5	120 ±1.6	172 ±2.0	166 ±1.8	147** ±1.3	144** ±1.3	135** ±1.1
RMP (mV)	-84 ±0.3	-82 ±0.3	-73 ±0.4	-72 ±0.4	-71 ±0.5	-84 ±0.5	-82 ±0.5	-75 ±0.5	-73 ±0.4	-72 ±0.3
AT (ms)	4.6 ± 0.1	4.7 ± 0.1	4.7 ± 0.1	4.8 ± 0.1	5.1 ± 0.2	4.6 ± 0.2	4.7 ± 0.2	4.7 ± 0.1	4.8 ± 0.1	5.1 ± 0.1

Table S4: Action potential characteristics in wildtype and *Scn5a*-M1875T$^{+/-}$ left atria at all pacing cycle lengths tested using the sharp microelectrode technique. Stated are means ± SEM for: action potential durations (APDs) at 30 (APD30), 50 (APD50), 70 (APD70) and 90% (APD90) repolarisation, action potential amplitude (APA), peak upstroke velocity (dV/dt), resting membrane potential (RMP) and activation times (ATs), at pacing cycle lengths (PCLs) of 80, 100, 120, 300 and 1000 ms. At 1000 ms PCL, APD50 and APD90 were significantly reduced in *Scn5a*-M1875T$^{+/-}$ left atria relative to wildtype. APA was significantly larger in *Scn5a*-M1875T$^{+/-}$ mutants at PCLs of 80-300 ms. dV/dt was faster in mutants when tested at PCLs of 80-120 ms. No significant changes in RMP or AT were detected at any PCL. Values are shown here for reference and as mean ± SEM. *p<0.05, **p<0.01, WT vs *Scn5a*-M1875T$^{+/-}$, N=8 per group, n=24 WT, n=25 *Scn5a*-M1875T$^{+/-}$).

Extended methods

Generation of the *Scn5a*-M1875T construct and knock-in mouse model

Targeting construct design:

The 3.7 kb genomic region, containing exon 28 of the *Scn5a* gene and right flanking region (RFR) was PCR amplified from mouse genomic DNA and (T-C) mutated using combination of subsequent PCR reactions with help of oligonucleotide pairs SCN5aA1d / SCN5aA1r, SCN5aA2d / SCN5aA2r and SCN5aMUT, subcloned and sequenced. The 5.1 kb left flanking region (LFR) containing exons 25-27, and intronic sequences was PCR amplified from mouse genomic DNA using oligonucleotides SCN5aBcld / SCN5aBclr and subcloned. The 1.3 kb genomic region, containing exon 24 and intronic sequences was added to the LFR. All individual clones were verified by sequencing and assembled into the final targeting construct (pSCN5a_targ3) in the order depicted in Figure 1a. The pBluescript based plasmid backbone together with the negative selection marker (thymidine kinase cassette) were added to the left flanking region (not shown). The 1.9 kb DNA fragment, containing a positive selection marker (neomycin cassette flanked by two LoxP sites) was cloned between LFR and RFR.

Southern blot DNA probes cloning:

The 1.4 kb HR probe was PCR amplified from mouse genomic DNA using oligonucleotides SCN5aHRd2 and SCN5aHRr2, subcloned and sequenced. The So1, So2, So3, So4 and So5 probes were PCR amplified from mouse genomic DNA, subcloned and sequenced using pairs of oligonucleotides: SCN_SO1D/SCN_SO1R, SCN_SO2D/SCN_SO2R, SCN_SO3D/SCN_SO3R, SCN_SO4D/SCN_SO4R, and SCN_SO5D/SCN_SO5R accordingly.

Scn5a exon 28 specific gRNA's selection and cloning for the CRISPR/cas9 system:

Three gRNA targets were selected in a close proximity to the mutation site. These gRNAs were cloned in plasmid gRNA_Cloning Vector (gift from George Church (Addgene plasmid # 41824))[1] digested with the *Afl*II restriction endonuclease, using the Gibson assembly methods with help of oligonucleotide pairs: SCN5a_ Insert_F/SCN5a_ Insert_R, SCN5a_ Insert_F2/SCN5a_ Insert_R2, and SCN5a_Insert_F3/SCN5a_Insert_R3 resulting in plasmids pgRNA_SCN1, pgRNA_SCN2, and pgRNA_SCN3 accordingly.

ES cell transfection and selection of targeted clones

CV19 ES cells (passage 13 [129Sv x C57BL/6J]) were expanded in HEPES-buffered Dulbecco's modified Eagle's medium supplemented with 15% fetal bovine serum (PAA), nonessential amino acids, L-glutamine, β-mercaptoethanol, 1,000 U per mL of recombinant leukemia inhibitory factor (LIF)

(MERCK Millipore), and antibiotics (penicillin [100 U/ml] and streptomycin [100 µg/ml]). For electroporation, 2 x 10^7 cells were resuspended in 0.8 ml Capecchi buffer (20 mM HEPES [pH 7.4], 173 mM NaCl, 5 mM KCl, 0.7 mM Na_2HPO_4, 6 mM dextrose, 0.1 mM β-mercaptoethanol)[2]. The targeting vector DNA pSCN5a_targ3 (100 µg) was electroporated together with 70 µg of each plasmid DNA's: pgRNA_SCN1, pgRNA_SCN2, pgRNA_SCN3 and hCAS9 (cas9 coding plasmid was a gift from George Church (Addgene plasmid # 41815))[1] at 25 µF and 400V in 0.8 mm electroporation cuvettes (Gene Pulser; Bio-Rad). After electroporation, cells were cultivated for 10 min at room temperature and plated onto ten 100-mm diameter culture dishes containing a gamma-irradiated monolayer of mouse primary G418-resistant fibroblast feeder cells. Thirty-two hours later, 350 µg of G418 (Invitrogen) per mL and 0.2 µM 2'-deoxy-2'-fluoro-β-D-arabinofuranosyl-5-iodouracil (FIAU) (Moravek Biochemicals and Radiochemicals, USA) were added to the culture medium. The medium was replaced every day, and colonies were picked and analysed 8 days after plating.

DNA Southern blot analysis

Positively targeted ES cell clones were analyzed using the Southern-blot DNA method. Approximately 5-10 µg of genomic DNA was digested with *Eco*RI, fractionated on 0.8% agarose gels, and transferred to GeneScreen nylon membranes (NEN DuPont). The membranes were hybridized with a ^{32}P-labeled 1.4 kb HR probe and washed with (final concentrations) 0.5x SSPE (1x SSPE is 0.18 M NaCl, 10 mM NaH_2PO_4, and 1mM EDTA [pH 7.7]) and 0.5% sodium dodecyl sulfate at 65°C. After first screening, correctly targeted clones were proven using the *Bam*HI and additionally *Hind*III digestion, using a ^{32}P-labeled 1.8 kb probe So3 containing internal sequences to the targeted homology. The Southern blot analysis of DNA samples isolated from F1 mouse tail biopsy using probe So3 is presented on (Figure 1b).

Blastocyst injection

Correctly targeted ES cells from 9C clone were injected into 3.5-day B6D2F1 blastocysts. Routinely, we are injecting 12 to 14 ES cells into one blastocoele. After injection, blastocysts were kept in KSOM medium and subsequently transferred into the uteri of 2.5-day pseudopregnant CD-1 foster mice. The mice carried pups to term. Chimeras were identified by their agouti coat colour contribution. For the germ-line transmission high percentage male chimaeras were crossed to the C57BL/6J female mice. Heterozygous agouti offsprings (*Scn5a*-M1875$^{+/-}$) were confirmed by Southern blot analysis (Figure 1b), and the mutated part of exon 28 was PCR amplified using primers pair SCN5a_Sequenc_F/ SCN5a_Sequenc_R and sequenced (Figure 1c and Supplementary Figure 1a). Mice were kept in specific pathogen-free animal facilities.

Deletion of the neo cassette

The deletion of the Neo cassette (Figure 1a) was performed by crossing mice with the total CRE deleter transgenic animals and verified by PCR analysis and further confirmed by the Southern blot analysis (not shown), using different probes, including the probe containing the Neo cassette sequences.

List of oligonucleotides used in the study:

SCN5aA1d	*TGATATC*GTGAGGAGCTGGAAGCCTTGAG
SCN5aA1r	CCGTCTGGATCTTCAGGGCATCCATCTC
SCN5aA2d	TGAAGATCCAGACGGAGGAGAAATTCATGG
SCN5aA2r	*TGCGGCCGC*ATTTATACACGAAGCTTAGTGAGAAGTG
SCN5aMUT	GAGATGGATGCCCTGAAGATCCAGACGGAGGAGAAATTCATGG
SCN5aBcld	*TGTCGAC*TGCATGCACTTGATGGCCTCAC
SCN5aBclr	*TGAATTC*CCTAGTCCATCTCCTCCTAACA
SCN5aHRd2	GACTAAGTGATGCTAAAACACAT
SCN5aHRr2	TGTGTGTATGTGTAGAGGTTGTC
SCN_SO1D	*CAGTCTCAAGCGTCTCTTGGAGTCGA*CCTCACTACAGCCGCACACTCAC
SCN_SO1R	*CTGCTCTAGACGTCTCTGAGAGTCGA*CCAAGAAAGTCAGGCTAGCAGAGAG
SCN_SO2D	*CAGTCTCAAGCGTCTCTTGGAGTCGAC*AGAATAAATAACATCTACTCCATAAG
SCN_SO2R	*CTGCTCTAGACGTCTCTGAGAGTCGAC*AAGTCAAGGAAGACATAGCAG
SCN_SO3D	*CAGTCTCAAGCGTCTCTTGGAGTCGA*CTAGGCTGATGCAGTGCTGAAG
SCN_SO3R	*CTGCTCTAGACGTCTCTGAGAGTCGAC*ACATGTACAGTGTGTTTCCCGTT
SCN_SO4D	*CAGTCTCAAGCGTCTCTTGGAGTCGAC*TCCTGCTGGCTTTTGATTGTGC
SCN_SO4R	*CTGCTCTAGACGTCTCTGAGAGTCGAC*AAAAGGGACATCTCTTGGGAAACT
SCN_SO5D	*CAGTCTCAAGCGTCTCTTGGAGTCGA*CAGAAAACTTGAGCCAATCCAC

SCN_SO5R	*CTGCTCTAGACGTCTCTGAGAGTCGA*CCCCGTGGGCACCGTTTAG
SCN5a_ Insert_F	TTTCTTGGCTTTATATATCTTGTGGAAAGGACGAAACACCGGCCCTGAAGATCCAGATGG
SCN5a_ Insert_R	GACTAGCCTTATTTTAACTTGCTATTTCTAGCTCTAAAACCCATCTGGATCTTCAGGGCC
SCN5a _Insert_F2	TTTCTTGGCTTTATATATCTTGTGGAAAGGACGAAACACCGCTCGGGGAGTCTGGGGAGA
SCN5a _Insert_R2	GACTAGCCTTATTTTAACTTGCTATTTCTAGCTCTAAAACTCTCCCCAGACTCCCCGAGC
SCN5a _Insert_F3	TTTCTTGGCTTTATATATCTTGTGGAAAGGACGAAACACCGTAGGAGATCTTGGAAGGAT
SCN5a _Insert_R3	GACTAGCCTTATTTTAACTTGCTATTTCTAGCTCTAAAACATCCTTCCAAGATCTCCTAC
SCN5a_Sequenc_F	GCCCTGTCCGACTTTGCCGAT
SCN5a_Sequenc_R	CTGGCGGAAGAGGAAGGAAGCAT

Sequences used for cloning are italicized. Scn5a-M1875T mutated nucleotide is underlined.

mRNA and protein expression levels

RNA preparation and quantitative real-time PCR

RNA was purified from LA and left ventricle tissue as previously described [3]. Briefly, LA and left ventricle tissue was homogenised using the Precellys homogeniser (Precellys) and the RNA was purified using the RNEasy mini kit (Qiagen). Total RNA (1 µg) was used as a template for reverse transcription with the High-Capacity cDNA Reverse Transcription kit (Thermo Fisher) according to the manufacturer's protocol. A TaqMan® probe to *Scn5a* (Mm01342518_m1; Applied Biosystems) was used to quantify mRNA levels by RT-PCR using TaqMan™ Universal PCR Master Mix. *Gapdh* (Mm99999915_g1; Applied Biosystems) was used for normalisation. The results of six separate experiments, each calculated from three technical replicates, were pooled using the ΔΔCt method.

Western blotting methods

Western blotting of whole LA, RA and LV protein lysate was carried out as previously described [3]. Briefly, snap-frozen cardiac chambers were lysed in ice-cold radioimmune precipitation buffer (Sigma) with Halt Protease and Phosphatase Inhibitor mixture (Thermo Fisher) using a mechanical Precellys

24 tissue homogeniser (Precellys) or cryogrinding. Total protein concentration was quantified using the DC Protein Assay kit (Bio-Rad). After normalisation of protein concentration using SDS reducing sample buffer, samples were denatured at 95°C for 5 minutes before being resolved by SDS-PAGE and immunoblotted using primary antibodies directed against Nav1.5 (D9J7S; Cell Signaling) or pro-ANP (ab180649, Abcam). Quantification of GAPDH protein expression (14C10; Cell Signaling) served as a loading control. Protein-antibody complexes were visualised using HRP-based chemiluminescence.

To collect a membrane enriched LA protein lysate, the LA was homogenised in ice cold lysis buffer (50 mM Tris-Base (pH 7.5), 2 mM EDTA, 5 mM EGTA, 5 mM DTT, 0.05% Digitonin) supplemented with Halt Protease and Phosphatase Inhibitor mixture. Cytoplasmic fraction was collected through centrifugation at 17,000 g for 30 minutes at 4°C. The resulting pellet was resuspended in ice cold lysis buffer supplemented with 1% Triton-X before repeating centrifugation. The resulting supernatant was defined as a membrane-enriched fraction. Protein concentration was determined using DC protein assay (Bio-Rad). $Na_v1.5$ protein expression was determined in the membrane fraction using Western capillary electrophoresis (WES) method (ProteinSimple, San Jose, CA). Left atrial membrane fractions from wild-type mice and mice possessing the mutation were loaded into WES 13-well plates for separation using capillary electrophoresis (66-440 kDa) following manufacturer's instructions. Antibodies directed against $Na_v1.5$ (Cell Signalling) and Vinculin (Cell signalling) were both used at a dilution of 1:50 in antibody diluent (ProteinSimple). The relative amount of each protein was analysed through the areas under peaks from the chemiluminescence chromatograms by Compass for SW software (ProteinSimple).

ECG recordings *in vivo*

Non-invasive electrocardiograms (ECG) were recorded in conscious young adult mice (8-19 weeks) using a tunnel system for gentle restraint (ecgTunnel, EMKA Technologies, Paris, France) [4]. ECG recordings of 3-6 minutes were analysed using ECGauto software (EMKA Technologies, Paris, France). by constructing 3-5 average signals from 20 consecutive beats each. ECGs were also recorded in isoflurane-sedated mice during echocardiography as below.

Echocardiography *in vivo*

Transthoracic echocardiography was performed in sedated mice (0.5-2% isoflurane, supplemented with 100% O_2) kept on a heated platform using the Vevo® 2100 system (VisualSonics, Amsterdam, Netherlands) as reported previously [5]. In order to improve image quality, the thorax of the mice was

shaved and remaining hair removed using depilatory cream. Heart rate was maintained at 450 ± 70 bpm.

Left atria (LA) were visualised in the parasternal long axis view in the plane of the aortic root. LA area and diameter were measured during pre-atrial contraction, using the P-wave of the limb ECG trace as a guide.

Histological analysis

Hearts were fixed in formalin and paraffin-embedded tissues were cut into slices of 4 µm. Sections were dewaxed, stained with hematoxylin and eosin for overviews and subsequently dehydrated, embedded and imaged on a NanoZoomer 2.0-HAT (Hamamatsu).

Slides used for quantitative analysis were cooked in citrate buffer for antigen retrieval. Autofluorescence was quenched with a 0.25% Sudan black solution for 30 min and samples were blocked with 2% BSA/2.2% Glycine for 1 h at room temperature (RT). Wheat germ agglutinin (WGA) with Alexa Fluor™ 488 Conjugate (1:200, W11261, Invitrogen) was applied for 2 h at RT.

Images of WGA-stained cardiac tissue were obtained with a confocal microscope equipped with an Aurox Clarity (Aurox Ltd.) spinning disc unit and a 20x EC Plan-Neofluar objective (420353-9900-000, Zeiss, NA=0.5) run with Aurox Visionary (Aurox Ltd.) software.

Quantitative analysis of WGA-stained area and cardiac cell diameters was carried out using a published ImageJ plugin for atrial histological analysis (JavaCyte[6]), with minor adjustments.

Atrial cardiomyocyte isolation

Murine hearts were excised under deep terminal anaesthesia (4% isoflurane inhalation in O_2, 1.5 L/min) and perfused at 4 mL.min^{-1} at 37°C on a vertical Langendorff apparatus with the following solutions, equilibrated with 100% O_2: (i) HEPES-buffered, Ca^{2+}-free, modified Tyrode's solution containing in mM: NaCl 145, KCl 5.4, $MgSO_4$ 0.83, Na_2HPO_4 0.33, HEPES 5, and glucose 11 (pH 7.4, NaOH) x 5 min; (ii) Tyrode's enzyme solution containing 640 µg/mL collagenase type II (270 U/mg), 600 µg/ml collagenase type IV (270 U/mg) and 50 µg/mL protease (Worthington, Lakewood, NJ), 20 mM taurine and 3 µM $CaCl_2$ × 8-12 min. The heart was removed from the Langendorff setup and perfused with 5 mL of modified Kraftbruhe (KB) solution containing in mM: DL-potassium aspartate 10, L-potassium glutamate 100, KCl 25, KH_2PO_4 10, $MgSO_4$ 2, taurine 20, creatine 5, EGTA 0.5, HEPES 5, 0.1% BSA, and glucose 20 (pH 7.2, KOH).

The LA was dissected free and cardiomyocytes were dissociated gently with fire-polished glass pipettes (2 to 1 mm diameter in sequence). Cells were re-suspended in 2 mL KB buffer and Ca^{2+} was

gradually reintroduced to the cell suspension incrementally over a period of 2 hours to reach a final concentration of 1 mM. All experiments were performed within 8 hours of isolation.

Whole-cell patch clamp electrophysiology of isolated atrial cardiomyocytes

Dissociated murine LA cardiomyocytes were plated on, and allowed to adhere to, laminin-coated coverslips (10 mm diameter) for at least 20 minutes. Coverslips were transferred to a recording chamber and were continually superfused at 3 mL.min^{-1}, with a low Na^+ external solution containing in mM; NaCl 10, KCl 4.5, $C_5H_{14}ClNO$ 130, $CaCl_2$ 1, $MgCl_2$ 1.2, HEPES 10 and glucose 10 (pH 7.4 with CsOH). To block L-type Ca^{2+} currents, 2 mM $NiCl_2$ was added to the superfusate. Experiments were performed at 22 ± 0.5°C. Whole-cell patch clamp recordings were obtained in voltage-clamp mode using borosilicate glass pipettes (tip resistances 1.5-3 MΩ) .

For Na^+ current recordings, the pipette solution contained in mM: CsCl 115, NaCl 5, EGTA 10, HEPES 10, MgATP 5, TEACl 20 and $MgCl_2$ 0.5 (pH 7.2, KOH). Voltage-dependent Na^+ currents were evoked by 5 mV step depolarisations (100 ms) from a holding potential of -100 mV to test potentials ranging from -95 mV to +40 mV. Cells were excluded from analysis if there was no reversal of the sodium current by +40mV. To investigate $Na_v1.5$ voltage-dependent inactivation kinetics, cells were subject to 500 ms pre-pulses ranging from -120 mV to -40 mV, followed by a 100 ms step to -30 mV. For $Na_v1.5$ time-dependent recovery kinetics, a standard two pulse protocol was used (-120 mV to -30 mV, 20 ms), with the time between the two pulses incrementally varying between 5 and 950 ms.

All recordings and analysis protocols were performed using an Axopatch 200B amplifier (Molecular Devices, USA) and digitized at 50 kHz using a CED micro1401 driven by Signal v6 software (Cambridge Electronic Design, Cambridge, UK). Series resistance was compensated, ranging between 60-100% for all cells. Experiments were terminated if series resistance abruptly changed or was above 10 MΩ.

Atrial microelectrode recordings

Our investigations focus on the left atrium (LA). This is mostly due to practical reasons, e.g. less spontaneous activity in the left compared to the right atrium.

As previously described [7-9], following isolation the LA was immediately transferred into a dissecting chamber and continuously superfused at 10 mL.min^{-1} with a bicarbonate buffered Krebs-Henseleit (KH) solution containing in mM: NaCl 118; $NaHCO_3$ 24.88; KH_2PO_4 1.18; Glucose 11; $MgSO_4$ 0.83; $CaCl_2$ 1.8; KCl 3.52, equilibrated with 95% O_2/5% CO_2, 36-37°C, pH 7.4. Micro-dissection and pinning out of the LA was performed using a dissection microscope (Stemi SV 11, Zeiss, Germany). The LA was paced at 1–10 Hz via bipolar platinum electrodes. Action potentials (APs) were recorded from freely contracting LA using custom made glass floating microelectrodes containing 3 M KCl, (resistance 15-

30 MΩ). Voltage signals were amplified and digitised at 20 kHz and were unfiltered (Axoclamp 2B; Molecular Devices, California, USA; Spike2 software Cambridge Electronic Design, Cambridge, UK). Measured parameters included the resting membrane potential (RMP), action potential amplitude (APA), peak depolarisation rate (dV/dt) and action potential duration (APD) at 30-90% repolarisation. APs were only analysed following sufficient rate adaptation achieved after at least 50 stimulated APs at each frequency.

Atrial optical mapping

Optical mapping of the LA was conducted as previously described [10, 11]. Isolated whole hearts were loaded on to a vertical Langendorff apparatus and perfused with a standard KH solution. Hearts were perfused at 4 mL.min^{-1} (equilibrated with 95%O_2/5%CO_2 and heated to 36-37°C, pH 7.4). Hearts were loaded with 25 µL of voltage sensitive dye Di-4-ANEPPS at a concentration of 5 mg/mL, diluted in 1 mL of KH solution and delivered via bolus port injection over 3-5 minutes. The LA was then isolated and pinned in a superfusion chamber containing 37°C KH solution for transfer to the optical mapping setup, anterior surface facing up.

In the optical mapping system, atria were superfused with KH solution (95%O_2/5%CO_2, 36-37°C) containing contraction uncoupler Blebbistatin (35 µM). For imaging, atria were illuminated by two dual LEDs at 530 nm. A 630 nm long-pass filter was used to separate emitted fluorescence, imaged using an ORCA flash 4.0 CMOS camera (Hamamatsu, Japan). Images were acquired at a framerate 0.987 kHz and pixel size of 71 µm/pixel^2. Atria were paced using bipolar platinum electrodes delivering 2 ms pulses at twice diastolic threshold (minimum voltage required to elicit APs).

One-minute baseline recording was taken following a 10 minute equilibration period to ensure contraction uncoupling and temperature re-stabilisation. During imaging, atria were initially paced at 330 ms pacing cycle length (PCL). A 'ramp' pacing protocol was then initiated, in which the atria were paced at 120 ms PCL for 100 stimuli and then PCL was reduced from 120 ms to 80 ms in 10 ms intervals every 20 stimuli. After taking baseline recordings, LED illumination was switched off and the superfusion solution replaced with an identical solution containing flecainide, a clinically-used sodium channel blocker[12] at a concentration of 1 µM and then 5 µM (or control solution without flecainide for time control experiments).

Subsequent recordings were then made as described above after 20 minutes superfusion with 1 µM flecainide solution, and then further 15 minutes with 5 µM flecainide solution. Atria were paced at 330 ms PCL continuously in dark conditions between recordings.

From these recordings, APD and conduction velocity (CV) were mapped across the LA using ElectroMap software [11]. Atria were removed from analysis at a given PCL if loss of 1:1 capture ratio with pacing stimuli (i.e. missed beats) was observed.

Supplemental References

[1] Mali P, Yang L, Esvelt KM, Aach J, Guell M, DiCarlo JE, et al. RNA-guided human genome engineering via Cas9. *Science (New York, NY)* 2013; **339**: 823-826.

[2] Thomas KR, Capecchi MR. Site-directed mutagenesis by gene targeting in mouse embryo-derived stem cells. *Cell* 1987; **51**: 503-512.

[3] Reyat JS, Chua W, Cardoso VR, Witten A, Kastner PM, Kabir SN, et al. Reduced left atrial cardiomyocyte PITX2 and elevated circulating BMP10 predict atrial fibrillation after ablation. *JCI Insight* 2020; **5**.

[4] Silbernagel N, Walecki M, Schafer MK, Kessler M, Zobeiri M, Rinne S, et al. The VAMP-associated protein VAPB is required for cardiac and neuronal pacemaker channel function. *FASEB J* 2018; **32**: 6159-6173.

[5] Blana A, Kaese S, Fortmüller L, Laakmann S, Damke D, van Bragt K, et al. Knock-in gain-of-function sodium channel mutation prolongs atrial action potentials and alters atrial vulnerability. *Heart Rhythm* 2010; **7**: 1862-1869.

[6] Winters J, von Braunmuhl ME, Zeemering S, Gilbers M, Brink TT, Scaf B, et al. JavaCyte, a novel open-source tool for automated quantification of key hallmarks of cardiac structural remodeling. *Scientific reports* 2020; **10**: 20074.

[7] Holmes AP, Yu TY, Tull S, Syeda F, Kuhlmann SM, O'Brien SM, et al. A Regional Reduction in Ito and IKACh in the Murine Posterior Left Atrial Myocardium Is Associated with Action Potential Prolongation and Increased Ectopic Activity. *PLoS One* 2016; **11**: e0154077.

[8] Syeda F, Holmes AP, Yu TY, Tull S, Kuhlmann SM, Pavlovic D, et al. PITX2 Modulates Atrial Membrane Potential and the Antiarrhythmic Effects of Sodium-Channel Blockers. *J Am Coll Cardiol* 2016; **68**: 1881-1894.

[9] Lemoine MD, Duverger JE, Naud P, Chartier D, Qi XY, Comtois P, et al. Arrhythmogenic left atrial cellular electrophysiology in a murine genetic long QT syndrome model. *Cardiovascular research* 2011; **92**: 67-74.

[10] Yu TY, Syeda F, Holmes AP, Osborne B, Dehghani H, Brain KL, et al. An automated system using spatial oversampling for optical mapping in murine atria. Development and validation with monophasic and transmembrane action potentials. *Prog Biophys Mol Biol* 2014; **115**: 340-348.

[11] O'Shea C, Holmes AP, Yu TY, Winter J, Wells SP, Correia J, et al. ElectroMap: High-throughput open-source software for analysis and mapping of cardiac electrophysiology. *Sci Rep* 2019; **9**: 1389.

[12] Ramos E, O'Leary M E. State-dependent trapping of flecainide in the cardiac sodium channel. *J Physiol* 2004; **560**: 37-49.

8 Chapter VIII - Conclusions

8.1 Thesis outcomes

The overall aim of this thesis was to gain new insights into inheritable drivers of atrial arrhythmia. Clinical observations were used as a basis for murine experimental study designs. Several methodologies as outlined in 'Thesis motivation and structure' were validated and applied and findings are detailed in published work and preprints.

An audit of ARVC patients seen at an inherited cardiac conditions clinic at UHB allowed to confirm that atrial arrhythmias are a common clinical feature of ARVC. Underlying atrial remodeling is indicated by changes in P wave characteristics in these patients. We also report a phenocopy of human atrial ECG features found in ARVC in mice used as a disease model, confirming the eligibility of these models to study atrial electrophysiology in this context.

By chronically increasing testosterone concentrations in mice, a disease modifier of both ARVC and AF was studied. Testosterone elicits expression of pro-inflammatory, pro-fibrotic and hypertrophic gene signatures in murine atria. In atrial cardiomyocytes with vulnerable desmosomes, increased concentrations of testosterone cause a decrease in atrial peak sodium currents. Super-resolution microscopy of atrial cardiomyocytes and subsequent modelling suggest reduced clustering and availability of the $Na_v1.5$ at the cardiomyocyte membrane as an underlying mechanism.
Apart from desmosomes, , another cellular microdomain involved in arrhythmogenesis, the cardiac sodium channel, was investigated. The point mutation M1875T in the C-terminus of the cardiac sodium channel alpha-subunit $Na_v1.5$ leads to a gain-of-function and atria show a blunted response to the clinically used sodium channel blocker flecainide. These observations can at least in part explain the ectopic activity inert to anti-arrhythmic therapy observed in patients carrying this mutation.

Overall, these findings confirm that important lessons can be learned from electrophysiological studies in murine models and gained insights can potentially be translated back to clinical practice.

8.2 General conclusions and limitations

The pathogenesis and penetrance of arrhythmia syndromes like ARVC and AF appears very diverse [1-8]. With this broad spectrum, generating a "one size fits all" therapeutic approach seems unlikely. Instead, therapy likely has to become personalized, highlighting the need to identify and characterize subgroups of patients, e.g. those suffering from inherited forms of arrhythmias. Murine models are an important tool to understand individual drivers of (atrial) arrhythmia and hence can potentially guide clinical decision making if confirmed in patients. However, due to differences in cardiac anatomy and electrophysiology between mice and men, obtained results require careful validation.

8.2.1 Limitations of electrophysiological studies in murine models

One obvious difference between human and murine cardiac cardiovascular physiology is the size of the heart. Different parts of the atria and conduction system can possess different expression patterns of e.g., ion channels and connexins and resulting electrical and structural properties [9, 10]. Spatially resolving these parts using experimental approaches in murine models is challenged by their small size, but technological advancements have made investigating e.g. different parts of the atria possible. With 400 bpm [11] at rest and up to 750 bpm during stress [12] the heart rate in mice is up to 10 times higher than in humans. A marked difference in heart rate might entail differences in energy consumption and metabolism. A higher heart rate inherently comes with shorter duration of cardiac action potentials. Differences in action potential shape between mouse and men are mainly caused by deviations in potassium currents, carrying the plateau and repolarization phase of the action potential [13-18]. Even though differences are present for the plateau and the repolarization phase of the action potential, **de**polarizing currents share great similarity between mice and men [19]. Depolarization is mainly driven by opening of $Na_v1.5$ channels in both species. The mouse therefore

is an eligible model to decipher changes in sodium current and resulting pathophysiological effects, like the case for the two murine studies conducted in this thesis.

The repolarization differences of action potentials also impact ECG morphology and hence not all ECG features are shared between mice and humans. Most prominently, the murine ECG displays a J wave, but lacks an isoelectric ST segment [20, 21]. However, P wave morphology is very similar across both species, as reported by others [22] and in shown in Chapter VI. Interestingly, the PR interval, another parameter studied in this thesis, scales with body mass [23]. Even subintervals of the PR scale with the same exponent [24] because of conserved anatomical properties of cardiac pacemaking and conduction.

8.2.2 Eligibility of murine models to decipher ARVC

The usage of mouse models for ARVC research has been debated, since the profile of the human disease phenotype is not always recapitulated fully in these models. Cardiac fatty infiltration is lacking in mice, but has ceased to be a diagnostic criterion in patients just as well. Previously reported and new findings from our group confirm the phenocopy of main disease features, including ventricular arrhythmias [25] and ECG abnormalities described in Chapter VI.

In the past 25 years, more than 20 different mouse models have been used to study the ARVC-related desmosomal genes and proteins Plakophilin-2, Plakoglobin, Desmoplakin and Desmoglein 2 [26, 27]. With identification of variants in non-desmosomal genes this list can be extended. Murine models led to important discoveries in the field and were instrumental to causally link desmosomal defects to the human disease when it was first described [27].

Alternative models like induced pluripotent stem cell-derived cardiomyocytes are often still limited in their ability to possess electrical and mechanical integrity at the level of a mature heart [28]. Organized intercalated disc structures are hardly observed but seem essential to start with, when aiming to draw conclusions about pathophysiological mechanisms resulting from vulnerable cell

contacts. Further maturing three dimensional contracting engineered heart tissue seems attractive in order to use this as a model for cardiomyopathy.

8.2.3 Eligibility of murine models to decipher AF

Murine models have been employed to study mechanisms of atrial arrhythmia due to alterations in G-protein coupled receptor signaling, ion channel function, anchoring and junctional complexes, calcium dynamics, transcriptional, post transcriptional and epigenetic regulation as well as growth factors and cytokines [29]. Even though neglected by some [30], spontaneously occurring sustained atrial arrhythmia have been described in transgenic mice [31, 32]. This observation goes in line with the fact that the ratio of atrial circumference to wavelength, a quantitative measure for the possible number of reentrant waves to "fit" into the atrium does not majorly increase with increasing body mass [23]. The likelihood of sustained atrial arrhythmia in mice should therefore not be smaller than in men. With atrial effective refractory period (ERP) and conduction velocity (CV), two important factors for e.g., formation of reentrant arrhythmia do proportionally increase with body mass. Irrespective of their relatively small ERP and slow CV, applying the ERP-shortening neurotransmitter acetylcholine can still facilitate arrhythmia induction in murine atria [33, 34].

Murine models offer the big advantage of enabling us to study alterations in ion channel function in a physiological setting with all accessory and interacting proteins, as opposed to e.g., monolayers of cells in vitro, lacking these features. Furthermore, channels like $Na_v1.5$ are highly conserved across species. Hence, murine models can be employed to learn how anti-arrhythmic agents targeting the channel elicit their effect or might have no or even harmful effects in patients with certain arrhythmia syndromes.

Overall, animal models offer the major advantage of enabling molecular and electrophysiological cardiac studies at different scales. Investigations can range from intact organs down to single cells by applying various available experimental techniques and can be correlated with in vivo data, e.g. ECG and echocardiography from the very same organism, which is inherently difficult to realize for

affected patients. It remains a major challenge to piece together molecular knowledge on isolated arrhythmia drivers and transfer this to the often complex clinical picture where patients present with various comorbidities and environmental influences. Nevertheless, understanding the individual pieces in full detail will no doubt be essential in tackling this challenge.

Taken together, mouse models are an eligible tool to investigate those inheritable drivers of atrial arrhythmogenesis that were considered in this thesis.

8.3 Outlook

Research questions to be pursued in the future resulting from work in Chapters VI and VII are given below.

Chapter VI highlights that vulnerable desmosomes and increased concentrations of androgenic anabolic steroids jointly impair atrial conduction. Reduced availability of clustered cardiac sodium channels in the membranes of atrial cardiomyocytes were shown as a possible underlying mechanism. It would be of interest to study how localization of sodium channels to the membrane is impaired. Analysis at transcriptional level (RNA sequencing) did not reveal any changes, hence underlying mechanisms affected by the interventions are likely to be mediated at post-translational level. Transport of the channels to the membrane could be insufficient or deteriorated or the membrane-localized sodium channels might run down. Trafficking of sodium channels in cardiomyocytes is still poorly understood[35], which implies the utility of this model to study this process.

Super-resolution microscopy (dSTORM) enabled us to visualize sodium channels at almost single channel level, mainly in the lateral membranes of the atrial cardiomyocytes. The changes were apparent in the lateral membrane , even though a primarily desmosomal defect was studied. It would hence be of great interest to study channel localization and clustering at the intercalated disc microdomain. The dSTORM approach uses a TIRF/HILO configuration for the imaging process which

would require to 'flip' and fixate the isolated cardiomyocytes by 90 degrees. 3D dSTORM [36], requiring even more sophisticated imaging systems, could facilitate investigating the intercalated disc directly.

It remains to be addressed whether the same changes are observed when desmosomal vulnerability is caused by deficiency of other desmosomal genes. Collaborative efforts to build international registries with deeply phenotyped patient data are needed to describe genotype-phenotype correlations in ventricular and atrial pathology. Reduced availability of sodium currents in subgroups of patients would request careful clinical management in regard to anti-arrhythmic drug therapy, i.e., refrain from usage of sodium channel blockers like flecainide. In fact, others have shown flecainide to provoke lethal ventricular arrhythmia in a mouse model heterozygously depleted for the desmosomal gene PKP-2 [37]. On the other hand, a pilot randomized clinical trial (NCT03685149, clinicaltrials.gov) completed in July 2022 with results pending is investigating the effectiveness of flecainide to reduce the number of ventricular ectopic beats in ARVC patients. Certainly, patients should carefully and continuously be evaluated when under this drug regimen.

Chapter VII shows that the point mutation M8175T in the cardiac sodium channel leads to an increased peak sodium current in atrial cardiomyocytes. Additionally, atria of mice heterozygously harboring the mutation show a dampened response to the conduction-slowing effect of the anti-arrhythmic agent flecainide. It is yet to be addressed what is causing the gain-of-function of the sodium channel in mammals. Since we did not observe prolongation of action potentials in the murine model and patients as well as mice exhibited normal QT intervals, we do not expect an enhanced **late** sodium current to be the underlying cause. Patch clamp experiments in murine atrial cardiomyocytes excluded changes in recovery/availability of the sodium channels and protein quantification in membrane-enriched fractions did not reveal major run-down in available channels in this compartment. Altered dimerization or multimerization of sodium channels could be a reason

for increased function. As described in 1.3.4, the methionine residue affected by the mutation is predicted to be part of the interacting surface of two sodium channel C-termini. It would therefore be of interest to investigate sodium channel dimerization in e.g., cardiomyocytes of the Scn5a-M1875T$^{+/-}$ model in comparison to wild types. Dimerization could be studied with the help of a FRET (Förster resonance energy transfer) system, fusing wildtype and mutated channel constructs to CFP (Cyan fluorescent protein)/YFP (Yellow fluorescent protein), respectively. Expressing these fused constructs in a less complex cell model like HEK293 cells first and then move to viral transfection of isolated cardiomyocytes presents a possible approach. Moreover, computational modeling of the interaction of two predicted sodium channel whole protein structures [38] (so far not possible to crystallize) could aid this effort.

Furthermore, it should be addressed whether the (early) changes in atrial electrophysiological properties uncovered translate to spontaneous arrhythmia in the mouse model. So far, we were able to pick up sinus arrhythmia via ECG recordings in young adult mice, but no ectopic activity or sustained arrhythmia. Single time point ECG recordings only provide a snapshot and cannot be used to conclude on the real arrhythmia burden. Continuous monitoring via telemetry[11] would massively increase the likelihood of picking up arrhythmias. Inducibility of atrial arrhythmias by stimulation protocols can also be tested in isolated heart ex vivo (see Chapter III). Both approaches could be combined with testing the effect of additional stressors, such as adrenergic challenge since some of the patients carrying the mutation suffered from atrial fibrillation after exercise. On the other hand, cholinergic stimulation has been reported to provoke arrhythmic events in models of sodium channel mutations[11] and could also be applied here. Studying the murine model at older age would also be of interest, as SCN5A mutations can show age-dependent phenotypes[39]. Chronically disturbed ion channel homeostasis might lead to more pronounced electrical and even structural remodeling.

We only observed murine offspring heterozygous for the M1875T mutation and no homozygous mice. Intrauterine lethality has been reported for homozygous depletion of the whole *Scn5a* gene [40]

and also for homozygous expression of the ΔKPQ variant [41] in mice and usually occurs around day E10.5. Once established that Scn5a-M1875T$^{+/+}$ embryos are initially present and until what day in embryonic development they survive, this genetic model could be employed to study how a gain-of-function SCN5A variant interferes with cardiac development.

Finally, another lesson learned from the model relates to the dampened effect of the sodium channel blocker flecainide. The mutated residue at position 1875 and the flecainide interaction site within the channel lie within relatively close proximity. The dampened effect of flecainide in atria with this point mutation could be caused by an induced conformational change in the secondary and tertiary structure of the protein. The sodium channel pore-blocking agent flecainide prohibits the entrance of Na^+ ions. This interaction could be less effective in the mutated channels or there might be a higher number of channels to start with. Flecainide occupies a comparatively large binding surface in the channel [42]. Structural changes induced by the mutation might affect flecainide interaction. Applying flecainide during patch clamp could describe the effect further. Testing the effectiveness of other, smaller molecule sodium channel blockers like lidocaine in the Scn5a-M1875T$^{+/-}$ model would allow to pin down a reason for the dampened effect of flecainide. Before-mentioned modeling of the sodium channel protein structure, including induced changes by the point mutation and subsequently interaction with the different drug molecules could be of great support. Knowledge gained would not only enhance the understanding of sodium channel drug interaction, but also guide treatment of patients carrying the investigated mutation.

8.4 References Chapter VIII

[1] Schotten U, Verheule S, Kirchhof P, Goette A. Pathophysiological mechanisms of atrial fibrillation: a translational appraisal. *Physiological reviews* 2011; **91**: 265-325.
[2] Fabritz L, Crijns H, Guasch E, Goette A, Hausler KG, Kotecha D, et al. Dynamic risk assessment to improve quality of care in patients with atrial fibrillation: the 7th AFNET/EHRA Consensus Conference. *Europace : European pacing, arrhythmias, and cardiac electrophysiology : journal of the working groups on cardiac pacing, arrhythmias, and cardiac cellular electrophysiology of the European Society of Cardiology* 2021; **23**: 329-344.
[3] Fabritz L, Guasch E, Antoniades C, Bardinet I, Benninger G, Betts TR, et al. Expert consensus document: Defining the major health modifiers causing atrial fibrillation: a roadmap to underpin personalized prevention and treatment. *Nature reviews Cardiology* 2016; **13**: 230-237.
[4] DeWitt ES, Chandler SF, Hylind RJ, Beausejour Ladouceur V, Blume ED, VanderPluym C, et al. Phenotypic Manifestations of Arrhythmogenic Cardiomyopathy in Children and Adolescents. *J Am Coll Cardiol* 2019; **74**: 346-358.
[5] Protonotarios A, Elliott PM. Arrhythmogenic Cardiomyopathy: A Disease or Merely a Phenotype? *Eur Cardiol* 2020; **15**: 1-5.
[6] Dalal D, James C, Devanagondi R, Tichnell C, Tucker A, Prakasa K, et al. Penetrance of mutations in plakophilin-2 among families with arrhythmogenic right ventricular dysplasia/cardiomyopathy. *J Am Coll Cardiol* 2006; **48**: 1416-1424.
[7] Quarta G, Muir A, Pantazis A, Syrris P, Gehmlich K, Garcia-Pavia P, et al. Familial evaluation in arrhythmogenic right ventricular cardiomyopathy: impact of genetics and revised task force criteria. *Circulation* 2011; **123**: 2701-2709.
[8] Chen L, Song J, Chen X, Chen K, Ren J, Zhang N, et al. A novel genotype-based clinicopathology classification of arrhythmogenic cardiomyopathy provides novel insights into disease progression. *European heart journal* 2019; **40**: 1690-1703.
[9] Hoogaars WM, Engel A, Brons JF, Verkerk AO, de Lange FJ, Wong LY, et al. Tbx3 controls the sinoatrial node gene program and imposes pacemaker function on the atria. *Genes Dev* 2007; **21**: 1098-1112.
[10] Christoffels VM, Burch JB, Moorman AF. Architectural plan for the heart: early patterning and delineation of the chambers and the nodes. *Trends in cardiovascular medicine* 2004; **14**: 301-307.
[11] Fabritz L, Damke D, Emmerich M, Kaufmann SG, Theis K, Blana A, et al. Autonomic modulation and antiarrhythmic therapy in a model of long QT syndrome type 3. *Cardiovascular research* 2010; **87**: 60-72.
[12] Gehrmann J, Hammer PE, Maguire CT, Wakimoto H, Triedman JK, Berul CI. Phenotypic screening for heart rate variability in the mouse. *American journal of physiology Heart and circulatory physiology* 2000; **279**: H733-740.
[13] Li GR, Feng J, Yue L, Carrier M, Nattel S. Evidence for two components of delayed rectifier K+ current in human ventricular myocytes. *Circ Res* 1996; **78**: 689-696.
[14] Bokil NJ, Baisden JM, Radford DJ, Summers KM. Molecular genetics of long QT syndrome. *Mol Genet Metab* 2010; **101**: 1-8.
[15] Xu H, Guo W, Nerbonne JM. Four kinetically distinct depolarization-activated K+ currents in adult mouse ventricular myocytes. *J Gen Physiol* 1999; **113**: 661-678.
[16] Clancy CE, Rudy Y. Na(+) channel mutation that causes both Brugada and long-QT syndrome phenotypes: a simulation study of mechanism. *Circulation* 2002; **105**: 1208-1213.
[17] Li H, Guo W, Yamada KA, Nerbonne JM. Selective elimination of I(K,slow1) in mouse ventricular myocytes expressing a dominant negative Kv1.5alpha subunit. *American journal of physiology Heart and circulatory physiology* 2004; **286**: H319-328.

[18] Lopatin AN, Nichols CG. Inward rectifiers in the heart: an update on I(K1). *J Mol Cell Cardiol* 2001; **33**: 625-638.
[19] Odening KE, Gomez AM, Dobrev D, Fabritz L, Heinzel FR, Mangoni ME, et al. ESC working group on cardiac cellular electrophysiology position paper: relevance, opportunities, and limitations of experimental models for cardiac electrophysiology research. *Europace : European pacing, arrhythmias, and cardiac electrophysiology : journal of the working groups on cardiac pacing, arrhythmias, and cardiac cellular electrophysiology of the European Society of Cardiology* 2021; **23**: 1795-1814.
[20] Boukens BJ, Hoogendijk MG, Verkerk AO, Linnenbank A, van Dam P, Remme CA, et al. Early repolarization in mice causes overestimation of ventricular activation time by the QRS duration. *Cardiovascular research* 2013; **97**: 182-191.
[21] Speerschneider T, Thomsen MB. Physiology and analysis of the electrocardiographic T wave in mice. *Acta Physiol (Oxf)* 2013; **209**: 262-271.
[22] Boukens BJ, Rivaud MR, Rentschler S, Coronel R. Misinterpretation of the mouse ECG: 'musing the waves of Mus musculus'. *J Physiol* 2014; **592**: 4613-4626.
[23] Kaese S, Verheule S. Cardiac electrophysiology in mice: a matter of size. *Frontiers in physiology* 2012; **3**: 345.
[24] Noujaim SF, Lucca E, Munoz V, Persaud D, Berenfeld O, Meijler FL, et al. From mouse to whale: a universal scaling relation for the PR Interval of the electrocardiogram of mammals. *Circulation* 2004; **110**: 2802-2808.
[25] Kirchhof P, Fabritz L, Zwiener M, Witt H, Schafers M, Zellerhoff S, et al. Age- and training-dependent development of arrhythmogenic right ventricular cardiomyopathy in heterozygous plakoglobin-deficient mice. *Circulation* 2006; **114**: 1799-1806.
[26] Lodder EM, Rizzo S. Mouse models in arrhythmogenic right ventricular cardiomyopathy. *Frontiers in physiology* 2012; **3**: 221.
[27] Gerull B, Brodehl A. Genetic Animal Models for Arrhythmogenic Cardiomyopathy. *Frontiers in physiology* 2020; **11**: 624.
[28] Cumberland MJ, Riebel LL, Roy A, O'Shea C, Holmes AP, Denning C, et al. Basic Research Approaches to Evaluate Cardiac Arrhythmia in Heart Failure and Beyond. *Frontiers in physiology* 2022; **13**: 806366.
[29] Riley G, Syeda F, Kirchhof P, Fabritz L. An introduction to murine models of atrial fibrillation. *Frontiers in physiology* 2012; **3**: 296.
[30] Schuttler D, Bapat A, Kaab S, Lee K, Tomsits P, Clauss S, et al. Animal Models of Atrial Fibrillation. *Circ Res* 2020; **127**: 91-110.
[31] Chen HH, Baty CJ, Maeda T, Brooks S, Baker LC, Ueyama T, et al. Transcription enhancer factor-1-related factor-transgenic mice develop cardiac conduction defects associated with altered connexin phosphorylation. *Circulation* 2004; **110**: 2980-2987.
[32] Kirchhof P, Marijon E, Fabritz L, Li N, Wang W, Wang T, et al. Overexpression of cAMP-response element modulator causes abnormal growth and development of the atrial myocardium resulting in a substrate for sustained atrial fibrillation in mice. *Int J Cardiol* 2013; **166**: 366-374.
[33] Kovoor P, Wickman K, Maguire CT, Pu W, Gehrmann J, Berul CI, et al. Evaluation of the role of I(KACh) in atrial fibrillation using a mouse knockout model. *J Am Coll Cardiol* 2001; **37**: 2136-2143.
[34] Wakimoto H, Maguire CT, Kovoor P, Hammer PE, Gehrmann J, Triedman JK, et al. Induction of atrial tachycardia and fibrillation in the mouse heart. *Cardiovascular research* 2001; **50**: 463-473.
[35] Dong C, Wang Y, Ma A, Wang T. Life Cycle of the Cardiac Voltage-Gated Sodium Channel NaV1.5. *Frontiers in physiology* 2020; **11**: 609733.
[36] Shen X, van den Brink J, Hou Y, Colli D, Le C, Kolstad TR, et al. 3D dSTORM imaging reveals novel detail of ryanodine receptor localization in rat cardiac myocytes. *J Physiol* 2019; **597**: 399-418.
[37] Cerrone M, Noorman M, Lin X, Chkourko H, Liang FX, van der Nagel R, et al. Sodium current deficit and arrhythmogenesis in a murine model of plakophilin-2 haploinsufficiency. *Cardiovascular research* 2012; **95**: 460-468.

[38] Jumper J, Evans R, Pritzel A, Green T, Figurnov M, Ronneberger O, et al. Highly accurate protein structure prediction with AlphaFold. *Nature* 2021; **596**: 583-589.
[39] Liu M, Yang KC, Dudley SC, Jr. Cardiac sodium channel mutations: why so many phenotypes? *Nature reviews Cardiology* 2014; **11**: 607-615.
[40] Papadatos GA, Wallerstein PM, Head CE, Ratcliff R, Brady PA, Benndorf K, et al. Slowed conduction and ventricular tachycardia after targeted disruption of the cardiac sodium channel gene Scn5a. *Proc Natl Acad Sci U S A* 2002; **99**: 6210-6215.
[41] Nuyens D, Stengl M, Dugarmaa S, Rossenbacker T, Compernolle V, Rudy Y, et al. Abrupt rate accelerations or premature beats cause life-threatening arrhythmias in mice with long-QT3 syndrome. *Nat Med* 2001; **7**: 1021-1027.
[42] Jiang D, Shi H, Tonggu L, Gamal El-Din TM, Lenaeus MJ, Zhao Y, et al. Structure of the Cardiac Sodium Channel. *Cell* 2020; **180**: 122-134 e110.